Vibration Analysis in Non-Destructive Detection of Milk Powder Blockage in the Cyclone of a Spray Dryer

Li Li

A thesis submitted to
Auckland University of Technology
in partial fulfilment of the requirements for the degree of
Master of Engineering (ME)

2008

School of Engineering

Primary Supervisor: Ahmed Al-Jumaily

Table of contents

TABLE OF CONTENTS ..... **I**

LIST OF FIGURES ..... **IV**

LIST OF TABLES ..... **IX**

LIST OF ABBREVIATIONS ..... **XII**

STATEMENT OF ORIGINALITY ..... **XIII**

ACKNOWLEDGEMENTS ..... **XIV**

CONFIDENTIAL MATERIAL-PG18 FORM ..... **XV**

ABSTRACT ..... **XVI**

CHAPTER 1 INTRODUCTION **1**

1.1 Background 1

1.2 Milk powder spray drying system 2

1.2.1 Structure and principle of a spray dryer 2

1.2.2 Cyclone separator 3

1.2.3 Reasons for the formation of milk powder deposition or blockages 5

1.3 Objectives 6

1.4 The structure of the thesis 7

CHAPTER 2 NON-DESTRUCTIVE TESTING (NDT) AND LITERATURE REVIEW **8**

2.1 Introduction 8

2.2 Ultrasonic method 8

2.2.1 Conventional ultrasonic techniques 9

2.2.1.1 Application of conventional ultrasonic to measure thickness 10

2.2.1.2 Application of conventional ultrasonic in monitoring deposition 11

2.2.2 Guided wave 13

2.2.2.1 Application of guided wave for detecting defect 14

2.2.2.2 Guided wave attenuation for detecting deposit on pipe wall 16

2.3 Vibration analysis 18

2.4 Acoustic impact method 20

2.5 Possible NDT techniques for this research 21
2.6 Research methodology 22
2.7 Closure 24

CHAPTER 3 MODAL ANALYSIS 25

3.1 Introduction 25
3.2 Natural frequency 25
3.2.1 Circular cylindrical shell vibration theory 27
3.2.2 Numerical analysis 30
3.2.2.1 Modelling using ABAQUS 31
3.2.2.2 Closure 38
3.2.3 Beam theory 38
3.2.4 Transverse vibration of beam-mass systems 42
3.2.4.1 Exact analysis 42
3.2.4.2 Approximate method 50
3.3 Damping ratio 52
3.3.1 Logarithmic decrement method 52
3.3.2 Half-power bandwidth method 53
3.4 Closure 54

CHAPTER 4 VIBRATION TESTING AND EXPERIMENTAL MODAL ANALYSIS 56

4.1 Introduction 56
4.2 Frequency response function 57
4.3 Resonance search test methods 59
4.4 Experimental testing procedures 60
4.4.1 Vibration testing instrumentation 61
4.4.2 Simulated amount mass 66
4.4.3 Flour induced blockage 68
4.4.4 Onsite experiment 68
4.4.5 Forced vibration testing 71
4.5 Closure 72

CHAPTER 5 RESULTS AND DISCUSSION 73

5.1 Introduction 73
5.2 Empty shell natural frequencies 73

5.3 Damping ratio extraction.....78
5.3.1 Hilbert envelope curve method 79
5.3.2 Damping ratio calculation process 80
5.3.3 Isolate other 7 experimental resonant frequencies and its top envelope curve 83
5.4 Natural frequencies of shell with simulated amount mass inside 88
5.5 Natural frequencies and its damping ratio of the shell with inside flour blockage 92
5.5.1 Flour blockage at bottom support point 92
5.5.2 Flour blockage at 1/10 from the bottom support point 97
5.5.3 Conclusion.....102
5.6 Onsite experiment 103
5.6.1 Natural frequencies of the cyclone 103
5.6.2 Natural frequencies of the dropper tube 104
5.6.3 Conclusion.....108

CHAPTER 6 CONCLUSION AND FUTURE WORK.....109

6.1 Conclusion.....109
6.2 Future Work 113

APPENDIX I DATA PROCESSING CODES 114

AI.1 Analysis in time and frequency domain.....114
AI.2 Obtain the envelope curve and damping ratio 118
AI.3 Envelope function.....119

APPENDIX II FRF OF SIMULATED MASS EXPERIMENT.....122

APPENDIX III DATA OF DAMPING RATIO OF INDUCED FLOUR AT BOTTOM SUPPORT POINT.....155

REFERENCES ……...163

LIST OF FIGURES

Figure 1-1 An open-cycle, co-current spray drying system 2
Figure 1-2 4 types of cyclone separators 4
Figure 1-3 Cyclone proportions 4
Figure 2-1 The principle of two ultrasonic testing methods 10
Figure 2-2 Detecting the thickness of wax layer on the petrol pipeline using pulse-echo method 12
Figure 2-3 Ultrasonic echoes from steel/wax and wax layer 12
Figure 2-4 Interference between longitudinal and shear wave to create guided wave ... 14
Figure 2-5 Circumferential (top) and longitudinal (bottom) guided wave fouling detection 14
Figure 2-6 Pulse-echo configuration about detecting the artificial defects on the pipe .. 15
Figure 2-7 Signals from 70º incidence angle for four integrity conditions 15
Figure 2-8 Rectified and denoised signals (a) no defect (b) defect 4 mm (c)defect 7mm and (d) through defect 16
Figure 2-9 Experimental guided waves in a plate setup 17
Figure 2-10 Results from the experimental guided waves in a plate tests 17
Figure 2-11 FRF with and without the cardboard liner 19
Figure 2-12 Acoustic impact method experimental setup 20
Figure 2-13 Wave velocity of the blocked and good pipe 21
Figure 2-14 Possible non-destructive methods for milk powder deposition and blockage detection 22
Figure 2-15 Structure of a cyclone 23
Figure 2-16 The prototype and support type 24
Figure 3-1 Closed circular cylindrical shell and coordinate system 28
Figure 3-2 Illustration of parameter n and m 30
Figure 3-3 Geometric part of the empty cylindrical shell 32
Figure 3-4 meshed cylindrical shell 34
Figure 3-5 Eigenfrequencies (mode 1-20) meshed by 0.014 element size 35
Figure 3-6 Eigenfrequencies (mode 1-30) meshed by 0.005 element size 35
Figure 3-7 First bending natural frequency 81Hz with 0.005 element size mesh 36
Figure 3-8 Second bending natural frequency 316Hz with 0.005 element size mesh 37
Figure 3-9 381 Hz modal shape 37
Figure 3-10 401 Hz modal shape 38

Figure 3-11 The first three modal shapes for the beam with both ends simply supported 40
Figure 3-12 The geometry of the prototype with an added mass at L1 43
Figure 3-13 The first bending natural frequency with the mass ratio and position.....47
Figure 3-14 The second bending natural frequency with the mass ratio and position....47
Figure 3-15 The third bending natural frequency with the mass ratio and position.....48
Figure 3-16 Effect of the concentrated mass location on the first natural frequency.....49
Figure 3-17 The first and third natural frequencies with the added mass at midpoint of the beam with both ends simply supported 51
Figure 3-18 Free decay vibration of SDOF system.....53
Figure 3-19 Half-power bandwidth method.....54
Figure 4-1Modal hammer.....61
Figure 4-2 (a) Eletrodynamic shaker (b) power amplifier (c) signal generator.....62
Figure 4-3 Accelerometer and its power supply 62
Figure 4-4 Polytec laser senor head, its vibrometer controller and Tektronix osccilloscope 63
Figure 4-5 Schematic diagram of bias resistors for DIFF mode.....65
Figure 4-6 Experimental bias resistors connection with multiplexer board for the DIFF mode.....65
Figure 4-7 The front panel of LabView Data acquisition programme.....66
Figure 4-8 The schematic diagram of the experimental setup for the simulated mass ...67
Figure 4-9 One of experimental mass.....67
Figure 4-10 The schematic diagram of the flour blockage experimental setup 68
Figure 4-11 The schematic diagram of the cyclone and onsite experimental setup 69
Figure 4-12 The photo of onsite experimental setup.....70
Figure 4-13 The rubber hammer 70
Figure 4-14 A block diagram of the forced vibration experimental setup 72
Figure 5-1 All the time domain signals.....74
Figure 5-2 Impulse force in time and frequency domain.....75
Figure 5-3 The method of obtaining the FRF 76
Figure 5-4 FRFs from bottom accelerometer, top accelerometer and laser.....76
Figure 5-5 Raw data acquired from laser senor. 80
Figure 5-6 Data from anti-aliasing filter and hamming window.....81
Figure 5-7 Filtered data and top envelope curve using 4 order 70-85 Hz Band Pass. 82
Figure 5-8 Useful top envelope curve.....82

Figure 5-9 Discrete natural logarithm of the 79Hz envelope and its linear fit curve.....83
Figure 5-10 Time domain response of 270Hz mode shape and its top envelope curve..84
Figure 5-11 Time domain response of 380Hz mode shape and its top envelope curve..84
Figure 5-12 Time domain response of 398Hz mode shape and its top envelope curve..85
Figure 5-13 Time domain response of 456Hz mode shape and its top envelope curve..85
Figure 5-14 Time domain response of 568Hz mode shape and its top envelope curve..86
Figure 5-15 Time domain response of 715Hz mode shape and its top envelope curve..86
Figure 5-16 Time domain response of 775Hz mode shape and its top envelope curve..87
Figure 5-17 The variation of the first resonant frequency (79Hz) with 0.64kg, 1.6kg and 2.5kg mass at 11 locations.....90
Figure 5-18 The variation of the second resonant frequency (270Hz) with 0.64kg, 1.6kg and 2.5kg mass at 11 locations.....91
Figure 5-19 The variation of the third resonant frequency (380Hz) with 0.64kg, 1.6kg and 2.5kg mass at 11 locations.....91
Figure 5-20 The variation of the fourth resonant frequency (398Hz) with 0.64kg, 1.6kg and 2.5kg mass at 11 locations.....92
Figure 5-21 FRFs with a plastic board inserted at the bottom support point.....93
Figure 5-22 FRFs with 2 cups of flour added on the plastic board at the bottom.....94
Figure 5-23 FRFs with 4 cups of flour added on the plastic board at the bottom.....94
Figure 5-24 FRFs with 6 cups of flour added on the plastic board at the bottom.....95
Figure 5-25 FRFs with 8 cups of flour added on the plastic board at the bottom.....95
Figure 5-26 Modal damping ratio with the added amount of flour at the bottom.....97
Figure 5-27 FRFs with a plastic board inserted at 1/10 from the bottom support point .98
Figure 5-28 FRFs with 2 cups of flour added on the plastic board at the bottom.....98
Figure 5-29 FRFs with 4 cups of flour added on the plastic board at the bottom.....99
Figure 5-30 FRFs with 6 cups of flour added on the plastic board at the bottom.....100
Figure 5-31 FRFs with 8 cups of flour added on the plastic board at the bottom.....101
Figure 5-32 Accelerometer reading FRF of the cyclone.....103
Figure 5-33 Accelerometer reading FRF of the cyclone after 6 hours later 104
Figure 5-34 Impulse time domain laser reading from the dropper tube.....105
Figure 5-35 Filtered laser reading data from anti-aliasing and hamming window.....106
Figure 5-36 Filtered laser reading data from the dropper tube 106
Figure 5-37 Laser reading FRF and 100-135Hz band pass filtered FRF of the dropper tube.....107
Figure 5-38 Impulse time domain accelerometer reading from the dropper tube.....107

Figure 5-39 Accelerometer reading FRF and 320-350Hz band pass filtered FRF of the dropper tube 108
Figure II-1 FRF of 0.64 kg added mass at the bottom point 122
Figure II-2 FRF of 0.64 kg added mass at 1/10 of 1.87m from the bottom point 123
Figure II-3 FRF of 0.64 kg added mass at 2/10of 1.87m from the bottom point 124
Figure II-4 FRF of 0.64 kg added mass at 3/10 of 1.87m from the bottom point 125
Figure II-5 FRF of 0.64 kg added mass at 4/10 of 1.87m from the bottom point 126
Figure II-6 FRF of 0.64 kg added mass at 5/10 of 1.87m from the bottom point 127
Figure II-7 FRF of 0.64 kg added mass at 6/10of 1.87m from the bottom point 128
Figure II-8 FRF of 0.64 kg added mass at 7/10 of 1.87m from the bottom point 129
Figure II-9 FRF of 0.64 kg added mass at 8/10 of 1.87m from the bottom point 130
Figure II-10 FRF of 0.64 kg added mass at 9/10 of 1.87m from the bottom point 131
Figure II-11 FRF of 0.64 kg added mass at the top point 132
Figure II-12 FRF of 1.6 kg added mass at the bottom point 133
Figure II-13 FRF of 1.6 kg added mass at 1/10 of 1.87 from the bottom point 134
Figure II-14 FRF of 1.6 kg added mass at 2/10 of 1.87 from the bottom point 135
Figure II-15 FRF of 1.6 kg added mass at 3/10 of 1.87 from the bottom point 136
Figure II-16 FRF of 1.6 kg added mass at 4/10 of 1.87 from the bottom point 137
Figure II-17 FRF of 1.6 kg added mass at 5/10 of 1.87 from the bottom point 138
Figure II-18 FRF of 1.6 kg added mass at 6/10 of 1.87 from the bottom point 139
Figure II-19 FRF of 1.6 kg added mass at 7/10 of 1.87 from the bottom point 140
Figure II-20 FRF of 1.6 kg added mass at 8/10 of 1.87 from the bottom point 141
Figure II-21 FRF of 1.6 kg added mass at 9/10 of 1.87 from the bottom point 142
Figure II-22 FRF of 1.6 kg added mass the top point 143
Figure II-23 FRF of 2.5 kg added mass at the bottom point 144
Figure II-24 FRF of 2.5 kg added mass at 1/10 of 1.87 from the bottom point 145
Figure II-25 FRF of 2.5 kg added mass at 2/10 of 1.87 from the bottom point 146
Figure II-26 FRF of 2.5 kg added mass at 3/10 of 1.87 from the bottom point 147
Figure II-27 FRF of 2.5 kg added mass at 4/10 of 1.87 from the bottom point 148
Figure II-28 FRF of 2.5 kg added mass at 5/10 of 1.87 from the bottom point 149
Figure II-29 FRF of 2.5 kg added mass at 6/10 of 1.87 from the bottom point 150
Figure II-30 FRF of 2.5 kg added mass at 7/10 of 1.87 from the bottom point 151
Figure II-31 FRF of 2.5 kg added mass at 8/10 of 1.87 from the bottom point 152
Figure II-32 FRF of 2.5 kg added mass at 9/10 of 1.87 from the bottom point 153
Figure II-33 FRF of 2.5 kg added mass the top point 154

Figure III-1 79 Hz damping ratio with amount of flour 155
Figure III-2 270 Hz damping ratio with amount of flour 156
Figure III-3 380 Hz damping ratio with amount of flour 157
Figure III-4 398 Hz damping ratio with amount of flour 158
Figure III-5 456 Hz damping ratio with amount of flour 159
Figure III-6 715 Hz damping ratio with amount of flour 160
Figure III-7 715 Hz damping ratio with amount of flour 161
Figure III-8 775 Hz damping ratio with amount of flour 162

LIST OF TABLES

Table 3-1 Natural frequencies with different mass ratio and position parameter 46
Table 5-1 The first several natural frequencies of the prototype under experimental, theoretical and analytical methods.....77
Table 5-2 Lower and upper bound of the band pass filter 83
Table 5-3 Experimental first 8 mode shape natural logarithm slope and damping ratio87
Table 5-4 The first 6 resonant frequencies with 0.64kg mass inserted at 11 locations inside of the experimental cylindrical shell 88
Table 5-5 The first 6 resonant frequencies with 1.6kg mass inserted at 11 locations inside of the experimental cylindrical shell 89
Table 5-6 The first 6 resonant frequencies with 2.5kg mass inserted at 11 locations inside of the experimental cylindrical shell 89
Table 5-7 Modal damping ratio with the added amount of flour at the bottom.....96
Table 5-8 The first 8 resonant frequencies with 2 cups of flour at 1/10 99
Table 5-9 The first 8 resonant frequencies with 4 cups of flour at 1/10 100
Table 5-10 The first 8 resonant frequencies with 6 cups of flour at 1/10 101
Table 5-11 The first 8 resonant frequencies with 8 cups of flour at 1/10 102
Table 5-12 The first 8 resonant frequencies with different amount of flour at 1/10.....102
Table 5-13 The clear resonant frequencies of dropper tube and its modal damping ratio 105
Table II-1 The first 6 resonant frequencies of 0.64 kg added mass at the bottom point 122
Table II-2 The resonant frequencies of 0.64 kg added mass at 1/10 of 1.87m from the bottom point.....123
Table II-3 The resonant frequencies of 0.64 kg added mass at 2/10 of 1.87m from the bottom point.....124
Table II-4 The resonant frequencies of 0.64 kg added mass at 3/10 of 1.87m from the bottom point.....125
Table II-5 The resonant frequencies of 0.64 kg added mass at 4/10 of 1.87m from the bottom point.....126
Table II-6 The resonant frequencies of 0.64 kg added mass at 5/10 of 1.87m from the bottom point.....127
Table II-7 The resonant frequencies of 0.64 kg added mass at 6/10 of 1.87m from the bottom point.....128

Table II-8 The resonant frequencies of 0.64 kg added mass at 7/10 of 1.87m from the bottom point 129
Table II-9 The resonant frequencies of 0.64 kg added mass at 8/10 of 1.87m from bottom point 130
Table II-10 The resonant frequencies of 0.64 kg added mass at 9/10 of 1.87m from bottom point 131
Table II-11 The resonant frequencies of 0.64 kg added mass at the top point 132
Table II-12 The resonant frequencies of 1.6 kg added mass at the bottom point 133
Table II-13 The resonant frequencies of 1.6 kg added mass at 1/10 of 1.87m from the bottom point 134
Table II-14 The resonant frequencies of 1.6 kg added mass at 2/10 of 1.87m from the bottom point 135
Table II-15 The resonant frequencies of 1.6 kg added mass at 3/10 of 1.87m from the bottom point 136
Table II-16 The resonant frequencies of 1.6 kg added mass at 4/10 of 1.87m from the bottom point 137
Table II-17 The resonant frequencies of 1.6 kg added mass at 5/10 of 1.87m from the bottom point 138
Table II-18 The resonant frequencies of 1.6 kg added mass at 6/10 of 1.87m from the bottom point 139
Table II-19 The resonant frequencies of 1.6 kg added mass at 7/10 of 1.87m from the bottom point 140
Table II-20 The resonant frequencies of 1.6 kg added mass at 8/10 of 1.87m from the bottom point 141
Table II-21 The resonant frequencies of 1.6 kg added mass at 9/10 of 1.87m from the bottom point 142
Table II-22 The resonant frequencies of 1.6 kg added mass at the top point 143
Table II-23 The resonant frequencies of 2.5 kg added mass at the bottom point 144
Table II-24 The resonant frequencies of 2.5kg added mass at 1/10 of 1.87m from the bottom point 145
Table II-25 The resonant frequencies of 2.5kg added mass at 2/10 of 1.87m from the bottom point 146
Table II-26 The resonant frequencies of 2.5kg added mass at31/10 of 1.87m from the bottom point 147

Table II-27 The resonant frequencies of 2.5kg added mass at 4/10 of 1.87m from the bottom point 148
Table II-28 The resonant frequencies of 2.5kg added mass at 5/10 of 1.87m from the bottom point 149
Table II-29 The resonant frequencies of 2.5kg added mass at 6/10 of 1.87m from the bottom point 150
Table II-30 The resonant frequencies of 2.5kg added mass at 7/10 of 1.87m from the bottom point 151
Table II-31 The resonant frequencies of 2.5kg added mass at 8/10 of 1.87m from the bottom point 152
Table II-32 The resonant frequencies of 2.5kg added mass at 9/10 of 1.87m from the bottom point 153
Table II-33 The resonant frequencies of 2.5kg added mass the top point 154
Table III-1 79 Hz of natural logarithm slope and damping ratio 155
Table III-2 270 Hz of natural logarithm slope and damping ratio 156
Table III-3 380 Hz of natural logarithm slope and damping ratio 157
Table III-4 398 Hz of natural logarithm slope and damping ratio 158
Table III-5 456 Hz of natural logarithm slope and damping ratio 159
Table III-6 568 Hz of natural logarithm slope and damping ratio 160
Table III-7 715 Hz of natural logarithm slope and damping ratio 161
Table III-8 775 Hz of natural logarithm slope and damping ratio 162

LIST OF ABBREVIATIONS

symbol	meaning
NDT	Non-destructive testing
SDOF	Single Degree of Freedom
MDOF	Multiple Degree of Freedom
FEA	Finite Element Analysis
FEM	Finite element method
FT	Fourier transform
FRF	Frequency Response Function
DAQ	Data acquisition
DIFF	Differential
RSE	Reference single ended
NRSE	Nonreferenced single ended
Acc1	Top accelerometer
Acc2	Bottom accelerometer
FFT	Fast Fourier transform
DFT	Discrete Fourier transform

STATEMENT OF ORIGINALITY

"I hereby declare that this submission is my own work and that, to the best of my knowledge and belief, it contains no material previously published or written by another person (except where explicitly defined in the acknowledgements), nor material which to a substantial extent has been submitted for the award of any other degree or diploma of a university or other institution of higher learning."

…….. (signed)

…….. (date)

Acknowledgements

I wish to express my thanks to the many people who have helped make this thesis possible. Without their help and encouragement, this thesis would not have been possible.

Firstly, I would like to deliver my sincere thanks to my supervisor Professor Ahmed Al-Jumaily, for his guidance and support in this research. His knowledge and help has ensured that I finish this research successfully. I have learned more than I expected in the course of this research during the past two years.

I am grateful to my company mentor Rob Crawford from Fonterra Co-operative Group Limited for his suggestions, encouragement and kindly help during the Te Rapa onsite research and experiment. I also wish to thank Tuan Truong and Frank Lin for their generous help during the onsite experiment.

Special thanks go to Dr. Maximiano Ramos for his help in setting up the experiment, revising the thesis and his many valuable suggestions. My thanks also goes to all my colleagues in BioMedical Engineering Centre, especially Robert Paxton, Gijs, Alex Du, Prasika Manilal, Vivian Lin, Bhupendra Gohil, Joe, Johnny Huang, Ashis and Mazhar, who always offered their help whenever I needed it. Thanks to Xiaojing Ma for the cooperation in sharing one computer and kind help throughout.

Lastly, I give my most sincere appreciation to my parents and family for their understanding and support. Lovely thanks to my two children, they always inspire me to go further.

Confidential Material-PG18 Form

AUT UNIVERSITY

APPLICATION FOR RESTRICTED ACCESS TO A MASTER'S THESIS / DISSERTATION / EXEGESIS

Author: Li Li

Title of thesis/dissertation/exegesis: Non-Destructive Detection the Milk Powder Deposition or Blockage in the Cyclone of the Spray Dryer

Degree: Master of Engineering Year of submission: 2007

An embargo is requested on the public availability of the print and digital copies of the above thesis/dissertation/exegesis for 36 months (maximum normally 36) from the date of submission for examination because it contains confidential or sensitive information which if publicly available may: *(tick all that apply)*

✓ Jeopardise the future intellectual property rights of the author (eg a patent application or publication)

☐ Breach a prior contractual arrangement with an external organisation
Please attach a copy of the relevant agreement(s)

☐ Infringe or endanger the right to privacy or cultural respect of an individual or group

The embargo would apply to: *(tick one)*

✓ The complete thesis/dissertation/exegesis

☐ A portion of the document which will be bound as a separate annex

Signatures

Student: 李莉 Li Li Date: 16/05/2007

Primary Supervisor: D White Date: 23.05.07

Restricted access approved by Faculty Dean

Signed: Date: 5.7.07

Instructions for use of this form:
The completed form, signed by the student and the primary supervisor, should be submitted to the appropriate Faculty Postgraduate Office when the thesis/dissertation/exegesis is lodged for examination. If the application is approved by the Faculty Postgraduate Committee, the form will be signed by the Dean and sent to the University

Abstract

This research investigates possible monitoring methods to non-invasively detect blockages in the cyclone of milk powder spray driers to avoid costly production shutdowns. Two possible solutions have been identified. These are guided wave and vibration analysis. This research focuses on vibration analysis method, based on variation in the natural frequencies and/or damping ratios caused by blockages.

Experimental simulation studies the performance to assess the viability of the vibration analysis method in identifying blockage in the cyclone. To test this method, a 1.87m long vertical cylindrical steel tube with both ends simply supported was setup as a prototype and flour was used as the powder conveyed by the tube. Analytical, numerical and experimental methods were implemented on the prototype using vibration analysis techniques. Experimental resonant frequencies of the empty shell from the impact hammer excitation were compared with analytical and numerical solutions to analyse the modal shapes. The first bending mode was determined as 79 Hz, which decreased with the amount of added mass and location closer to the middle point. This was validated by the simulated mass experiment, which also matched with the beam-mass theory. Flour induced experiment further validated the variation of the first bending mode. Experimental 270Hz, 380Hz and 398Hz resonant frequencies increased with the amount of added mass, which was validated by the simulated mass and flour induced experiment. Besides the variation of the natural frequencies, the damping ratio was also studied and quantified using the Hilbert transform envelope curve method. Onsite monitoring of the vibration of the cyclone in a spray dryer was done at Fonterra Te Rapa and clear resonant frequencies were obtained.

The research results from the prototype demonstrate that vibration analysis as a non-destructive method to detect the milk powder deposition or blockage in the cyclone is possible and promising. However, more work is required before industry application.

Chapter 1 Introduction

1.1 Background

Milk powders are produced by drying liquid milk in a multi-stage drying process that includes a unit operation known as spray drying. The spray drying process involves the atomization of a concentrated liquid feed with hot air in a drying chamber and the separation of milk powder from moist air in the cyclone.

The longer the milk powder spray drier operates, the greater the chance for deposit formation. The latest design of the spray drying plants has tried its best to minimize deposit formation and permit operation over longer periods of time. However, it is impossible to avoid the milk powder deposit formation on the surface of the spray dryer. Milk powder contains fat, sugar and protein which produce hygroscopic characteristics at the given temperature and humid conditions during processing. Thus milk powder becomes sticky under these operation conditions and causes blockages in the critical parts of the process, especially the cyclones.

Milk powder deposition on the internal wall of the spray driers and blockages is not desirable and has to be washed away after a few production runs because of fire safety, product quality and hygiene requirements [1]. The milk powder deposit may cause spontaneous fire in very high temperature environments, such as 180ºC inlet air temperature if the deposit layer becomes very thick. Deposits undergo oxidation and browning or scorching and will degrade the final product if they fall off and mix with it. The humidity in the deposit in the cooler parts may cause bacterial growth which results in hygiene problems. The deposit may be removed by periodic pneumatic hammer hitting at the early stage, however mechanical removal and chemical washing must be undertaken if serious blockages happen. Frequently washing the dryer results in high cleaning costs as well as lost production time.

Thus, milk powder deposition or blockage is a big production issue in the milk powder processing. At present the algorithms that have been developed to predict a blockage according to the physical parameters inside the drier such as pressure, like in milk fouling detection [2], do not give enough warning time of a total blockage and need to

be tuned to each particular plant. This research is proposed to investigate the non-destructive techniques to locate possible blockages, thus avoiding the costly shutdown associated with a total blockage.

1.2 Milk powder spray drying system

In this section the structure of the spray dryer and the formation of milk powder deposition or blockage will be discussed. In addition, the objectives of this research will be outlined.

1.2.1 Structure and principle of a spray dryer

Spray dryers are widely used to manufacture products in dairy, food, chemical and pharmaceutical industries. Spray drying involves both particle formation and drying. It consists of the following four process operations: atomization of feed into a spray, spray-air contact, drying in a stream of hot and dry air, and separation of dried powder from moist air [1].

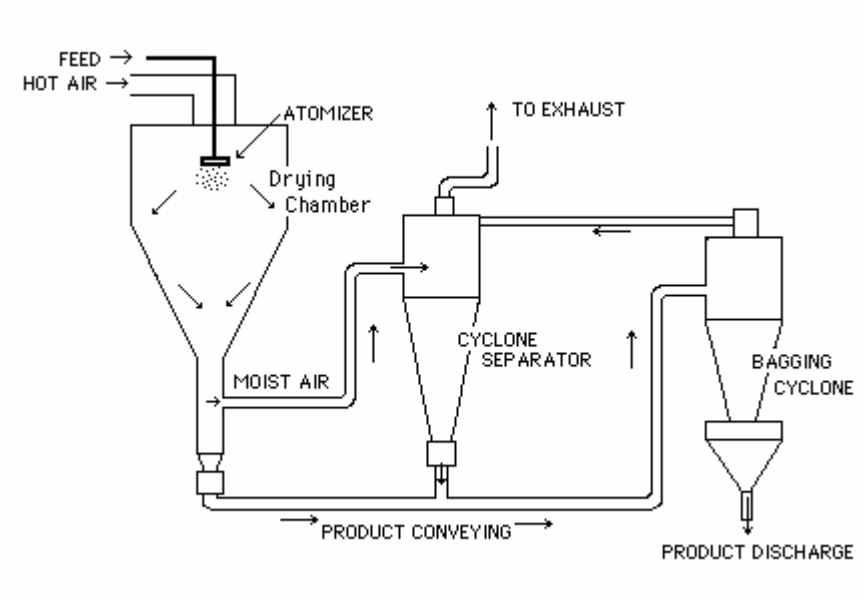

Figure 1-1 An open-cycle, co-current spray drying system

Figure 1.1 illustrates a typical open-cycle co-current spray drying operation, which utilizes a centrifugal atomizer and a cyclone separator [3]. Spray drying involves pumping a concentrate of the liquid product to the atomizing device where it is broken into small droplets. These droplets meet a stream of hot air and then lose their moisture

very rapidly to become milk powder, most of which is discharged. The exhaust air mixed with powder particles enter into the cyclone where they are separated by centrifugal action, which is caused by the great increase in air speed when the mixture of particles and air enters the cyclone system. The dense powder particles are forced toward the cyclone walls while the lighter, moist air is directed away through the exhaust pipes. The powder settles to the bottom of the cyclone where it is removed through a discharging device. Sometimes the air-conveying ducts for the dry powder are connected with cooling systems, which admit cold air for transport of the product through conveying pipes. Cyclone dryers have been designed and widely used for large production schedules capable of drying large tons of powder per hour.

The atomization and airflow pattern are the drying features of a spray dryer and play an important role in the quality of products. There are rotary atomizers and nozzles to form sprays. The selection of the type of atomizers depends on the nature of the feed and desired characteristics of the product. Feed and hot air pass through in co-current, counter-current or mixed-current flow. That is, spray and air enter the spray dryer in the same, opposite or both directions. Powder characteristics can be controlled to produce either fine or coarse particle powders, agglomerates or granulates by the physical and chemical properties of the feed and the dryer design and operation. In dairy industries a co-current air flow spray drying system is mostly used due to the milk powder characteristics.

1.2.2 Cyclone separator

A cyclone separator is a settling chamber in the form of a vertical cylinder and is useful for removing dry product from air in food industries. The first cyclone separators were built about 1885 by Knickerboker Company in the United States. There are four commonly used cyclone separators which are classified according to geometrical configuration. They are called tangential inlet axial discharge (a), tangential inlet peripheral discharge (b), axial inlet and discharge (c), and axial inlet peripheral discharge (d) as shown in Figure 1.2 [4].

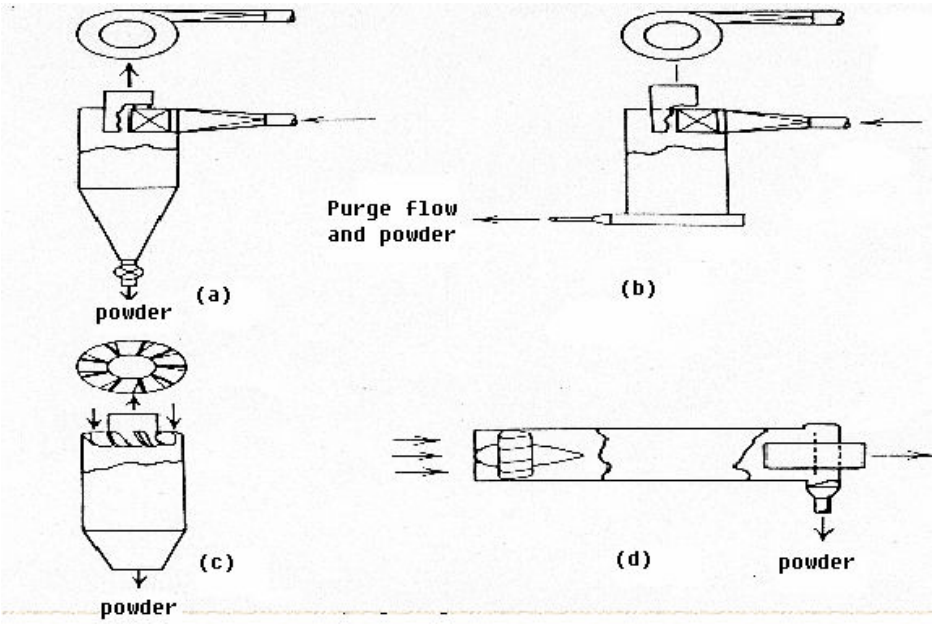

Figure 1-2 4 types of cyclone separators

According to Heumann [5], axial flow cyclones like Figure 1.2 (c) are the most commonly used. However, the basic operating principles of the 4 types of cyclone separators are all based on the conventional cyclone. The mixture gas enters tangentially and spins in a vortex as it goes down. A cone section causes the vortex diameter to decrease until the gas reverses on and spins up the center to the outlet pipe. Powder is centrifuged toward the wall and discharged by inertial impingement. Body diameter, body length and cone length are important factors to determine the efficiency of a cyclone separator. Columbus [6] introduced two commonly used cyclones which are LD, 1D3D (body length=diameter, cone length=3*diameter), and 2D2D (body length and cone length=2*diameter) as shown in Figure 1.3.

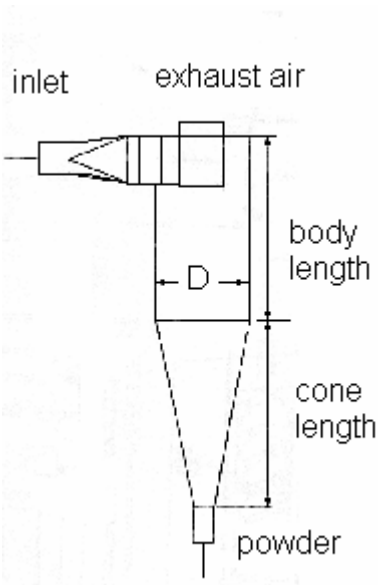

Figure 1-3 Cyclone proportions

1.2.3 Reasons for the formation of milk powder deposition or blockages

Milk powder deposition or blockages often happen in cyclone separators, due to clogging of particles resulting from its chemical and physical properties. There are many influencing factors for milk power deposition including the temperature, moisture content, particle size, powder composition (fat, lactose and protein), surface roughness and deformation of the powder material [7-10] .A deposit formation is related to the drying cohesion characteristics of a particular product. Stickiness or cohesion characteristics of powder play an important mechanical role in the deposition on the surface of a spray drier. There is much literature investigating these influencing factors to reduce the chance of deposition and blockages. Chen [7] researched the effects of fat content in whole milk powder and lactose content in skim milk powder, together with temperature changes in relation to deposition. Buma [9] investigated the relationship between the products cohesion and the temperature by comparing whole milk powder and skim milk powder. Although, the physical factors causing clogging, such as particle size and its distribution, are very complicated and hard to prevent, clogging due to the product chemical properties may be reduced by improving equipment design and controlling process parameters.

There are three main occurrences causing the product deposition on the chamber walls in the spray dryer. These are semi-wet deposits, sticky deposits and surface dusting [1].

- Semi-wet deposits are caused by the coarse droplets in a spray hitting the wall or by incomplete atomization. These deposits can be eliminated by improving the atomizer performance.
- Sticky deposits are caused by the nature of the product at the temperature of the dryer. The chemistry of the product can cause it to bond or cement. This type of clogging can be prevented by improving thermal insulation, controlling the specified operating conditions and meticulous equipment maintenance [11].
- Surface dusting results from the inevitable contact between dried particles and the wall. The degree of dusting depends upon the powders state, the geometry of the wall, wall cleanliness, local air velocity and electrostatic forces between the particle and the wall.

The reasons for milk powder cohesion during processing are complicated and depend on a variety of factors. Although the deposit formation can be minimized by incorporating integrated fluid beds, choice of material and optimum design, it is impossible to totally eliminate this in the spray drying process. Hence, there is a need to develop a non-destructive testing method for detecting particle deposition built-up within the cyclone of the spray drying system, so that mitigating action can be implemented. A non-destructive test would be an effective method for providing useful information to predict the possible blockages without affecting normal production.

1.3 Objectives

Structurally the cyclone of the spray dryer is a very complicated system. To investigate any technique for identifying blockage in such a system would be very cumbersome exercise. Therefore, a simplified prototype tube system is considered. Although such a prototype may seem very simplistic, it is believed it will give sufficient information and knowledge as backup foundation material to investigate any blockage identification technique. As the structure of the proposed prototype is between a shell and a beam, the shell theory will be used first to identify the general vibration characteristics of the system. Since it is very difficult to analyse a shell with a localised mass, further approximation beam theory is used.

The main objective of this research is to identify a non-destructive method and validate its feasibility for application in detecting blockages that happen within the cyclone or dropper tube of a milk powder spray drier. To achieve this objective, the following works will be undertaken:

1) Research potential non-destructive techniques and identify the one to be employed in this study.

2) Simplify the cyclone or dropper tube of a milk powder spray dryer and build a prototype.

3) Mathematically model the prototype and employ a numerical method to identify the modal shapes of the prototype.

4) Conduct experimental research on the prototype and compare with the mathematical model and numerical results to examine the feasibility of this technique.

5) Implement experimental research on the simplified prototype into onsite cyclone monitoring.

1.4 The structure of the thesis

This chapter has introduced the focus of this research and the problem that this thesis will investigate. Chapter 2 introduces the non-destructive techniques and summarizes the literature to deduce the possible techniques that can be employed in this research. Chapter 3 mathematically models the prototype and employs a numerical method to obtain the solutions of the natural frequencies and modal shape. The beam-mass system is researched to get the variation of the bending modals with the added mass. In addition, the analysis methods of damping ratio are introduced in this chapter. Chapter 4 introduces the definition of Frequency Response Function and resonant frequency search methods. Different experimental setups are introduced. In Chapter 5, the experimental results are discussed and compared with the theoretical research. Chapter 6 concludes the research and provides suggestions for future work relating to the use of vibration analysis to detect blockages in the cyclone system.

Chapter 2 Non-Destructive Testing (NDT) and literature review

2.1 Introduction

Non-destructive testing (NDT) is defined as all methods of testing an object without causing permanent damage and rendering it unfit for service, or contaminating the product. Other terms such as non-destructive evaluation, non-invasive testing and non-destructive inspection are also used [12]. Established test methods include radiography, ultrasonic inspection, magnetic particle inspection liquid penetrant inspection, thermography, electrical and magnetic methods, and visual optical testing [13]. In addition, guided wave, acoustics and vibration analysis are also attracting attention in the NDT field.

To date, no known research has explored the detection of the deposition or blockage in the spray dryer using NDT method. However, NDT methods have been used in relevant applications like the fouling detection in dairy industry, wax deposit detection in the petrol industry and defect detection in material or structure. It is therefore appropriate to discuss these different NDT methods to determine the possibility of using them in powder blockage identification.

2.2 Ultrasonic method

Ultrasonic is the sound above the range of human hearing, that is, its frequency is greater than 20,000Hz. The principle of ultrasonic testing in NDT is to analyse the resulting sequence signal received from the test object into which there is ultrasonic energy transmitted. In 1931, Mulhauser [12] obtained a patent for using two ultrasonic transducers to detect flaws in solids. Firestone (1940) and Simons (1945) [12] developed pulsed ultrasonic testing using a pulse-echo technique.

Usually there are three types of scan display in ultrasonic testing: A-Scans, B-Scans and C-Scans [12].

- A-Scans are known as a plot of amplitudes of the received echoes on the y-axis versus time subsequent to the input pulse on the t-axis.
- In the B-Scans, the display is a grey scale with brightness proportional to the amplitude of any reflections appearing at that y-z coordinates in the test object.

In the C-scans, the transducer is swept rapidly back and forth in the x direction while being stepped in the y direction after each sweep.

In the engineering field A-Scans are widely used because it is economical and suitable for most applications. The B-Scans and C-Scans are usually employed in the medical field.

Non-destructive ultrasonic testing is based on the discontinuities of acoustic impedance between boundaries which cause the ultrasonic waves to be reflected. The fraction of the energy reflected R_E to the boundary between specific acoustic impedance Z_1 and Z_2 is

$$R_E = \left(\frac{Z_2 - Z_1}{Z_2 + Z_1} \right)^2 \qquad (2.1)$$

where $Z_1$and Z_2 are acoustic impedance of each side of the boundary.

Acoustic impedance of the medium characterizes the behaviour of sound waves in that kind of medium. It is known as

$$Z = \rho V \qquad (2.2)$$

where ρ is the density of the material and V is wave velocity.

Gases have extremely low acoustic impedance; liquids have values closer to those of solids. The specific acoustic impedance of air is 3.3×10^2 Rayl, compared to that of steel 44.7×10^6 Rayl which is 10^5 times of acoustic impedance of air. So at almost all air solid boundaries, 100% energy is reflected [13]. Therefore when a transducer is placed against a test piece, a couplant is needed to increase the transmission of the ultrasonic pulse energy into the test piece to avoid a layer of air between the transducer and solid surface, which would transmit only a very weak beam.

2.2.1 Conventional ultrasonic techniques

Usually two methods of pulse-echo method and through transmission method are used in the ultrasonic testing applications as shown in Figure 2.1. Pulse echo method is used extensively. This method requires only one transducer acting as a transmitter and as a receiver. A transducer touches the surface of the specimen through the couplant, sending a pulse of ultrasonic waves though the medium. The echo which is reflected by

the discontinuity or from the rear surface is detected by the same transducer. Oscilloscope can be used to display the pulse and echo with time. By interpreting the display in the oscilloscope, the defects or the nature of the specimen can be determined.

The through transmission method requires two transducers: one as a transmitter and the other as a receiver. It is often used for thin sheet metals where pulse echo testing is impractical due to the dead zone effect, which is the distance between the front face of the transducer and the first echo resulted from transducer ringing and reverberations from the interface between the transducer and the test object. It is also used when small defects are present which do not give adequate refection signal in the pulse echo mode [13].

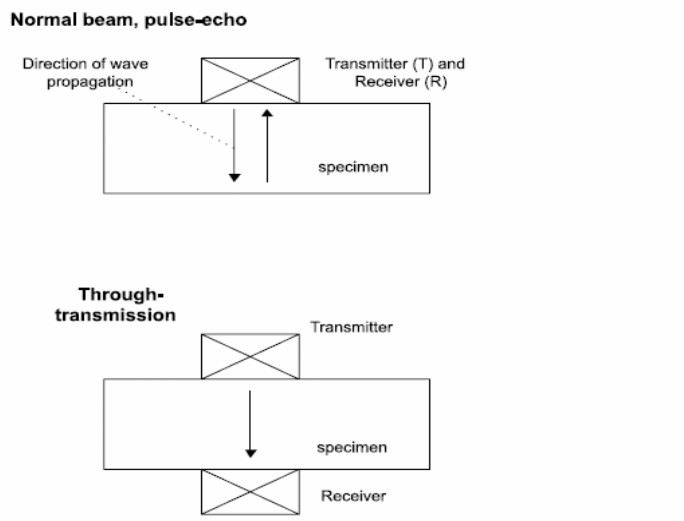

Figure 2-1 The principle of two ultrasonic testing methods

2.2.1.1 Application of conventional ultrasonic to measure thickness

Pulse-echo A-scan method is commonly used to detect and monitor the deposit formation in the pipeline wall. There are two kinds of methods used in this technique, the resonance method and the echo method.

- The resonance method

  The principle of the resonance method is that resonance occurs when the reflected wave is exactly in phase with the incident wave. The thickness of the test piece is

$$\Delta = \frac{V}{2[\nu_{n+1} - \nu_n]} \tag{2.3}$$

where V is sound velocity, ν_n and ν_{n+1} is the adjacent resonance frequencies.

- The echo method

  The thickness of the test piece is

$$\Delta = Vt \tag{2.4}$$

  where V is sound velocity in the test piece, t is the time from initial pulse to rear wall echo of the test piece.

The echo method is more widely used in the engineering field.

2.2.1.2 Application of conventional ultrasonic in monitoring deposition

Anderson [14] from Christian Michelsen Research developed a clamp-on deposition monitoring system based on ultrasonic pulse-echo technique, which could measure the thickness of a wax layer or hydrate on the petroleum conveying pipeline wall. The milk powder deposition on the inside wall of the cyclone and its dropper tube is very similar as the wax layer or hydrate on the petroleum pipeline wall. Therefore it is possible to extend this method to the similar application like milk powder deposition detection of the cyclone of a spray dryer.

Thickness d is estimated as the Equation 2.5 and as shown as Figure 2.2 and 2.3.

$$d = c_{wax} \frac{\Delta t}{2} \tag{2.5}$$

where, c_{wax} is the speed of sound in the wax layer and $\Delta t = t_2 - t_1$ is the time between echoes form the steel/wax and wax/gas interfaces.

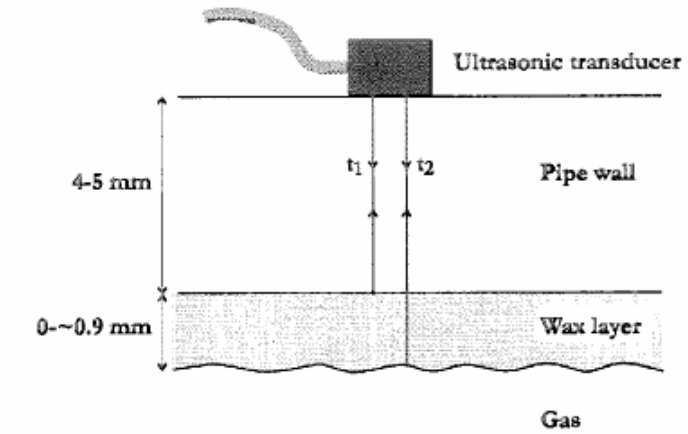

Figure 2-2 Detecting the thickness of wax layer on the petrol pipeline using pulse-echo method

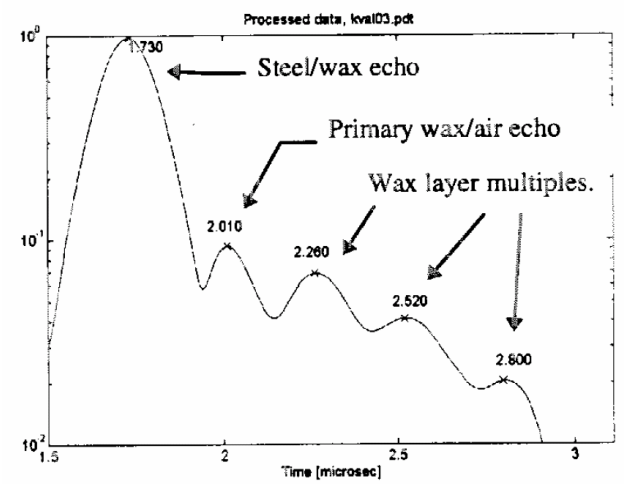

Figure 2-3 Ultrasonic echoes from steel/wax and wax layer

High frequency ultrasonic pulses greater than 10MHz were employed in order to get good echoes. Based on Andersen's [14] research, detection and quantification of scale deposits in petroleum pipelines using conventional ultrasound scans is encouraging, however it can not be directly used because strong reverberation echoes within the pipe wall mask the weak required signals reflected off the deposit wall.

Gunarathne [15, 16] developed the synthetic A-scan approach in which the deposit was indirectly identified by modelling and extracting representative features from the background and strong reverberating signals. This approach based on mathematical models, scan feature extraction by curve fitting, frequency domain signal analysis, preferential filtering and signal enhancement had been used under laboratory conditions and gave scale thickness an accuracy of 0.5mm, which suppress reverberations and enhance weak signal emanating from scale deposits to enable estimation scale thickness. The laboratory test used $BaSO_4$ and $SrSO_4$ as scale samples to resolve the deposit.

However, the mineral deposits in the petroleum pipelines may be a mixed composition which makes identification and measurement more complex. Gunarathne [15, 16] concluded that using synthetic A-scan approach to estimate scale thickness is applicable as long as the return echoes from scales are sufficiently strong.

The conventional ultrasonic method is promising when used to detect wax, scale deposits and milk fouling film [17, 18] as a non-destructive detection technique. However, there are limits of the ultrasonic method when it is used to detect milk powder deposition. The presence of particulates or gas bubbles can limit its application owing to excessive scattering of the signal and the irregular deposition surface will cause scattered signal. Furthermore, the mismatch between the acoustic properties of the pipe wall and deposition will result in drowning the small reflection from deposition compared to the larger reverberation echoes within the pipe wall.

2.2.2 Guided wave

Conventional beam ultrasonic is limited by its ability to inspect on a point by point basis. On the other hand, guided waves can be used to inspect large regions of a specimen at once instead of conventional ultrasonic point to point testing. Therefore the transducer does not move around to obtain detailed information. Guided waves have a capacity of propagating at a long distance without substantial attenuation and have excellent sensitivity to viscous deposit on the internal surface of pipeline and show potential in NDT applications, just as acoustic emission and vibration analysis techniques.

A Conventional ultrasound beam runs vertical into the test sample, however there is only a longitudinal wave in the conventional ultrasound beam. When an incident longitudinal wave enters the test sample in an oblique incidence, transmitted longitudinal and shear waves are created. The difference in their angles can be calculated using Snell's Law. Based on this calculation, guided waves [19] can be created from the interference between longitudinal and shear waves when the thickness of the specimen is similar to or less than the wavelength of the ultrasonic wave as shown in Figure 2.4. Circumferential guided waves and longitudinal guided waves are also used as shown in Figure 2.5.

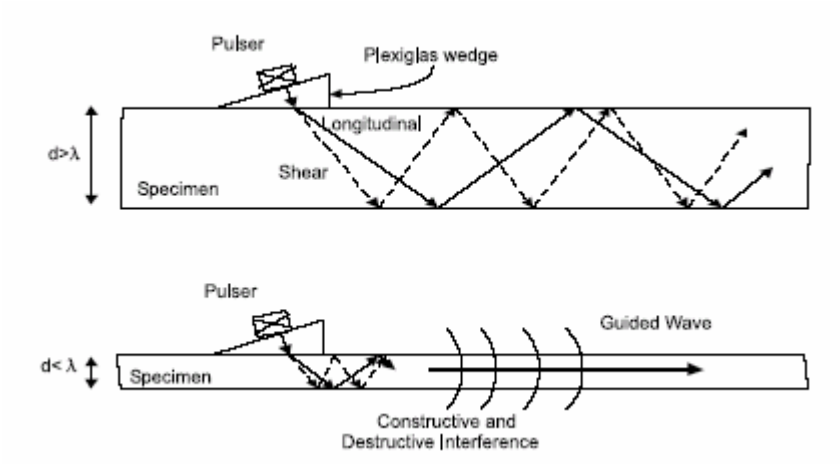

Figure 2-4 Interference between longitudinal and shear wave to create guided wave

.

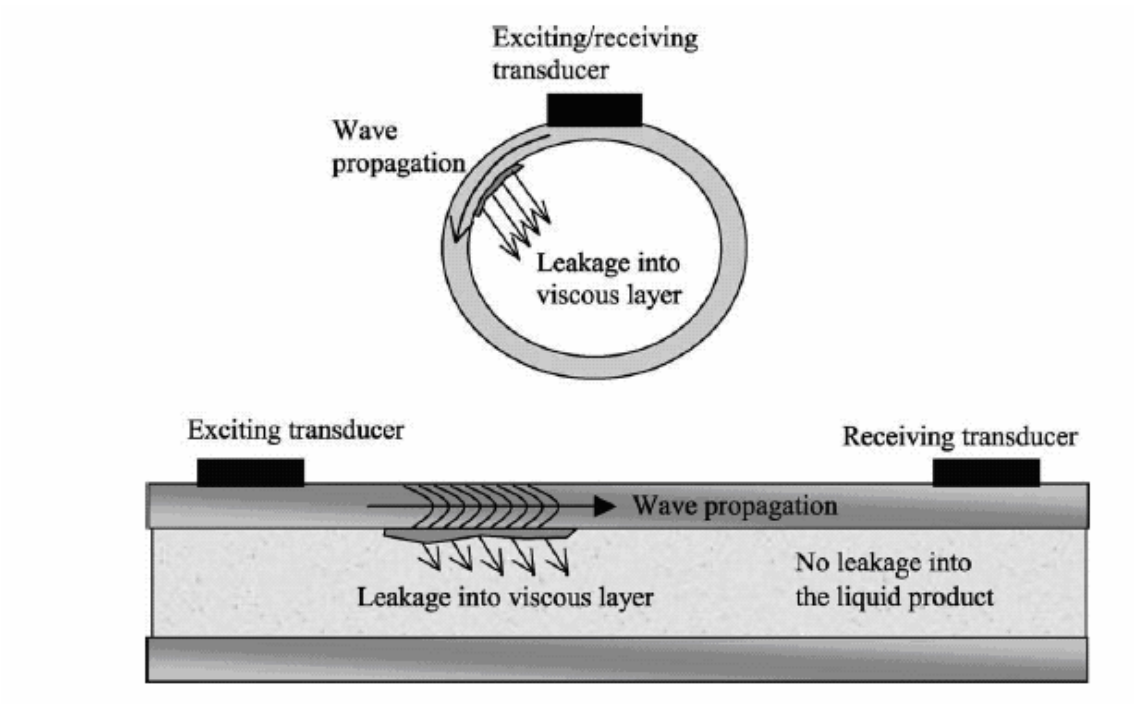

Figure 2-5 Circumferential (top) and longitudinal (bottom) guided wave fouling detection

2.2.2.1 Application of guided wave for detecting defect

Guided wave can be used in defect detection. The presence and location of defects are determined by any reflections and their arrival times. Siqueira, Gatts, Da Silva, and Rebello [20] utilised the guided wave for pipe defect inspection. Frequency band pass filter and wavelet analysis were introduced to analyse the result. The echo produced by different size defects clearly appeared in the oscilloscope. A 70° wedge was used to get the clear reflection from the pipe-end and the defects. The experiment setup and results

with and without de noised is shown in Figures 2.6, 2.7 and 2.8. The amplitude of defect echo was displayed with the size defect in the result signal.

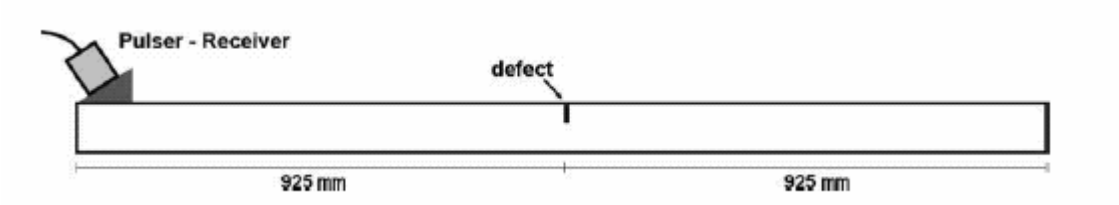

Figure 2-6 Pulse-echo configuration about detecting the artificial defects on the pipe

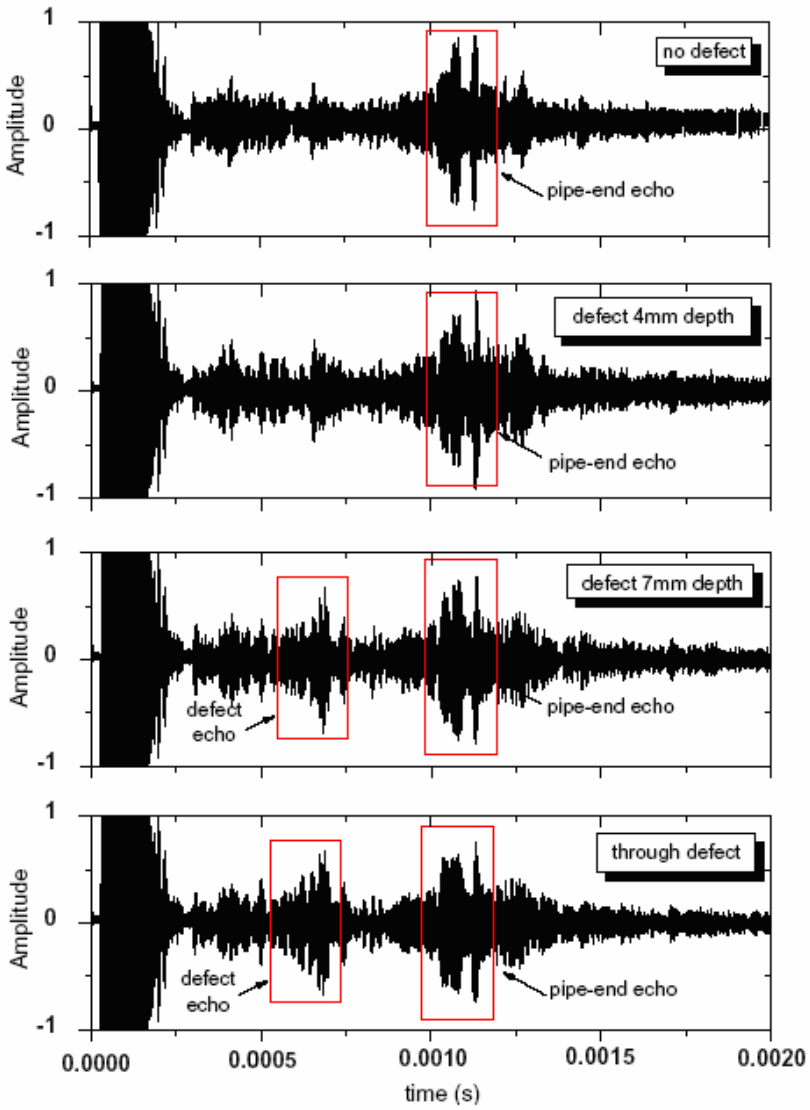

Figure 2-7 Signals from 70º incidence angle for four integrity conditions

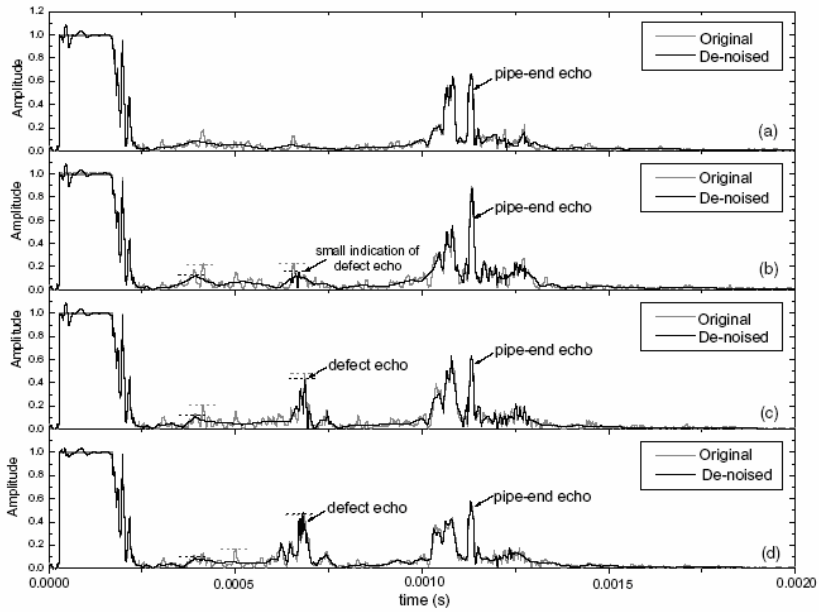

Figure 2-8 Rectified and denoised signals (a) no defect (b) defect 4 mm (c)defect 7mm and (d) through defect

2.2.2.2 Guided wave attenuation for detecting deposit on pipe wall

As with the conventional ultrasonic, there are two kinds of methods for detecting the deposit using guided wave, one is pulse-echo and the other is through transmission. Pulse-echo guided wave method is used to investigate the change of the echo from the end of the pipe. Through transmission guided wave method is employed to see the attenuation of some wave form mode due to the presence of the deposit.

Lohr and Rose [21] have investigated pipe fouling detection using ultrasonic guided wave. The principle of guided wave approach is energy loss with the viscous or semi-solid fouling on a plate or pipe. The possibility and potential value in fouling detection was demonstrated using guided wave methods, however, the quantification of fouling had not been achieved. The plate experimental guided waves pulse-echo setup is shown in Figure 2.9. The received back wall echo decreased as the characteristic of the loading material changes as shown in Figure 2.10.

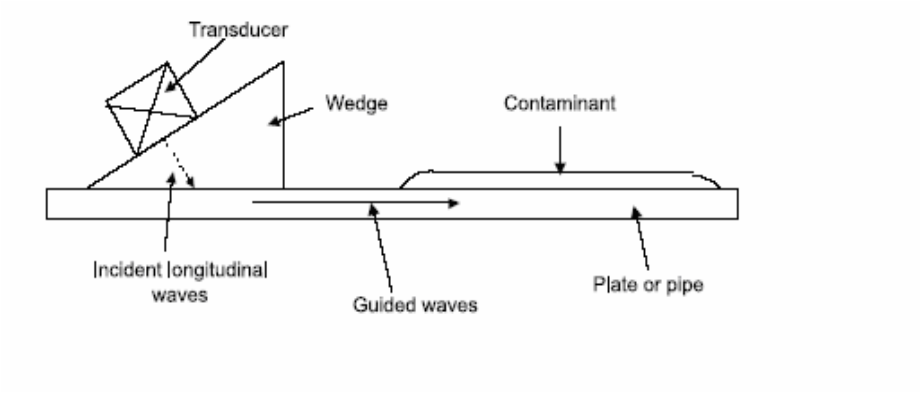

Figure 2-9 Experimental guided waves in a plate setup

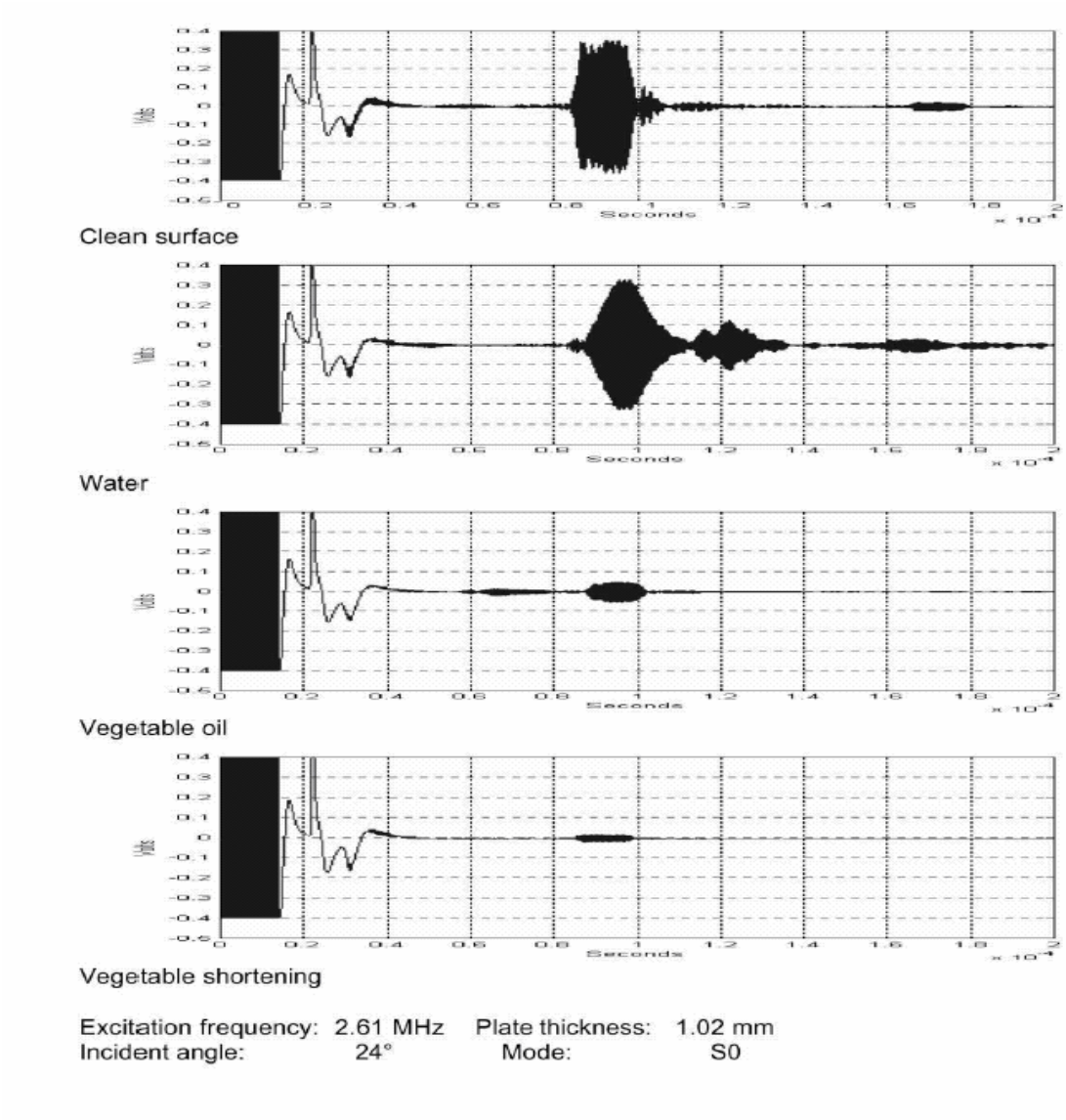

Figure 2-10 Results from the experimental guided waves in a plate tests

Moussaoui, Chati, Leon, and Klauson [22] investigated the longitudinal wave attenuation at particular frequencies caused by a circular shape deposit on the pipe wall

from theoretical analysis and experimental results. The chosen waves must be sensitive to the deposit, hence the axisymmetric waves A_0 (1.15MHz), S_0 (1.70MHz) A_1 (2.41MHz), and S_1 (2.56MHz) were generated by a piezoelectric transducer which was placed at one end of the pipe. A comb PVDF transducer acted as a receiver measuring the waves at the other end. It was found that the normalized amplitude of each mode decreased when the width of the deposit increased.

Hay and Rose [19] used guided wave through transmission test set up and investigated the change of axisymmetric L (0, 4) waveforms for empty pipe, water loaded pipe, and water loaded pipe with fouling inside. The L (0, 4) mode showed excellent sensitivity to the fouling as demonstrated by 6 dB amplitude drop relative to a clean pipe in a 2m through transmission at 2.5MHz. This technique provides a qualitative diagnosis on monitoring the fouling built-up processing. Accurate measurement of fouling thickness is difficult because the fouling film is often not uniform.

Cawley, Fromme, Wilcox, and Lowe [23] from Imperial College London collaborated with British Nuclear Fuels and NDT Solutions Ltd on the project "A non-intrusive guided wave method for detecting blockages in pipes". No article was published on this project, however his previous guided wave researches were mainly on plate-like component defect detection such as corrosion or crack. A ring of piezoelectric transducer elements array for the inspection of plates has been designed and built around the pipe at single location for the excitation and reception of the first antisymmetric Lamb wave mode A_0. The structure defect could be determined by comparing and analysing the data from the transducer array.

These studies show that ultrasonic guided wave technique has excellent potential in detecting the deposit contents or blockages on the inner of the piping. However, what kinds of waveforms generated by transducer that can be used sensitively enough is a big barrier for this technique to be of any practical use. At present it is still at the experimental research stage and requires further work for commercial use.

2.3 Vibration analysis

Vibration analysis is mainly applied to the investigation of a system's vibration characteristics which include natural frequencies and damping parameters. The tested

system with and without deposition will result in the variation of its natural frequencies and damping parameters.

Foulkes, Fromme, Wilcox and Lowe [24] studied the vibration effect of inserting a cardboard liner into a thin cylindrical shell. His studies showed that the liner adds significant modal stiffness and damping to most modes; while an increase modal mass was also observed for a certain type of mode. The shell was set up by free-free boundary condition, an impact hammer excited the shell and accelerometer and microphone were placed to obtain the vibration. Figure 2.11 shows the frequency response function of the shell with and without a cardboard liner. It can be seen that the resonant frequencies and damping ratio significantly changes when the liner is introduced.

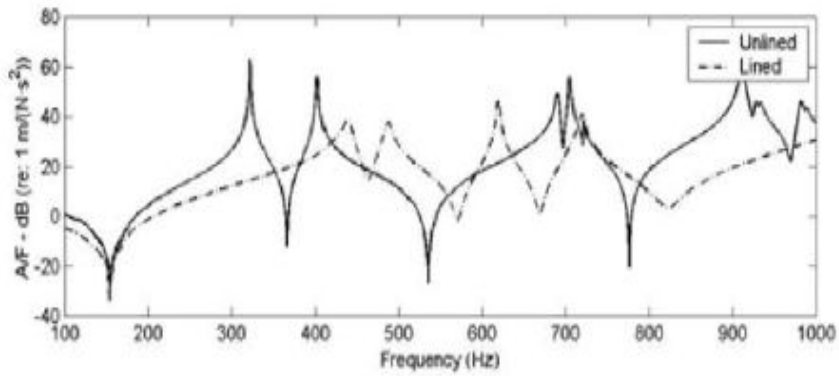

Figure 2-11 FRF with and without the cardboard liner

The deposition of scale or wax on the internal bore of a pipeline leads to the increase of damping ratio. Gelman et al. [25, 26] investigated the Power Spectral Density and Fourier components method on pattern recognition and validated findings through numerical simulation by Matlab Simulink package. Babitsky and Veprik [27] studied the damping effect of forced vibrations of beams with a moving washer under mono-harmonic, stationary random and impulsive excitations utilizing mathematical model and experimental method. Furthermore, Shahruz [28] confirmed the washer effect in suppressing the vibration of beams and additional damping effect in the beam as seen in Babitsky's experimental results.

2.4 Acoustic impact method

Acoustic impact method relies on the changes in wave velocity and signal attenuation to the existence of fouling. Lohr and Rose's experimental setup is shown in Figure 2.12 [21]. Hammer impact generated sonic and ultrasonic waves. One ultrasonic sensor was used as a trigger of oscilloscope and the other recorded the waveform. Two sensors separated a certain distance to measure wave velocity. The two sensor separation distances was 1.524m and 2.057m, outside diameter of pipe was 88.9mm and inside one was 77.85mm. The wave velocities were calculated from the leading edge of the pulse. It was found that the wave velocities for the blockage pipe decreased a significant amount compared to the good one as shown in Figure 2.13. This method showed a capability for quantification of deposit detection, even though localization of the deposit was impossible.

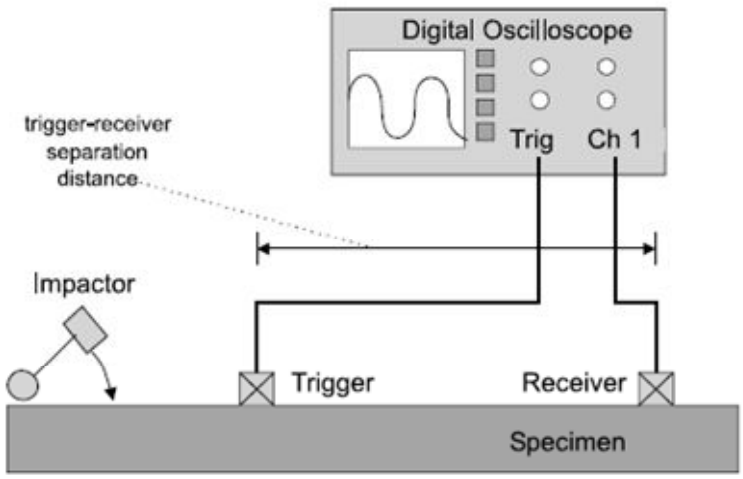

Figure 2-12 Acoustic impact method experimental setup

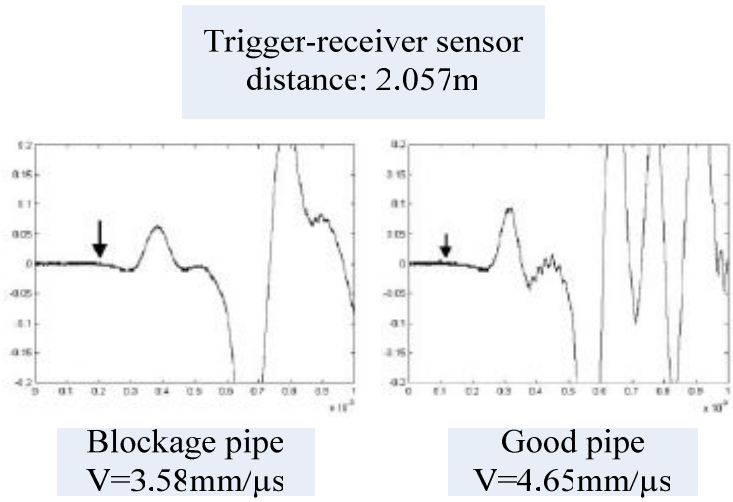

Figure 2-13 Wave velocity of the blocked and good pipe

Donskoy and Sutin [29] developed a nonlinear Vibro-acoustic method based on the fact that the defects in the material have nonlinear response by modulation of a higher frequency (Ω) ultrasonic probe wave with a lower frequency (ω) vibration. The result of this modulation was sidebands between (Ω+ ω) and (Ω- ω) in frequency domain. The presence of a defect would change the phase and amplitude of signal while the frequencies would be unchanged. Thus modulation should produce sidebands in the frequency domain if there was degradation. Unfortunately this method was only applicable to detect the presence of the contact-type defects in the materials or structures and would not be suitable for the deposition detection.

2.5 Possible NDT techniques for this research

Figure 2.14 shows the possible non-destructive techniques that could be employed for detecting the milk powder deposition or blockage in the cyclone of a spray drying system. From the literature reviewed, two possible methods were identified. These are the ultrasonic and the vibration analysis methods. For the ultrasonic technique, guided wave attenuation has more advantages than the conventional ultrasonic method because it can travel long distance in a very short time without moving the transducers around the tested system. Conventional ultrasonic is also sensitive to the air bubble in the milk powder blockage and will stop travelling in the milk powder.

Vibration analysis is another promising technique in NDT given that the deposition or blockage on the internal tube will change its vibration characteristics. Due to the

available instrumentation, this project mainly employed this technique to research the variation of natural frequencies, and its modal damping ratio with the amount of the deposition or blockage and its location.

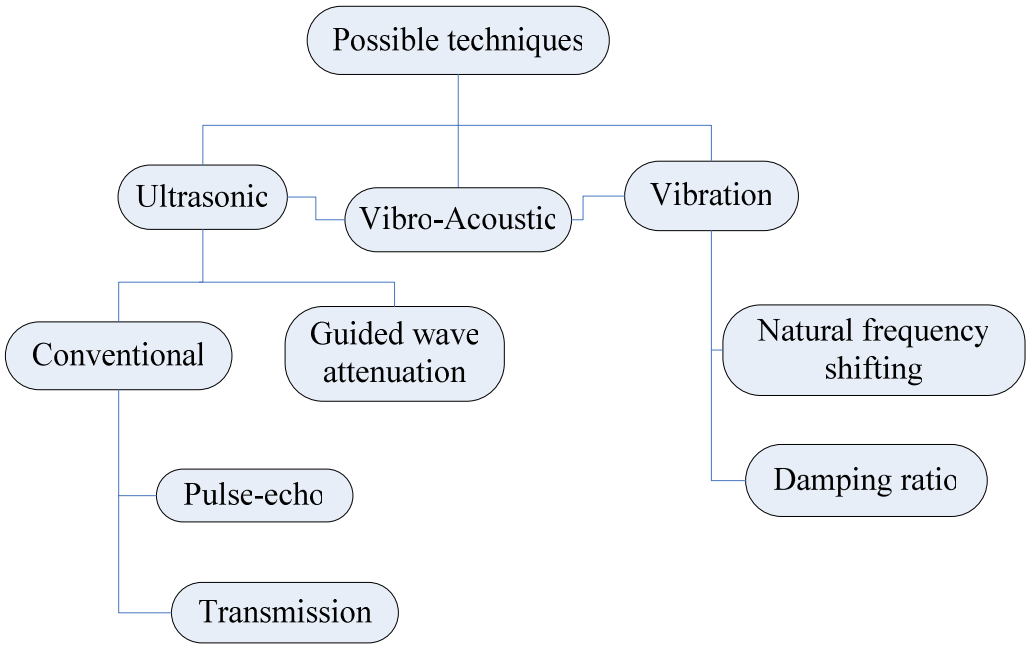

Figure 2-14 Possible non-destructive methods for milk powder deposition and blockage detection

2.6 Research methodology

Vibration analysis method has been determined to identify blockages in the cyclone or dropper tube of a spray dryer. The cyclone consists of cone and cylindrical shapes as shown in Figure 2.15. The bottom end of the cyclone joins a dropper tube with a 15cm cloth sock. Using vibration analysis, every piece between two support points becomes an individual vibration system, thus the cyclone and dropper tube will become at least two separate vibration systems. The milk powder deposition may happen anywhere inside the surface, but the milk powder build-up often happens at the bottom of the dropper tube. Therefore, this research will focus on the cyclone and its dropper tube.

Figure 2-15 Structure of a cyclone

Given the preliminary nature of this research, it is felt that simplifying the cyclone structure and dropper tube by a single vertical prototype will help in understanding the technique under investigation and in mathematically modelling the system. Both experimental testing and the theoretical modelling will be taken as the basis for future field investigation. Hence, a two-meter long cylindrical stainless steel tube is set up vertically with both ends supported by the musen ring which is fixed to the wall as shown in Figure 2.16. This stainless steel tube acts as a prototype of the cyclone or dropper tube. This research only focuses on the length between the two supported points that is 1.87m because it is an individual vibration system. To ensure the man-made blockage or flour can be easily put into the tube and stably held at a certain location to simulate the blockage build-up at the cyclone, both ends of the tube are supported.

Figure 2-16 The prototype and support type

This prototype represents a reasonably simplified model of the part of the cyclone or dropper tube, which will achieve the research goal and can be extended for a similar application as long as the cyclone's boundary conditions are determined according to the real situation. The mathematical model and experimental research both focus on the 1.87m long cylindrical tube. Use of the prototype will prove that vibration analysis method is feasible if experimental research matches with the mathematical model.

2.7 Closure

NDT techniques have been introduced in this chapter. The NDT literatures on wax or defect detection of pipeline in petroleum field and milk fouling detection are discussed due to no relevant research in the milk powder spray dryer field. Two possible NDT techniques were identified through a broad literature search and vibration analysis was determined as the technique for study in this project. In addition, a simplified cyclone or dropper tube was determined for use as the prototype. The prototype's vibration characteristics including natural frequencies and damping ratio will be developed in the next chapter.

Chapter 3 Modal Analysis

3.1 Introduction

Natural frequency of a system is defined as the frequency of oscillation of the system where the amplitude achieves maximum. The corresponding shape of the moving parts of the system is called a mode shape [30]. For simple Single Degree of Freedom (SDOF) system such as a spring-mass system, the oscillation is constrained in only one direction and mode, so it has one natural frequency and one mode shape. Practical systems, such as rods, beam, plates, shells, etc., have an infinite number of particles and are called continuous systems. This type of system has an infinite number of natural frequencies and natural modes. The natural frequencies are also called the resonant frequencies because the resonance occurs when the system is excited at the natural frequency. During resonance, the amplitude of vibration increases infinitely and can only be controlled by the amount of damping present in the system. Damping describes the energy dissipation properties of a material or system under cyclic stress. For the continuous system, the modal damping is to the energy dissipation properties for a particular modal shape.

The natural frequencies and modal shapes are useful and important properties of a dynamic system. Modal analysis to understand these properties of a dynamic system is important in engineering for design, control or diagnostics. The characteristic of a dynamic system can be determined by theoretical, numerical or experimental method. This thesis employed all three methods to deal with the modal analysis of a circular tube with inside deposition or blockage, with particular emphasis on the experimental modal analysis.

3.2 Natural frequency

A prototype consisting of a 1.87m long vertical stainless steel tube was built. The prototype's geometric dimensions are: R/h=31.77, L/R=37.97, h=1.55mm, L=1870mm, R=49.47mm, R is the inside radius, h is the thickness of the tube, L is the length, density is 7850kg/m3 and Young's elastic modulus is 210e9Pa.

According to Leissa.[31], the shell with R/h ≧ 500 is considered very thin and shell theories are more suitable for a thin shell than a thick one (R/h≦ 20). However, in the instance that a shell has L/R≦0.25, shell theories are considered unsuitable due to end effects. Additionally, shell theories are suitable for a very long shell (L/R ≧ 20). Although the exact dimensions of the cyclone and dropper tube are not available, it is assumed that their length/radius ratio is larger than 0.25 and radius/thickness is larger than 20, so shell theories are the best ones to analyze their vibration. According to Leissa's shell definition [31], the prototype falls into a very long thin shell category, so it is suitable to use shell vibration theory to do vibration analysis.

Shell vibration theory was studied to analyse the circumferential and axial vibration modes of the prototype, the Finite Element Analysis (FEA) solution was presented as an alternative to identify mode shapes by making comparisons with the experimental results. According to the Yu [32] assumption of neglecting the circumferential mode, the shell theory was simplified and introduced as beam theory. The analytical solution of the prototype used to identify the axial bending modes in the experimental results was presented. The accumulated milk powder deposit or blockage can be seen as an added mass to a cyclone or dropper tube, thus the cyclone or dropper tube with milk powder deposition or blockage inside can be modelled as a beam-mass system. Therefore the shell vibration theory, Bernoulli-Euler beam theory and beam-mass theory were employed to analyse the prototype's natural frequencies, modal shapes and variations.

Some assumptions were introduced to the prototype in order to make all horizontal theories suitable for the vertical prototype. Gravity force has a significant influence on the lower frequencies of long slender beam structure [33], but its effect can be discarded for the beam structure with high bending stiffness. Therefore, the gravity effect on the prototype can be neglected due to its high bending stiffness. Saito's research [34] found that the first natural frequency of a vertical rod with different boundary conditions was affected by the axial force due to the weight of the added mass and the effect increased with the amount of added mass by comparison mass ratio (added mass/mass of rod) 30 and 60. The mass of the prototype is $\rho\pi(R^2 - r^2)L = 7.15kg$, maximum simulated mass is 2.5 kg and maximum flour induced mass is 2kg. Thus, maximum mass ratio of

this prototype is 0.35. Based on Saito's research, the gravity effect of the added mass is so small that it can be neglected. According to the above assumptions, horizontal cylindrical shell, beam or beam-mass theory can be used for the vertical prototype.

3.2.1 Circular cylindrical shell vibration theory

Many shell theories and various solution methods have been developed in the literature. Since it was hard to obtain the exact solution without simplifying the complicated eight-order motion equation of shell vibration, all approximation solution methods included different assumption to simplify the motion equation in order to obtain the analytical solution with different boundary conditions.

Mously [35] compared three approximation solution methods: Weingarten–Soedel approximation, the Calladine–Koga improved classical-beam-on-Winkler-foundation model, and the Timoshenko-beam-on-Pasternak-foundation analogy of the shell, and found that the approximate solutions could only be valid within the limitation of their hypothesis and might fall within the limits of the validity of their hypothesis because the exact solutions were often presented in graphical and table forms. With the rapid development of computing technology many researchers have employed the Finite Element Method (FEM) to analyse the vibration behaviour of finite length cylindrical shells [24, 36, 37]. In this research the finite element analysis of the natural frequencies and its mode shapes of effective 1.87m long cylindrical empty shell were also investigated using ABAQUS, a finite element software package.

The closed circular cylindrical shell and coordinate system are shown in Figure 3.1 [31]. The cylindrical shell can be specified by three dimensions: length l, thickness h and radius R. Its shape can be specified by two nondimensional physical parameters,
Thickness/radius ratio: h/R
Length/radius ratio: l/R.

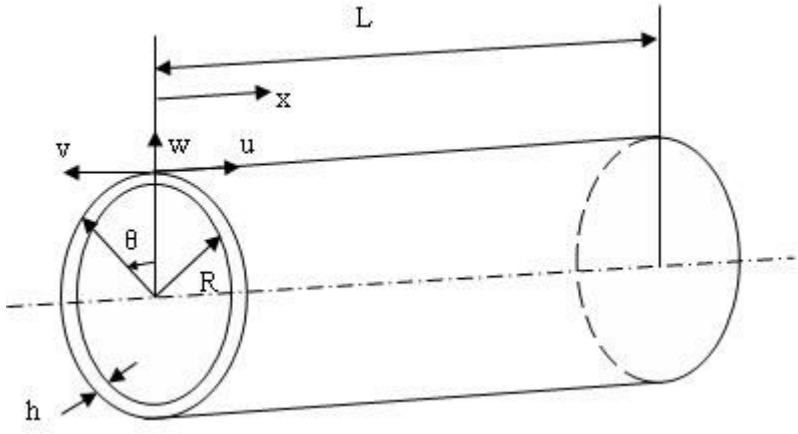

Figure 3-1 Closed circular cylindrical shell and coordinate system

The standard or classical theories of thin shells are governed by eighth order systems of differential equations. The equations of motion for thin circular cylindrical shells can be written in matrix form as

$$[\Im]\{u_i\} = \{0\} \tag{3.1}$$

where $\{u_i\}$ is the displacement vector.

$$\{u_i\} \equiv \begin{bmatrix} u \\ v \\ w \end{bmatrix} \tag{3.2}$$

where u, v and w are the orthogonal components of displacement in the x, θ and radial directions respectively, and $[\Im]$ is a matrix differential operator and can be expressed as the sum of two operators

$$[\Im] = [\Im_{D-M}] + k[\Im_{MOD}] \tag{3.3}$$

where $[\Im_{D-M}]$ is the differential operator according to the Donnell-Mushtari theory, $[\Im_{MOD}]$ is a "modifying" operator which alters the Donnell-Mushtari operator to yield another shell theory, and k is the nondimensional thickness parameter defined by

$$k \equiv h^2 / 12R^2 \tag{3.4}$$

The closed circular cylindrical shell of finite length with both ends simply supported whose boundary conditions are

$$w = M_x = N_x = v = 0 \quad \text{at } x = 0, l$$

The characteristic equation is,

$$\Omega^6 - (K_2 + \Delta K_2)\Omega^4 + (K_1 + k\Delta K_1)\Omega^2 - (K_0 + k\Delta K_0) = 0 \tag{3.5}$$

where Ω is the nondimensional frequency parameter

$$\Omega = \frac{\omega R}{2\pi}\sqrt{\frac{\rho(1-\upsilon^2)}{E}} \tag{3.6}$$

where ω is the natural frequency and its unit is Hz.

K_0, K_1,K_2 are constants arising from the Donnell-Mushtari theory [31] as Equation 3.7, and $\Delta K_1, \Delta K_2, \Delta K_3$ are modifying constants depending on the shell theory being used.

$$\left.\begin{aligned} K_2 &= 1 + \frac{1}{2}(3-\upsilon)\left(n^2+\lambda^2\right) + k(n^2+\lambda^2)^2 \\ K_1 &= \frac{1}{2}(1-\upsilon)\left[(3+2\upsilon)\lambda^2 + n^2 + (n^2+\lambda^2)^2 + \frac{(3-\upsilon)}{(1-\upsilon)}k(n^2+\lambda^2)^3\right] \\ K_0 &= \frac{1}{2}(1-\upsilon)\left[\left(1-\upsilon^2\right)\lambda^4 + k\left(n^2+\lambda^2\right)^4\right] \end{aligned}\right\} \tag{3.7}$$

where

$$\lambda = m\pi R / l \tag{3.8}$$

For fixed values of n and λ the Equation 3.5 will have three roots Ω^2. The modes for each frequency can be classified as primarily radial (or flexural), longitudinal (or axial), or circumferential (or torsional).

Typical radial nodal patterns for circular cylindrical shells supported by shear diaphragms are shown in Figure (3.2) [31], where (a) and (b) present the circumferential nodal pattern and axial nodal pattern respectively. n is circumferential mode parameter, m is axial mode parameter. The circular cylindrical shell may vibrate at any combined modal shapes. Figure (3.2) (c) shows n=2 and m=3 modal arrangement.

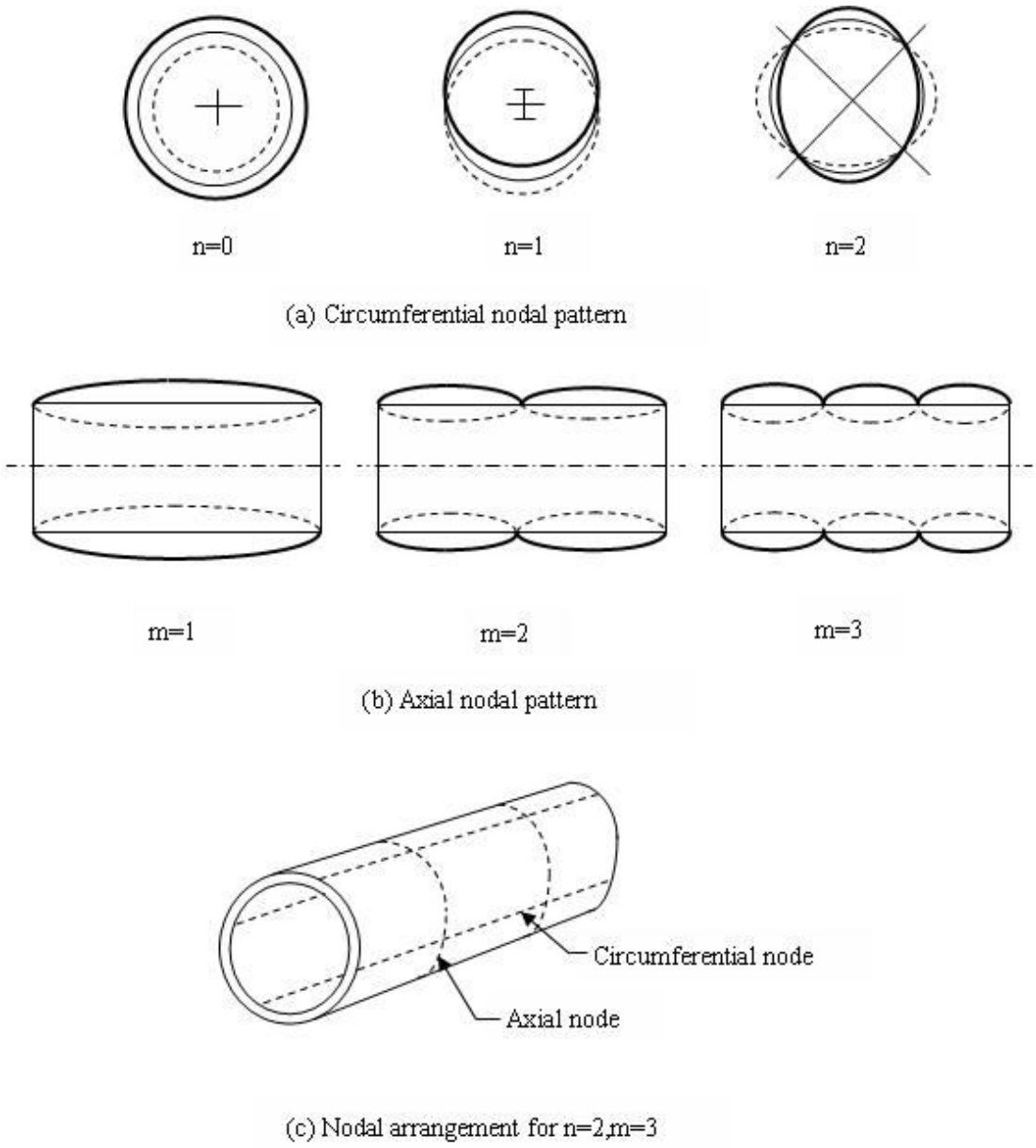

Figure 3-2 Illustration of parameter n and m

Solving the eight order cylindrical shell equation is extremely complex, so the FEA solutions for the effective 1.87 m long prototype shell will be presented in next section as the alternative to the analytical solutions and modal shape analysis.

3.2.2 Numerical analysis

FEA uses a numerical technique called Finite Element Method (FEM), a powerful tool for getting the numerical solution of a wide range of engineering problems. FEA was first developed in 1943 by Courant [38], who utilised the Ritz method of numerical analysis and minimization of variational calculus to obtain approximate solutions to vibration systems. By the early 1970s, FEA was limited to use in the aeronautics,

automotive, defense, and nuclear industries due to the expensive mainframe computers. Since the rapid decline in the cost of computers and the phenomenal increase in computing power, FEA has been developed for incredible precision to produce accurate results for all kinds of parameters. FEA can be used in new product design and existing product refinement. This method of product design and testing will reduce the new product development time and cost by predicting failure before manufacturing. Nowadays FEA is playing an important role in product design and development in the engineering field.

The analytical solutions to the eight order partial equation of the shell theory are difficult to obtain, so the FEA is an effective way to investigate the numerical solutions. There are many finite element software packages. In this research, ABAQUS was employed because of its powerful performance, quality and ability.

3.2.2.1 Modelling using ABAQUS

In this research, the numerical model is mainly to investigate the natural frequencies and mode shapes of the experimental cylindrical empty shell with both ends simply supported. ABAQUS is a suite of powerful engineering finite element method software that can solve problems ranging from relatively simple linear analyses to the most challenging nonlinear simulations. ABAQUS/CAE [39] is the complete ABAQUS environment that includes capabilities for creating ABAQUS models, interactively submitting and monitoring ABAQUS jobs, and evaluating results. ABAQUS/CAE consists of modules, such as defining the geometry, defining material properties, and generating a mesh, where each module defines a logical aspect of the modeling process. The FEA model can be built up by moving from module to module. When the model is complete, ABAQUS/CAE generates an input file for submitting to the ABAQUS analysis product. Two main analysis products: ABAQUS/Standard or ABAQUS/Explicit perform the analysis, sends information to ABAQUS/CAE to monitor the progress of the job, and generates an output database. Finally, the visualization module can be used to read the output database and view the analysis results. ABAQUS version 6.6.1 is used in this research.

The following steps were used in the ABAQUS to analyze the natural frequency of the cylindrical shell.

- Create the geometry parts
- Define material properties
- Assemble model
- Define analysis steps
- Define loads and boundary condition
- Mesh the model
- Run and get the results

Geometry parts can be created in the ABAQUS/CAE or imported from other applications. The three-dimensional, deformable solid body of cylindrical shell was built in ABAQUS/CAE by sketching the two-dimensional profile of the shell (two circles) and extruding it. Two concentric circles with diameters 0.0508m and 0.04925m were sketched and extruded to 1.87m long. ABAQUS/CAE displays an isometric view of the new part, as shown in Figure 3.3.

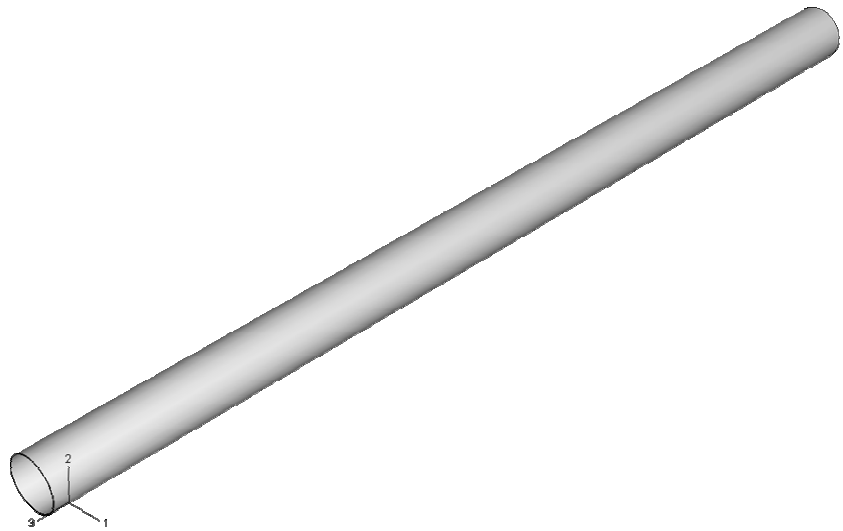

Figure 3-3 Geometric part of the empty cylindrical shell

After the geometry part was designed, a steel material for the cylindrical shell was created in the Materials container of the Model Tree. Next the elastic data form was obtained. ABAQUS/CAE displayed the Elastic data form and typed a value of 210E9 Pascal for Young's modulus and a value of 0.3 for Poisson's ratio in the respective fields.

A homogeneous solid section is the simplest section type. The solid section contains a reference to the material steel created in the previous module. The default selection of steel for the material associated with the section was accepted. The section was then assigned to the cylindrical shell.

The next module defines the geometry of the assembly by creating instances of a part and then positioning the instances relative to each other in a global coordinate system. A single instance was created for the cylindrical shell. ABAQUS/CAE positioned the instance so that the origin of the sketch that defined the circles profile overlaid the origin of the assembly's default coordinate system.

Frequency analysis was defined in the step module. ABAQUS uses eigensolver to figure out the frequency problems, the symmetric matrix solver was chosen and normalized eigenvectors by displacement. The boundary conditions were defined as simply supported both ends, in the ABAQUS it is U1=U2=UR1=UR2=0, which means that the cylindrical shell can only move and rotate in z-axis.

There are three-dimensional solid element types in ABAQUS/Standard element library —hexahedral, triangular prism (or called wedge), and tetrahedral. The default 3-dimension hex element was used to mesh the modal part. The element type is C3D8R which is 8-node linear brick, reduced integration, hourglass control. The meshed modal with the default global seed size 0.014 was shown as in Figure 3.4, which is too coarse, so approximate global size 0.005 was also used to obtain a fine analysis result.

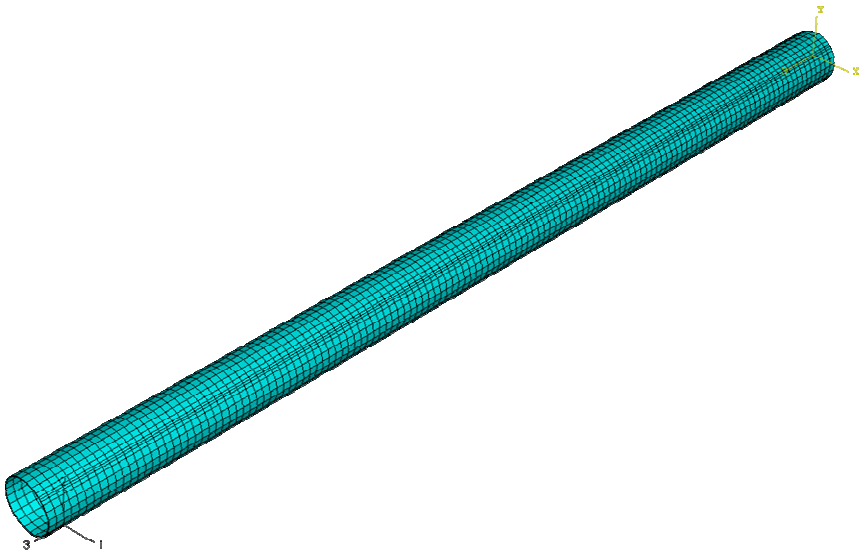

Figure 3-4 meshed cylindrical shell

After the model part was meshed, a job that was associated with model could be created and submitted for analysis. The eigenfrequencis and eigenvalues were available in the Field Output in the Result Module to be displayed. The eigenfrequencies of the cylindrical shell FEA model meshed by 0.014 element size and 0.005 element size were calculated by ABAQUS software as shown in Figure 3.5 and 3.6. More vibration mode shapes were shown in the fine meshed model than coarse one. Although it took more computing time to obtain the result, the fine meshed model gave more accurate results.

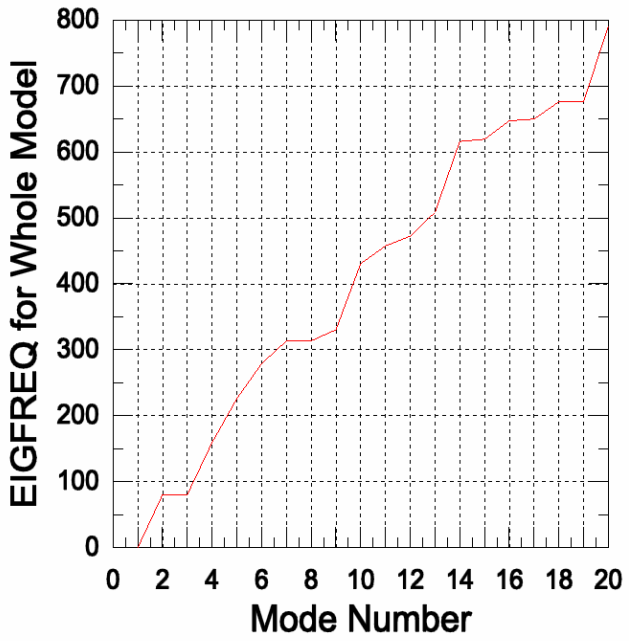

Figure 3-5 Eigenfrequencies (mode 1-20) meshed by 0.014 element size

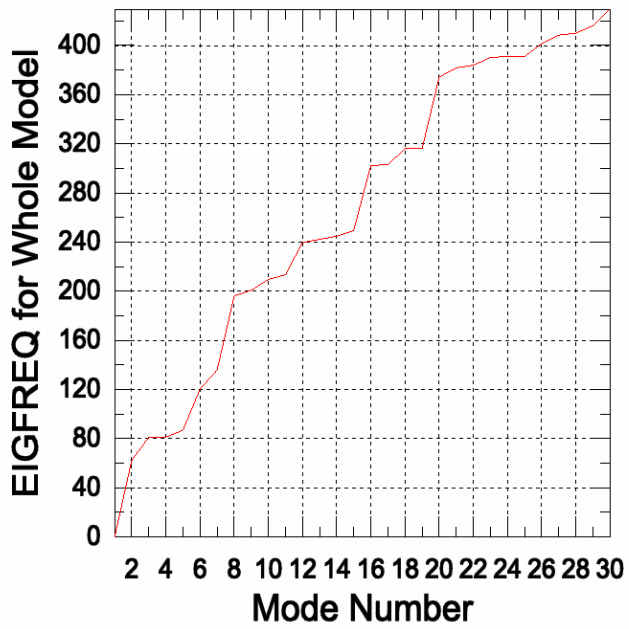

Figure 3-6 Eigenfrequencies (mode 1-30) meshed by 0.005 element size

The bending frequencies of the 0.005 element size meshed cylindrical shell were closer to the analytical solution, which are 81, 316Hz as shown in Figure 3.7 and 3.8 compared to the analytical solution 82, 329 Hz. In addition, the bending frequencies of the coarse

mesh element size (0.014) were 80, 313 Hz. There was 1 Hz for the first bend mode and 3 Hz for the second bending mode increase with the mesh element size increased from 0.014 to 0.005. This indicates the FEA results may vary according to the mesh element size. In general, the smaller the element size the better the approximation to the analytical solution but the more computing time needed. Due to the limit of the chosen mode number, the third mode bending shape did not show in this FEA analysis. Although there was still a gap between the fine mesh FEA result and beam theory analytical solution, 1 Hz for the first bending mode and 13 Hz for the second bending mode can accepted and improved by extra fine mesh.

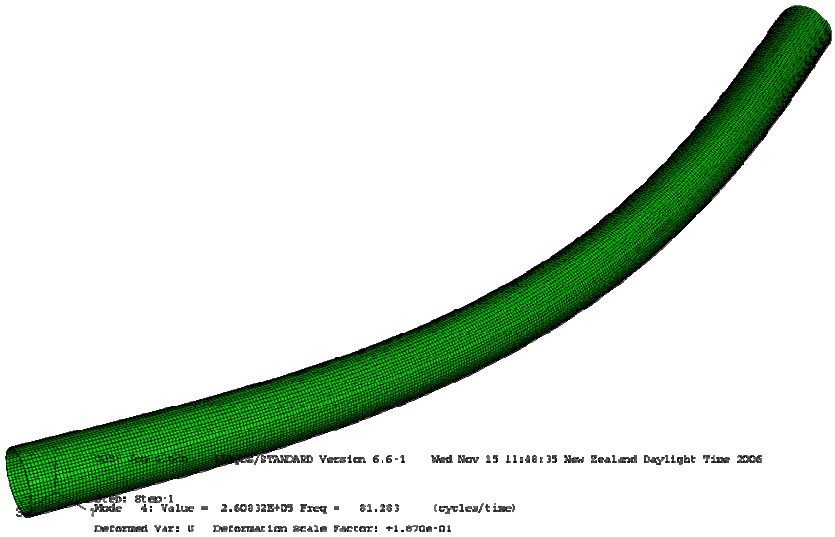

Figure 3-7 First bending natural frequency 81Hz with 0.005 element size mesh

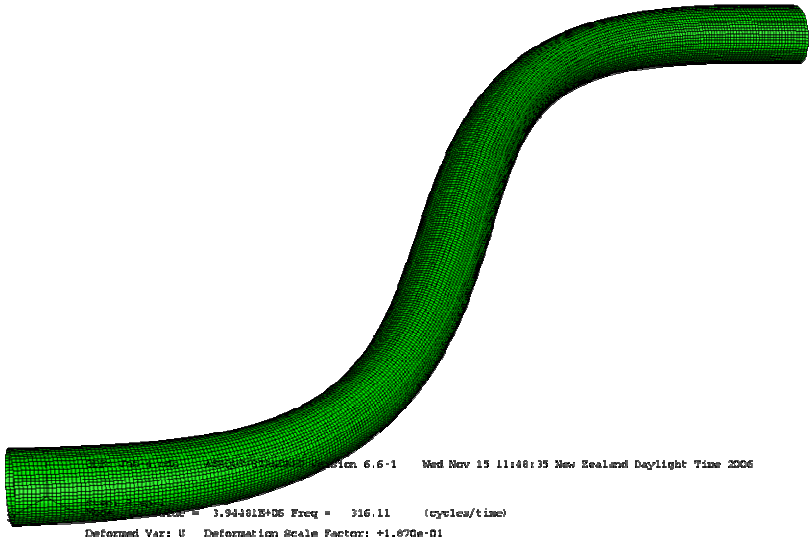

Figure 3-8 Second bending natural frequency 316Hz with 0.005 element size mesh

With the exception of the pure bending natural frequency, all other frequencies might be pure circumferential mode or a combination of the circumferential mode and bending mode. Figure 3.9 showed the 381Hz vibration modal shape which was m=1and n=4 and Figure 3.10 showed the 401Hz modal shape which was m=3 and n=4. These two modes were also identified clearly in the experiment. They will be further discussed in Chapter 5.

Figure 3-9 381 Hz modal shape

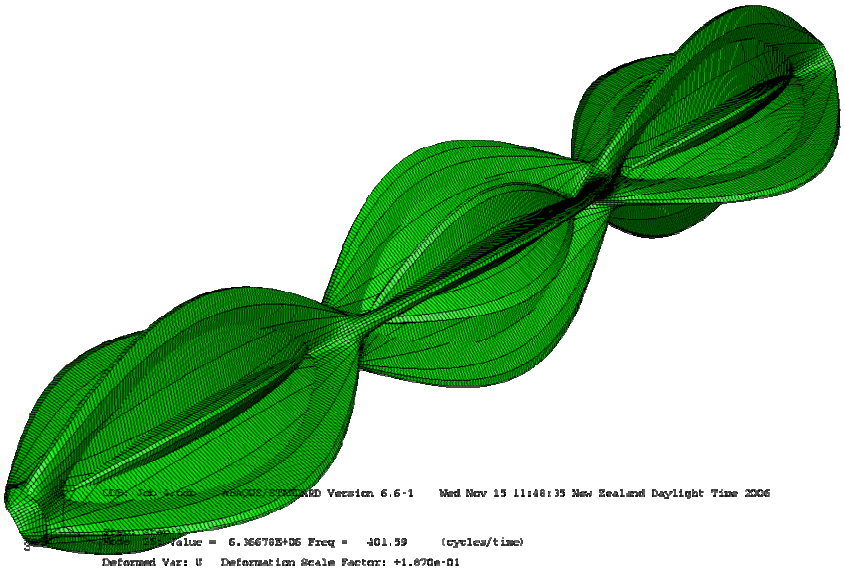

Figure 3-10 401 Hz modal shape

3.2.2.2 Closure

FEA of ABAQUS links the relationship between the analytical and experimental results by displaying the modal shapes. It helps to identify the modal shapes of the experimental natural frequencies. This offers better understanding of the experimental results and can be used to match with the theory of the beam with an added mass. The main objective of this project is to investigate the vibration characteristics using experimental modal analysis method, so FEA was limited to researching the empty cylindrical shell as an alternative of the unavailable analytical shell theory result to identify the experimental modal shapes by matching theoretical beam bending modes.

The simplified model and boundary condition definition has proven to be feasible to obtain accurate mode shapes and natural frequencies. In summary, numerical modelling is a good approximation to the analytical solution as shown in experimental validation.

3.2.3 Beam theory

Within all the approximation solutions to the cylindrical shell, Yu [32] made a big assumption, to neglect small circumferential deformation effect compared to the axial one and approximate the characteristic equation of cylindrical shell to that of Bernoulli-Euler beam. So the eighth order differential equation was reduced to the fourth.

The partial differential equation of motion for the transverse vibration of beam[40] is known as Equation 3.9.

$$\frac{\partial^2 y}{\partial t^2} + \lambda \frac{\partial^4 y}{\partial x^4} = 0 \qquad (3.9)$$

where y = deflection of the beam

x = coordinate along the longitudinal axis of the beam

$$\lambda^2 = EI/A\rho \qquad (3.10)$$

EI = the flexural rigidity of the beam

A = area of cross section

ρ= Beam's density

When a beam vibrates transversely in one of its natural modes, the deflection at any location varies harmonically with time, as follows:

$$y(t) = (A\cos\omega_n t + B\sin\omega_n t) \qquad (3.11)$$

where ω_n = natural frequency, so taking Equation 3.11 into Equation 3.9, we get,

$$\frac{d^4 y}{dx^4} - k^4 y = 0 \qquad (3.12)$$

where $k^2 = \omega_n/\lambda$

The general solution for Equation 3.12 is

$$y = (C_1\cos kx + C_2\sin kx + C_3\cosh kx + C_4\sinh kx) \qquad (3.13)$$

The Boundary condition of the prototype could be situated between simply supported and fixed. The following part will introduce these two kinds of boundary conditions and calculate their first three natural frequencies. And these natural frequencies will be used to compare with numerical and experimental results to determine the prototype's boundary condition.

In the case of both ends simply supported beam, the displacement and the bending moment at each end are all equal to zero. That is, the boundary conditions are

$$y(0,t) = y(L,t) = 0,\ M(0,t) = M(L,t) = 0$$

And the bending moment equation is given as Equation 3.14,

$$M(x,t) = EI\frac{\partial^2 y(x,t)}{\partial x^2} \tag{3.14}$$

Apply these boundary conditions to Equation 3.13. Get $C_1=C_3=C_4=0$
And a characteristic frequency equation is as Equation 3.15.

$$\sin kL = 0 \tag{3.15}$$

Then the eigenvalues is

$$kL = i\pi \tag{3.16}$$

where i=1,2,3,……

So the modal shapes (or eigenfuctions) become

$$y_i = \sin i\pi x / L \tag{3.17}$$

The first three vibration modal shapes for a simply supported beam are shown in Figure 3.11 below.

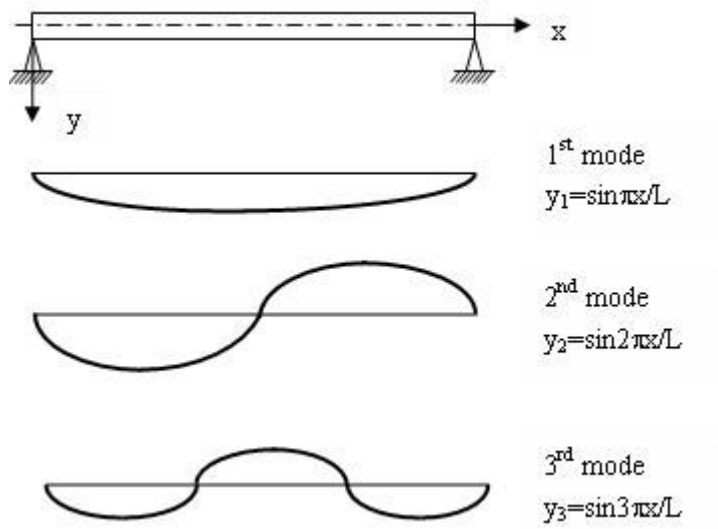

Figure 3-11 The first three modal shapes for the beam with both ends simply supported

For the beam with a clamped end or fixed end, the deflection and slope of the deflection curve are zero, and the boundary conditions are

$$y(0,t) = y(L,t) = 0, \frac{\partial y(0,t)}{\partial x} = \frac{\partial y(L,t)}{\partial x} = 0$$

The frequency equation for beam with fixed ends is

$$\cos kL \cosh kL = 1 \tag{3.18}$$

Then the eigenvalues are

$$k_i L = \left(i + \frac{1}{2} \right) \pi \tag{3.19}$$

where I=1,2,3,……

And natural frequencies is

$$f_i = \frac{k_i^{\,2}}{2\pi} \sqrt{\frac{EI}{\rho A}} \tag{3.20}$$

For the test cylindrical shell we have the parameters as follows,

Young modulus E=210GPa

Moment of inertia I= (pi/4)*(R^4-r^4)

The cross area A=pi*(R^2-r^2)

Density ρ=7850kg/m^3

Length of the tube L=1.87m

Outside radius R=0.0508m

Inside radius r=0.04925m

Taking all the parameters of the experimental tube into Equation 3.16 and 3.20, the bending natural frequencies of the prototype with both ends simply supported are,

f_1=82.19Hz f_2=328.77 Hz f_3= 739.74 Hz f_4=1315.1 Hz

For the case that the beam has fixed ends boundary conditions, the bending natural frequencies of the prototype are,

f_1=186.32 Hz f_2=513.58 Hz f_3= 1006.9 Hz f_4=1664.4 Hz

3.2.4 Transverse vibration of beam-mass systems

From previous section, the cyclone of spray drier can be simplified as a Bernoulli-Euler beam and the milk powder accumulated at a section in the cyclone may be modelled as a point mass along the beam. Thus, the cyclone with accumulated milk powder inside can be seen as a beam-mass system.

An Euler-Bernoulli beam with a concentrated mass on it is considered a beam-mass system [41]. This system is often used as a design model in engineering and the natural frequencies of a beam-mass system are of practical interest in many engineering fields. Some approximate methods and exact analysis have been used to obtain the solutions to this problem [41-47]. Ozkaya.[41, 46] obtained the exact frequencies for linear parts of the vibration for the beam-mass system with different boundary conditions which included both ends fixed and both ends simply supported, and researched the approximate solution of the non-linear part using the method of multiple scales, a perturbation technique to correct the liner part. The exact analyses of the natural frequency can be obtained by solving the determinant of the frequency equation using the Bernoulli-Euler theory. Computer technology makes it possible to research the natural frequencies of a beam with more than one mass. Low [43] presented the Euler-Bernoulli type beam carrying three masses on various locations under three respective boundary conditions. The method of eigenanalysis and Rayleigh's estimation was employed to reduce the computing time. Yoo [48] investigated the modal characteristics of a rotating cantilever beam with a concentrated mass located in an arbitrary position and found that the magnitude and location of the added mass significantly influenced the natural frequencies.

3.2.4.1 Exact analysis

Ozkaya [41] analysed non-linearity resulting from stretching during the vibrations because of immovable end conditions by using the methods of multiple scales, a perturbation technique. The natural frequencies and mode shapes of the linearity are displayed with the location and the magnitude of the mass under five different sets of boundary conditions. The non-linear frequency-amplitude variation and corrections to the linear problem are also presented. It was found that the natural and non-linear

frequencies decrease when the concentrated mass increases regardless of the supporting condition, but if mass is located at a node, the frequencies may remain unchanged. When the mass is increased, the effect of stretching on the non-linear frequencies decreases for all cases.

The prototype in this study can be simplified as a beam with a concentrated mass located at L_1 as Figure 3.12.

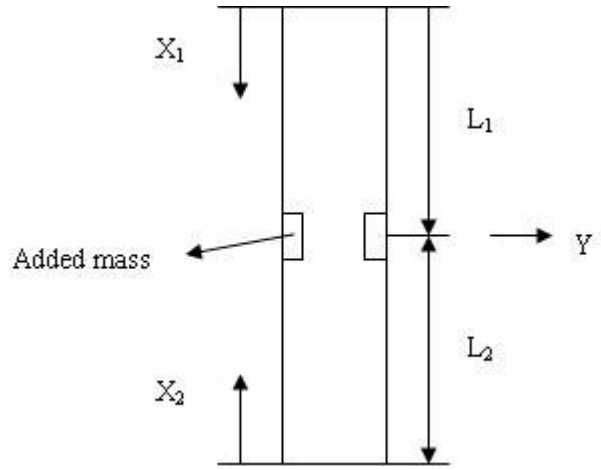

Figure 3-12 The geometry of the prototype with an added mass at L_1

The differential equations of motion for the transverse vibration of beam-mass system are,

$$\begin{cases} \dfrac{\partial^2 y_1}{\partial t^2} + \lambda^2 \dfrac{\partial^4 y_1}{\partial x_1^{\,4}} = 0 \\ \dfrac{\partial^2 y_2}{\partial t^2} + \lambda^2 \dfrac{\partial^4 y_2}{\partial x_2^{\,4}} = 0 \end{cases} \tag{3.21}$$

The boundary conditions for the simple support beam are

$$(Y_1)_{x_1=0} = 0 \quad \left(\frac{\partial^2 Y_1}{\partial x_1^{\,2}}\right)_{x_1=0} = 0$$

$$(Y_2)_{x_2=0} = 0 \quad \left(\frac{\partial^2 Y_2}{\partial x_2^{\,2}}\right)_{x_2=0} = 0$$

The boundary conditions at the location of the concentrated mass are as follows:

$$\begin{cases} (Y_1)_{x_1=L_1} = (Y_2)_{x_2=L_2} \\ \left(\dfrac{dY_1}{dx_1}\right)_{x_1=L_1} = \left(\dfrac{dY_2}{dx_2}\right)_{x_2=L_2} \\ \left(\dfrac{\partial^2 Y_1}{\partial x_1^{\,2}}\right)_{x_1=L_1} = \left(\dfrac{\partial^2 Y_2}{\partial x_2^{\,2}}\right)_{x_2=L_2} \\ EI\left(\dfrac{\partial^3 Y_1}{\partial x_1^{\,3}}\right)_{x_1=L_1} - EI\left(\dfrac{\partial^3 Y_2}{\partial x_2^{\,3}}\right)_{x_2=L_2} = M\left(\dfrac{\partial^2 Y_1}{\partial x_1^{\,2}}\right)_{x_1=L_1} \end{cases} \tag{3.22}$$

The Equation 3.22 can be made dimensionless through the definitions

eigenvalue β ($\beta_i = k_i L$ for mode i),

$\beta^2 = \omega_n$ and ω_n is the natural frequencies,

Position parameters $\eta = L_1/L$, $L_1 + L_2 = L$,

And mass ratios $\alpha = M/\rho AL$.

Then,

$$\begin{cases} Y_1(\eta) = Y_2(\eta) \\ Y_1^{'}(\eta) = Y_2^{'}(\eta) \\ Y_1^{''}(\eta) = Y_2^{''}(\eta) \\ Y_1^{'''}(\eta) - Y_2^{'''}(\eta) + \alpha\beta^4 Y_1(\eta) = 0 \end{cases} \tag{3.23}$$

The solutions for the Equation 3.21 are,

$$\begin{aligned} Y_1 &= C_1 \cos kx_1 + C_2 \sin kx_1 + C_3 \cosh kx_1 + C_4 \sinh kx_1 \\ Y_2 &= C_1^{'} \cos kx_2 + C_2^{'} \sin kx_2 + C_3^{'} \cosh kx_2 + C_4^{'} \sinh kx_2 \end{aligned} \tag{3.24}$$

From these boundary conditions the unknown constants $C_1, C_2, C_3, C_4, C_1^{'}, C_2^{'}, C_3^{'}$ and $C_4^{'}$ can be evaluated.

From $(Y)_{x_1=0} = 0$, then,

$C_1 + C_3 = 0$,

From $\left(\dfrac{\partial^2 Y_1}{\partial x_1^{\,2}}\right)_{x_1=0} = 0$, then,

$-C_1 + C_3 = 0$

From these two equations, $C_1 = C_3 = 0$

Same thing we have

$C_1^{'} = C_3^{'} = 0$

Now, Equation 3.24 turns into,

$$\begin{aligned} Y_1 &= C_2 \sin kx_1 + C_4 \sinh kx_1 \\ Y_2 &= C_2^{'} \sin kx_2 + C_4^{'} \sinh kx_2 \end{aligned} \tag{3.25}$$

Combine Equations 3.23 and 3.25, we get,

$$\begin{cases} C_2 \sin\eta + C_4 \sinh\eta - C_2^{'} \sin\eta - C_4^{'} \sinh\eta = 0 \\ C_2 \cos\eta + C_4 \cosh\eta - C_2^{'} \cos\eta - C_4^{'} \cosh\eta = 0 \\ -C_2 \sin\eta + C_4 \sinh\eta + C_2^{'} \sin\eta - C_4^{'} \sinh\eta = 0 \\ C_2\left(\alpha\beta^4 \sin\eta - \cos\eta\right) + C_4\left(\cosh\eta + \alpha\beta^4 \sinh\eta\right) + C_2^{'} \cos\eta - C_4^{'} \cosh\eta = 0 \end{cases} \tag{3.26}$$

Then the Equation 3.26 can be written as,

$$AC=0 \tag{3.27}$$

in which $A = \begin{bmatrix} a_{11} & a_{12} & a_{13} & a_{14} \\ a_{21} & a_{22} & a_{23} & a_{24} \\ a_{31} & a_{32} & a_{33} & a_{34} \\ a_{41} & a_{42} & a_{43} & a_{44} \end{bmatrix}$, $C = \begin{bmatrix} C_2 \\ C_4 \\ C_2^{'} \\ C_4^{'} \end{bmatrix}$

$$\begin{array}{llll} a_{11} = \sin\eta & a_{12} = \sinh\eta & a_{13} = -\sin\eta & a_{14} = -\sinh\eta \\ a_{21} = \cos\eta & a_{22} = \cosh\eta & a_{23} = -\cos\eta & a_{24} = -\cosh\eta \\ a_{31} = -\sin\eta & a_{32} = \sinh\eta & a_{33} = \sin\eta & a_{34} = -\sinh\eta \\ a_{41} = \alpha\beta^4 \sin\eta - \cos\eta & a_{42} = \cosh\eta + \alpha\beta^4 \sinh\eta & a_{43} = \cos\eta & a_{44} = -\cosh\eta \end{array}$$

Solving for the constants C by equating to zero the (4x4) characteristic determinant, that is,

$$\begin{vmatrix} a_{11} & a_{12} & a_{13} & a_{14} \\ a_{21} & a_{22} & a_{23} & a_{24} \\ a_{31} & a_{32} & a_{33} & a_{34} \\ a_{41} & a_{42} & a_{43} & a_{44} \end{vmatrix} = 0$$

The frequency equation det (A) =0, can be derived symbolically by virtue of Maple software of matlab toolbox. The characteristic equation is written in terms of eignvalue β, position parameter η and mass ratio α. The characteristic frequency equation and modal shapes of beam-mass system with both ends simply supported were given as Equations 3.28 and 3.29 by Ozkaya [41].

$$2\tanh\beta\tan\beta+\alpha\beta\left\{\begin{array}{l}\tanh\beta\sin\beta\eta\left(\sin\beta\eta-\tan\beta\cos\beta\eta\right)\\+\tan\beta\sinh\beta\eta\left(\tanh\beta\cos\beta\eta-\sinh\beta\eta\right)\end{array}\right\}=0 \quad (3.28)$$

$$\left\{\begin{array}{l}y_1(x)=C\left\{\begin{array}{l}\tanh\beta\left(\cot\beta\sin\beta\eta-\cos\beta\eta\right)\sin\beta x\\+\left(\tanh\beta\cosh\beta\eta-\sinh\beta\eta\right)\sinh\beta x\end{array}\right\}\\y_2(x)=C\left\{\begin{array}{l}\tanh\beta\sin\beta\eta\left(\cot\beta\sin\beta x-\cos\beta x\right)\\+\sinh\beta\eta\left(\tanh\beta\cosh\beta x-\sinh\beta x\right)\end{array}\right\}\end{array}\right. \quad (3.29)$$

The characteristic frequency Equation 3.28 is solved by using the Newton-Raphson method. Table 3.1 shows the first three bending natural frequencies for different mass ratio, position parameter under the simple support boundary condition [41] using the dimensions of the prototype.

Table 3-1 Natural frequencies with different mass ratio and position parameter

A	η	ω_1	ω_2	ω_3
1	0	82.19	328.76	739.72
	0.1	74.92	248.91	550.20
	0.2	62.08	224.40	612.20
	0.3	53.25	247.75	722.26
	0.4	48.69	293.45	666.04
	0.5	47.30	328.76	565.35
10	0	82.19	328.76	739.72
	0.1	44.40	165.69	492.16
	0.2	27.15	183.66	589.37
	0.3	21.05	222.94	717.40
	0.4	18.53	280.48	643.47
	0.5	17.82	328.76	520.08

Figures 3.13, 3.14 and 3.15 show that the first three bending natural frequencies change with the mass ratio α=1 and 10 and position parameter from 0.1 to 0.5.

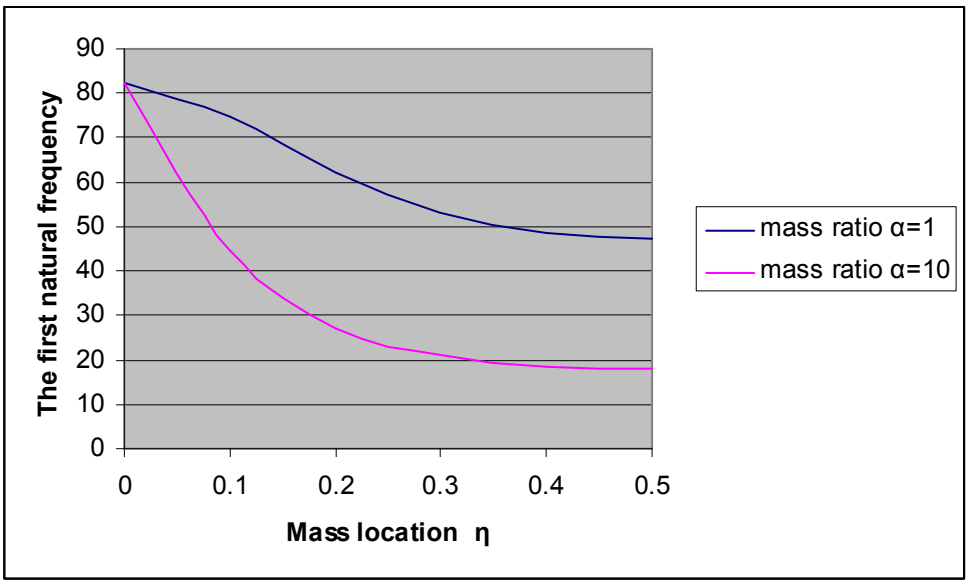

Figure 3-13 The first bending natural frequency with the mass ratio and position

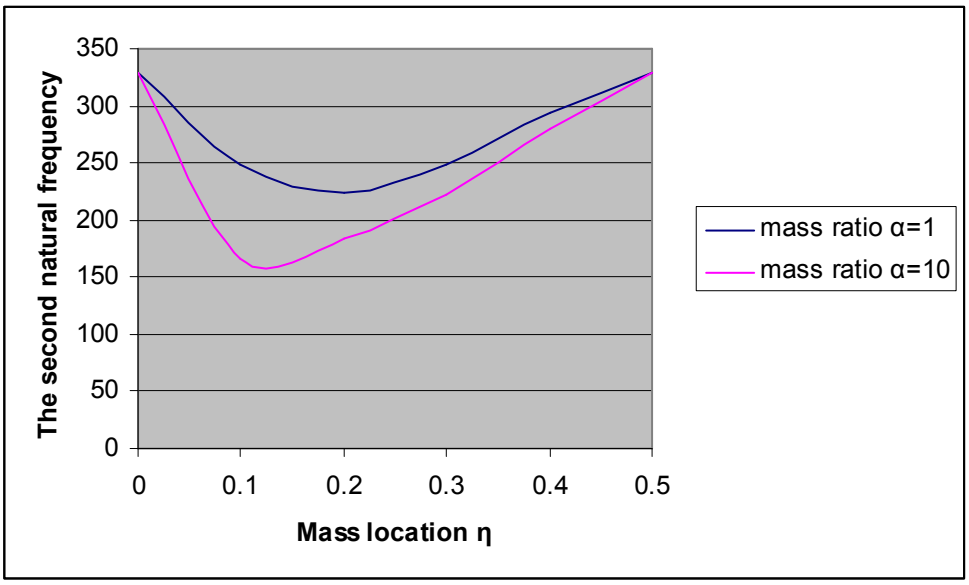

Figure 3-14 The second bending natural frequency with the mass ratio and position

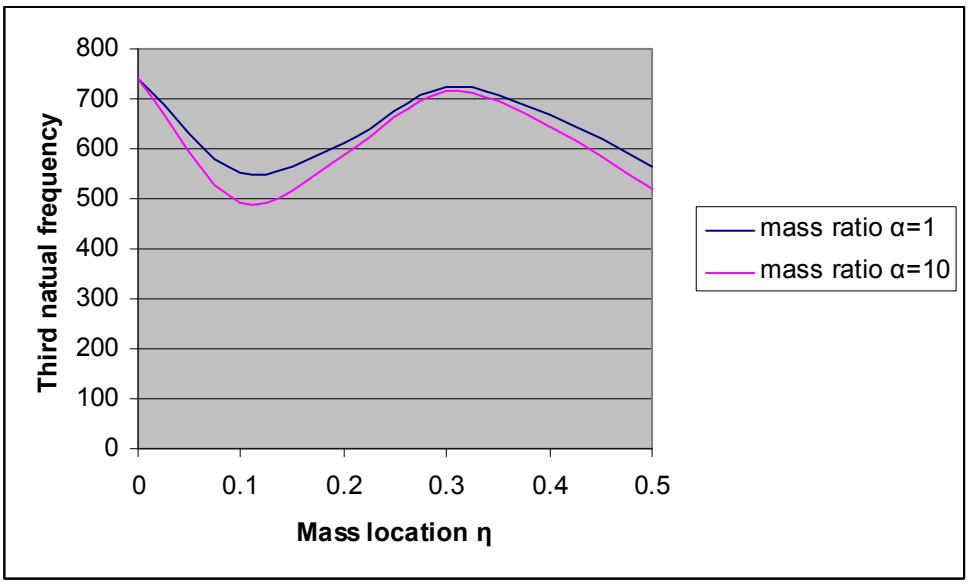

Figure 3-15 The third bending natural frequency with the mass ratio and position

Due to the symmetry support for the beam-mass system with simple support ends, Table 3.1 and Figures 3.13-3.15 only show the natural frequencies up to η=0.5. It can be seen that all natural frequencies decreased with the added mass except that the added mass was placed at the node. The first natural frequency decreased with the increase of mass and close to the midpoint of the test cylindrical tube. It reached the minimum when close to the midpoint. The two supported ends were the vibration nodes of the first natural frequency. Besides the two supported ends, η=0.5 became another node for the second natural frequency. The two supported ends, η=1/3 and η=2/3 made up the nodes of the third natural frequency. If the added mass was put at a vibration node, the corresponding natural frequency would not change, as with the one without added mass. The natural frequency decreased to minimum between the two corresponding vibration nodes.

Ozkaya [46] also presented the non-linear frequencies using the method of multiple scales, a perturbation technique to research beam-mass system with both ends fixed. A multi-layer, feed-forward, back propagation artificial neural network (ANN) algorithm was employed to calculate the natural frequencies and non-linear corrections, which drastically reduced the computational time compared to the conventional Newton-Raphson techniques. The variation of the first three natural frequencies of beam-mass system with both ends fixed beam followed the same trend as that with both ends simply supported, just the values of the natural frequencies were different and higher than that with both ends simply supported.

Yoo [48] did the vibration analysis of rotating cantilever with a concentrated mass at an arbitrary position of the beam. The motion equations were derived and transformed into dimensionless forms by using four dimensionless parameters, α, β, γ and δ, denoting the concentrated mass ratio, concentrated mass location ratio, angular speed ratio and hub radius ratio respectively. Figure 3.16 shows the effect of the location and magnitude of a concentrated mass on the first bending natural frequency. The first natural frequency increases to an extent and then decreases as the concentrated mass moves from the fixed end to the free end. The variation of the first natural frequency increases as the concentrated mass ratio increases.

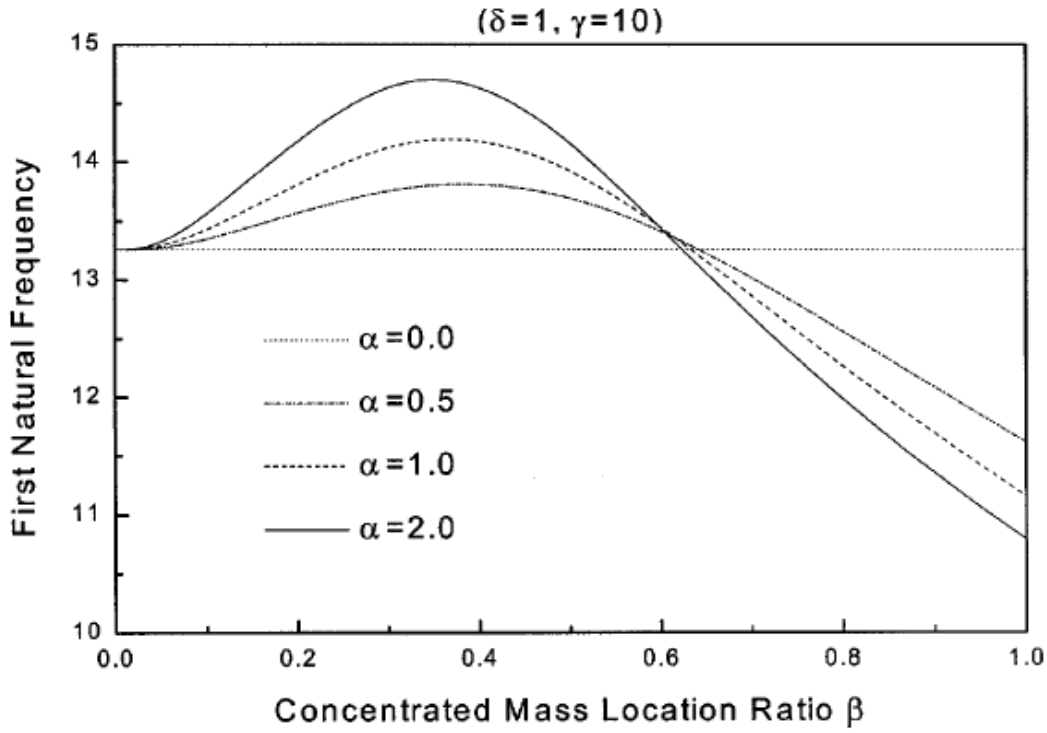

Figure 3-16 Effect of the concentrated mass location on the first natural frequency

The bending natural frequencies of a beam-mass system vary with the concentrated mass ratio and location ratio no matter what kinds of boundary conditions. Therefore as long as the boundary conditions are determined for a practical application, the corresponding equations of the vibration motion can be derived and solved to illustrate the variation of the natural frequencies with the added mass ratio and location ratio.

3.2.4.2 Approximate method

McConnell [49] assumed that the added mass was so small that original mode shapes and modal stiffness were not significantly altered, while modal mass was altered by adding the mass, and the beam mass distribution was given by

$$\rho(x) = \rho + m\delta(x - x_0) \tag{3.30}$$

where ρ is the beams mass per unit length.

$\delta(x - x_0)$ is the Dirac delta function.

x_0 is the location of added mass m.

The mode shapes of a simply supported beam are given by Equation 3.17.
The modal mass is given as

$$m_p = \int_0^l \rho(x) y_i^2(x) dx \tag{3.31}$$

Taking Equations 3.30 and 3.31 into Equation 3.17, the modal mass of a simply supported beam with an added mass is

$$m_p' = \frac{\rho l}{2} + m \sin^2\left(\frac{i\pi x_0}{l}\right) \tag{3.32}$$

Compared to the modal mass without an added mass

$$m_p = \frac{\rho \quad l}{2} \tag{3.33}$$

We can see that the second part in Equation 3.32 shows the effect of the added mass to the modal mass.

The natural frequencies with added mass f_{after} are altered as Equation 3.34, compared to the original ones f,

$$f_{after} = f\sqrt{\frac{m_p}{m_p'}} \tag{3.34}$$

This is a simple and quick method to obtain the natural frequency change with an added mass however it has limitations due to the assumption that the added mass does not alter the modal stiffness.

Figure 3.17 [49] showed the change of the first and third natural frequencies with the added mass at midpoint of the beam with simply supported two ends. The solid line means theoretical prediction natural frequencies and diamond points represent experimental natural frequencies.

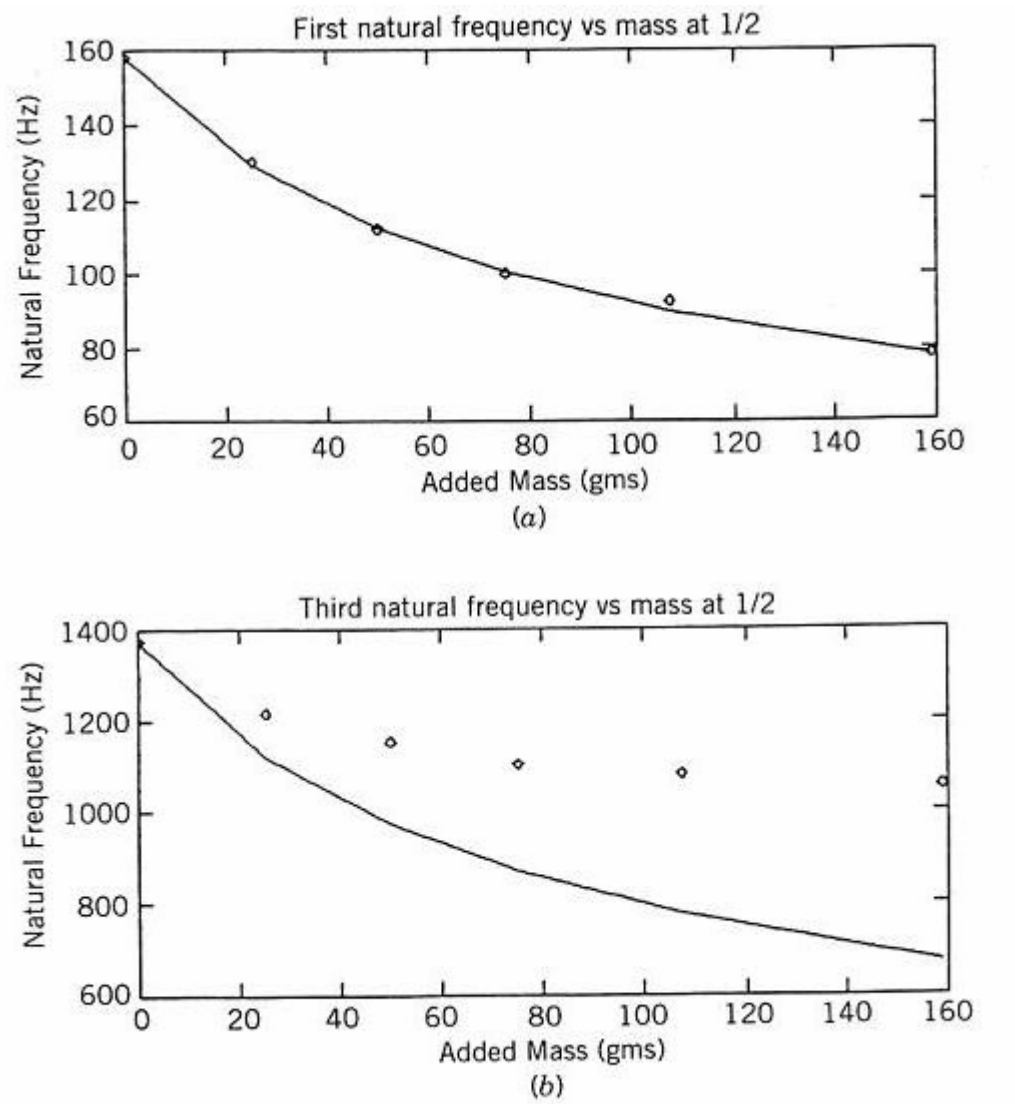

Figure 3-17 The first and third natural frequencies with the added mass at midpoint of the beam with both ends simply supported

The experimental and theoretical first natural frequency fit very well; however, the experimental natural frequencies are much greater than those predicted by theory for the third natural frequency. This is because the first mode shape changes little and the modal stiffness remains constant regardless of the mass added. This is not the case for the third mode. The mode shape and modal stiffness and modal mass are altered by the addition of the added mass. Hence, the method has limitations where the added mass should be less than 10 percent or less of the beam's mass [49].

3.3 Damping ratio

Modal damping ratio is the most difficult to be accurately obtained in all the modal parameters. There are several methods to measure the damping ratio of a vibration system. The following introduces two common methods, the logarithmic decrement method and bandwidth method [50, 51].

3.3.1 Logarithmic decrement method

For the SDOF system, logarithmic decrement method obtains the damping from the rate of free decay vibration of the system in time domain. Figure 3.18 and Equation 3.35 illustrate how to calculate the damping using this method.

Logarithmic decrement (δ) can be calculated using Equation 3.35,

$$\delta = \frac{1}{m} \ln \frac{x_n}{x_{n+m}} \tag{3.35}$$

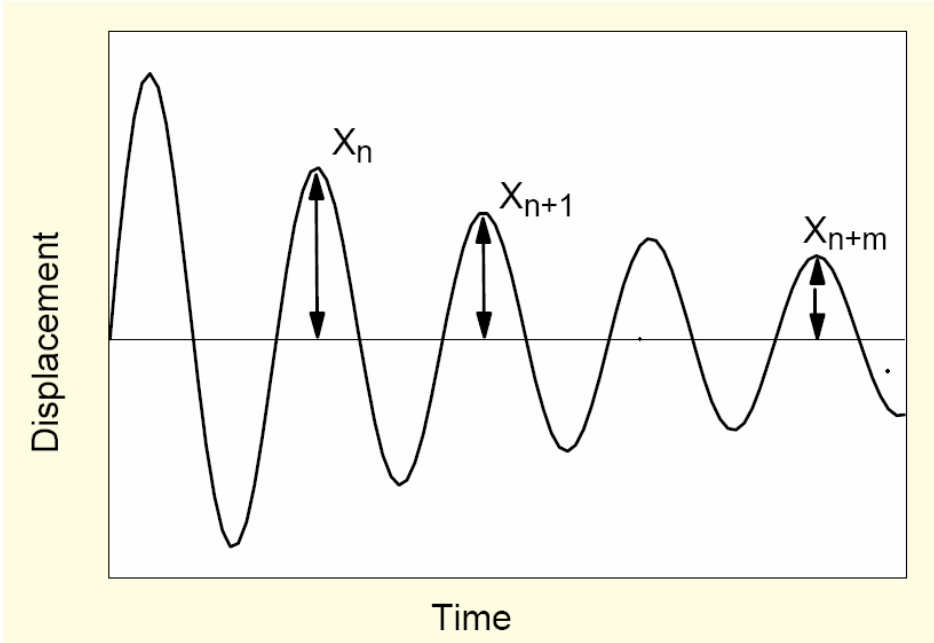

Figure 3-18 Free decay vibration of SDOF system

Logarithmic decrement of SDOF system can be also expressed as,

$$\delta = \frac{2\pi\varsigma}{\sqrt{1-\varsigma}} \tag{3.36}$$

Rewriting Equation 3.36 we have damping ratio,

$$\varsigma = \frac{\delta}{\sqrt{4\pi^2 + \delta^2}} \tag{3.37}$$

SDOF is too realistic to be applied in practical engineering field. The time domain signal must be filtered to SDOF before logarithmic decrement method is applied.

3.3.2 Half-power bandwidth method

Half-power bandwidth method can be used to estimate damping ratio in the frequency domain. It is defined as the ratio of the frequency range between the two half power points to the natural frequency at that mode as shown in Figure 3.19 and Equation 3.38.

$$\varsigma = \frac{\omega_2 - \omega_1}{2\omega_0} \tag{3.38}$$

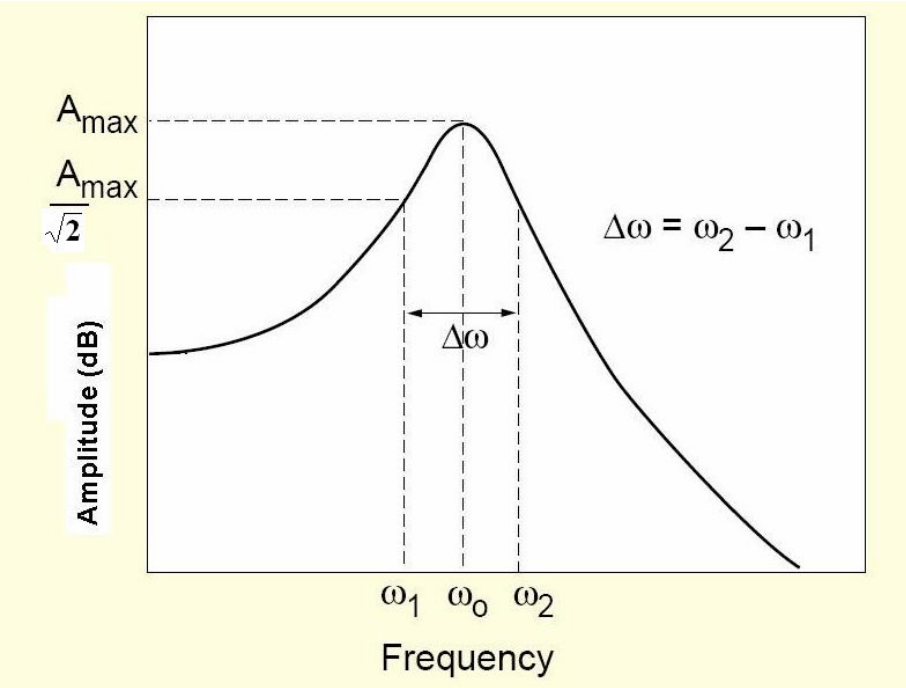

Figure 3-19 Half-power bandwidth method

For the decibel scale, half-power points down from the natural frequency means a –3 dB drop from the resonant peak A_{max}. So half-power bandwidth method is also called as the 3 dB method.

It can be seen from Figure 3.19 that the high damping ratio leads to the wide bandwidth of the two half power points and a low peak at resonant frequency. On the other hand, the low damping ratio system has narrow bandwidth and a sharp peak at the resonant frequency. Therefore, the difference in the damping ratio can be easily qualitatively distinguished by the bandwidth of the two half power points and peak shape from the FRF curve.

3.4 Closure

Two vibration characteristics: natural frequency and damping ratio were researched in this chapter. Shell theory and its numerical solutions of the prototype with both ends simply supported were presented, followed by beam theory as a simplified shell theory. Solutions with both ends simply supported and fixed were obtained as a reference to compare with numerical shell theory solution and experimental results to identify the boundary condition of the prototype. Beam-mass theories with different boundary conditions were investigated and the variation of first several bending natural

frequencies of the beam with simply supported and cantilever beam were presented. Two basic damping ratio extraction methods: logarithmic decrement and half-power bandwidth method were researched as well. In the next chapter, the principle of experimental vibration testing will be introduced. The experimental instruments and the prototype's experimental setup will be presented in addition to onsite experiments of monitoring dropper tube and cyclone.

Chapter 4 Vibration testing and experimental modal analysis

4.1 Introduction

To simulate the milk blockage process a vertical stainless steel shell as a prototype is considered. The main objective of this project is to study the vibration characteristics of the prototype with and without powder accumulated in it. Firstly, the shell resonant frequencies need to be determined. The variation of the first several natural frequencies and its damping ratio with differing extent of blockage inside the shell is of importance. Lastly the experiment was extended to monitor one of the cyclones onsite in the Te Rapa Fonterra plant.

In order to identify the vibration characteristic of the prototype by experimental method, the concept of transfer function and frequency response function need to be clarified firstly. Transfer function is a mathematical method to research an unknown dynamic system. The concept of the operational transfer function [52] is widely used in the dynamic analysis and is about the relation between input and output. It can be written as Equation 4.1,

$$a_n \frac{d^n q_o}{dt^n} + a_{n-1} \frac{d^n q_o}{dt^{n-1}} + \ldots + a_1 \frac{dq_o}{dt} + a_0 q_o = b_m \frac{d^m q_i}{dt^m} + b_{m-1} \frac{d^m q_i}{dt^{m-1}} + \ldots + b_1 \frac{dq_i}{dt} + b_0 q_i \tag{4.1}$$

Where q_o = output quantity,

q_i = input quantity,

t = time,

a's, b's =combination of system physical parameters.

The Laplace-transform method can be employed for studying the linear system. The Laplace transfer function is the ratio of the Laplace-transform of the output quantity to the Laplace-transform of the input quantity. The Laplace transfer function of the Equation 4.1 would be written as,

$$\frac{q_o}{q_i}(s) = \frac{b_m s^m + b_{m-1} s^{m-1} + \ldots + b_1 s + b_0}{a_n s^n + a_{n-1} s^{n-1} + \ldots + a_1 s + a_0} \tag{4.2}$$

where $s = \sigma + i\omega$ is the complex variable of the Laplace-transform.

The most important and useful measurement response is Sinusoidal Transfer Function, a steady-state measurement response to a sinusoidal input. The amplitude ratio (output amplitude over input one) and phase angle, by which the output leads the input, are two main parameters to study the dynamic characteristics of an unknown system. Thus, the characteristic of an unknown system can be obtained by using transfer function concept.

4.2 Frequency response function

If a constant-parameter linear system is physically realizable and stable, the dynamic characteristics of the system can be described by a frequency response function $H(f)$, which is defined as the inverse Fourier Transform (FT) of the Impulse Response $h(\tau)$ of a system as in Equation 4.3 [53].

$$H(f) = \int_{-\infty}^{\infty} h(\tau) e^{-j2\pi\omega\tau} d\tau \tag{4.3}$$

The dynamic characteristics of a constant-parameter linear system can be described by an impulse response function, which is defined as the output of the system at any time to a unit impulse input applied a time. For any arbitrary input the system output is given by the convolution integral as Equation 4.4 [54].

$$y(t) = \int_{-\infty}^{\infty} h(\tau) x(t-\tau) d\tau \tag{4.4}$$

The value of the output $y(t)$ is given as a sum over the entire history of the input $x(t)$. For physical system, the effective lower limit of integration in Equation 4.4 is zero rather than $-\infty$ since $h(\tau)$=0 for $\tau < 0$.

An important relationship for the frequency response function of constant-parameter linear system is obtained by taking the FT of both sides of Equation 4.4. Letting

$X(f)$ be the FT of an input and letting $Y(f)$ be the FT of the resulting output, assuming these transforms exist, it will be as Equation 4.5.

$$Y(f) = H(f)X(f) \tag{4.5}$$

Before a frequency response function can be determined, it is necessary to define the input and output parameters of interest. In this experimental research, an impact hammer was used to generate the impulse force. At the same time the velocity of the vibration from laser sensor and acceleration of the vibration from accelerometer were recorded. So force is input and velocity or acceleration is output.

The definition of this kind of Frequency Response Function (FRF) is:

$$H(f) = \frac{X(f)}{F(f)} \tag{4.6}$$

The system response $X(f)$ is the FT of the behaviour, in time, of the excited system. The forcing function $F(f)$ is the FT, the frequency information about the function that is used to excite the system. The frequency transform of an impulse signal is white in the frequency domain, implying that its frequency components are uniformly distributed throughout the entire frequency range. Then its FT will be flat in the frequency domain. Therefore, the system FRF is proportional to the system response $X(f)$.

The FRF is useful for providing information about the frequency response of a system, even where the forcing function is not constant over the range of frequencies. This response function is therefore scaled to the input, and so is less responsive to bias from a non-flat spectrum.

The magnitude of FRF is typically shown on a logarithmic Y axis in dB which is decibel value and is defined in Equation 4.7.

$$\text{Decibel value} \equiv \text{dB} \equiv 20\log A \tag{4.7}$$

The FRF is generally a complex-valued quantity that may be conveniently thought of in terms of magnitude and as associated phase angle. This can be done by writing in complex polar notation as Equation 4.8.

$$H(f) = |H(f)|e^{-j\phi(f)} \tag{4.8}$$

The absolute value is called the system gain factor, the associated phase angle is called phase factor.

Although the formal definition of frequency response includes the magnitude and phase response of unit under test at all frequencies of interest, in common usage, the frequency response often only implies the magnitude.

4.3 Resonance search test methods

There are two types of resonance search test methods according to the nature of the excitation used: free vibration test and forced vibration test [30].

Free vibration test is also known as transient (or impulsive) excitation with cross spectrum and includes the hammer test and drop test. Impact hammer testing is an ideal source of broadband excitation and is widely used in the impulse test method. The modal hammer is an impact device that excites the structure with a constant force over a frequency range of interest. Impact hammer testing is a convenient and economical excitation method. It is highly portable for fieldwork and provides no unwanted mass loading to the structure under test.

Force vibration test uses signal generator to generate the sine wave to excite vibration of the test system and using oscilloscope to measure the output including the amplitude and phase. When a sine wave is added to the test system, the amplitude and phase of the output relative to the input at each frequency of interest will be measured. This process is repeated for each frequency. The gain of the system is the ratio of the amplitude of the output voltage to the input voltage. The phase angle is the delay of the output to the input. This method has the advantage of being low-cost and simple, but is quite slow. To reduce the testing time, the swept sine excitation is used in the resonant searching. This is a variant of the sine wave method in that it uses continuous swept sine waves,

instead of discretely stepped sine waves, making it faster than the ordinary sine wave method. Certain instruments may have "adaptive sweep," where the sweep rate adapts to the rate of change of the output signal. For example, when sweeping through a very sharp resonance, the sweep rate is reduced to fully resolve the resonance peak.

Besides the sine wave excitation, noise with cross spectrum excitation is widely used in force vibration method. Any signal containing frequency components in the range of interest can be used in the noise excitation. The signals are not required to have the same amplitude, however all measurements using noise excitation with cross spectral techniques require simultaneous measurement of both input and output signals, using simultaneously sampling A/D Converters. The fastest way to perform the measurement is to use a broadband excitation signal that excites all frequencies simultaneous and use Fast Fourier Transform (FFT) techniques to measure all frequencies at the same time. Using random noise excitation best minimises noise and non-linearity. Band limited white noise is a practical random signal suitable in the noise excitation, because its frequency content has no particular bias toward any frequency.

Compared with the above mentioned resonant search methods, impact hammer testing is easier to implement without introducing extra devices to the test system. The major experiments in this study employed impact hammer testing technique with forced vibration method to verify its modal shapes.

4.4 Experimental testing procedures

The main objective of this project is to investigate the variation of the resonant frequencies and damping ratio of the prototype with and without blockage. The experiment process includes four stages. First the resonant frequencies of the shell must be identified. Second, different mass values were inserted inside at different location. Third flour blockage was used to simulate different extent blockage. Finally, based on reasonable lab results, the experiment was extended to a real plant to monitor the cyclone vibrating using the impulse excitation method.

4.4.1 Vibration testing instrumentation

An experimental vibration system usually consists of the excitation, sensors and transducers, signal conditioning and signal acquisition [49]. The equipment used in this project were an impact hammer and its conditioner, electrodynamic shaker, signal generator, power amplifier, accelerometer and its conditioner, laser and controller, oscilloscope, LabView data acquisition card and computer.

ENDEVCO Modal Hammer model 2302 with piezoelectric force transducer and aluminum tip as shown in Figure 4.1 was used in the free vibration test to generate the impulse signal.

Figure 4-1Modal hammer

LDS V203 electromagnetic shaker driven by the TtiTG230 signal generator through the LDS PA25E power amplifier was used in the force vibration test to excite the test system as shown in Figure 4.2.

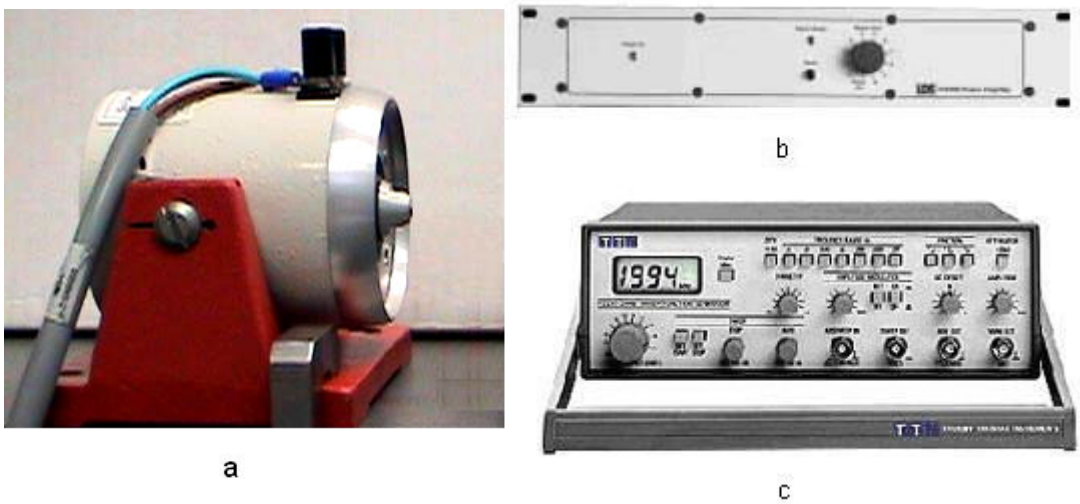

Figure 4-2 (a) Eletrodynamic shaker (b) power amplifier (c) signal generator

Accelerometer and laser act as the sensor to measure the responses of the test system to the excitation from shaker or impact hammer. The type of accelerometer is Brüel & Kjær Delta Tron Accelerometer 4399, with Delta Tron power supply WB1372 (shown in Figure 4.3). The WB1372 signal conditioner converts the charge produced by the piezoelectric accelerometer into a voltage signal.

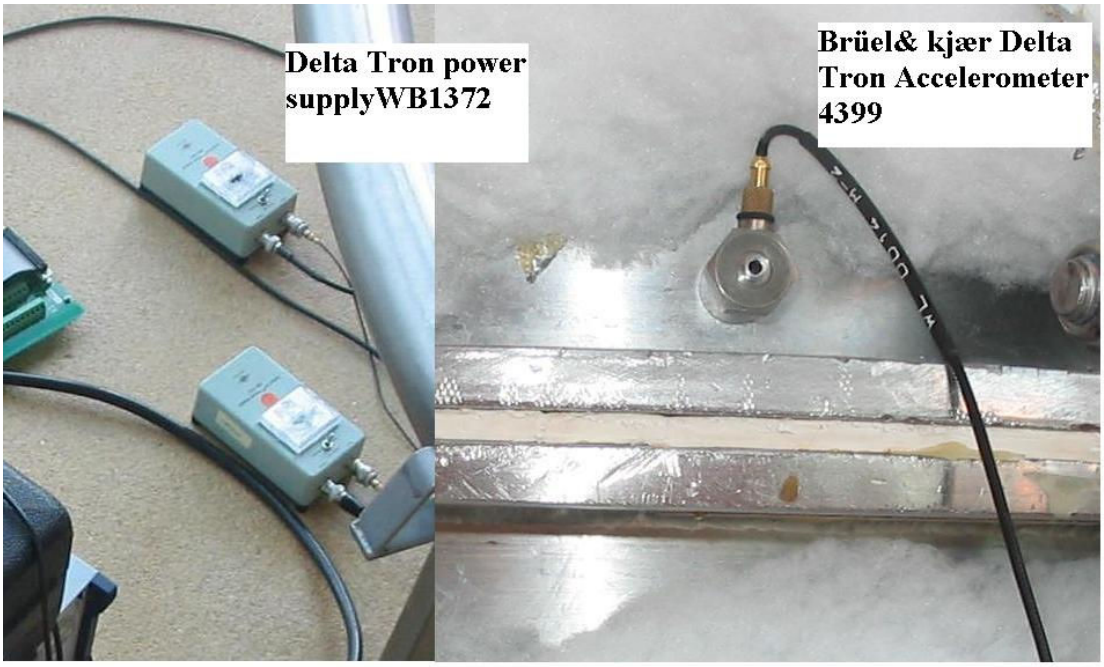

Figure 4-3 Accelerometer and its power supply

A Polytec OFV 505 laser sensor head and its OFV 5000 vibrometer shown in Figure 4.4 were also used as another type of sensor.

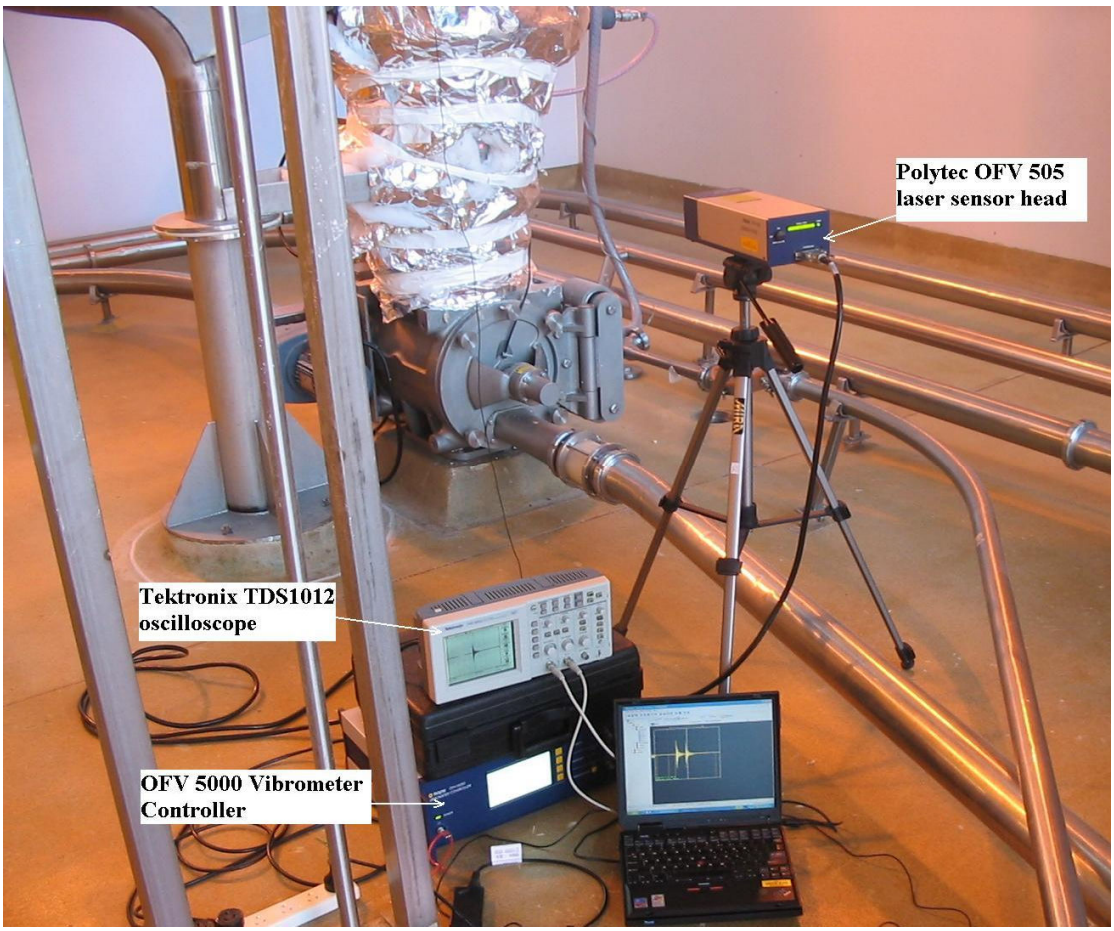

Figure 4-4 Polytec laser senor head, its vibrometer controller and Tektronix oscilloscope

A Tektronix TDS1012 oscilloscope was used to display the time domain vibration and its corresponding software 'Wavestar' was used to record the data to the computer (Figure 4.4). A limitation of the oscilloscope is that at its maximum, it can only record 2500 data; thus if the sample rate is 2500Hz then it can only record 1 second data. A display length of oscilloscope is also restricted by the sample rate, therefore it can not record long signals. The oscilloscope was only used at the early stage of the research; afterwards the LabVIEW Data acquisition (DAQ) board and LabView data record programme were used to collect the data.

The LabVIEW Data acquisition board modal is PCI-6024E, which has 16 channels analog input and three analog input measurement modes—differential (DIFF), reference single ended (RSE), and nonreferenced single ended (NRSE) [55]. When collecting vibration data using LabVIEW Data acquisition board, the reading floats even when there is no vibration. The following discussion introduces the channel configuration, explains the signal floating reason and provides a solution.

When a channel is configured for DIFF input, the signal uses two multiplexer inputs. The input signal is connected to the positive input and its reference signal is connected to the negative input.

A single ended connection is when the DAQ card analog input signal is referenced to a common ground with another input signal. The input signal is tied to the positive input and the ground is tied to the negative input. A maximum of eight analog input channels are available for DIFF configuration, compared to 16 for single ended configuration.

In this study, DIFF mode configuration was chosen in the experiment. DIFF input is preferable because it rejects the ground loop-induced errors and reduces environmental noise. If noise is present at both positive terminal V+ and negative terminal V-, it will be rejected in the amplified output. The amplifier only considers the difference between V+ and V-.

There are two types of signal; floating and ground referenced. A ground referenced signal shares a common ground with DAQ card by connecting its negative node to the building system ground. For example, a device that is plugged into a wall outlet generates a signal. A floating signal has an isolated ground reference point different from the building system ground like battery-powered devices, thermocouples, transformers, or strain gauge signal. The ground reference of a floating signal must be tied to the DAQCard analog input ground to establish a local reference, otherwise the reading from the measured input signal is random and floats because of bias currents, which cause the input voltage to drift out of the range of the DAQ board. The method to correct this problem is to place bias resistors from the inputs to ground as shown in Figure 4.5 [55].

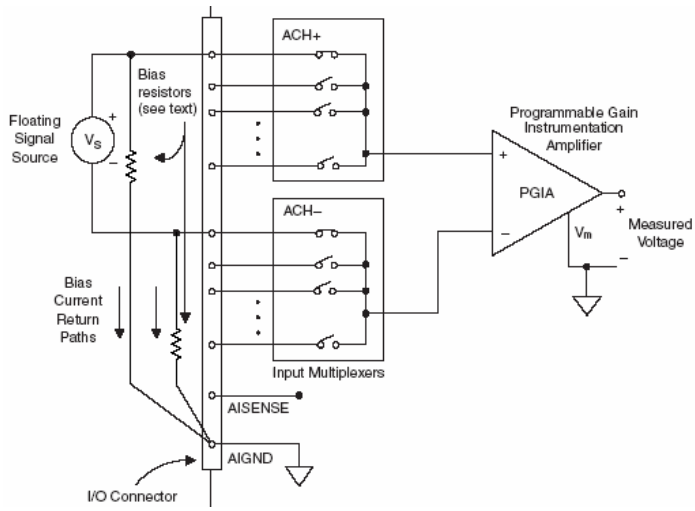

Figure 4-5 Schematic diagram of bias resistors for DIFF mode

Figure 4.6 shows two bias resistors connected in parallel with the signal leads of a floating signal source. If the resistors were not used and the signal was truly floating and the source has high output impedance, the same value resistor (100kΩ to 1MΩ) on both the positive and negative inputs can be use to balance the signal path. In this experiment, the signal-floating problem was solved by putting two 100k resistors on both positive and negative inputs.

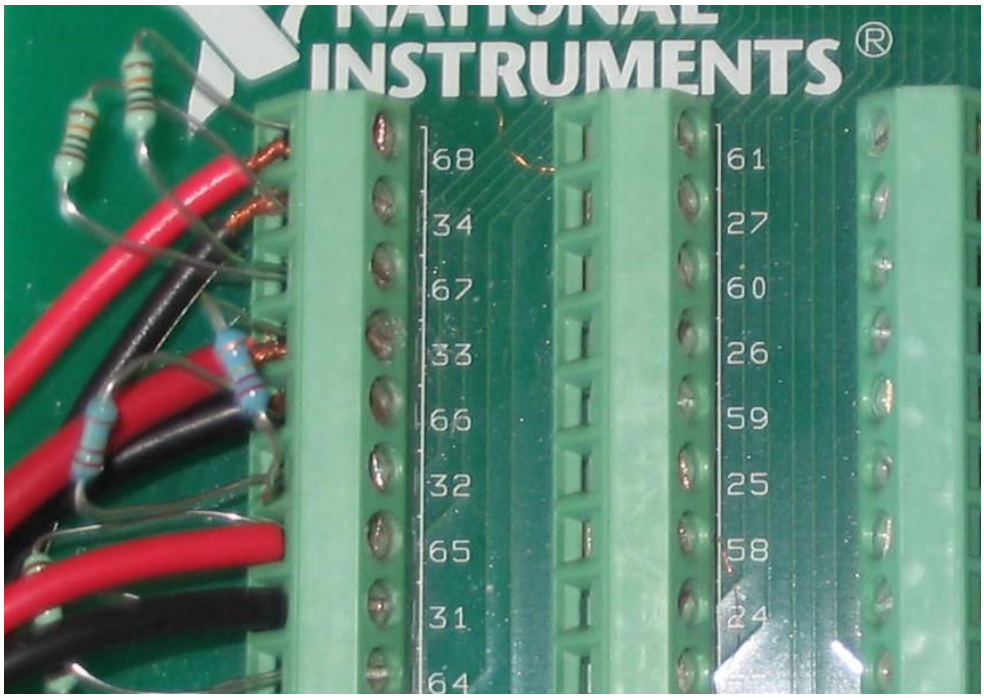

Figure 4-6 Experimental bias resistors connection with multiplexer board for the DIFF mode

A data programme was made to record the vibration generated by the impact hammer as shown in Figure 4.7. Plot0 recorded impulse generated by the impact hammer. Plot1

showed the top accelerometer and plot2 showed the bottom accelerometer. Plot 4 was the laser sensor.

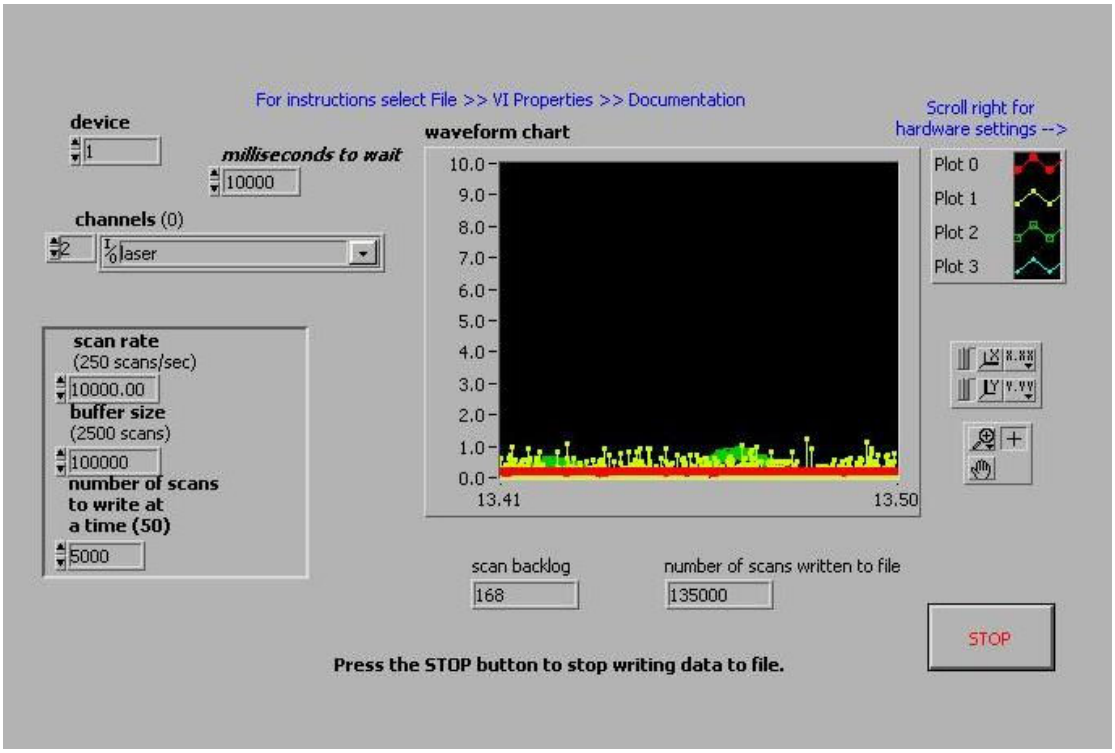

Figure 4-7 The front panel of LabView Data acquisition programme

To preserve the shape of the signal, the sample rate should be between 5 and 10 times the maximum frequency component of the signal [56]. The sample rate is 10,000Hz, and Nyquist critical frequency is 5,000Hz which is half of the sampling rate. The buffer size is 100,000 and the number of scans to write at a time is 5,000. Simultaneously, a ten order 1200Hz low pass filter was put before FFT in Matlab as an anti-aliasing filter.

4.4.2 Simulated amount mass

A schematic diagram of the experimental setup is shown in Figure 4.8. The two ends of the shell were clamped by the munsen ring and anchored onto the concrete wall. Two accelerometers were placed along the tube in the longitudinal direction; one was stuck 400mm from the top munsen ring, called top accelerometer (or Acc1), the other called bottom accelerometer (or Acc2) was 400mm from the bottom munsen ring. A laser sensor measured the vibration at 500mm from the bottom munsen ring. An impact hammer excited the shell 300mm from the top munsen ring, aligning with the directions of the accelerometers.

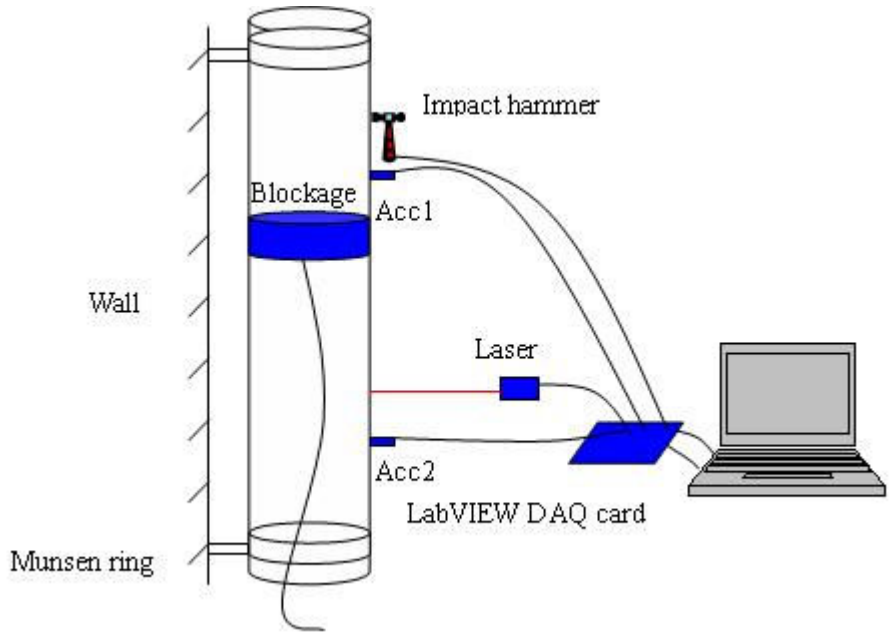

Figure 4-8 The schematic diagram of the experimental setup for the simulated mass

Three masses 0.64kg, 1.6kg and 2.5kg of mass ratio were 0.09, 0.23 and 0.37 respectively, were made in this experiment (Figure 4.9). The mass was placed at the top of the cylindrical shell and pulled down by a string, stopping at 11 regularly spaced locations.

Figure 4-9 One of experimental mass

When the cylindrical shell was struck, each mode of vibration represented by the different frequencies was excited. The shell vibrated until the damping effect of air brought it to a rest.

4.4.3 Flour induced blockage

The schematic diagram of the experimental setup is shown in Figure 4.10. Flour was used to simulate the blockage, with two location blockages established, one from the bottom munsen ring and the other starting at 1/10 of the tube length away from the bottom munsen ring. Firstly a plastic board was inserted into the cylindrical shell and then two, four, six, and eight cups of flour blockage were added. All sensors were placed at the same position as the previous experiment and impact hammer struck the same location.

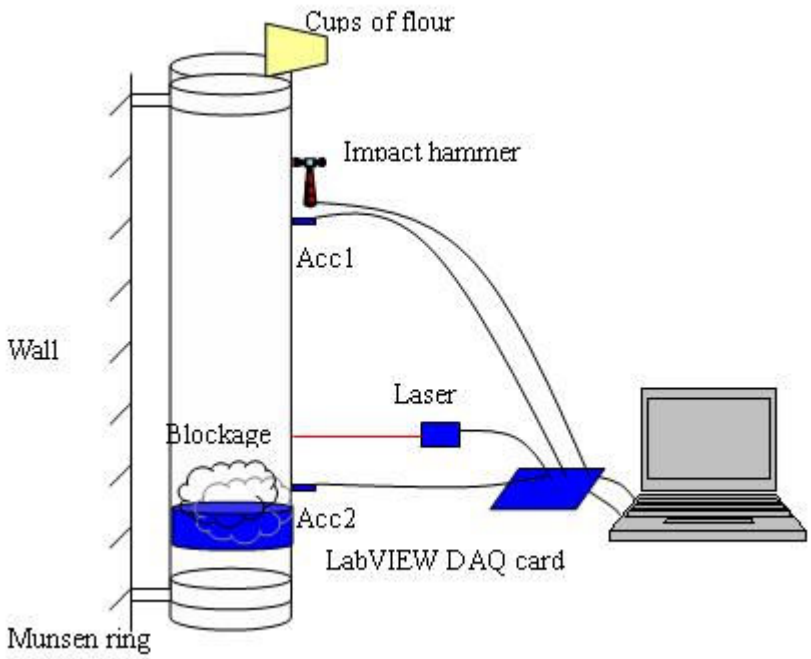

Figure 4-10 The schematic diagram of the flour blockage experimental setup

4.4.4 Onsite experiment

The tested milk powder spray dryer system on the Fonterra Te Rapa site has six cyclones. Cyclone 1 and 4 are joined together by one conveying system. The milk powder blockage generally happens in these two cyclones. Primarily the onsite experiment monitored cyclone 4. The structures of the cyclone and its geometry parts are shown in Figure 4.11. A 15cm-long cloth sock connects the cyclone and the bottom dropper tube, creating two separate vibrating systems. Usually the milk powder build-up starts from the dropper tube and keeps accumulating to block the cyclone. Therefore, the onsite research focused on the part that people can reach from ground to 2.1m high.

Firstly, the resonant frequencies of the bottom dropper tube and top part of the cyclone needed to be searched out. This is important for two reasons. One, this method can not be put into practical use if the clear resonant frequencies of the test system can not be seen. Two, the resonant frequencies are the fundamental data for comparing that with the inside blockage. More data was recorded for comparing any variation of the resonant frequencies and corresponding damping ratio with the inside blockage. Because the production is run 24 hours and the blockage is can not be predicted, the change of vibration modal parameters can not be detected during a short time of monitoring. However, the objective of the onsite experiment can be achieved by comparing every half-hour data.

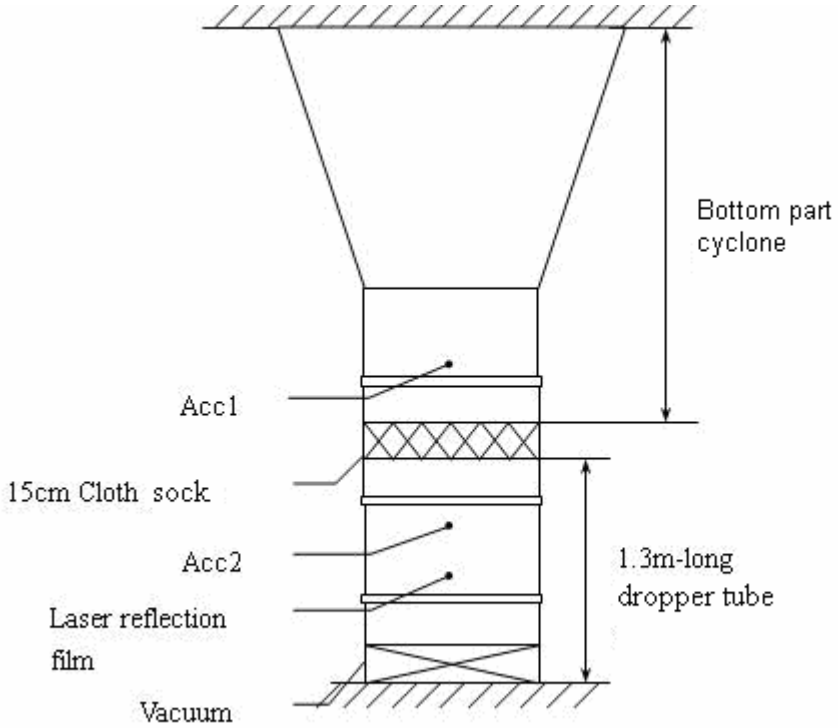

Figure 4-11 The schematic diagram of the cyclone and onsite experimental setup

The onsite experimental set-up is shown in Figure 4.12. Accelerometer one (Acc1) was glued 2.1m away from the floor to measure the vibration of the top part cyclone. Accelerometer two (Acc2) was positioned 1.1m away from the floor. The laser sensor supported by a tripod measured the vibration from 0.7-m position. The Acc2 and laser were used to get the vibration of the bottom dropper tube. LabView DAQ board with laptop computer was used to display and record the data. The impulse excitation was done by rubber hammer (see Figure 4.13) used every hour to hit the cyclone to make the

inside milk build-up fall down. Technicians listened to the tune to diagnose the inside build-up manually and by experience.

Figure 4-12 The photo of onsite experimental setup

Figure 4-13 The rubber hammer

The temperature at the very top of the inside cyclone is 85℃. To maintain the temperature, the parts down from the cone of the cyclone are covered by insulation

material. This helps reduce the chance of the blockage happening if the temperature of the bottom part can be kept the same as on top. The insulation material can be seen in the photos. Some of the insulation was peeled away to position the accelerometers and laser reflection film.

As stated above, there are two parts to the vibrating system. The impact hammer excites the top cyclone and the bottom dropper tube separately to make the system vibrate. The points of impact by the hammer are opposite the sensor position. The top part was hit around 2m from the floor. The dropper tube was hit 1.25m from the floor. Three column data from acc1, acc2 and laser were recorded for every hit. If the rubber hammer hit at the top part, the data of acc1 became available and the other two were useless. On the other hand if the bottom part was hit, then the data from acc2 and laser was available.

4.4.5 Forced vibration testing

Figure 4.14 shows the forced vibration testing setup, which consisted of an electromagnetic shaker driven by a signal generator through a power amplifier. The output signal was colleted by a vibrometer laser sensor and displayed on LabView programme through LabView DAQ data acquisition card. This experimental setup was used to identify the modal shapes of resonant frequencies from impulse excitation.

A frequency that was closer to one of the resonant frequencies for impulse excitation experiment was set by the signal generator and the amplitude was adjusted through the power amplifier to obtain stable and medium vibration. A rod is run through in axial direction from top to bottom. The amplitude of the vibration could be felt and the node at which amplitude is zero can be identified. From this, the node of the resonant frequency in axial direction could be determined.

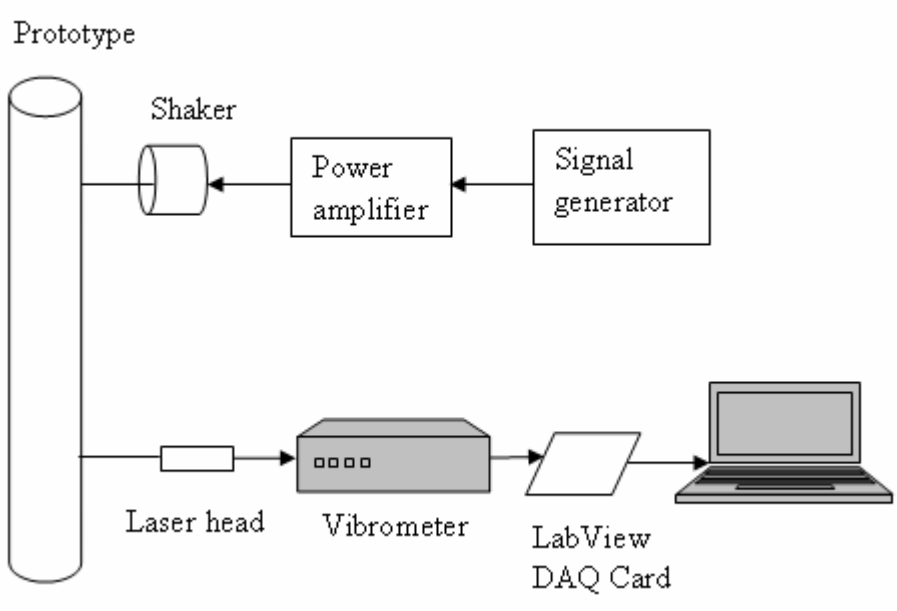

Figure 4-14 A block diagram of the forced vibration experimental setup

4.5 Closure

The principle of transfer function and frequency response function was presented in this chapter. Experimental resonant search methods were introduced and the vibration instruments of this research presented. Simulated mass experimental set up and flour induced experimental set up were determined. The forced vibration testing was set up as a supplement to identify the mode shape. Onsite monitoring experiment setup was also discussed. The following chapter explores the natural frequencies of the prototype from theoretical calculation, numerical solution and experimental results. The boundary condition and mode shapes of the prototype will be identified. The variations of the natural frequencies are discussed to see if they match with the beam-mass theoretical analysis by analyzing the data from simulated mass experiment and flour induced experiment. Damping ratio extraction method will be presented and variation of the modal damping ratio with the added amount of flour at the bottom of support point will be quantified.

Chapter 5 Results and Discussion

5.1 Introduction

This project mainly employs the experimental modal analysis method to investigate the trend of variation of the natural frequencies and the damping ratio of the prototype with blockage inside. To generalize the conclusions and obtain dependable recommendation from this work, theoretical modelling is implemented. Structurally the proposed prototype tube is an element which sits between a shell and a beam. Therefore, in the preliminary analysis of this work, shell theories are used to identify the vibration characterises of the system, However once an added mass is implemented, as a blockage element, the analytical solution become very complicated and beyond the scope of this work. Thus a simplified beam model with added mass is used to investigate the effect of the blockage location on the vibration characteristics: natural frequencies and modal damping. In order to investigate the dynamic characteristics of the cylindrical shell with blockage inside, the natural frequencies of the empty shell must be identified. The shell theory is employed to analyse the vibration modal shape. The beam theory is used to calculate the axial natural frequencies. ABAQUS numerical modelling is employed as an alternative solution to the analytical modelling and lastly the natural frequencies from experiment are compared with analytical results, FEA ABAQUS results and forced vibration experiment to confirm the vibration modal shapes of the empty cylindrical shell. Due to reasonable results from the simulated amount mass experiment and flour blockage experiment, this project was extended to a practical onsite experiment at Fonterra Te Rapa.

5.2 Empty shell natural frequencies

The impulse vibration data was recorded into text file in the LabView program. This was sampled into discrete time signal which could be transferred into frequency domain by the Discrete Fourier Transform (DFT).

The DFT is defined by Equation 5.1 [57] for a deterministic and periodic discrete time signal $x(t_j)$, which satisfies $\sum_{j=0}^{N-1} | x(t_j) | < \infty$, where N is the period of $x(t_j)$.

$$X_k \equiv \sum_{j=0}^{N-1} x(t_j) e^{-i2\pi jk/N} \tag{5.1}$$

where $k = -\frac{N}{2}+1,...,0,...,+\frac{N}{2}$

FFT is an algorithm used to calculate the DFT in an efficient way. The size of the data set (N) is a power of two to obtain maximum calculational efficiency. That is,

$$N = 2^m$$

where m=1,2,3…

It assumes that the data points are evenly spaced if the FFT is chosen to obtain the frequencies contained in the time signal.

Figure 5.1 shows the time domain signal from the impact hammer, top accelerometer, bottom accelerometer and laser. The unit of all amplitude is voltage. One scale of the amplitude of impact hammer stands for the force (N), that of accelerometer is for the acceleration (m/s^2), and that of laser one is for velocity (25mm/s).

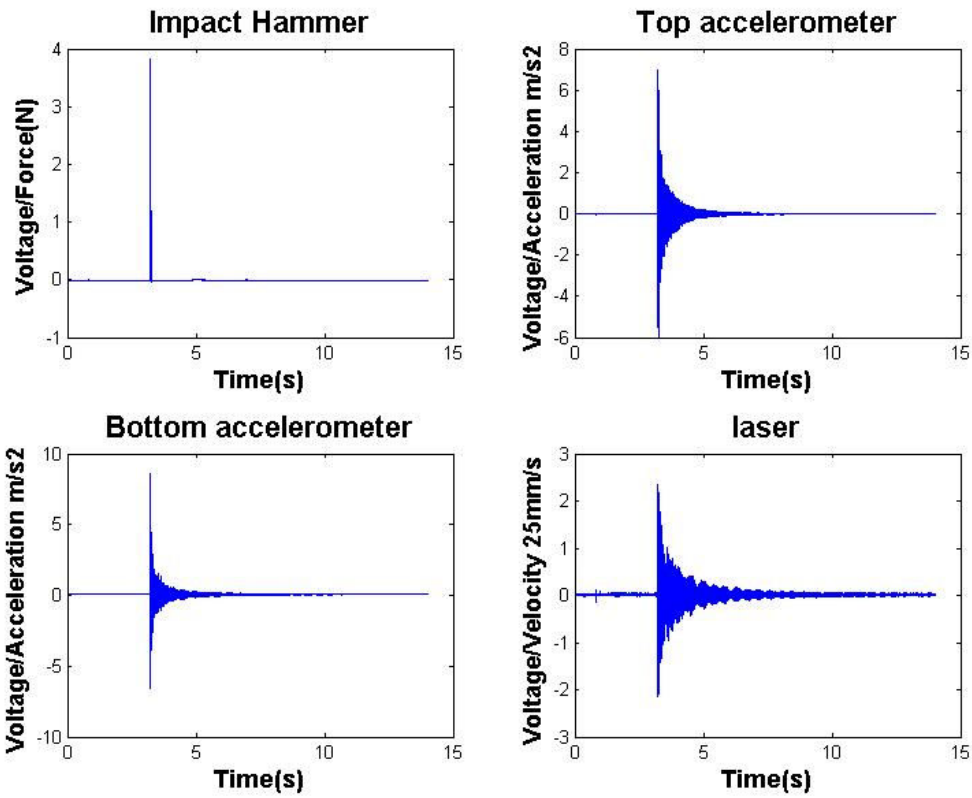

Figure 5-1 All the time domain signals

The input from the impact hammer was impulse. The output, no matter whether it was from accelerometer or laser, reached maximum at the same time when the hammer struck and then died out due to the damping to zero. That is input and output occurred simultaneously.

From a mathematical point, the impulse time signal would be transferred into a flat line in the frequency domain. In the practical experiment, the impulse signal in the frequency domain was nearly flat as shown in Figure 5.2.

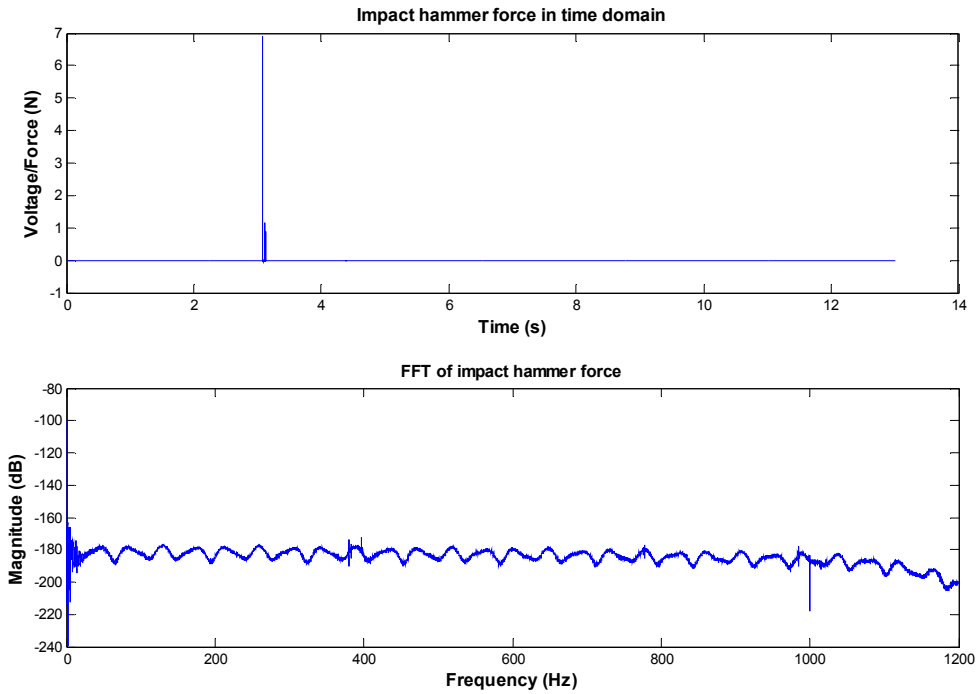

Figure 5-2 Impulse force in time and frequency domain

The FRF was obtained from the FFT of output signal divided by the FFT of the input impulse signal as shown in Figure 5.3. The scale of y-axis is dB which is a logarithmic unit ($dB=20\log_{10}V$), so the subtraction of the FFT of output signal and FFT of the input impulse signal was the FRF. There was little difference between the FRF and the FFT of the output response to impulse excitation. The resonant frequencies of the circular cylindrical shell which were the high peak were clearly seen from the FRF or the FFT of the circular cylindrical shell response to the impulse excitation.

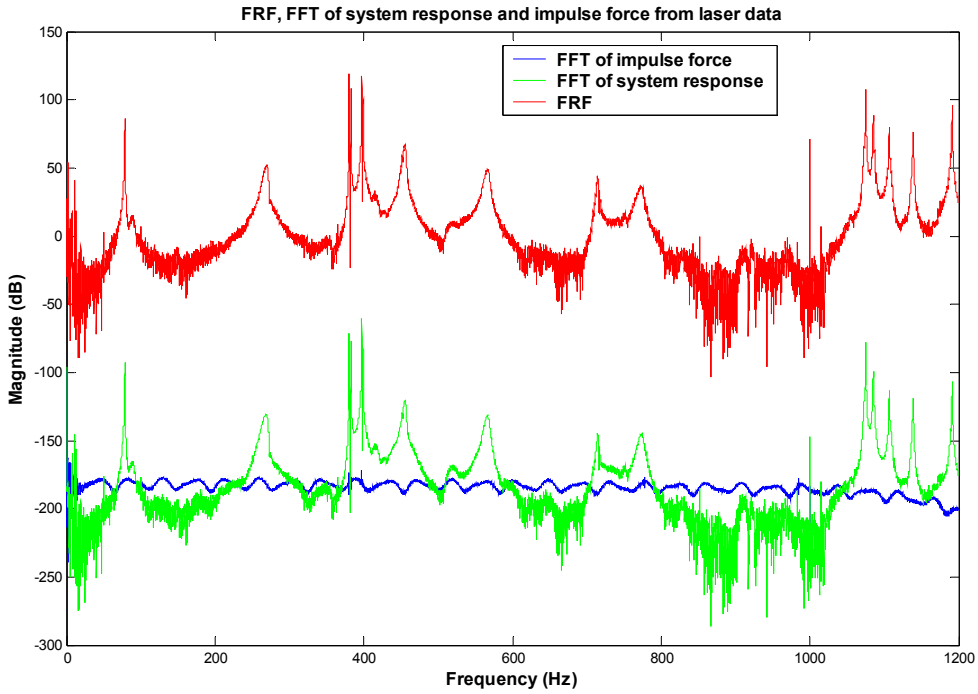

Figure 5-3 The method of obtaining the FRF

The FRFs of the empty circular cylindrical shell obtained from top accelerometer, bottom accelerometer and laser are shown in Figure 5.4. Results were similar whatever the data, from accelerometer or laser or data from the top or the bottom.

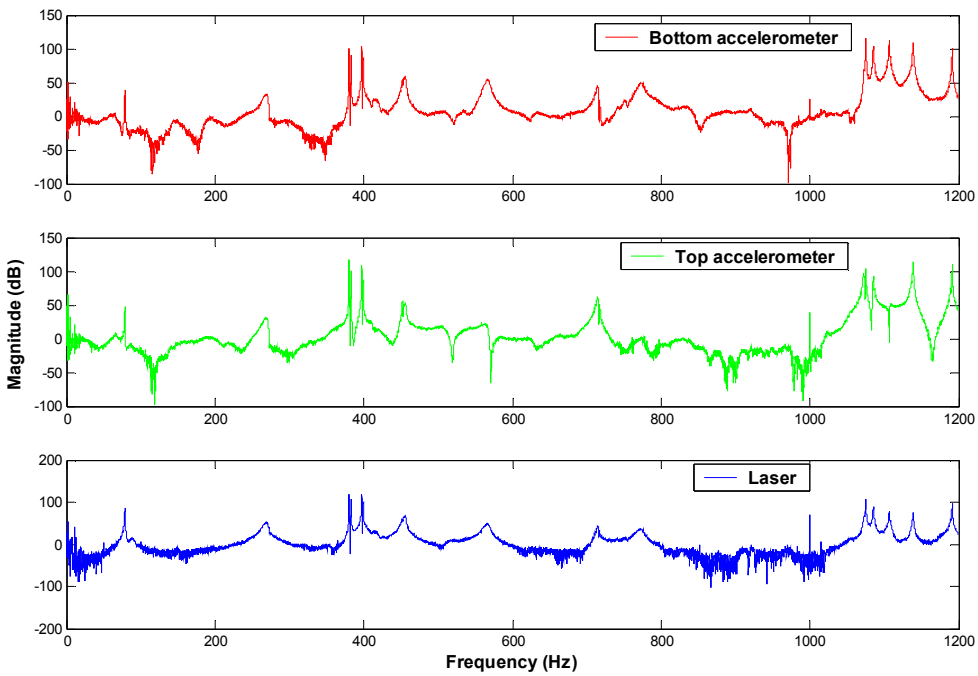

Figure 5-4 FRFs from bottom accelerometer, top accelerometer and laser

From Figure 5.4, every clear high peak showed the resonant frequencies from the impact hammer excitations experiment which was 79 Hz, 270 Hz, 380 Hz, 398 Hz, 456 Hz, 568 Hz, 715 Hz, and 775 Hz. Using the beam theory with both ends simply supported, the first three bending natural frequencies of the experimental shell were 82.19 Hz, 328.77 Hz and 739.74 Hz. If using beam theory with both ends fixed, they would be 186.32 Hz, 513.58 Hz, and 1006.9 Hz separately. In the ABAQUS FEA solution, the first bending modal shape was 81 Hz and the second bending modal shape was 316 Hz with both ends simply supported boundary condition as U1=U2=UR1=UR2=0 and element size 0.005.

Table 5-1 The first several natural frequencies of the prototype under experimental, theoretical and analytical methods

Natural frequencies (Hz)	Experimental resonant frequencies(Hz)	Theoretical frequencies (Hz)		FEA model (U1=U2=UR1=UR2=0) Natural frequencies (Hz)
		Simply supported ends	Fixed ends	
F_1	79	82.19	186.32	81
F_2	270	328.77	513.58	316
F_3	380	739.74	1006.9	381
F_4	398			401
F_5	456			

As shown in table 5.1, the boundary condition of the experimental prototype should be close to both ends simply supported, as the first experimental resonant frequency was validated by the analytical solution of beam with both ends simply supported and matched with FEA solution with boundary condition as U1=U2=UR1=UR2=0.

Combining beam theory, FEA result and forced vibration experiment, the experimental 79 Hz was identified as the first bending modal shape of the experimental cylindrical shell. According to the beam with an added mass theory, 79 Hz will go down with the amount of the added mass except that the added mass is put at the supported point, and will also go down with the location close to the middle point of the beam. Thus the minimum is reached when the added mass is put at the middle of the beam.

Second bending modal from FEA 316 Hz was 12 Hz less than the theoretical calculation that could be improved by increasing the FEA element size. However, no experimental resonant frequency can be matched with this. This means that the second bending modal shape did not come out of this experimental setup.

All other experimental resonant frequencies except 79 Hz combined the bending and circumferential mode shapes, in which the axial mode of 380 Hz and 398 Hz were identified by forced experiment as 1 and 3. This was the same as the ABAQUS analysis in which 380Hz are m=4, n=1 and 401Hz are m=4 and n=3. The results indicated that experimental 79 Hz was the first bending mode of the prototype and the other experimental natural frequencies were combination of the bending mode and circumferential modal.

5.3 Damping ratio extraction

Modal analysis extraction techniques have attracted many researchers seeking to obtain more reliable identification of the modal parameter. As a result, there is increasing literature on modal damping identification. Adhikari [58] presented a systematic study on analysis and identification of viscously and non-viscously damped multi-degree-of-freedom vibrating systems. Lamarque [59, 60] employed wavelet-based logarithmic decrement formula to estimate damping ratio of multi-degree-of freedom systems from time domain responses. Iglesias [61] compared 4 methods: the Rational Fraction Polynomial Method, The Prony or Complex Exponential Method, the Ibrahim Time Domain Method, and Hilbert Envelope Method to evaluate the damping ratio with various parameters and conditions. Karjalainen [62] studied a modal decay parameters estimation method which is based on the nonlinear optimisation of a model for exponential decay plus stationary noise floor, compared with traditional simulated measurement data decay parameter estimation techniques. Collot [63] believed using the Hilbert Transform Method to estimate damping gave good and fast results for the light damping system without improving the frequency resolution. Based on the above literature, it can be concluded that the Hilbert Transform Method is quick and efficiency way to estimate damping. The material of the prototype is stainless steel which is low damping. Therefore using a Hilbert envelope curve to extract and estimate the modal damping ratio is enough for this research to compare its variation. For practical application, extra research on damping ratio extraction from noise environment is required.

5.3.1 Hilbert envelope curve method

The shape of a free oscillation response of a Single Degree of Freedom (SDOF) in time domain is called "envelope". The Hilbert transform can be used to remove the oscillation from the signal to obtain its envelope. For a Multiple Degree of Freedom (MDOF) system, each natural frequency needs to be isolated to produce its envelope, and then the Hilbert envelope curve method can be used to find the damping factor for each resonant frequency.

Equation 5.2 describes the free oscillation response of a SDOF system with time which is an exponential damped sinusoid [51, 64].

$$x(t) = Ae^{-\zeta\omega_n t}\sin(\omega_d t) \qquad (5.2)$$

where A is residue,

ω_n is the natural frequency,

ζ is damping ratio,

ω_d is the damped natural frequency $\omega_d = \sqrt{1-\zeta^2}\,\omega_n$

The Hilbert transformation is equivalent to a filtering in which the amplitudes of the spectral components are left unchanged but their phases are altered by $\pi/2$.

The Hilbert transform [48, 57] to x(t) is

$$X_{Hi}(t) = -\frac{1}{\pi t}x(t) = f(t)x(t) = F^{-1}\{F(j\omega)X(j\omega)\} \qquad (5.3)$$

So, the Hilbert transform of Equation 5.2 is

$$X_{Hi}(t) = Ae^{-\zeta\omega_n t}\cos(\omega_d t) \qquad (5.4)$$

The analytical signal combines both the impulse response of a SDOF and its Hilbert transform as in Equation 5.5.

$$\overline{x(t)} = x(t) - iX_{Hi}(t) \qquad (5.5)$$

The analytical signal is

$$\overline{x(t)} = Ae^{-\zeta\omega_n t}(\sin\omega_d t + \cos\omega_d t) \qquad (5.6)$$

Its magnitude gives the envelope of the signal

$$\left|\overline{x(t)}\right| = \sqrt{(Ae^{-\zeta\omega_n t})^2(\sin^2\omega_d t + \cos^2\omega_d t)} = Ae^{-\zeta\omega_n t} \quad (5.7)$$

Taking natural logarithm of both side of Equation 5.7,

$$\ln\left|\overline{x(t)}\right| = \ln A - \zeta\omega_n t \quad (5.8)$$

Equation 5.8 is a straight line equation, so the damping ratio will be calculated by Equation 5.9

$$\zeta = \frac{-slope}{\omega_n} \quad (5.9)$$

5.3.2 Damping ratio calculation process

The 79 Hz experimental resonant frequency is used as an example to calculate the damping ratio. Data from the laser senor was acquired, as seen in Figure 5.5. Figure 5.6 shows the data filtered by 10 order 1200 Hz low pass anti-aliasing filter and hamming window.

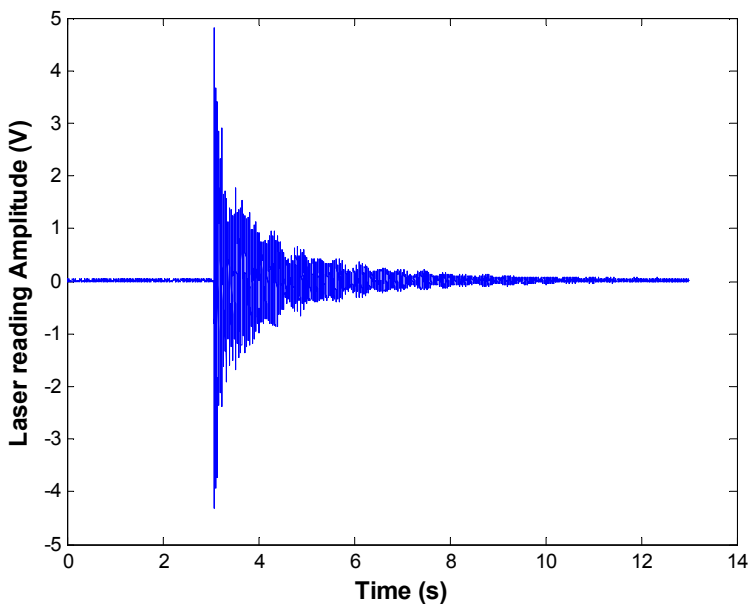

Figure 5-5 Raw data acquired from laser senor.

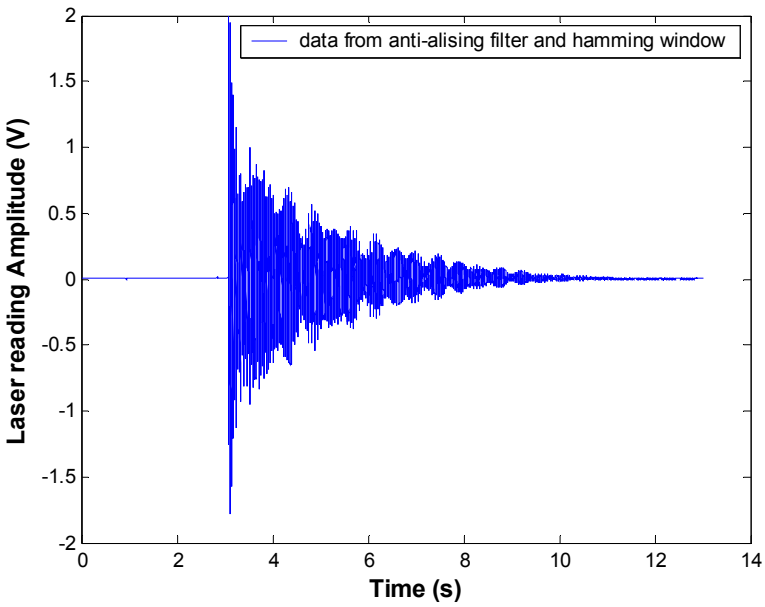

Figure 5-6 Data from anti-aliasing filter and hamming window

Struck by the impact hammer, the time domain response of the test system combined many mode shapes. The modal damping ratio is relative to a certain mode shape. So the response of a single mode can be found by attenuating the time domain data outside of a particular resonant frequency band through the band pass filter. The desired damped frequency was isolated from Figure 5.6 data using a 4 order 70-85 Hz band pass filter. The output from the filter and its top envelop curve are shown in Figure 5.7.

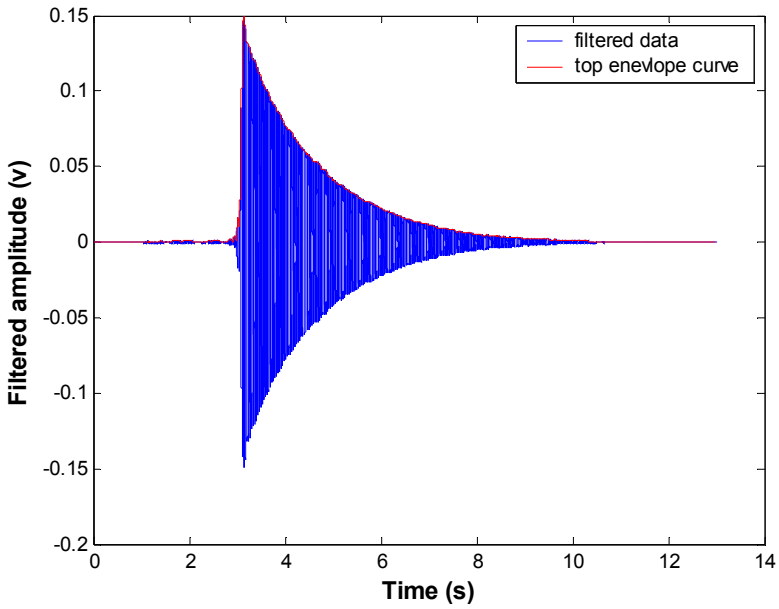

Figure 5-7 Filtered data and top envelope curve using 4 order 70-85 Hz Band Pass.

The right part envelope curve from the maxima was useful and moved to t=0 as shown in Figure 5.8.

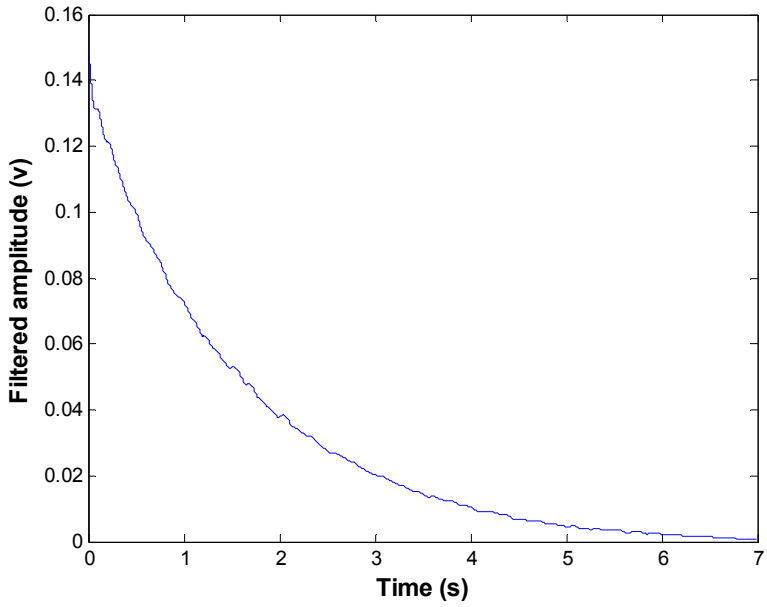

Figure 5-8 Useful top envelope curve

Natural logarithm of data in Figure 5.8 was discrete every 2,000 points. The liner curve fitting method was used to get the linear curve as shown in Figure 5.9.

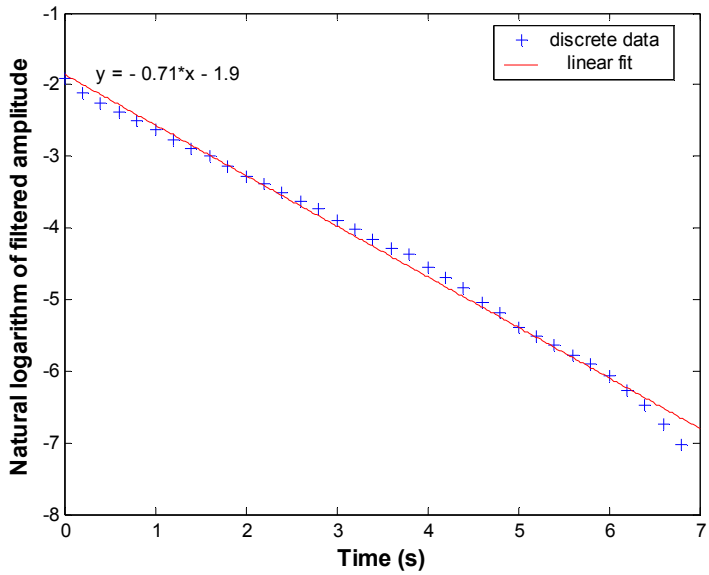

Figure 5-9 Discrete natural logarithm of the 79Hz envelope and its linear fit curve

The slope of the linear curve was $-\zeta\omega_n = -0.71$

So the damping ratio of the 79 Hz for the empty cylindrical shell was

$$\zeta = {0.71}/{2\pi \times 79} = 0.0143$$

5.3.3 Isolate other 7 experimental resonant frequencies and its top envelope curve

Table 5.2 summarises the lower and upper bounds of the band pass filters used in this research for all eight experimental resonant frequencies.

Table 5-2 Lower and upper bound of the band pass filter

RESONANT FREQUENCIES (HZ)	ORDER	LOWER BOUND (HZ)	UPPER BOUND (HZ)
79	4	70	85
270	4	250	300
380	5	372	388
398	5	392	410
456	4	440	475
568	4	550	580
715	4	700	730
775	4	750	800

Figures 5.10-5.16 show the isolated time domain response at the remaining seven experimental resonant frequencies and its top envelop curve.

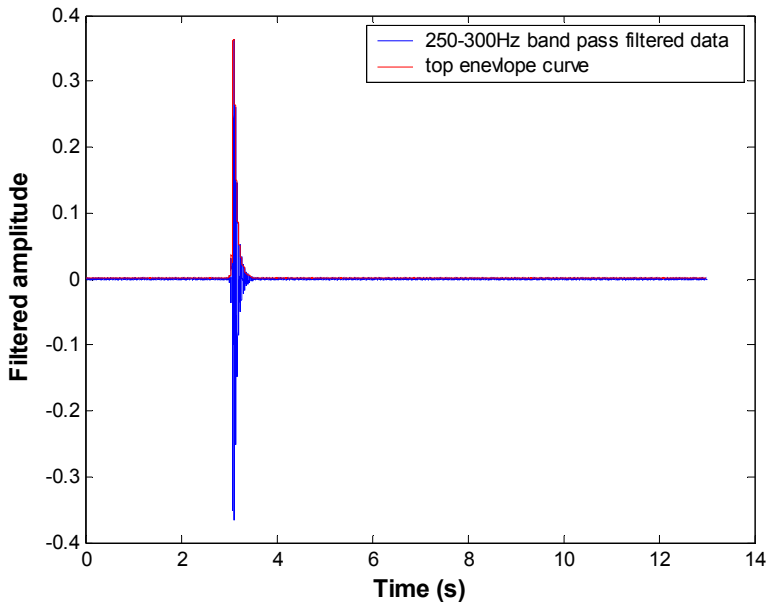

Figure 5-10 Time domain response of 270Hz mode shape and its top envelope curve

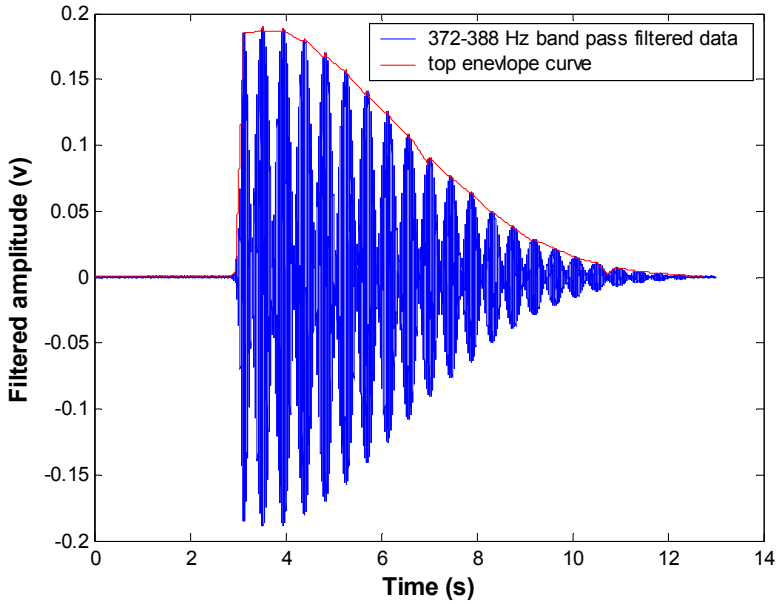

Figure 5-11 Time domain response of 380Hz mode shape and its top envelope curve

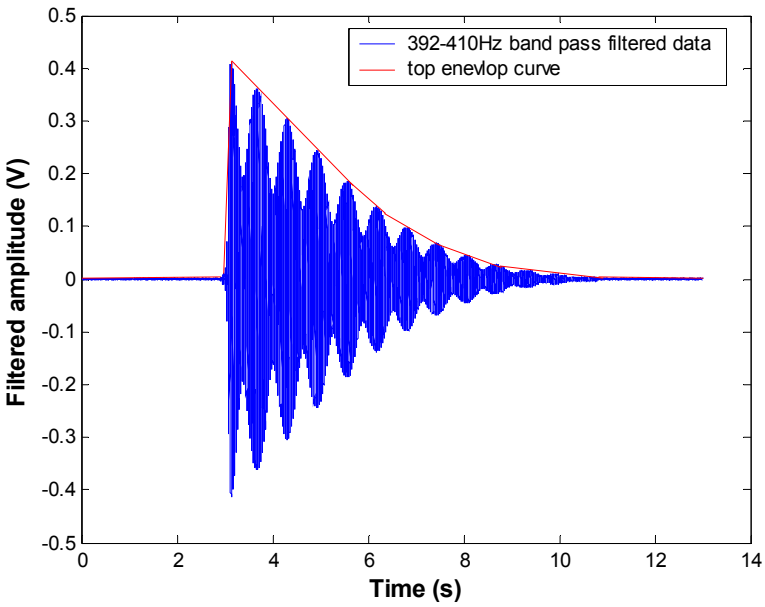

Figure 5-12 Time domain response of 398Hz mode shape and its top envelope curve

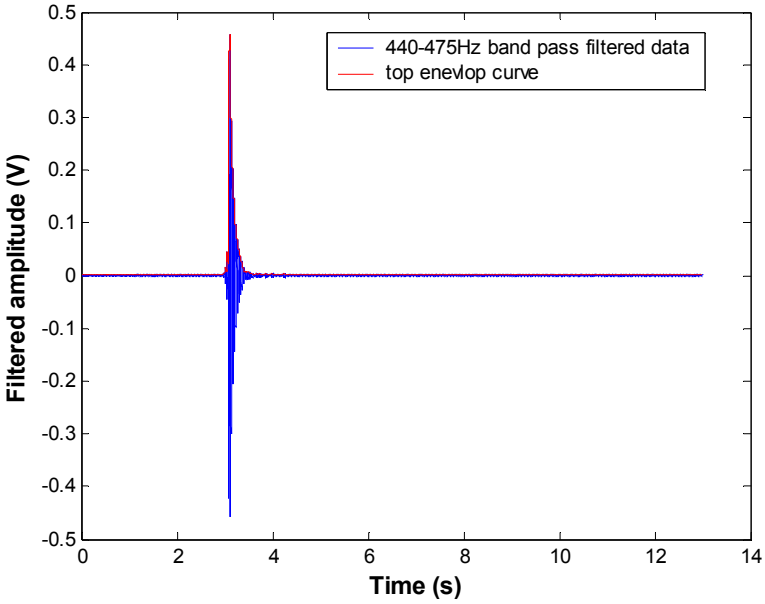

Figure 5-13 Time domain response of 456Hz mode shape and its top envelope curve

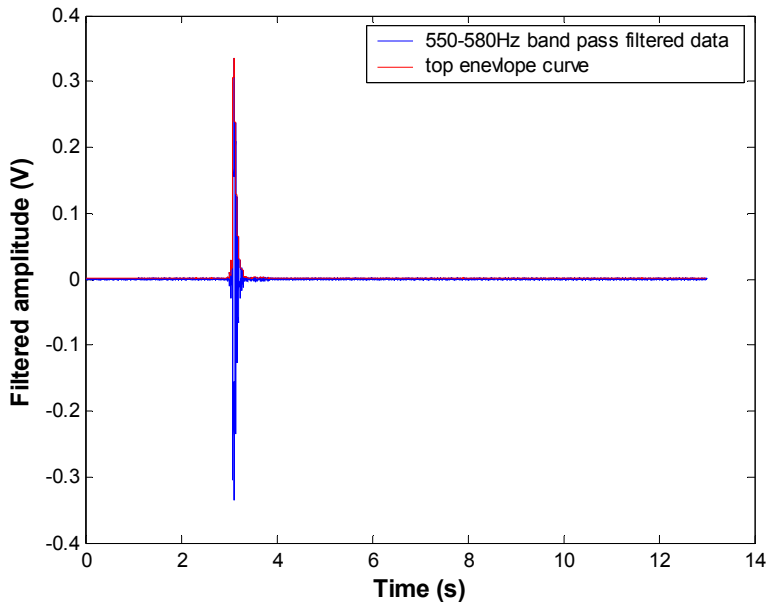

Figure 5-14 Time domain response of 568Hz mode shape and its top envelope curve

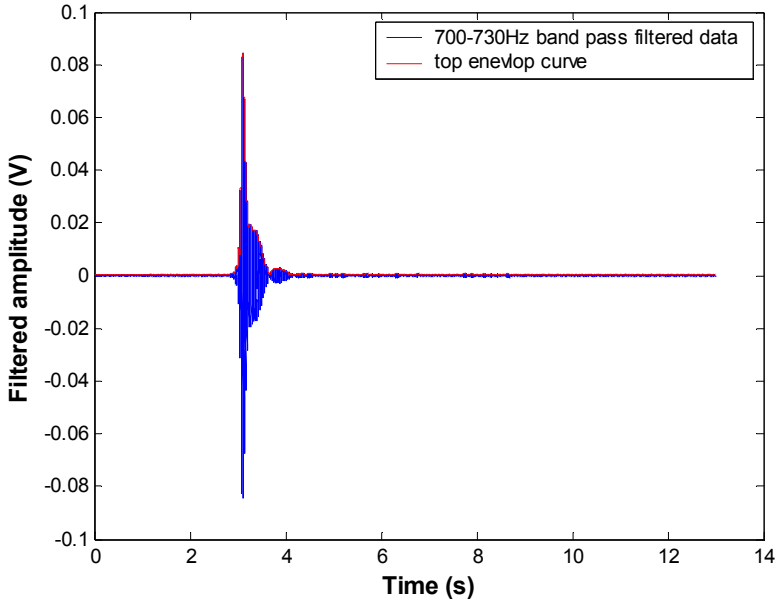

Figure 5-15 Time domain response of 715Hz mode shape and its top envelope curve

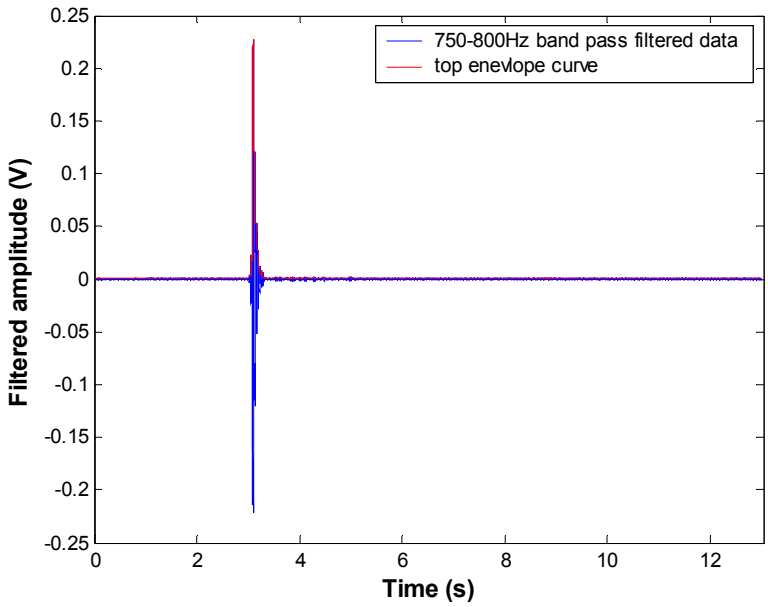

Figure 5-16 Time domain response of 775Hz mode shape and its top envelope curve

The slope of the natural logarithm of the isolated data from the three sensors and their average value were calculated and listed in Table 5.3. The damping ratio for each mode shape was calculated according to Equation 5.9 also shown in Table 5.3.

Table 5-3 Experimental first 8 mode shape natural logarithm slope and damping ratio

Natural frequency (Hz)	**Slope of the fitting natural logarithm data**				**Damping ratio ζ**
	Acc1	**Acc2**	**Laser**	**Average**	
79	0.70	0.72	0.71	0.71	0.001431
270	15.00	16.00	16.00	15.67	0.00924
380	0.40	0.43	0.40	0.41	0.000172
398	0.55	0.53	0.55	0.54	0.000217
456	11.00	9.20	11.00	10.40	0.003632
568	21.00	20.00	21.00	20.67	0.005794
715	4.10	3.90	4.00	4.00	0.000891
775	23.00	25.00	22.00	23.33	0.004794

5.4 Natural frequencies of shell with simulated amount mass inside

Tables 5.4-5.6 list the first main six resonant frequencies with 0.64kg, 1.6kg and 2.5kg mass inserted at 11 locations inside of the experimental cylindrical shell. "–" means that resonant frequency was not seen in the FRF curve because the FRF shapes depend on the impact hammer hit location and sensor location. The entire FRFs curve from the bottom accelerometer and laser senor and its resonant frequencies were recorded in appendix Ⅱ. The FRFs from the top accelerometer were not listed, as its shape was different from the other two due to being very close to the hit point. The data from the bottom accelerometer and laser sensor were enough for experimental validation. In addition to the main first six resonant frequencies that appeared in the empty cylindrical shell, one new one appeared which was shown in grey background in Tables 5.4-5.6 between the 79 Hz and 270 Hz. This was due to the introduction of a mass into the cylindrical shell.

Table 5-4 The first 6 resonant frequencies with 0.64kg mass inserted at 11 locations inside of the experimental cylindrical shell

Mass location	Resonant frequencies (Hz)						
0	77.475	-	269.55	382.5	397.5	453.4	565.35
0.1	73.895	90	270.7	382	397.5	454.45	564
0.2	70.53	95.37	271.15	382	397.5	453	565.9
0.3	69.08	97.05	270.7	382	397.5	454.15	566
0.4	66.83	104.21	271.2	381.9	397.55	454.65	566.05
0.5	66.91	101.4	270.1	383	397.45	453.5	566.75
0.6	66.68	102.1	271.85	380.7	397.45	454.85	566.3
0.7	67.21	98	270	380.65	397.5	454.9	566.5
0.8	68.66	92.7	269.7	382.55	396.85	455.85	565.5
0.9	71.41	88.04	270.45	382.5	397.25	455.5	565.5
1	77.13	-	270.3	382.4	397	454.9	566

"–" means that resonant frequency didn't be seen in the FRF curve due to the location of the hit point of the impact hammer and sensors
Grey colour column shows the new resonant frequency due to the added mass
Mass location 0 means the added mass located at the point of the bottom munsen ring.
Mass location 1 means the added mass located at the point of the top munsen ring.

Table 5-5 The first 6 resonant frequencies with 1.6kg mass inserted at 11 locations inside of the experimental cylindrical shell

Mass location	Resonant frequencies (Hz)						
0	75.97	86.94	275.65	382.55	397.5	454.5	567.5
0.1	74.27	-	279.7	382.7	399.55	459	570.8
0.2	69.88	-	280.25	383.9	404	463.35	569.95
0.3	66.03	-	280.55	385.45	408.25	458.05	567.65
0.4	62.87	-	276.55	387.6	404.95	456.1	571
0.5	61.8	-	273.35	390.95	398.3	462.1	569
0.6	61.95	-	273.7	388.4	400.5	460.6	570.55
0.7	63.82	-	277.85	386.6	406.85	455.3	569.5
0.8	67.79	-	282.65	384.75	407.6	462.25	567.5
0.9	71.22	84.5	280.9	383.5	402.55	463.5	569.5
1	75.71	86.14	276.7	382.5	398	457.4	569.8

Table 5-6 The first 6 resonant frequencies with 2.5kg mass inserted at 11 locations inside of the experimental cylindrical shell

Mass location	Resonant frequencies (Hz)						
0	-	83.045	275.5	382.5	397.6	456	568.45
0.1	71.6	-	280.25	383.2	401.35	461.35	572.35
0.2	68.09	117	283.15	384	404.9	466.1	573.8
0.3	59.395	147.5	279.3	388.3	412.7	456.35	575.05
0.4	56.88	-	274.35	392.85	403.25	464.4	573
0.5	56.34	160	271.6	399.9	-	467.5	569.2
0.6	58.17	150	279.5	389.9	410/419.85	457.15	576.3
0.7	61.455	-	283.2	386.4	414.55	462.25	567.9
0.8	66.31	-	282.95	384.5	407.05	468.7	574.8
0.9	72.25	83.535	279.35	383.05	397.9	461.25	573.45
1	-	81.865	274.55	382.5	397.7	456	568.65

Figures 5.17-5.20 show the variation of the first fourth resonant frequencies (79 Hz, 270 Hz, 380 Hz and 398 Hz) with 0.64kg, 1.6kg and 2.5kg at 11 different locations. The variation of the first resonant frequency matched well with the beam-mass theory. It was symmetrical with the midpoint of the length of the cylindrical shell, meaning that this resonant frequency was the first bending mode. It went down to the minimum until the added mass was inserted in the midpoint. It also went down with the amount of the mass as shown in Figure 5.17 as the midpoint about 10 Hz variation from 66.91 Hz with 0.64kg inserted to 56.34 Hz with 2.5 kg. 83 Hz and 80 Hz appeared when a 2.5kg mass

was inserted at the top and the bottom support point, which was higher than that in the empty shell. This can explain the new resonant frequency that appeared between the first and second resonant frequencies.

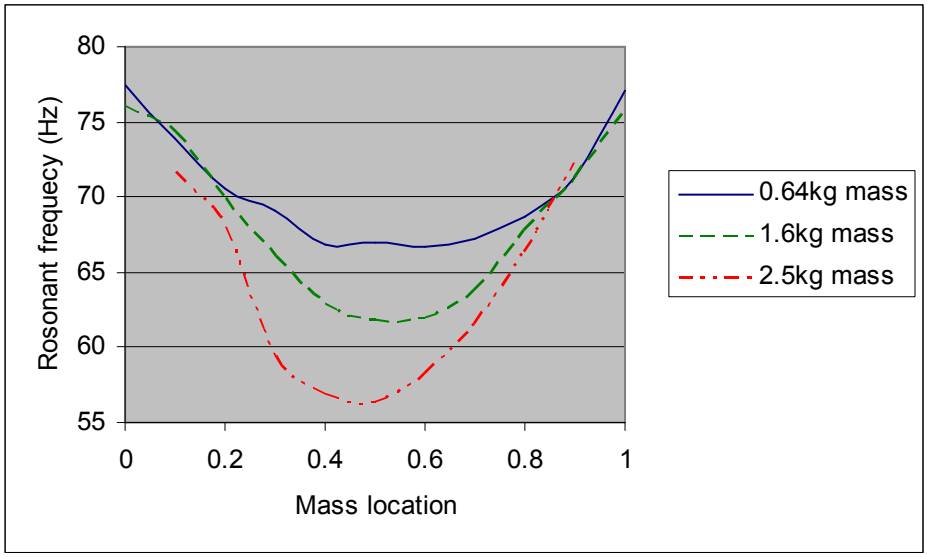

Figure 5-17 The variation of the first resonant frequency (79Hz) with 0.64kg, 1.6kg and 2.5kg mass at 11 locations

The 270 Hz, 380 Hz and 398 Hz resonant frequencies went up when a mass was introduced, which did not match with the beam-mass theory. This means these vibration modes were not pure bending modes and should be circumferential or combination of bending and circumferential modes. It can be seen that these three resonant frequencies went up with the amount of the added mass. The second and third ones had the same variation trend which reached the maximum when the added mass was at 1/4 and 3/4 of the whole length. The fourth resonant frequency had the opposite trend to the first one, which reached its maximum at the midpoint.

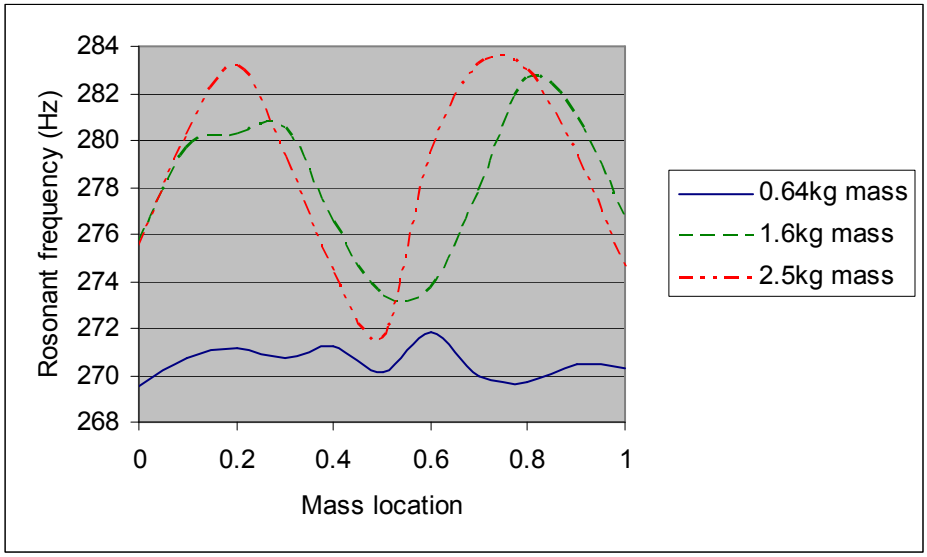

Figure 5-18 The variation of the second resonant frequency (270Hz) with 0.64kg, 1.6kg and 2.5kg mass at 11 locations

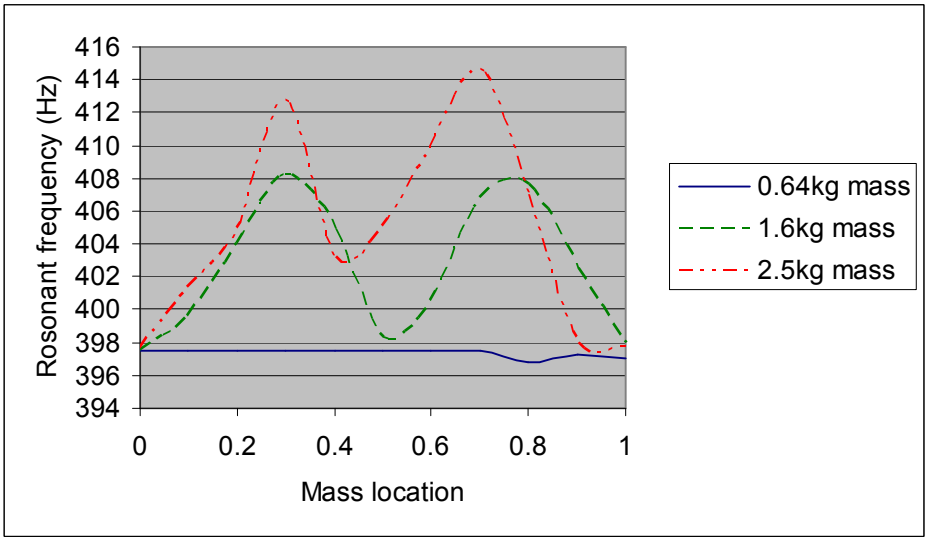

Figure 5-19 The variation of the third resonant frequency (380Hz) with 0.64kg, 1.6kg and 2.5kg mass at 11 locations

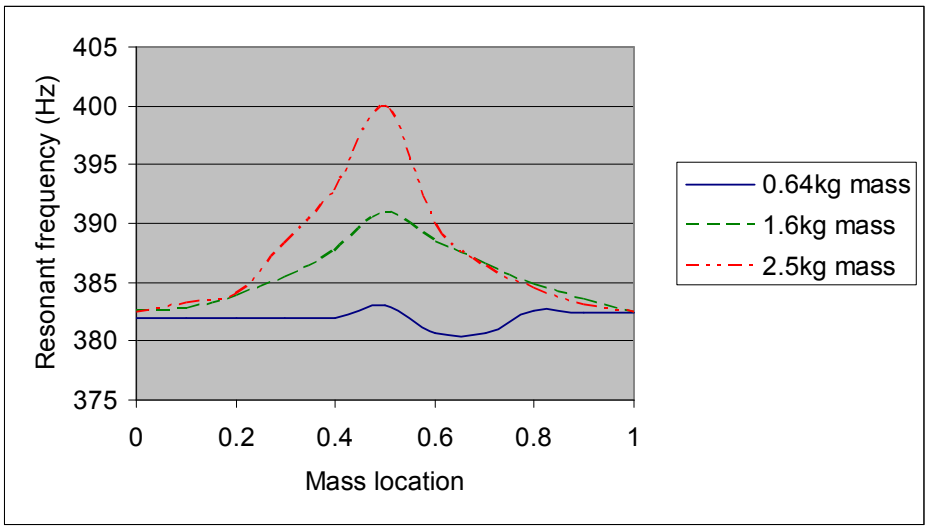

Figure 5-20 The variation of the fourth resonant frequency (398Hz) with 0.64kg, 1.6kg and 2.5kg mass at 11 locations

The remaining resonant frequencies also showed the variation with the amount and location of the added mass, which are not discussed here due to restrictions in thesis length. The first fourth ones provided enough clear information about the variation to the amount and location of the added mass.

5.5 Natural frequencies and its damping ratio of the shell with inside flour blockage

The natural frequencies of the prototype with different amounts of flour blockage starting from both bottom support point and 1/10 of 1.87m away from bottom support point were presented. Additionally the variation of modal damping ratios were discussed when flour blockage started from bottom support point.

5.5.1 Flour blockage at bottom support point

Figure 5.21 shows the FRFs with a plastic board inserted at the bottom support point. The FRFs were very similar to the empty one, which meant that the 20 g plastic board was too light to make any change to the FRFs. Figures 5.22-5.25 show the FRFs with 2, 4, 6, and 8 cups of flour added on to the plastic board. The weight of each cup of flour is 0.25kg. For each FRFs Figure, the first one showed the FRF from bottom accelerometer; middle one showed the FRF from top accelerometer and the last one from laser sensor.

From these figures, it can be seen that the resonant frequencies did not change with the added mass. This is because the support point is one of the vibration nodes. If the added mass was put at the vibration node, its resonant frequency to that node would not change. The two end support points were the nodes of all the 8 experimental resonant frequencies. So the resonant frequencies did not change with the amount of the added mass.

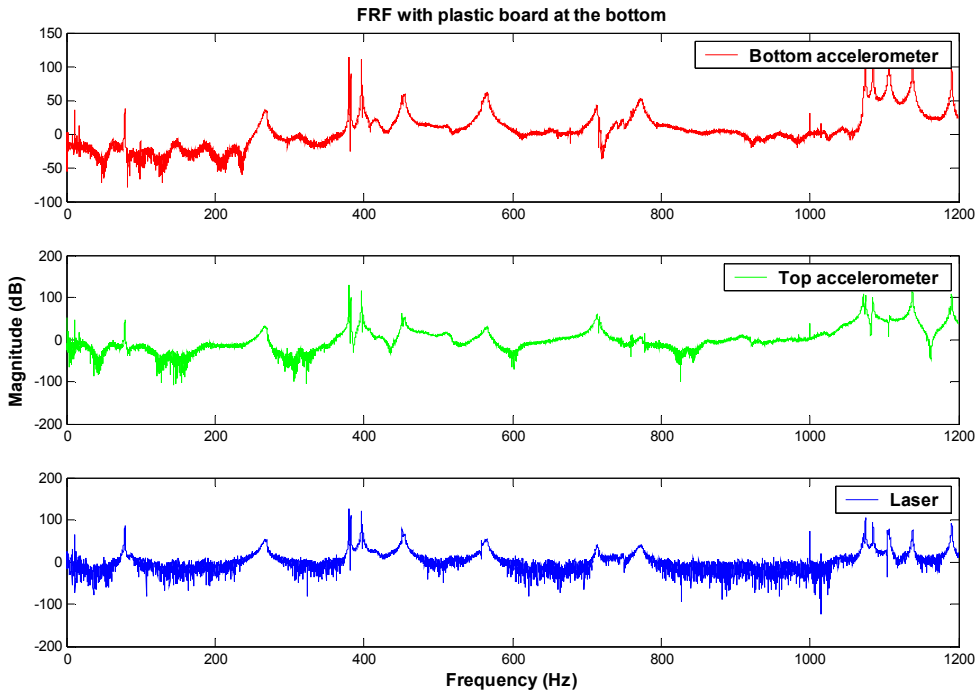

Figure 5-21 FRFs with a plastic board inserted at the bottom support point

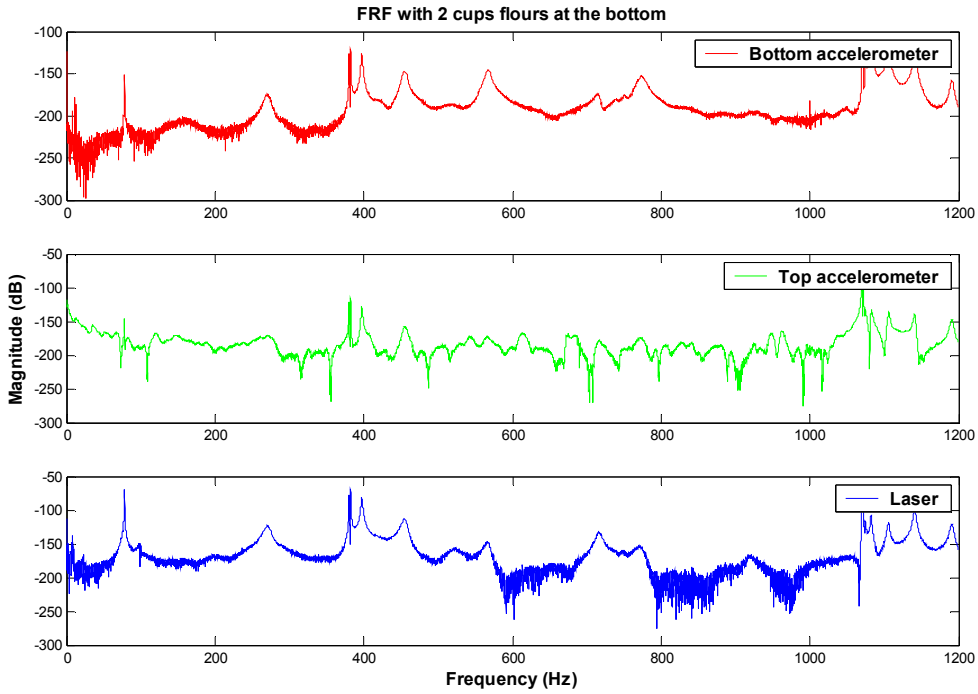

Figure 5-22 FRFs with 2 cups of flour added on the plastic board at the bottom

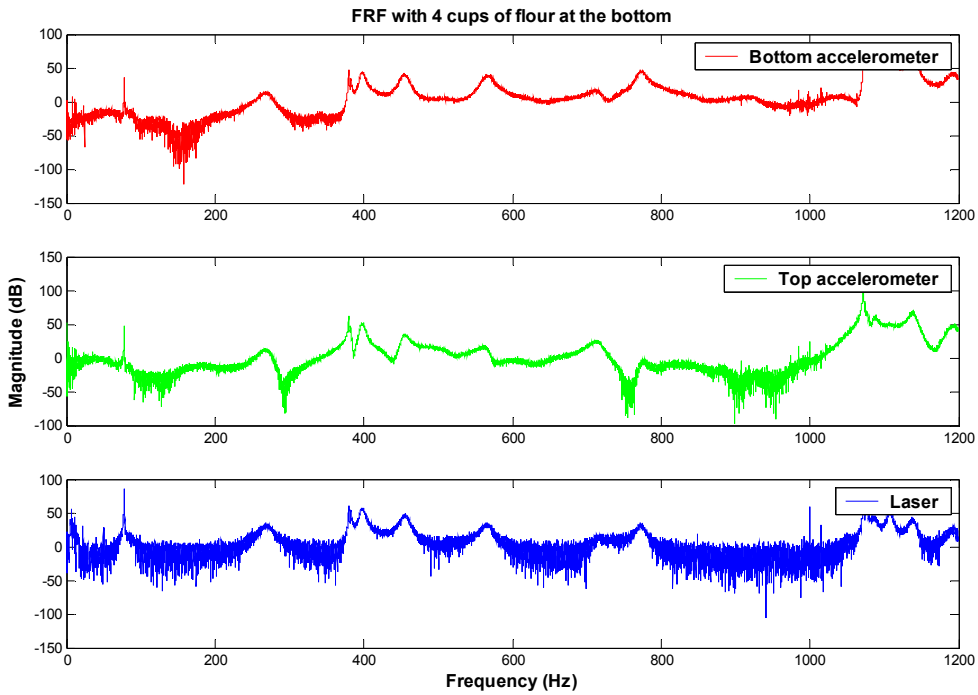

Figure 5-23 FRFs with 4 cups of flour added on the plastic board at the bottom

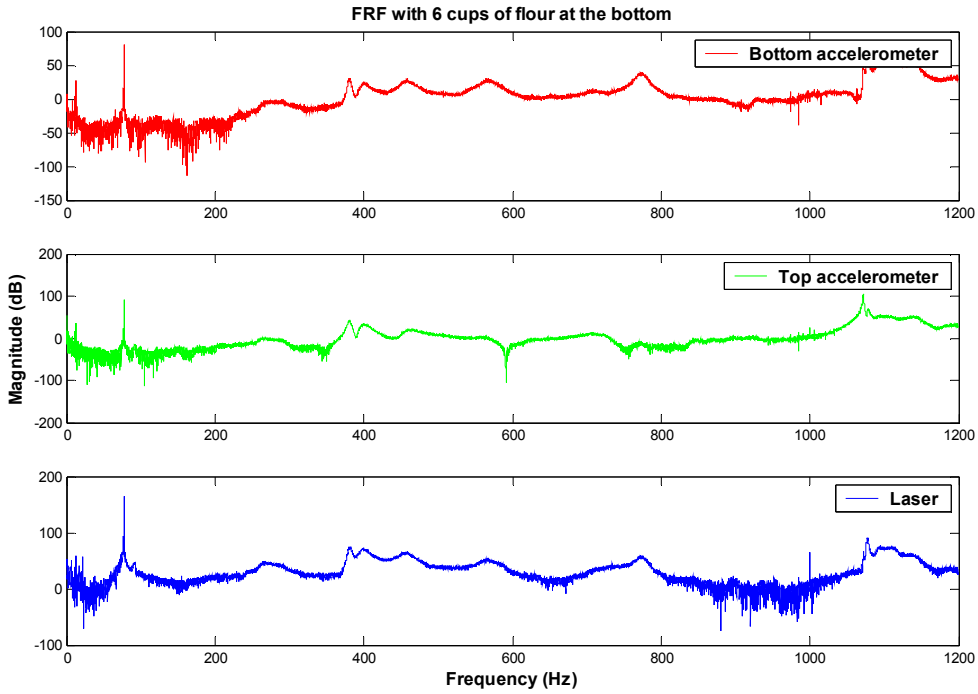

Figure 5-24 FRFs with 6 cups of flour added on the plastic board at the bottom

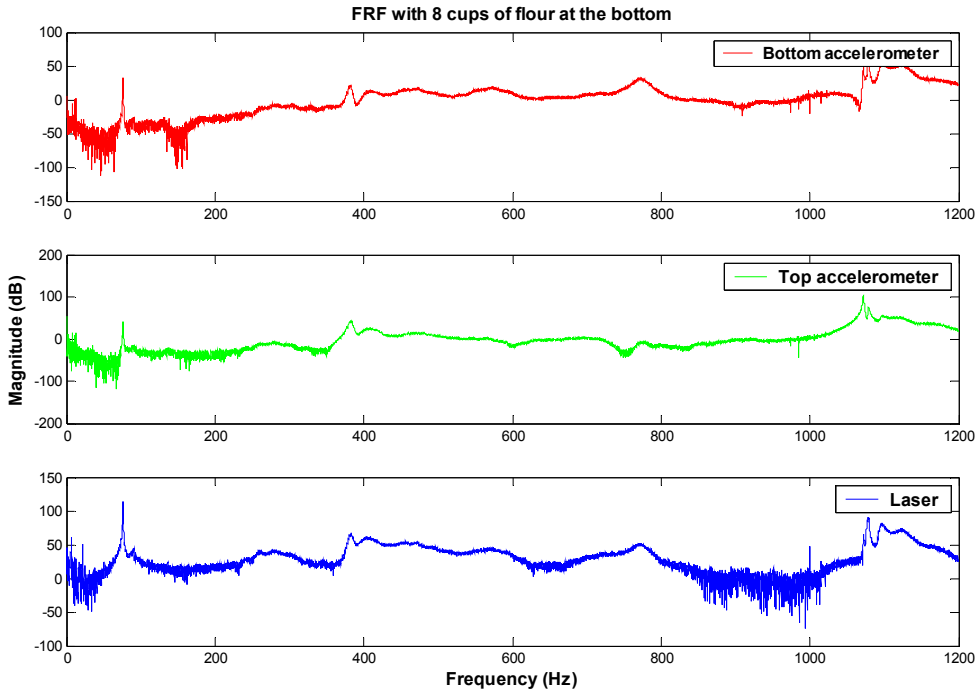

Figure 5-25 FRFs with 8 cups of flour added on the plastic board at the bottom

Although there was no change for the resonant frequencies when the added mass was inserted at the bottom point of the cylindrical shell, the damping ratio for each mode except the first one increased, which can be seen from the shape of the FRF using half-

power bandwidth method to qualitatively estimate damping ratio. The half-power bandwidth method shows that high damping ratio system has wide bandwidth and low peak in its FRF. Alternatively, the low damping system has narrow bandwidth and sharp peak in its FRF.

The modal damping ratios were extracted by Hilbert envelope method as shown in section 5.3.2. The slope of the natural logarithm and modal damping ratio are shown in AppendixIII.

Table 5.7 and Figure 5.26 reveal the modal damping ratio increased with the amount of the blockage. 0.1 was assumed as the plastic board mass effect. All the modal damping ratios except for the first mode increased with the amount of the blockage and the damping ratio at 270 Hz showed the most increase. The sensitivity of the variation of the damping ratio was reasonable. Two cups flour blockage made damping ratio at 270 Hz change from 0.009 to 0.017, which meant that the mass effect of two cups of flour doubled the empty shells modal damping ratio.

Table 5-7 Modal damping ratio with the added amount of flour at the bottom

Amount of flour (cups)	**Modal damping ratio ζ**							
	79Hz	**270Hz**	**380Hz**	**398Hz**	**456Hz**	**568Hz**	**715Hz**	**775Hz**
0	0.001431	0.00924	0.000172	0.000217	0.003632	0.005794	0.000891	0.004794
0.1	0.001532	0.008846	0.00026	0.000239	0.003445	0.005327	0.000906	0.004863
2	0.001424	0.017693	0.000894	0.004934	0.008381	0.008223	0.002969	0.004931
4	0.001243	0.031651	0.0019	0.009469	0.013735	0.011214	0.004157	0.005411
6	0.001438	0.041873	0.007124	0.010936	0.015132	0.012709	0.005345	0.006369
8	0.001666	0.043249	0.007682	0.01387	0.017693	0.014484	0.005939	0.008287

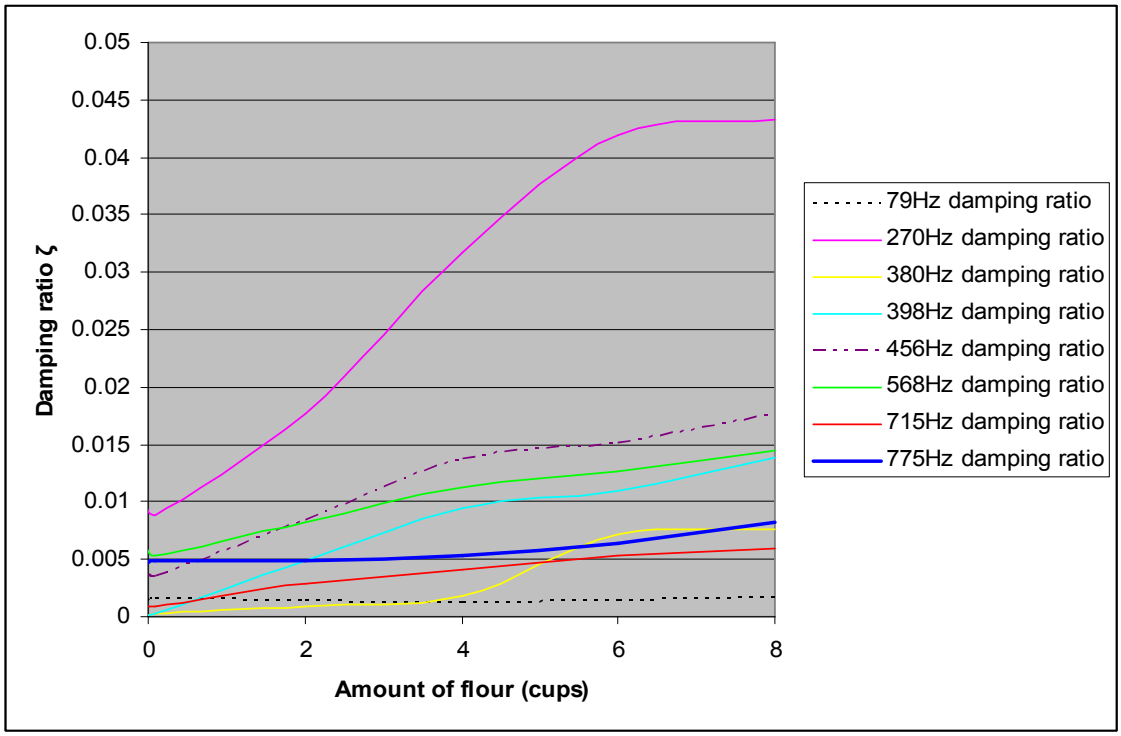

Figure 5-26 Modal damping ratio with the added amount of flour at the bottom

5.5.2 Flour blockage at 1/10 from the bottom support point

Figure 5.27 shows the FRFs with a plastic board inserted at 1/10 of the whole length (1.87m) from the bottom support point. Figures 5.28-5.31 show the FRFs with 2, 4, 6, and 8 cups of flour added on that plastic board. Each Figure displays the FRF from the bottom accelerometer, top accelerometer and laser sensor from top to the bottom.

Tables 5.8-5.11 summarise the first 8 resonant frequencies with 2, 4, 6 and 8 cups of flour added on the plastic board at 1/10 away the bottom support separately. Table 5.12 summarises the first 8 resonant frequencies with different amounts of blockage. It can be seen that the modal frequencies shift with the amount of the blockage. The first mode (79 Hz) went down and was about 1 Hz down with every 2 cups of flour added. This matches the beam-mass theory and previous simulated mass experiment proves again that 79 Hz resonant frequency was the first bending mode. The third (380 Hz) and fourth mode (398 Hz) increased with the amount of flour. The fourth mode increased rapidly with the amount the blockage to 418Hz when 4 cups of flour were added. The second mode damping ratio (270 Hz) increased with two cups of flour and its frequency rose to 280 Hz when four cups of flour were added, which was same as the previous simulated mass experiment. Afterwards it decreased to 225 Hz when another four cups

of flour were added. This may be explained by the 270 Hz mode not being detected by the sensor and hence, the new resonant frequency came out due to a larger blockage.

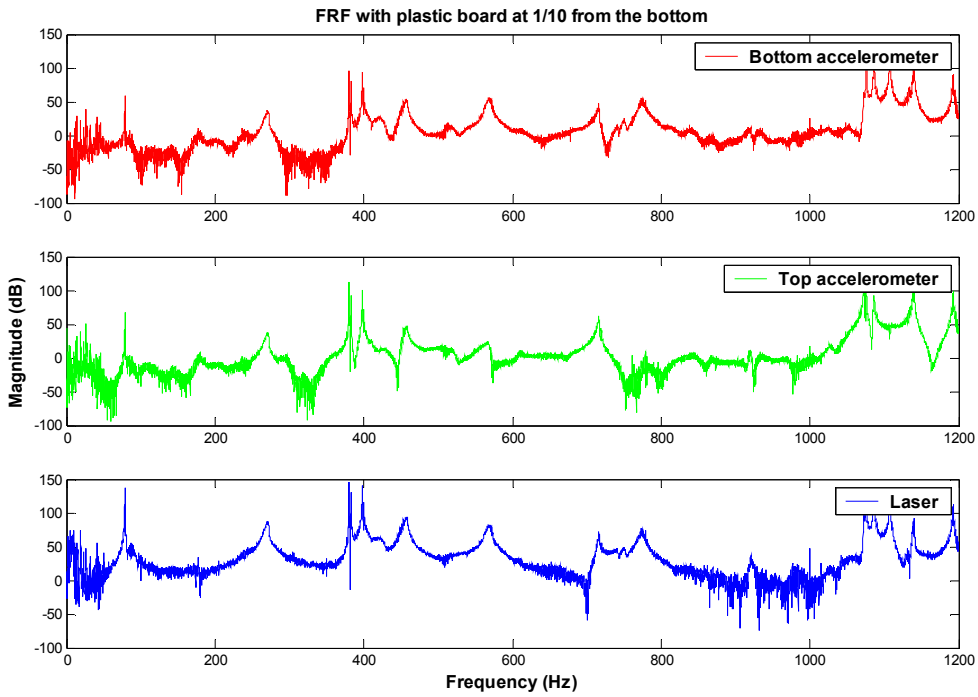

Figure 5-27 FRFs with a plastic board inserted at 1/10 from the bottom support point

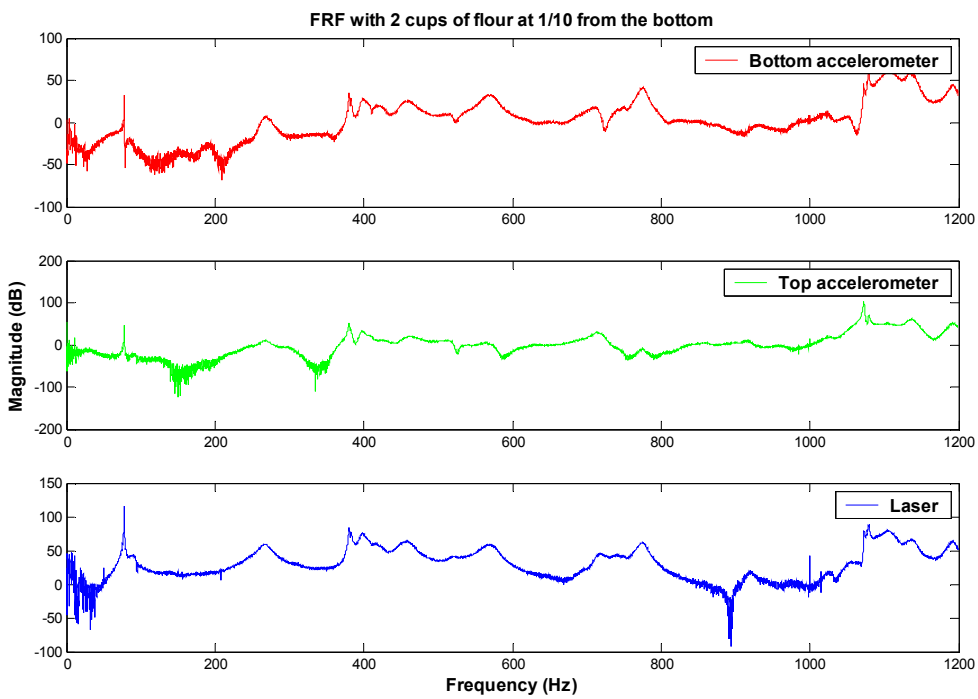

Figure 5-28 FRFs with 2 cups of flour added on the plastic board at the bottom

Table 5-8 The first 8 resonant frequencies with 2 cups of flour at 1/10

Natural frequencies of empty shell (Hz)	Natural frequencies of the shell with 2 cups of flour at 1/10 (Hz)			
	Acc1	Acc2	Laser	Average
79	77.9	77.9	77.9	77.9
270	268	268	268	268
380	383	383	383	383
398	398	398	398	398
456	460	460	456	458.67
568	566	566	566	566
715	718	715	720	718
775	775	775	780	777

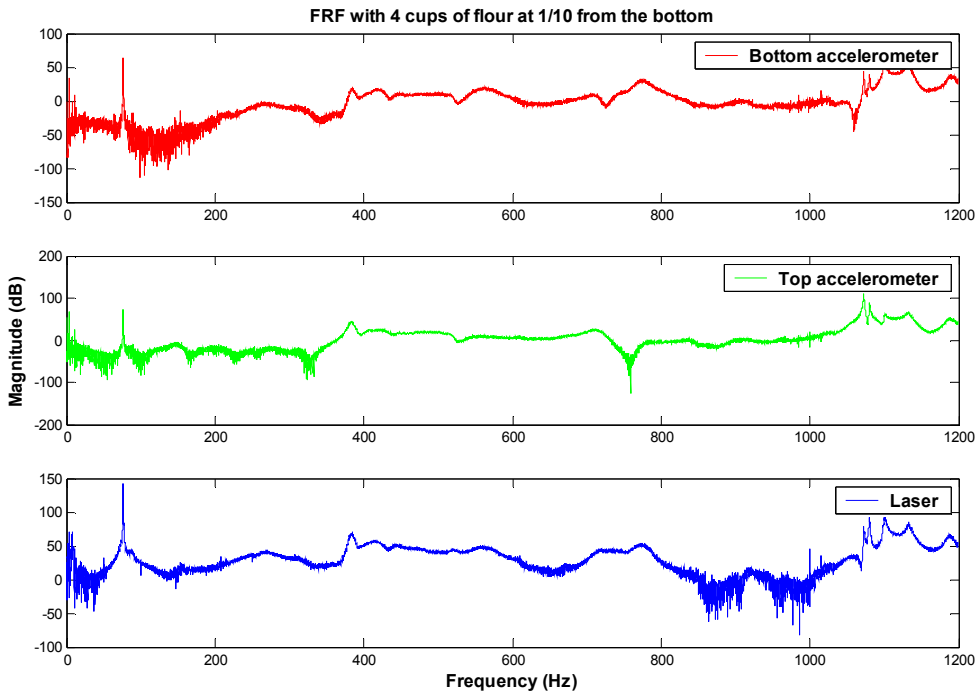

Figure 5-29 FRFs with 4 cups of flour added on the plastic board at the bottom

Table 5-9 The first 8 resonant frequencies with 4 cups of flour at 1/10

Natural frequencies of empty shell (Hz)	Natural frequencies of the shell with 4 cups of flour at 1/10 (Hz)			
	Acc1	Acc2	Laser	Average
79	76.83	76.83	76.83	76.83
270	280	280	280	280
380	385	385	385	385
398	418	418	418	418
456	460/518	460/520	460/520	460/519
568	-	560	560	560
715	703	700	710	704
775	-	770	770	770

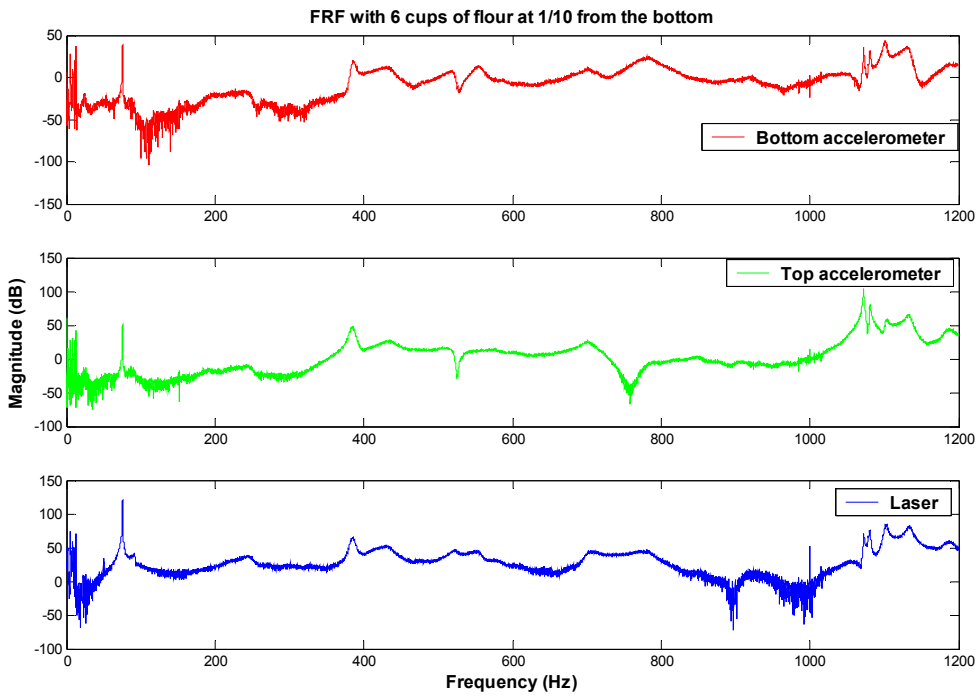

Figure 5-30 FRFs with 6 cups of flour added on the plastic board at the bottom

Table 5-10 The first 8 resonant frequencies with 6 cups of flour at 1/10

Natural frequencies of empty shell(Hz)	Natural frequencies of the shell with 6 cups of flour at 1/10 (Hz)			
	Acc1	Acc2	Laser	Average
79	75.61	75.61	75.61	75.61
270	243	243	243	243.00
380	385	385	385	385.00
398	434	434	430	432.67
456	518	518	522	519.33
568	556	556	550	554.00
715	703	703	710	705.33
775	-	780	775	777.50

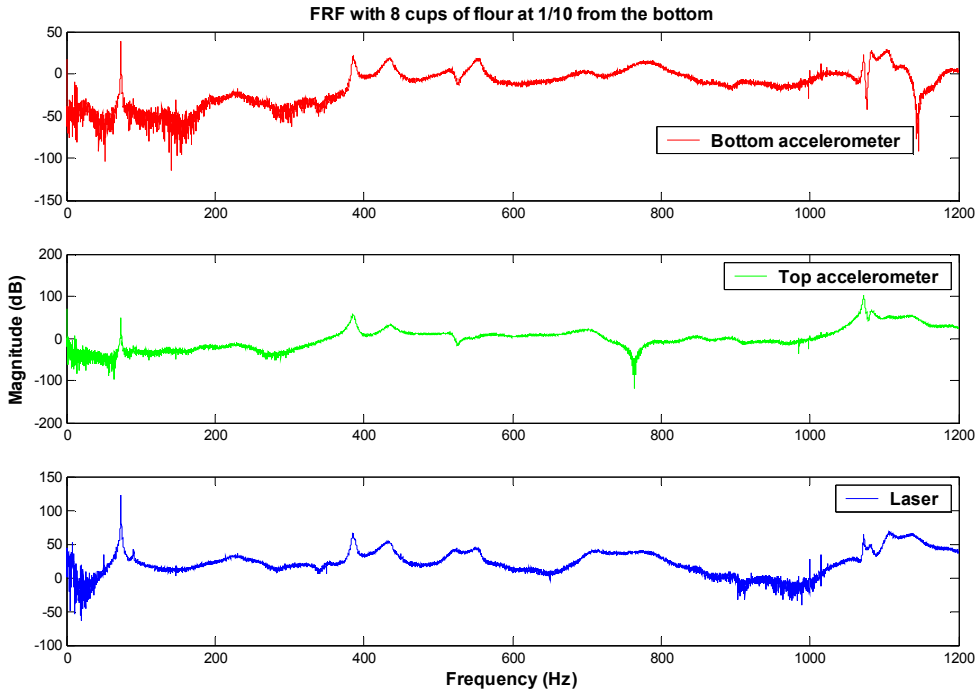

Figure 5-31 FRFs with 8 cups of flour added on the plastic board at the bottom

Table 5-11 The first 8 resonant frequencies with 8 cups of flour at 1/10

Natural frequencies of empty shell(Hz)	Natural frequencies of the shell with 8 cups of flour at 1/10 (Hz)			
	Acc1	**Acc2**	**Laser**	**Average**
79	73.77	73.77	73.77	73.77
270	225	225	225	225
380	386	386	386	386
398	435	435	435	435
456	-	518	520	519
568	-	554	554	554
715	705	705	710	707
775	-	770	770	770

Table 5-12 The first 8 resonant frequencies with different amount of flour at 1/10

Amount of flours (cups)	Natural frequencies (Hz)							
0	79	270	380	398	456	568	715	775
0.1	78.81	270	381	398	456	568	715	775
2	77.9	268	383	398	459	566	718	777
4	76.83	280	385	418	460/519	560	704	770
6	75.61	243	385	432	519	554	705	778
8	73.77	225	386	435	519	554	707	770

The modal damping ratio also increased with the amount of the blockage except for the slight change to the first resonant frequency 79Hz.

5.5.3 Conclusion

Due to the limit of the experiment setup, only two locations were studied. However the experiment demonstrated that the vibration analysis method is promising as a non-destructive method for detecting milk powder deposition or blockage in the cyclone. The resonant frequencies varied with the amount of the blockage and its location and

the modal damping ratio increased with the amount of the blockage, with the exception of the first bending mode.

5.6 Onsite experiment

Due to the promising results from the experiment done at Auckland University of Technology, onsite monitoring of the cyclone and the dropper tube was done in the Te Rapa plant using the method developed in the lab. The two goals of onsite research were to obtain FRFs of the test system and distinguish the clear resonant frequencies without too much effect because of the environmental noise; and to identify the variation of the natural frequencies and damping ratio with the inside milk powder built-up.

5.6.1 Natural frequencies of the cyclone

Figure 5.32 and 5.33 illustrate the accelerometer reading FRF of the cyclone with 6 hourly intervals. There is no significant change for the resonant frequencies within 6 hours of testing and its resonant frequencies are 134, 155, 170, 335Hz. The modal damping ratio is displays no change.

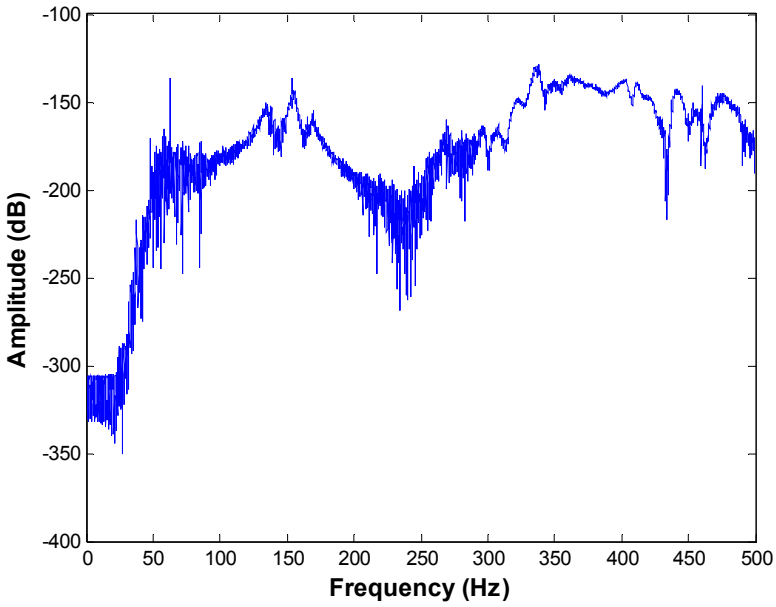

Figure 5-32 Accelerometer reading FRF of the cyclone

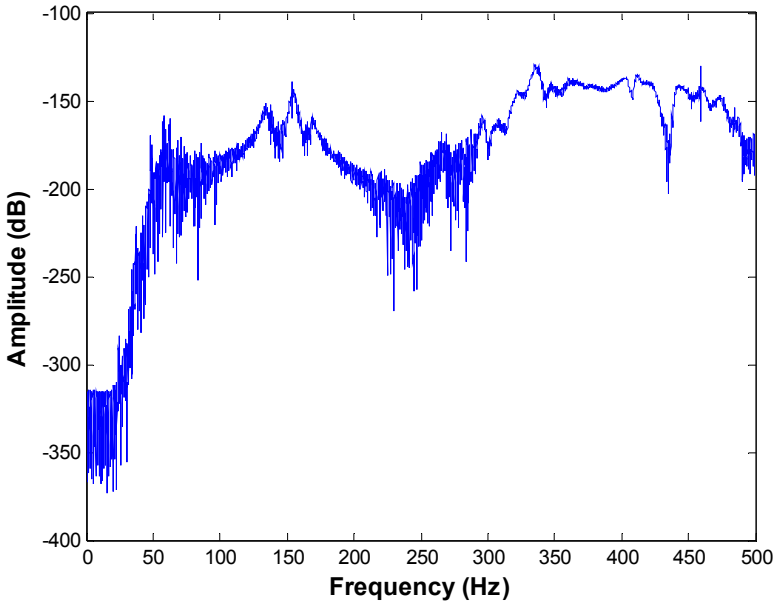

Figure 5-33 Accelerometer reading FRF of the cyclone after 6 hours later

5.6.2 Natural frequencies of the dropper tube

The milk powder blockage usually occurs at the bottom of the dropper tube. So the vibration characteristics of the dropper tube should be investigated deeply. From the ends support conditions the dropper tube can be seen as a cantilever. According to Yoo [48], the first natural frequency of the cantilever beam increases to some extent and then decreases as the concentrated mass moves from the fixed end to the free end and the variation of the first natural frequency increases as the concentrated mass ratio increases. The damping ratio will increase with the inside blockage build-up.

Figure 5.34 and Figure 5.38 show the raw time domain data from the laser sensor and accelerometer. Figure 5.35 shows the laser reading data from 5 order 1200 Hz low pass anti-aliasing filter and hamming window. Figure 5.36 shows 5 order 100-135Hz band pass filtered laser reading data. Figure 5.37 and Figure 5.39 reveal the FRF from the laser sensor and accelerometer which showed a similar trend.

The cyclone system should have infinite natural frequencies and the experimental resonant frequencies depend on the hammer struck and location of the sensors. In order to simplify the complicated cyclone, the clear resonant frequencies must be identified,

and then its modal damping ratio can be estimated to compare if there is any variation with time or milk powder build-up. The clear resonant frequencies and its damping ratio with 5 hours interval are shown in table 5.13. No variation with 5 hours testing in the resonant frequency and its damping ratio was exhibited.

Table 5-13 The clear resonant frequencies of dropper tube and its modal damping ratio

Natural frequencies(Hz)	Band pass filter	Damping ratio ζ	Damping ratio ζ （5hrs later）
118	5 order 100-135 Hz	0.03374	0.03374
300	3order 285-315 Hz	0.00955	0.00955
330	3order 20-335 Hz	0.01351	0.01351

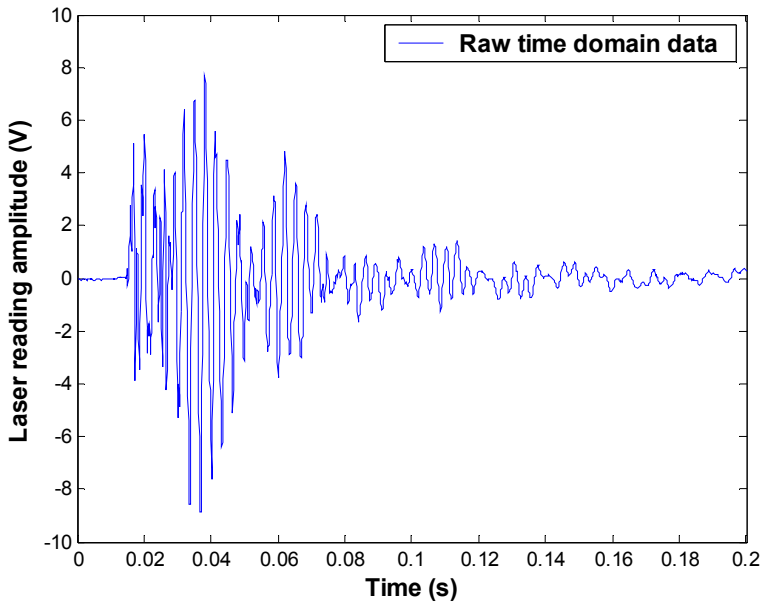

Figure 5-34 Impulse time domain laser reading from the dropper tube

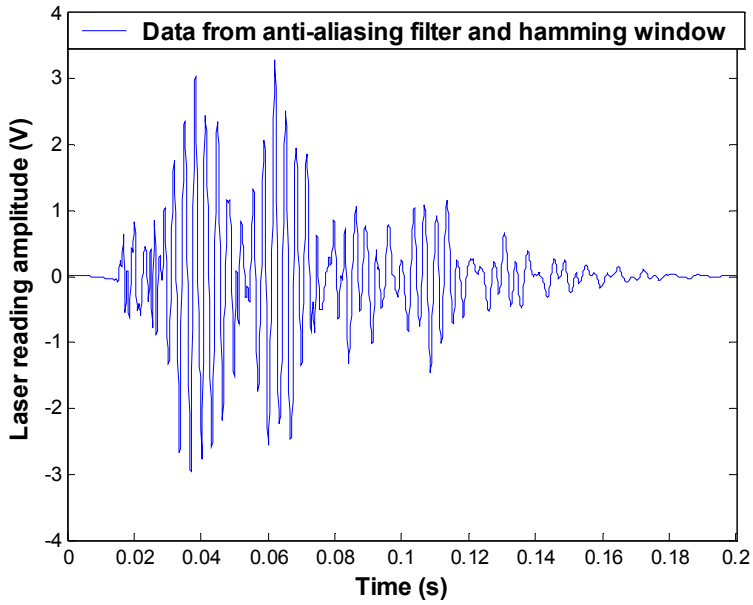

Figure 5-35 Filtered laser reading data from anti-aliasing and hamming window

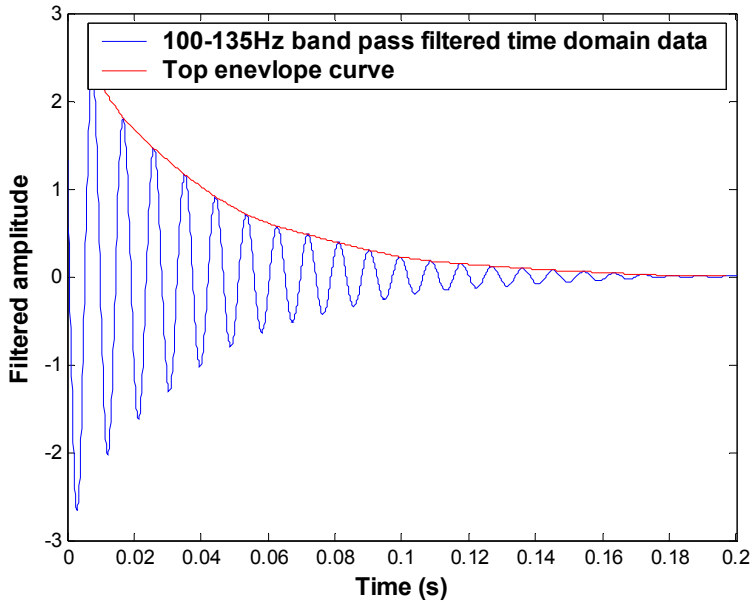

Figure 5-36 Filtered laser reading data from the dropper tube

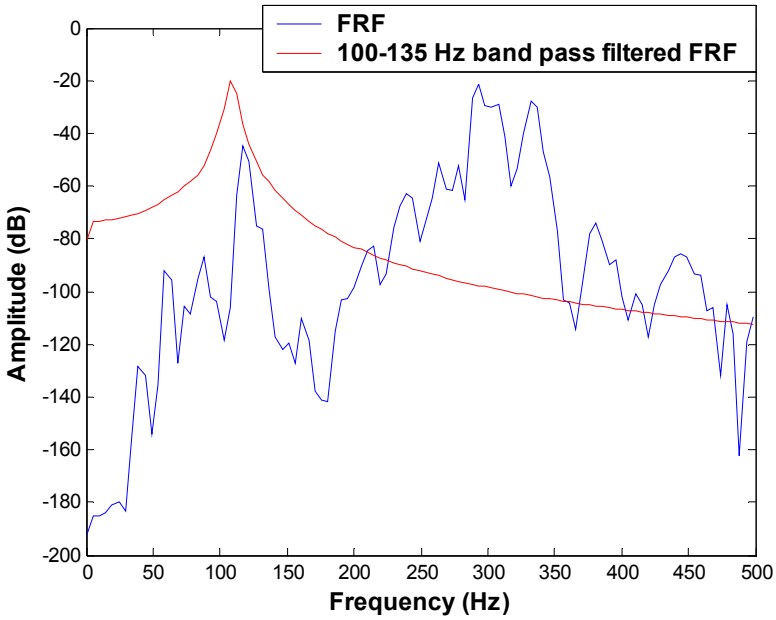

Figure 5-37 Laser reading FRF and 100-135Hz band pass filtered FRF of the dropper tube

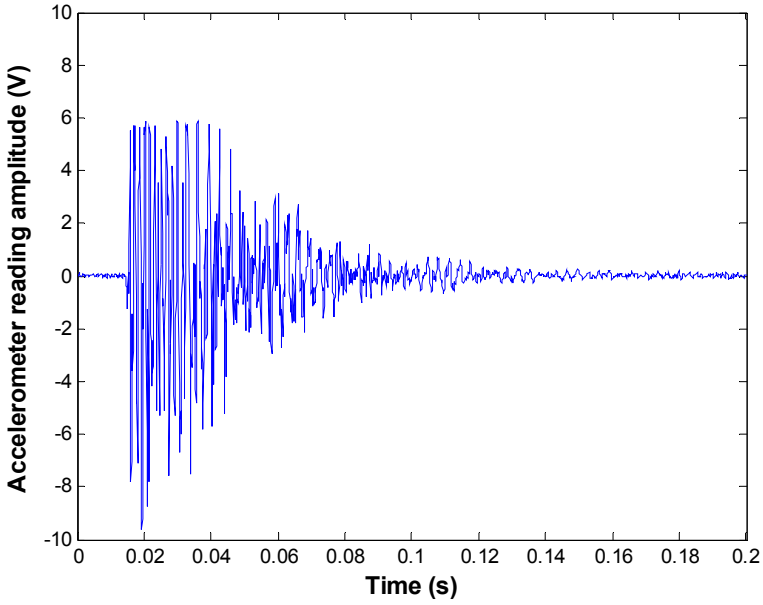

Figure 5-38 Impulse time domain accelerometer reading from the dropper tube

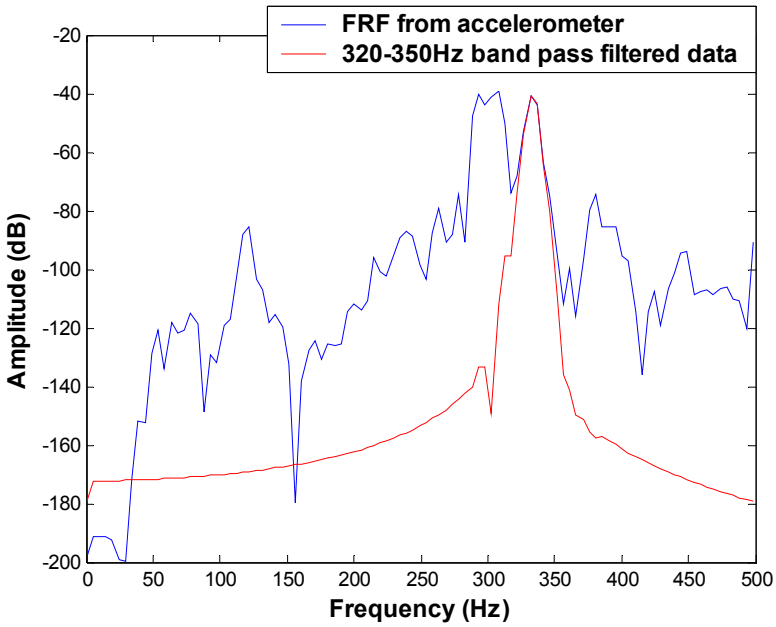

Figure 5-39 Accelerometer reading FRF and 320-350Hz band pass filtered FRF of the dropper tube

5.6.3 Conclusion

The FRFs of the dropper tube and the cyclone were obtained and clear resonant frequencies can be seen. After several hours of monitoring, it was found that they were consistent, which proved the impulse vibration analysis method is promising in blockage detection in the cyclone of a milk powder spray dryer. The first goal of onsite research was achieved successfully.

The variation of vibration modal parameters could not be detected because the milk powder blockage in the cyclone happened in an unpredictable manner and over a short time of monitoring. More data is needed to prove the variation of the vibration modal parameters with the deposition or blockages. This research could not achieve the second goal due to time limitations.

Chapter 6 Conclusion and Future work

6.1 Conclusion

The objective of this research was to develop a feasible non-destructive method to detect the milk powder blockage in the cyclone of spray dryers. Vibration analysis technique was identified from literature as a promising method to achieve the research objective. A 1.87m long vertical circular cylindrical steel shell with both ends simply supported as a prototype was built to investigate the dynamic vibration characteristics with and without added mass inside the shell. Natural frequencies and modal damping ratios were the main parameters which were studied analytically, numerically and experimentally. Analytical solutions using beam theory were obtained and compared with experimental results by numerical solutions to determine the modal shapes of the empty prototype. The first bending natural frequency was determined and became the experimental core when compared with the beam-mass theoretical calculation to see if experimental data could match the theory. Other modes were identified by modal analysis and researched in experimental stages as a supplement of the variation of the first bending natural frequency.

The experimental investigation was made up of two stages, one was by a simulated amount mass blockage and the other was by flour induced blockage. An impact hammer excitation method was used to study the frequency response of the prototype. Two accelerometers and one laser vibrometer were used as vibration sensors. The vibration data were recorded by the LabView software programme, which were later analysed using MATLAB to obtain the FRF curve and calculate the damping ratio. The experimental resonant frequencies of the empty cylindrical shell were 79 Hz, 270 Hz, 380 Hz and 398 Hz. Both the accelerometer and the laser vibrometer gave similar measurements, which meant that both sensors could be utilized for industry application.

In the ABAQUS FEA solution, the first bending modal shape was 81 Hz and the second bending modal shape was 316 Hz. The 381Hz vibration modal shape is identified as m=1and n=4 and the 401 Hz modal shape is identified as m=3 and n=4 in FEA solution, in which n was circumferential mode parameter and m was axial (bending) mode parameter. The 381 Hz and 401 Hz FEA modal natural frequencies closely match the 380 Hz and 398 Hz experimental resonant frequencies.

In the analytical beam theory solution, the first two bending modal shapes were 82.19Hz and 328.77 Hz respectively. These were 1 Hz more in the first bending mode and 12 Hz more in the second bending mode compared to the FEA results, which proved that the FEA results were reasonable and could be improved by mesh refinement.

From the analytical, numerical and experimental results, the 79 Hz obtained from the experiments was identified as the first bending mode of the prototype. 270 Hz, 380 Hz and 398 Hz might be the combination of a certain bending and a certain circumferential mode in which 380 Hz modal shape is m =1 and n=4 and the 398 Hz modal shape is m=3 and n=4.

According to the beam-mass theory, an added mass close to the middle point of the beam will lower the first bending natural frequency which will also go down with the increase in mass quantity. The simulated mass experiment shows that the resonant frequencies shifted with the amount of blockage and its location. The first experimental bending natural frequency decreased to its lowest value when the added mass was inserted in the midpoint. It also decreased with the amount of the mass, *e.g.* 66.91 Hz with 0.64 kg of added mass to 56.34 Hz with 2.5 kg of added mass. The three other resonant frequencies (270 Hz, 380 Hz and 398 Hz) increased with the amount of the added mass. The 270 Hz and 380 Hz experimental resonant frequencies show similar trends which reach their maximum value when the added mass was at 1/4 and 3/4 of the whole length. The 398 Hz experimental resonant frequency gives an opposite trend compared to the first bending mode, which reached its maximum at the midpoint. The simulated mass experiment demonstrates that the resonant frequencies vary with the added mass ratio and location, and the variation trend of the first bending mode aligns with the beam-mass theory.

Flour induced blockage show that the modal damping ratio increases with the amount of the flour except for the first bending mode. Additionally the resonant frequencies shift with the location and amount of the blockage. The damping ratio for each mode except for the first one increases and can be seen from the shape of the FRF using half-power bandwidth method to qualitative estimate damping ratio. Hilbert transform envelope curve method was used to quantitatively calculate the modal damping ratio. The damping ratio at 270 Hz shows the most increase. For example, two cups flour blockage

makes damping ratio at 270 Hz change from 0.009 to 0.017, which meant that the mass effect of two cups flours had doubled the empty shells modal damping ratio. This kind of variation was big enough for identification and as a diagnosis parameter for detecting the deposition or blockage inside of cylindrical shell.

There was no change for the resonant frequencies when the added mass was inserted at the bottom point of the cylindrical shell. This is because the added mass was put at one vibration node. It can be seen that the modal natural frequencies shifted with the amount of the blockage when induced flour blockage was put at 1/10 of the whole length from the bottom support point. The first bending mode 79 Hz went down with the amount of the blockage and reduced approximately 1 Hz with every two cups of flour added. This matched the beam-mass theory and previous certain mass experiment. The experimental 380 Hz mode and 398 Hz mode increased with the amount of flour e.g. the 398 Hz mode increased rapidly to 418 Hz when 4 cups of flour were added. This supports the simulated mass experiment.

Onsite monitoring of the cyclone of the spray dryer was done at Fonterra Te Rapa using the same methods used in the prototype testing. Due to the height restriction, only one accelerometer was positioned on the surface of the cyclone 2.1m from the floor. Further research was done to the dropper tube as the majority of blockages build from there. The clear and consistent resonant frequencies of the two parts can be identified in FRF curve. The damping ratio of 180 Hz, 300 Hz and 330 Hz resonant frequencies of the dropper tube were 0.03374, 0.00955 and 0.01351 respectively and the resonant frequencies and its damping ratio did not change within 5 hours of monitoring. The clear and consistent resonant frequencies of the cyclone and dropper tube proved that the vibration analysis was promising as a non-destructive technique in detecting the blockage in the cyclone of spray driers without much effect by the environmental noise. This also demonstrates that more effort into onsite monitoring of cyclones is deserved. Due to time limitations, this research could not achieve the variation of the vibration characteristics of the cyclone and dropper tube with the blockage.

The objectives of this thesis were achieved successfully and are summarised as follows:

1. The cyclone or dropper tube was mathematically modelled as a circular cylindrical thin shell and the inside milk powder blockage was modelled as the added mass to the shell. An effective 1.87m-long vertical cylindrical stainless steel shell with both ends simply supported was constructed as a prototype, achieving this objective.
2. The circular cylindrical thin shell theory was investigated to analyse the mode shapes of the natural frequencies. Due to unavailability of analytical solution, the FEA method was employed to investigate the natural frequencies and mode shapes of the prototype numerically. To simplify the shell theory, beam theory was employed to investigate the bending (or axial) vibration mode. Compared with numerical and experimental results, the first bending vibration mode of the prototype was identified. This objective was achieved.
3. Beam-mass theory was introduced to study effect of the added mass to the prototype analytically. This objective was achieved.
4. Impact hammer excitation test was used to investigate the variation of vibration characteristics of prototype with added mass inside. Two stages of experiments were conducted, which were simulated amount mass blockage experiment and flour induced blockage experiment. Forced vibration test was used as a method to identify the bending mode.
5. Simulated amount mass blockage experiment: Three different amount of mass were inserted into the prototype at 11 evenly location to experimentally investigate the variation of natural frequencies with amount and location of mass.
6. Flour induced blockage experiment: More simulation experiment as milk powder cyclone was done using differing amounts of flour blocked at two different bottom positions to study the variation of natural frequencies and damping ratio.
7. The modal shapes of the experimental resonant frequencies of empty prototype were identified by comparing the analytical, numerical, impact hammer excitation test and forced vibration test. The variation of the first several natural frequencies and its modal damping ratio with the blockage mass and location were presented and summarised in Chapter 5.
8. The clear and consistent FRFs curves of the cyclone were obtained in the onsite experiment although the variation of natural frequencies and modal damping ratio could not be detected.

6.2 Future Work

This research is an initial study on the non-destructive detection of milk powder blockage. Although it has shown the potential of vibration analysis as a NDT method, further work is still necessary to develop the technique.

- Further onsite monitoring cyclone experiments are needed to obtain the variation of the FRF of the dropper tube or cyclone with the milk powder deposition or blockage.
- Investigate cyclone FRF using the air hammer as an impact excitation. The cyclones of most milk power spray dryer system have air hammers to generate vibration regularly in order to reduce the chance of blockage. If it can be used as the impact excitation, it will increase vibration analysis advantage as a NDT method to detect the blockage.
- Damping ratio extraction methods need to be researched deeply in order to obtain more accurate modal damping ratio information by reducing the environmental noise effect.
- It is recommended that a full aspect LabView programme will be researched for the practical industry application, which includes data acquisition and signal analysis. Signal analysis includes data filter, FT, and damping ratio extraction technique.

Appendix I Data processing codes

The following Matlab codes were used to process the data.

AI.1 Analysis in time and frequency domain

```
clear;
close all;
clc;
%****************Process impact hammer data **************
%*****************************************************

%%%%%%%%%%%%%%
%-------Read data-------%
%%%%%%%%%%%%%%

filename=input ('input the filename:','s');  % Wait to input filename
fid=fopen(filename,'r');
tline = fgets(fid);                    % Take away the first row of data which is the sample
rate
sample_rate=10000;
array=fscanf(fid,'%g %g %g %g',[4,inf]);    % Read all the data into a 4 column matrix
array=array';
N = max(size(array));
tmax = N/sample_rate;
x = [0:tmax/(N-1):tmax];                  % Set x-axis
y=array(:,1);                             % Read the impact hammer force data
fclose(fid);

[b,a] = butter(10,1200/5000,'low');     % anti-aliasing filter
fy = filtfilt(b,a,y);

%%%%%%%%%%%%%%%%%%%%%%%%%%%%%
%------Compute FFT------%
%%%%%%%%%%%%%%%%%%%%%%%%%%%%%
```

```
w=hamming(length(fy));            % Hamming window
ffy=w.*fy;
NFFT = 2^(nextpow2(length(fy)));      % next highest power of 2 greater than or equal
to y to speed up FFT
yfft = fft(ffy,NFFT);
NumUniquePts = ceil((NFFT+1)/2);    % compute number of symmetric points in FFT
yfft = yfft(1:NumUniquePts);        % Take important part of FFT
MX = abs(yfft);                     % Take the magnitude of FFT of x
MX = MX/length(ffy);                % Scale the FFT so that it is not a function of the
length of x
MX = MX.^2;                         % Take the square of the magnitude of FFT of x
MX = MX*2;                          % Multiply by 2 to because you threw out the second half
of FFT above

MX(1) = MX(1)/2;                    % DC Component should be unique
if ~rem(NFFT,2)
   MX(end) = MX(end)/2;       % NFFT is even; therefore, Nyquist point is included
End

%%%%%%%%%%%%%%
%---Plot time domain----%
%%%%%%%%%%%%%%

plot(x,y);
xlabel('Time (s)');
ylabel('Voltage/Force (N)')
title('Impact hammer')
figure;
plot(x,ffy);
xlabel('Time (s)');
ylabel('Voltage/Force (N)')
title('Impact hammer data after anti-aliasing filter and hamming window')

%%%%%%%%%%%%%%%%%%
```

```
%---Plot frequency domain----%
%%%%%%%%%%%%%%%%%%

f = 0:10000/NFFT:1200;                % Frequency range in x-axis
yham=10*log(MX(1:length(f)));         % Decibel Value plot in y-axis
figure;
subplot(2,1,1)
plot(x,y);
xlabel('Time (s)');
ylabel('Voltage/Force (N)')
title('Impact hammer')
subplot(2,1,2)
plot(f,yham);
title('FRF of impact hammer force');
xlabel('Frequency (Hz)');
ylabel('Magnitude (dB)');

%*****************************************************************
*%*****************************************************************
**

%%%%%%%%%%%%%%%%%%%%%%%%%%
%---Process Accelerometer and laser data----%
%%%%%%%%%%%%%%%%%%%%%%%%%%
for i = 2:4
   figure;
   plot(x,array(:,i));
   [b,a] = butter(10,1200/5000,'low');
   fy(:,i) = filtfilt(b,a,array(:,i));

   % Compute FFT

   w=hamming(length(fy(:,i)));
   ffy(:,i)=w.*fy(:,i);
   NFFT = 2^(nextpow2(length(array(:,i))));
```

```
    yfft = fft(ffy(:,i),NFFT);
    NumUniquePts = ceil((NFFT+1)/2);
    yfft = yfft(1:NumUniquePts);
    MX(:,i) = abs(yfft);
    MX(:,i) = MX(:,i)/length(ffy(:,i));
    MX(:,i) = MX(:,i).^2;
    MX(:,i) = MX(:,i)*2;

    MX(1,i) = MX(1,i)/2;
    if ~rem(NFFT,2)
        MX(end,i) = MX(end,i)/2;
    end
    % Plots

    figure;
    plot(x,ffy(:,i));

    xlabel('Time (s)');
    ylabel('Normalised acceleration (mm/s)')



    f = 0:10000/NFFT:1200;
    yacc(:,i)=10*log(MX(1:length(f),i));
    figure;
    plot(f,yham,f,yacc(:,i),'g',f,yacc(:,i)-yham,'r');
    title('FRF');
    xlabel('Frequency (Hz)');
    ylabel('Magnitude (dB)');
end
figure;
for i=2:4
    subplot(3,1,i-1);
    plot(f,(yacc(:,i)-yham));
    title('FRF');
    xlabel('Frequency (Hz)');
```

```
    ylabel('Magnitude (dB)');
end
```

AI.2 Obtain the envelope curve and damping ratio

```
clear;
close all;
clc;
format long;

sample_rate = 10000;
filename=input('input the filename:','s');
fid=fopen(filename,'r');
tline = fgets(fid);
array=fscanf(fid,'%g %g %g %g',[4,inf]);
array=array';
y=array(:,4);                    % reading laser data
fclose(fid);

N = max(size(y));                % Number of samples
tmax = N/sample_rate;
x = [0:tmax/(N-1):tmax];
plot(x,y);
xlabel('Time (s)');
ylabel('Laser reading Amplitude (V)');
title('raw data');
figure;

% Narrow band pass filter

n = 5;
Wn = [70 85]/5000;
[B,A] = butter(n,Wn);

y2 = filtfilt(B,A,ffy);
```

```
figure;
plot(x,y2);
hold on

% Trace envelope of filtered data

[up,down] = envelope(x,y2,'linear');        % Calculate envelope of data
[up,down2] = envelope(x,up,'linear');       % Calculate envelope of top data to give
exponential decrease
plot(x,up,'r');
xlabel('Time (s)');
ylabel('Filtered amplitude');

% Move the maximum value to t=0

[q,w] = max(up);
upy = up(w:max(size(up)));
upx = x(1:max(size(up))-w+1);
figure;
plot(upx,upy);
xlabel('Time (s)');
ylabel('Filtered amplitude')
figure;

% Take natural logarithm to the top envelope and discrete it

lny=log(upy);
plot(upx,lny);
figure;
plot(upx(1:2000:max(size(upx))),lny(1:2000:max(size(upx))),'+');
xlabel('Time (s)');
ylabel('Natural logarithm of filtered amplitude');
```

AI.3 Envelope function

```
%ENVELOPE gets the data of upper and down envelope of the input (x,y).
```

```
%
%   Input parameters:
%    x              the abscissa of the given data
%    y              the ordinate of the given data
%    interpMethod    the interpolation method
%
%   Output parameters:
%    up      the upper envelope, which has the same length as x.
%    down    the down envelope, which has the same length as x.

function [up,down] = envelope(x,y,interpMethod)

if length(x) ~= length(y)
   error('Two input data should have the same length.');
end

if (nargin < 2)|(nargin > 3),
 error('Please see help for INPUT DATA.');
elseif (nargin == 2)
   interpMethod = 'linear';
end

% Find the extreme maxim values
% and the corresponding indexes
%----------------------------------------------------
extrMaxValue = y(find(diff(sign(diff(y)))==-2)+1);
extrMaxIndex =   find(diff(sign(diff(y)))==-2)+1;



% Find the extreme minim values
% and the corresponding indexes
%----------------------------------------------------
extrMinValue = y(find(diff(sign(diff(y)))==+2)+1);
extrMinIndex =   find(diff(sign(diff(y)))==+2)+1;
```

```
up = extrMaxValue;
up_x = x(extrMaxIndex);

down = extrMinValue;
down_x = x(extrMinIndex);

% Interpolation of the upper/down envelope data
%--------------------------------------------------
up = interp1(up_x,up,x,interpMethod);
down = interp1(down_x,down,x,interpMethod);
```

Appendix II FRF of simulated mass experiment

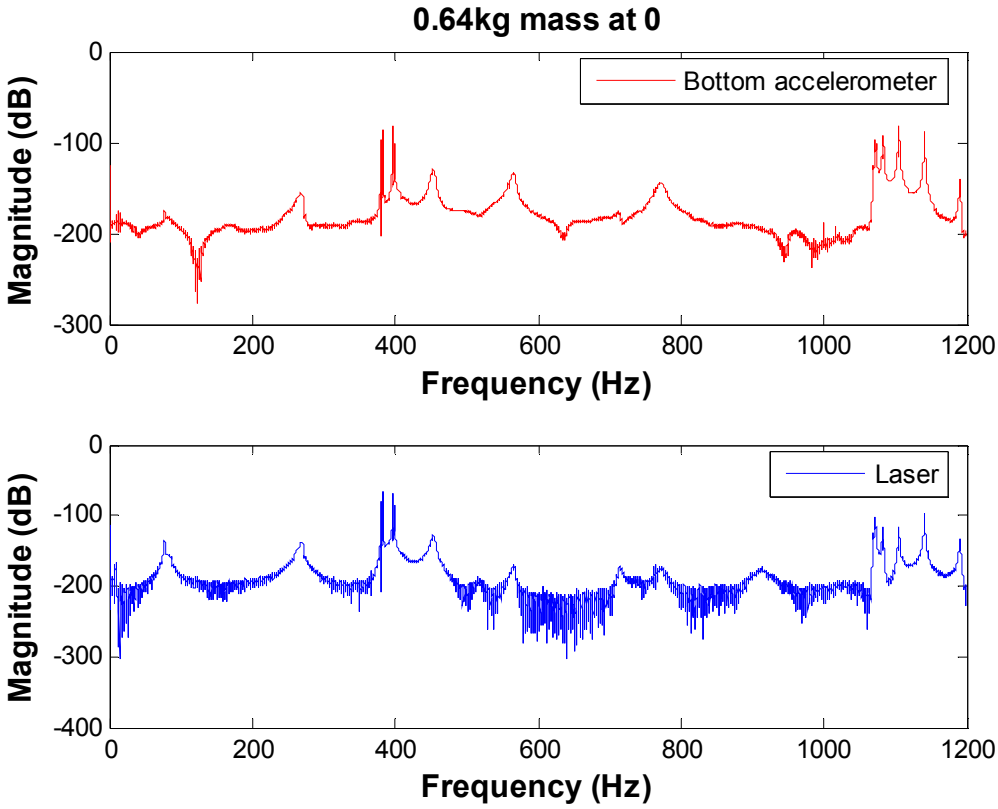

Figure II-1 FRF of 0.64 kg added mass at the bottom point

Table II-1 The first 6 resonant frequencies of 0.64 kg added mass at the bottom point

Sensor	Resonant frequencies (Hz)					
acc	77.51	269.4	382	397.5	453	564.7
laser	77.44	269.7	382	397.5	453.8	566
average	77.475	269.55	382	397.5	453.4	565.35

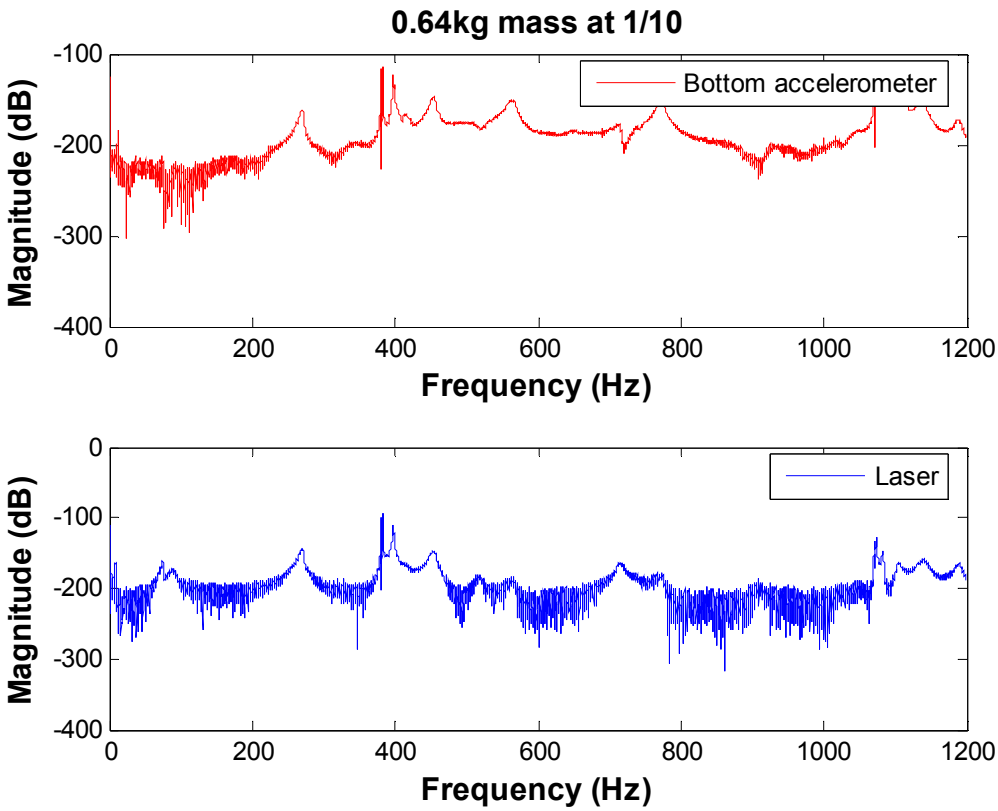

Figure II-2 FRF of 0.64 kg added mass at 1/10 of 1.87m from the bottom point

Table II-2 The resonant frequencies of 0.64 kg added mass at 1/10 of 1.87m from the bottom point

Sensor	Resonant frequencies (Hz)						
acc	73.78	-	270.8	382	397.5	455	564
laser	74.01	90	270.6	382	397.5	453.9	564
average	73.895	90	270.7	382	397.5	454.45	564

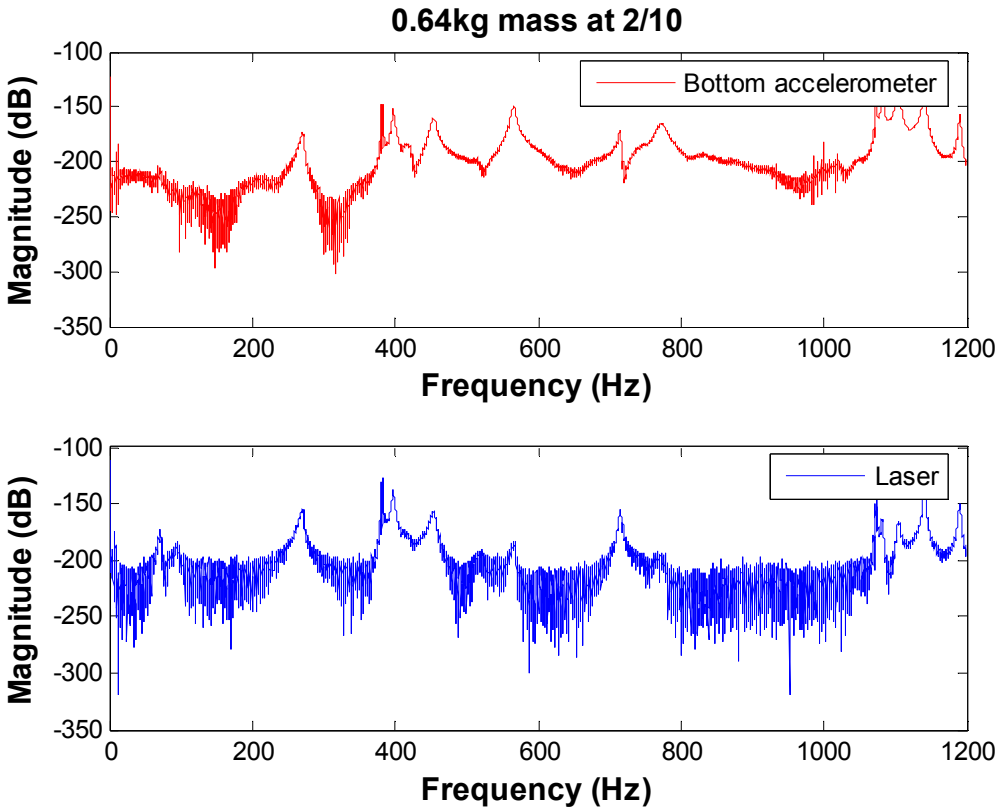

Figure II-3 FRF of 0.64 kg added mass at 2/10of 1.87m from the bottom point

Table II-3 The resonant frequencies of 0.64 kg added mass at 2/10 of 1.87m from the bottom point

Sensor	Resonant frequencies (Hz)						
acc	69.73	-	270.9	382	397.5	453	566
laser	71.33	95.37	271.4	382	397.5	453	565.8
average	70.53	95.37	271.15	382	397.5	453	565.9

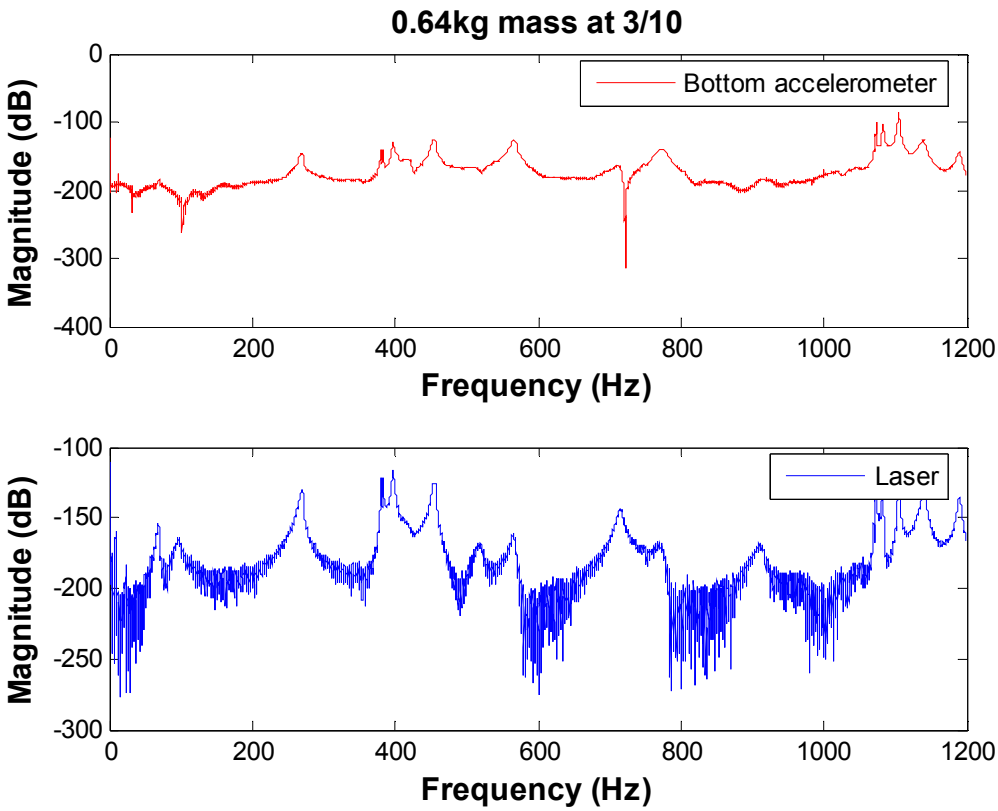

Figure II-4 FRF of 0.64 kg added mass at 3/10 of 1.87m from the bottom point

Table II-4 The resonant frequencies of 0.64 kg added mass at 3/10 of 1.87m from the bottom point

Sensor	Resonant frequencies (Hz)						
acc	69.27	-	270.9	382	397.5	453.7	567
laser	68.89	97.05	270.5	382	397.5	454.6	565
average	69.08	97.05	270.7	382	397.5	454.15	566

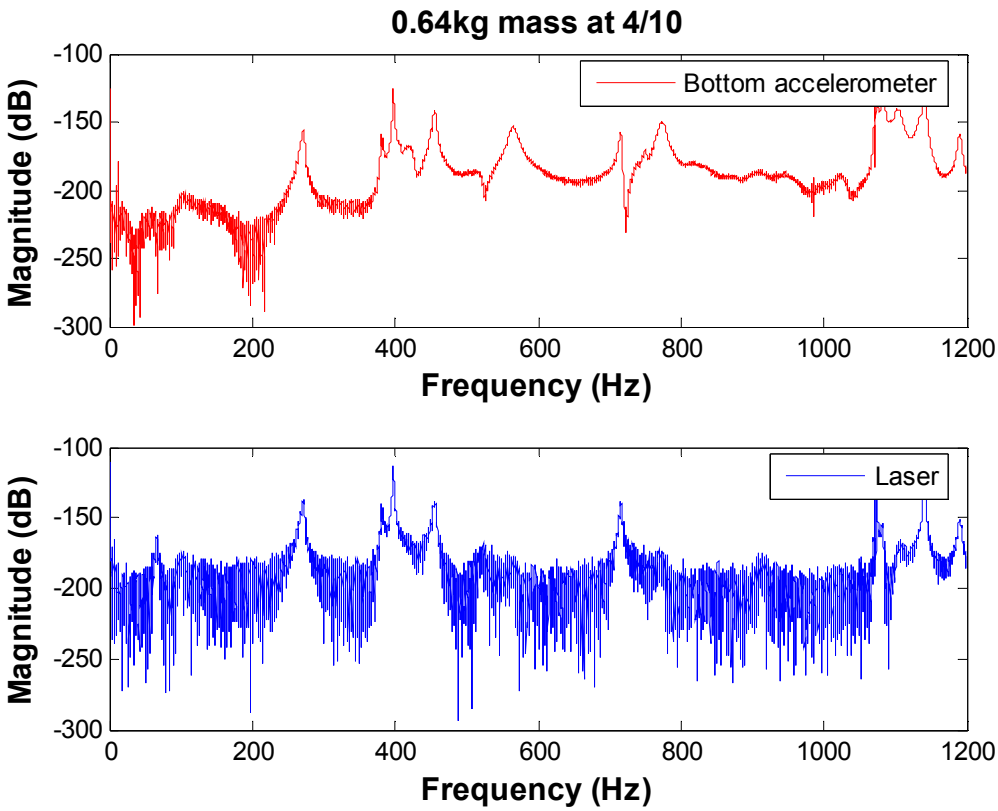

Figure II-5 FRF of 0.64 kg added mass at 4/10 of 1.87m from the bottom point

Table II-5 The resonant frequencies of 0.64 kg added mass at 4/10 of 1.87m from the bottom point

Sensor	Resonant frequencies (Hz)						
acc	-	104	271.9	381	397.6	455	565.2
laser	66.83	104.42	270.5	382.8	397.5	454.3	566.9
average	66.83	104.21	271.2	381.9	397.55	454.65	566.05

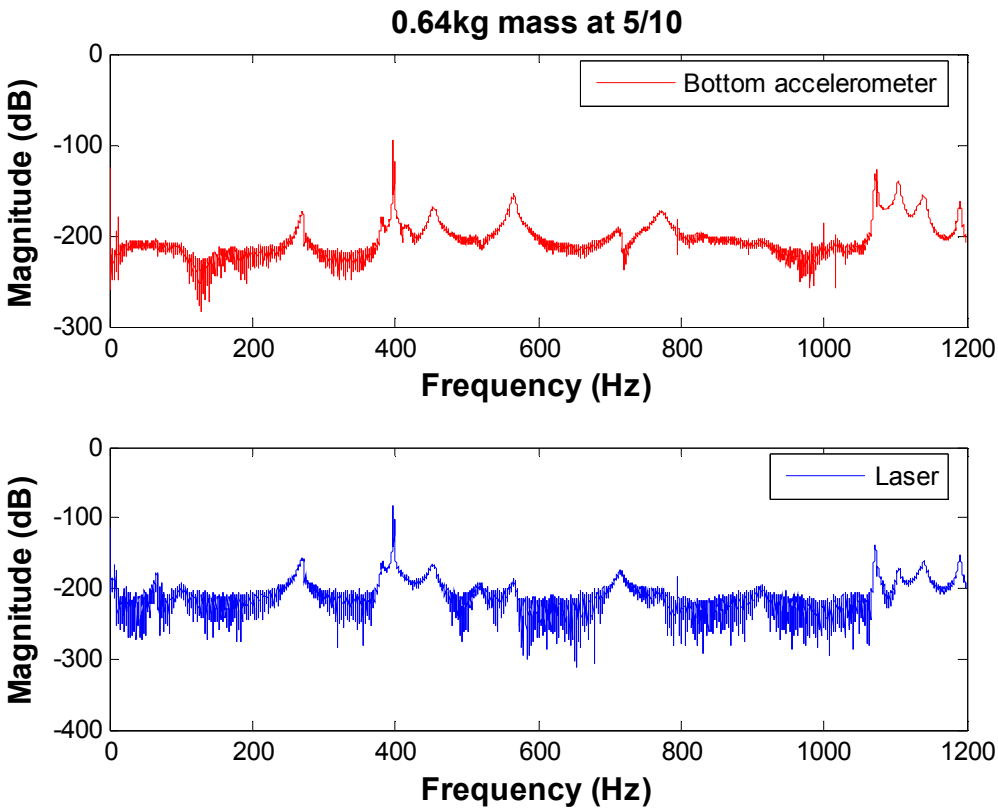

Figure II-6 FRF of 0.64 kg added mass at 5/10 of 1.87m from the bottom point

Table II-6 The resonant frequencies of 0.64 kg added mass at 5/10 of 1.87m from the bottom point

Sensor	Resonant frequencies (Hz)						
acc	-	-	270	383	397.4	454.3	566.6
laser	66.91	101.4	270.2	383	397.5	452.7	566.9
average	66.91	101.4	270.1	383	397.45	453.5	566.75

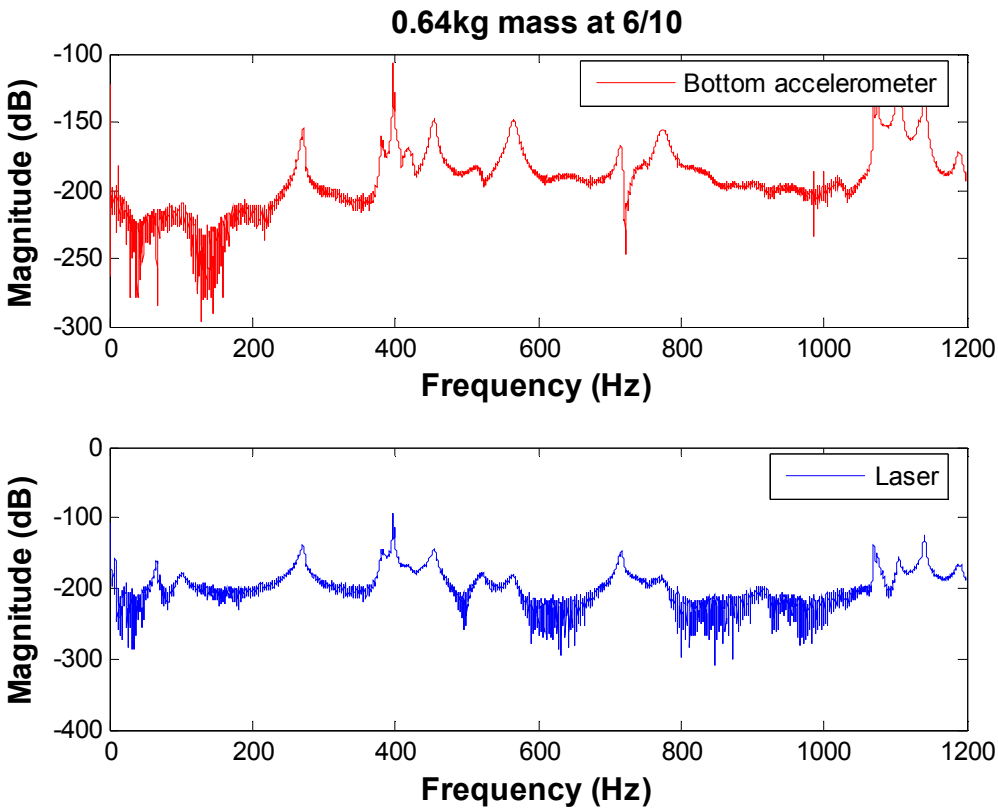

Figure II-7 FRF of 0.64 kg added mass at 6/10of 1.87m from the bottom point

Table II-7 The resonant frequencies of 0.64 kg added mass at 6/10 of 1.87m from the bottom point

Sensor	Resonant frequencies (Hz)						
acc	-	102	271.7	380.5	397.4	454.9	566.7
laser	66.68	102.2	272	380.9	397.5	454.8	565.9
average	66.68	102.1	271.85	380.7	397.45	454.85	566.3

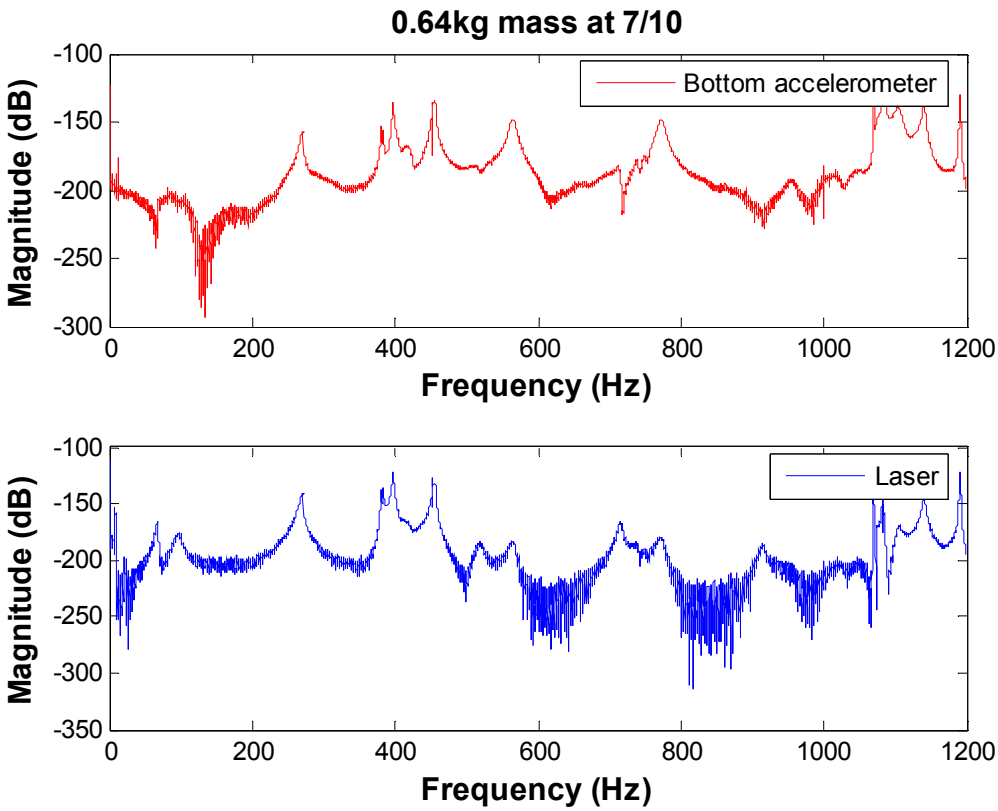

Figure II-8 FRF of 0.64 kg added mass at 7/10 of 1.87m from the bottom point

Table II-8 The resonant frequencies of 0.64 kg added mass at 7/10 of 1.87m from the bottom point

Sensor	Resonant frequencies (Hz)						
acc	-	-	270.5	380.5	397.5	454.8	566.7
laser	67.21	98	269.5	380.8	397.5	455	566.3
average	67.21	98	270	380.65	397.5	454.9	566.5

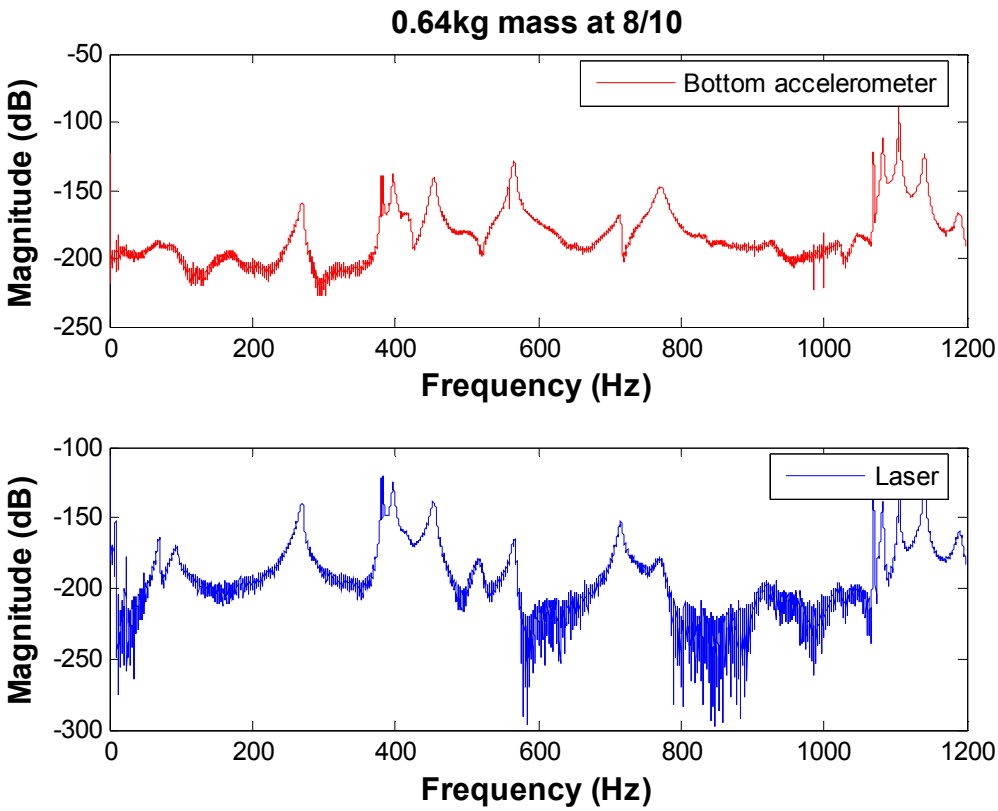

Figure II-9 FRF of 0.64 kg added mass at 8/10 of 1.87m from the bottom point

Table II-9 The resonant frequencies of 0.64 kg added mass at 8/10 of 1.87m from bottom point

Sensor	Resonant frequencies (Hz)						
acc	-	-	269.4	382.5	397	455.7	564.9
laser	68.66	92.7	270	382.6	396.7	456	566.1
average	68.66	92.7	269.7	382.55	396.85	455.85	565.5

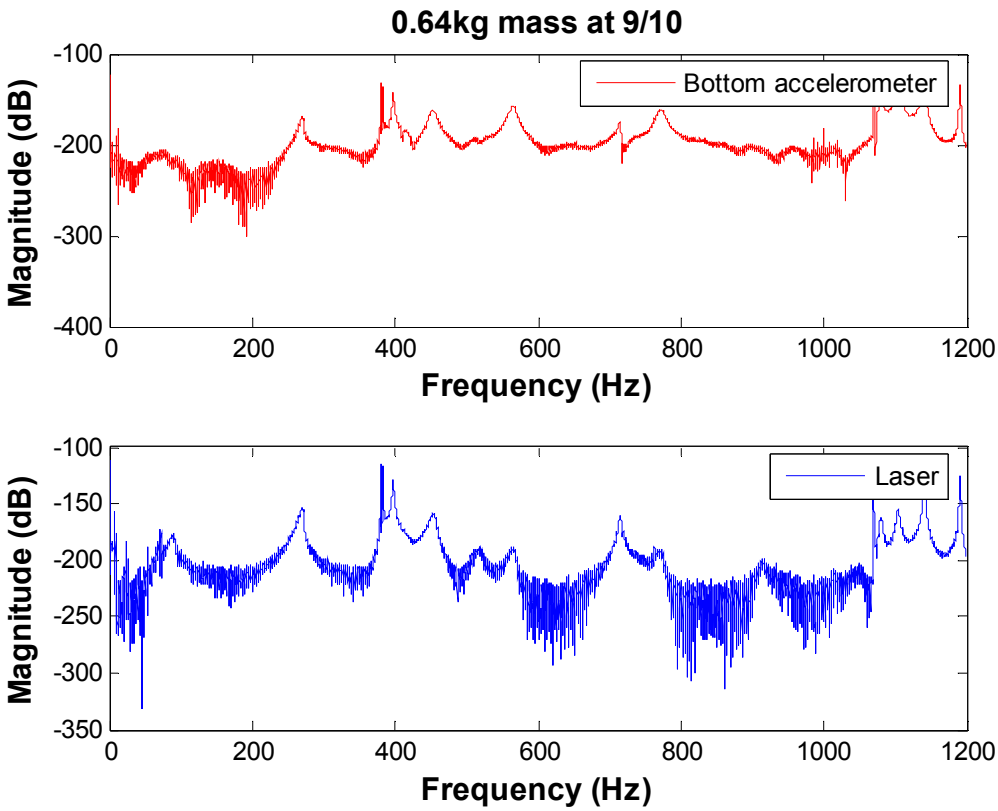

Figure II-10 FRF of 0.64 kg added mass at 9/10 of 1.87m from the bottom point

Table II-10 The resonant frequencies of 0.64 kg added mass at 9/10 of 1.87m from bottom point

Sensor	Resonant frequencies (Hz)						
acc	-	-	270.5	382.5	397.5	455	566
laser	71.41	88.04	270.4	382.5	397	456	565
average	71.41	88.04	270.45	382.5	397.25	455.5	565.5

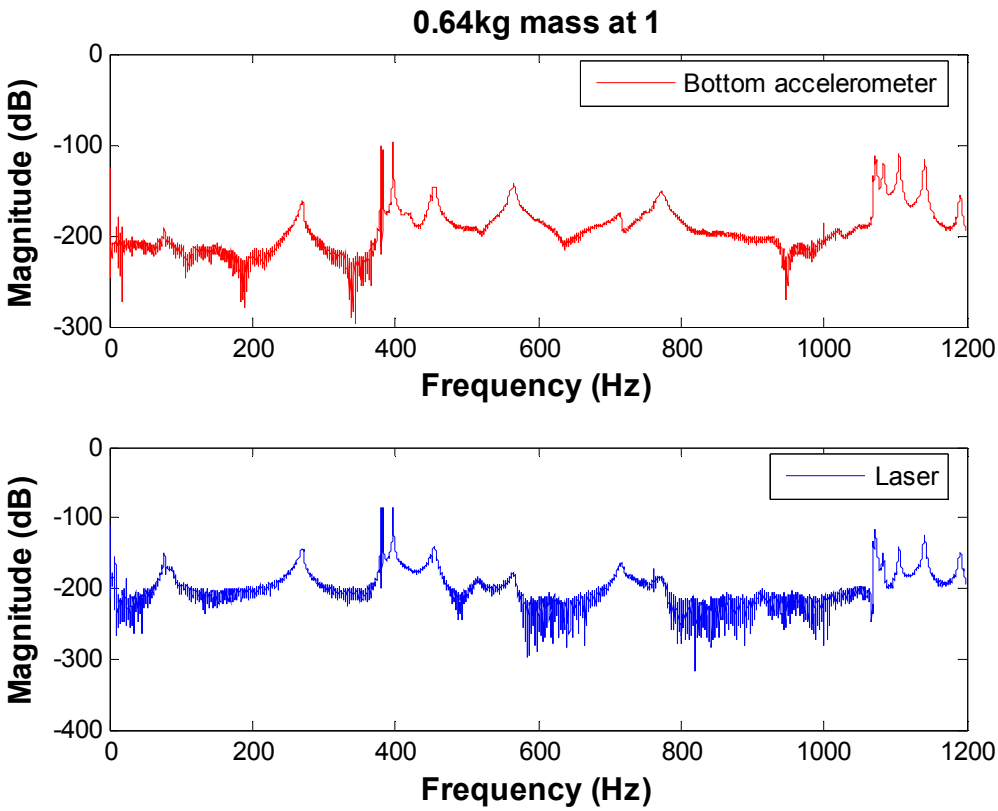

Figure II-11 FRF of 0.64 kg added mass at the top point

Table II-11 The resonant frequencies of 0.64 kg added mass at the top point

Sensor	Resonant frequencies (Hz)					
acc	77.13	269.6	382.5	397	454.8	566
laser	77.13	271	382.3	397	455	566
average	77.13	270.3	382.4	397	454.9	566

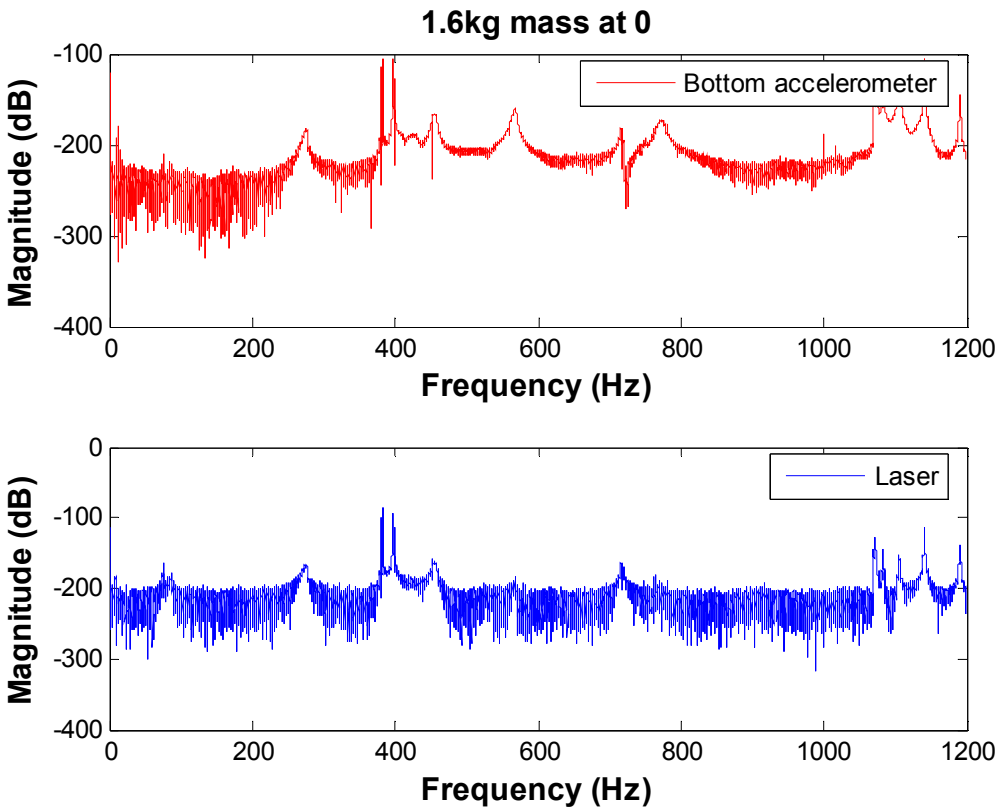

Figure II-12 FRF of 1.6 kg added mass at the bottom point

Table II-12 The resonant frequencies of 1.6 kg added mass at the bottom point

Sensor	Resonant frequencies (Hz)						
acc	75.99	86.86	275.7	382.6	397.5	454.1	568
laser	75.95	87	275.6	382.5	397.5	454.9	567
average	75.97	86.94	275.65	382.55	397.5	454.5	567.5

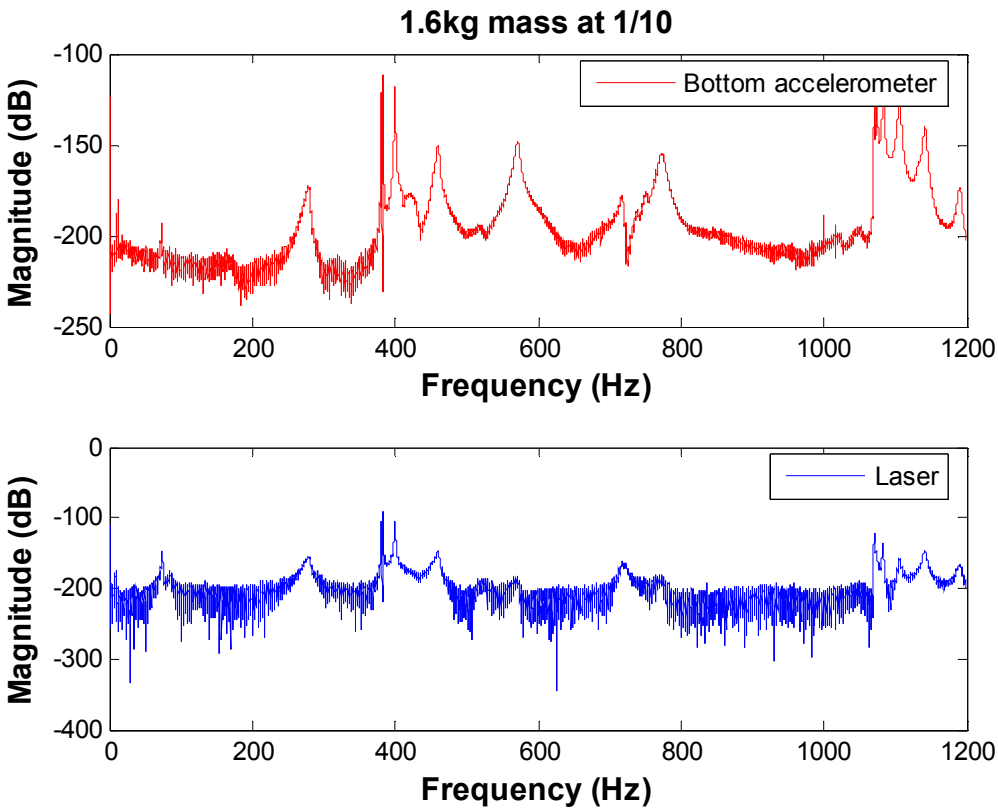

Figure II-13 FRF of 1.6 kg added mass at 1/10 of 1.87 from the bottom point

Table II-13 The resonant frequencies of 1.6 kg added mass at 1/10 of 1.87m from the bottom point

Sensor	Resonant frequencies (Hz)					
acc	74.23	279.8	382.5	399.6	460	571
laser	74.31	279.6	382.9	399.5	458	570.6
average	74.27	279.7	382.7	399.55	459	570.8

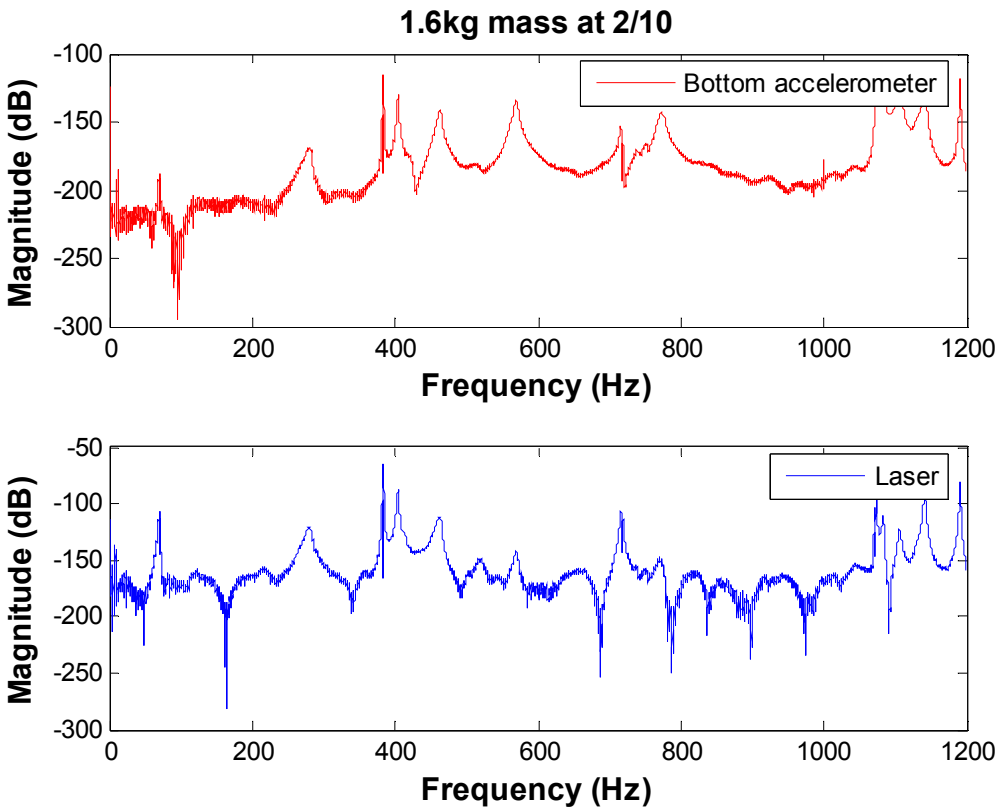

Figure II-14 FRF of 1.6 kg added mass at 2/10 of 1.87 from the bottom point

Table II-14 The resonant frequencies of 1.6 kg added mass at 2/10 of 1.87m from the bottom point

Sensor	Resonant frequencies (Hz)					
acc	69.96	280.1	383.9	403.8	463.8	569.7
laser	69.8	280.4	383.9	404.2	462.9	570.2
average	69.88	280.25	383.9	404	463.35	569.95

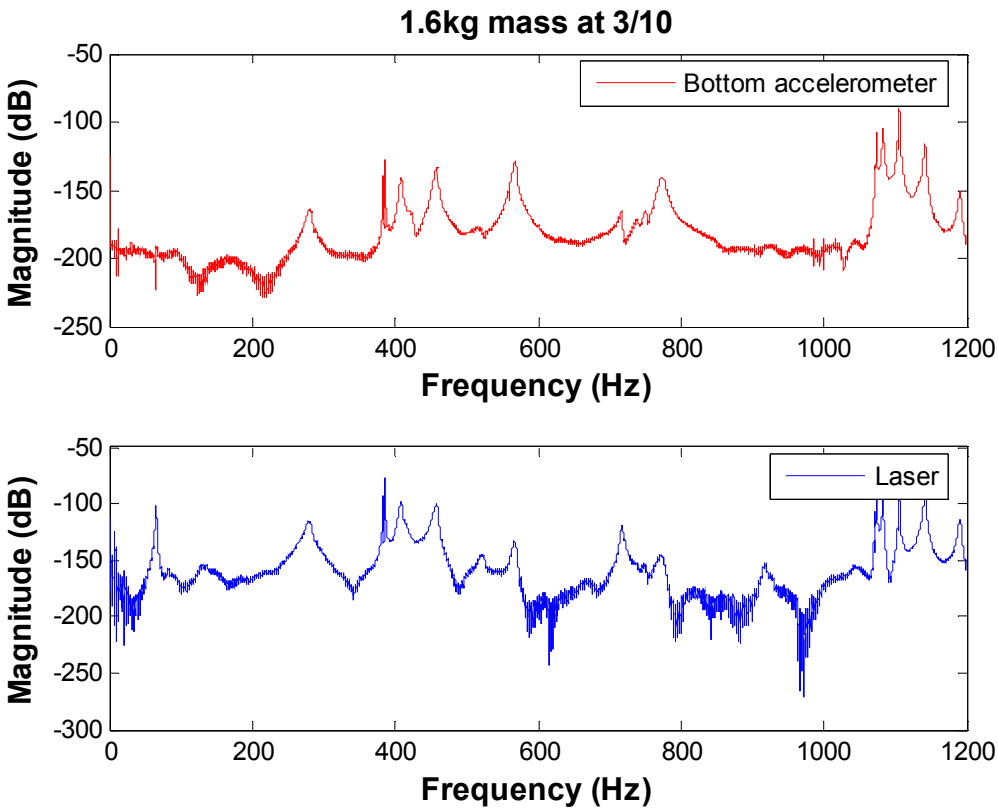

Figure II-15 FRF of 1.6 kg added mass at 3/10 of 1.87 from the bottom point

Table II-15 The resonant frequencies of 1.6 kg added mass at 3/10 of 1.87m from the bottom point

Sensor	Resonant frequencies (Hz)					
acc	66.45	280.2	385.7	408.3	458.1	567.8
laser	65.61	280.9	385.2	408.2	458	567.5
average	66.03	280.55	385.45	408.25	458.05	567.65

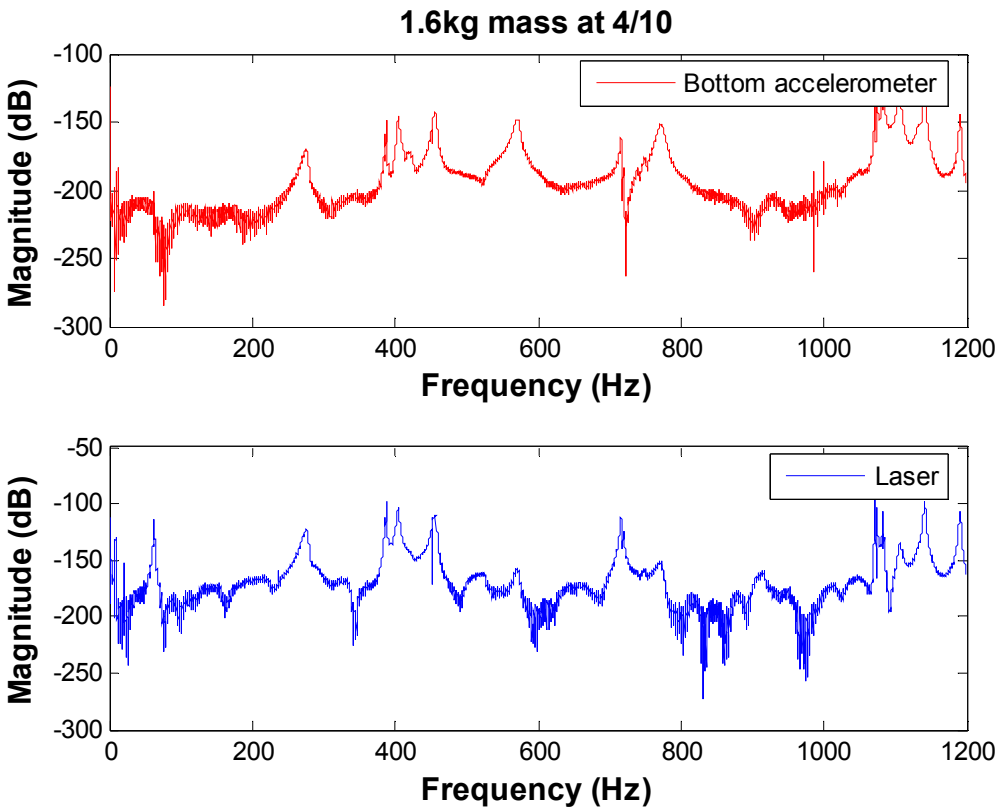

Figure II-16 FRF of 1.6 kg added mass at 4/10 of 1.87 from the bottom point

Table II-16 The resonant frequencies of 1.6 kg added mass at 4/10 of 1.87m from the bottom point

Sensor	Resonant frequencies (Hz)					
acc		276.6	387.6	405.2	456	571
laser	62.87	276.5	387.6	404.7	456.2	571
average	62.87	276.55	387.6	404.95	456.1	571

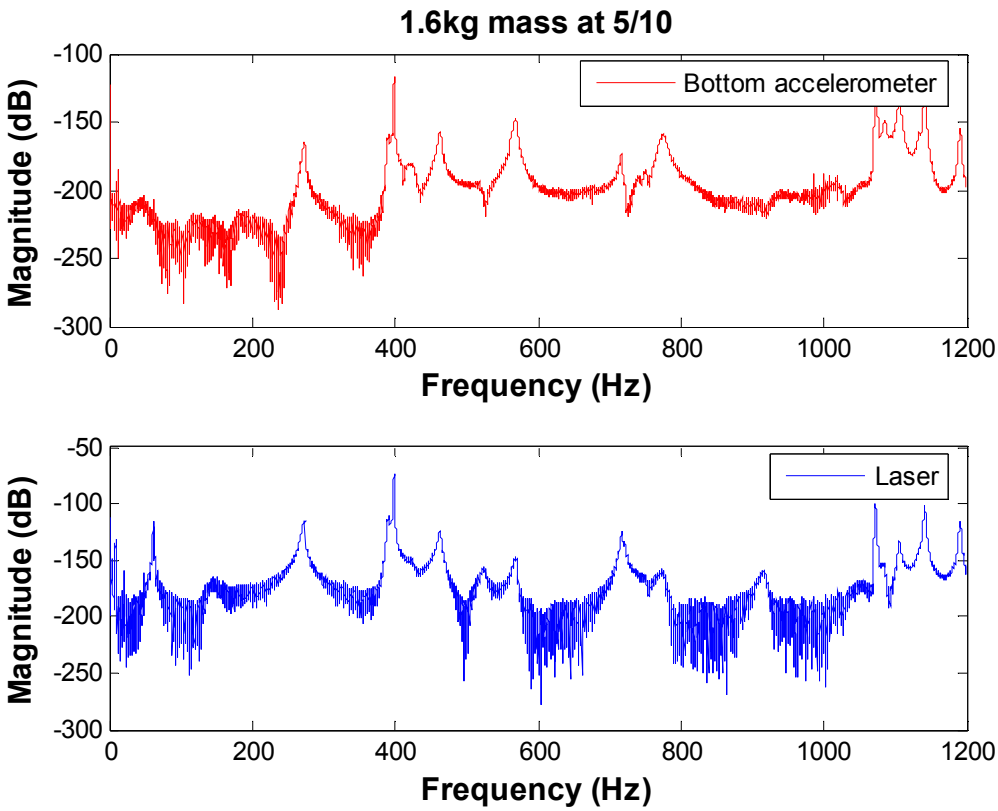

Figure II-17 FRF of 1.6 kg added mass at 5/10 of 1.87 from the bottom point

Table II-17 The resonant frequencies of 1.6 kg added mass at 5/10 of 1.87m from the bottom point

Sensor	Resonant frequencies					
acc		273.5	391	398.3	462.5	569
laser	61.8	273.2	390.9	398.3	461.7	569
average	61.8	273.35	390.95	398.3	462.1	569

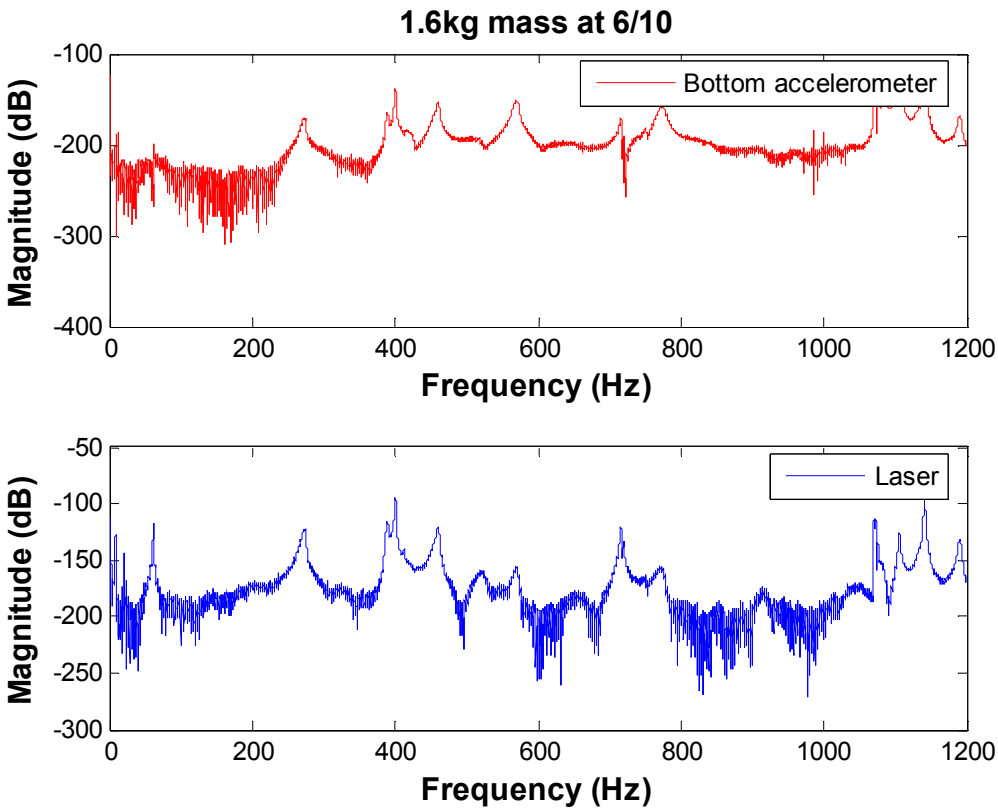

Figure II-18 FRF of 1.6 kg added mass at 6/10 of 1.87 from the bottom point

Table II-18 The resonant frequencies of 1.6 kg added mass at 6/10 of 1.87m from the bottom point

Sensor	Resonant frequencies (Hz)					
acc	61.95	273.7	388.5	400.5	461	570.5
laser	61.95	273.7	388.3	400.5	460.2	570.6
average	61.95	273.7	388.4	400.5	460.6	570.55

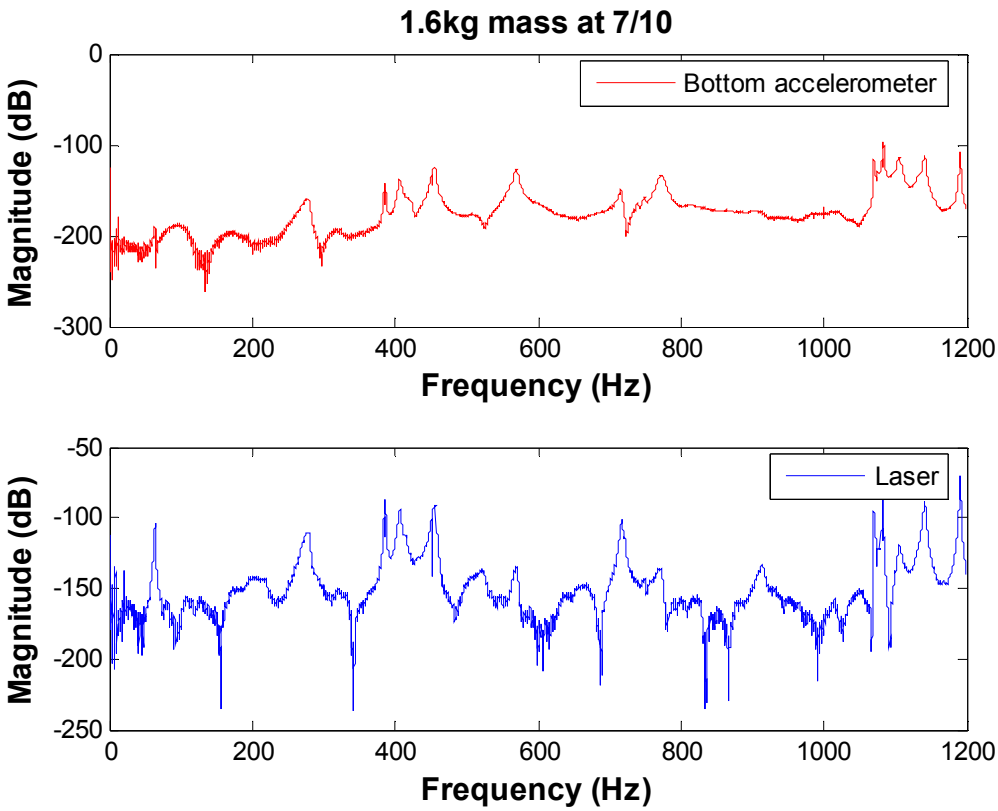

Figure II-19 FRF of 1.6 kg added mass at 7/10 of 1.87 from the bottom point

Table II-19 The resonant frequencies of 1.6 kg added mass at 7/10 of 1.87m from the bottom point

Sensor	Resonant frequencies (Hz)					
acc	63.32	277.4	386.5	407.8	455.4	569.9
laser	64.32	278.3	386.7	405.9	455.2	569.1
average	63.82	277.85	386.6	406.85	455.3	569.5

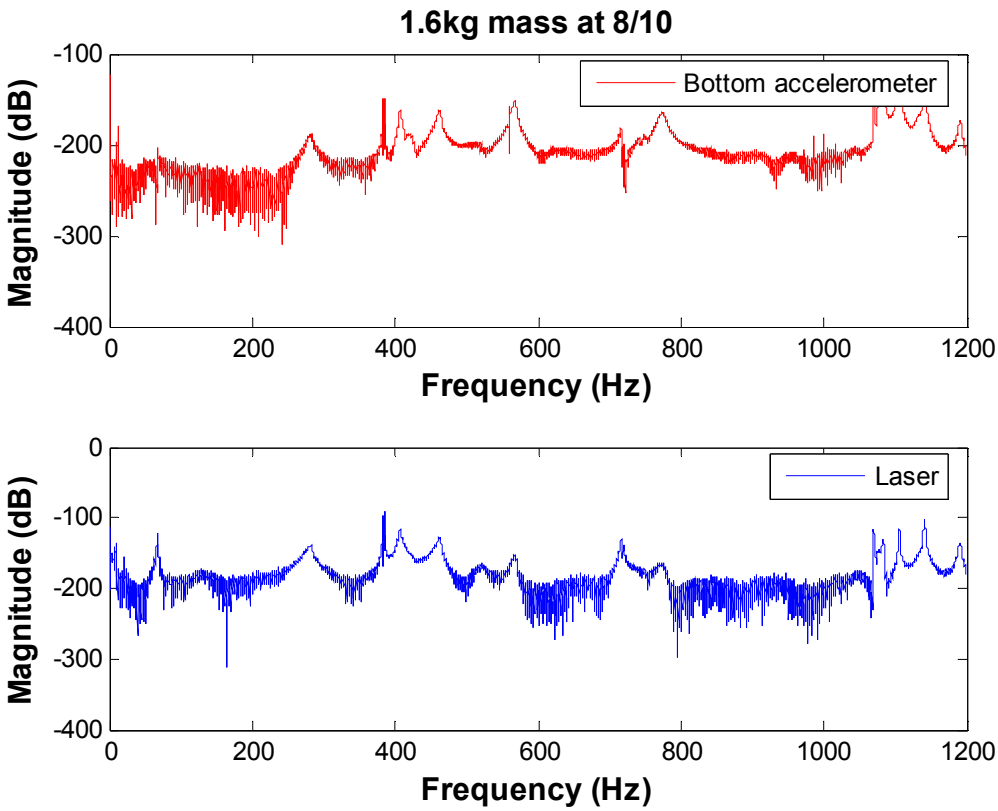

Figure II-20 FRF of 1.6 kg added mass at 8/10 of 1.87 from the bottom point

Table II-20 The resonant frequencies of 1.6 kg added mass at 8/10 of 1.87m from the bottom point

Sensor	Resonant frequencies (Hz)					
acc	67.98	283.2	384.8	407.4	462.4	568
laser	67.6	282.1	384.7	407.8	462.1	567
average	67.79	282.65	384.75	407.6	462.25	567.5

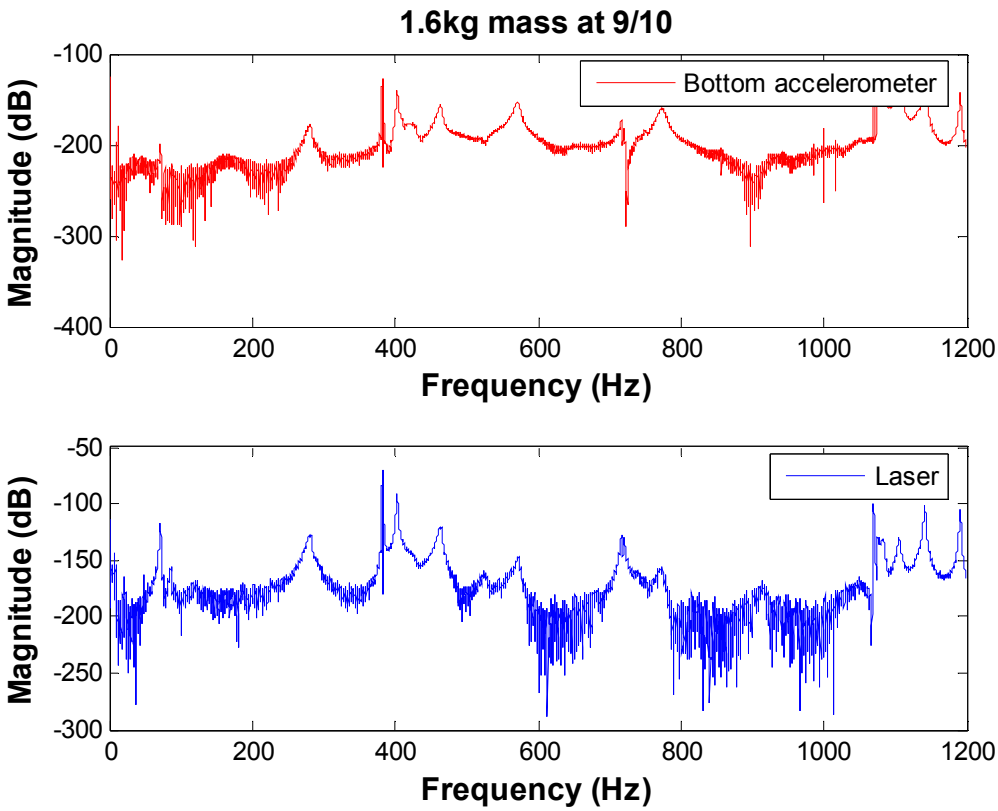

Figure II-21 FRF of 1.6 kg added mass at 9/10 of 1.87 from the bottom point

Table II-21 The resonant frequencies of 1.6 kg added mass at 9/10 of 1.87m from the bottom point

Sensor	Resonant frequencies (Hz)						
acc	71.26	-	280.9	383.5	402.5	463	567
laser	71.18	84.5	280.9	383.5	402.6	464	572
average	71.22	84.5	280.9	383.5	402.55	463.5	569.5

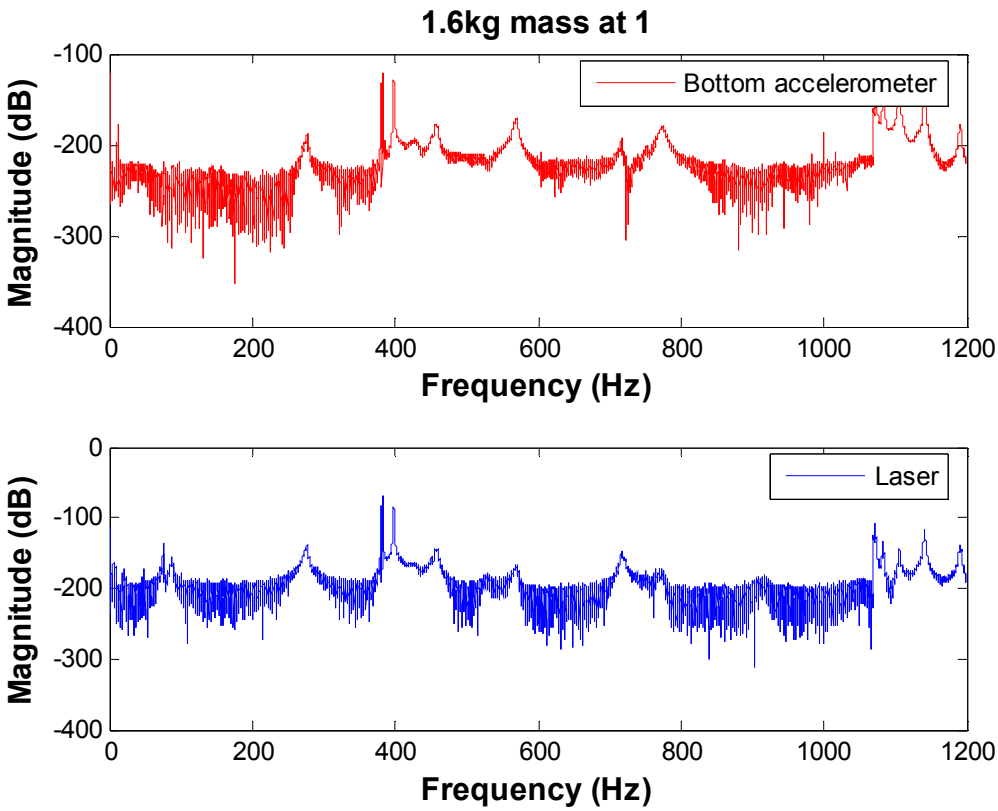

Figure II-22 FRF of 1.6 kg added mass the top point

Table II-22 The resonant frequencies of 1.6 kg added mass at the top point

Sensor	Resonant frequencies (Hz)						
acc	75.85	-	277.3	382.5	398	457.5	569.6
laser	75.57	86.14	276.1	382.5	398	457.3	570
average	75.71	86.14	276.7	382.5	398	457.4	569.8

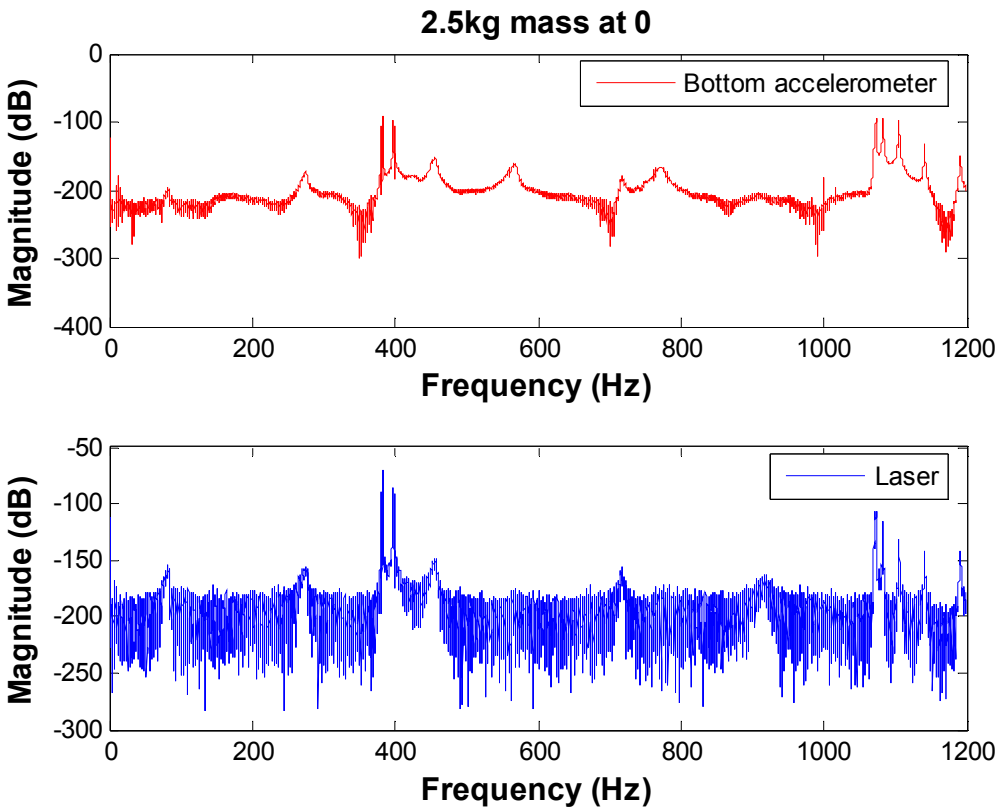

Figure II-23 FRF of 2.5 kg added mass at the bottom point

Table II-23 The resonant frequencies of 2.5 kg added mass at the bottom point

Sensor	Resonant frequencies (Hz)					
acc	82.7	275.1	382.5	397.6	456.2	567.7
laser	83.39	275.9	382.5	397.6	455.8	569.2
average	83.045	275.5	382.5	397.6	456	568.45

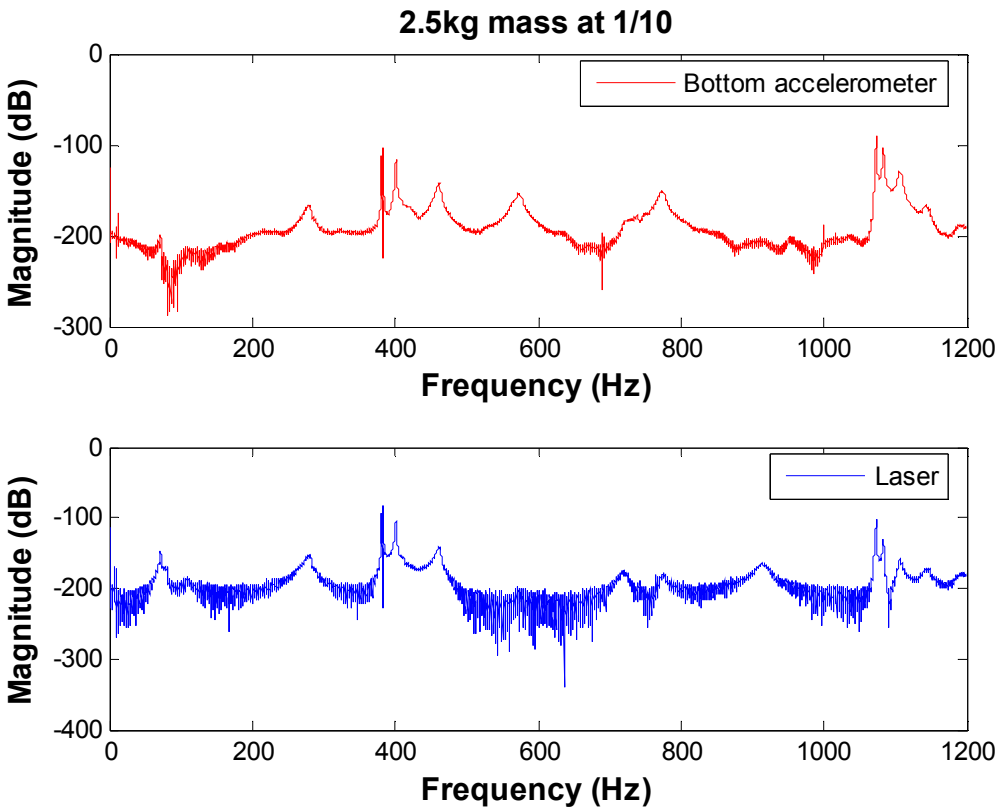

Figure II-24 FRF of 2.5 kg added mass at 1/10 of 1.87 from the bottom point

Table II-24 The resonant frequencies of 2.5kg added mass at 1/10 of 1.87m from the bottom point

Sensor	Resonant frequencies (Hz)					
acc	71.41	280.1	383.2	401.2	461	572.7
laser	71.79	280.4	383.2	401.5	461.7	572
average	71.6	280.25	383.2	401.35	461.35	572.35

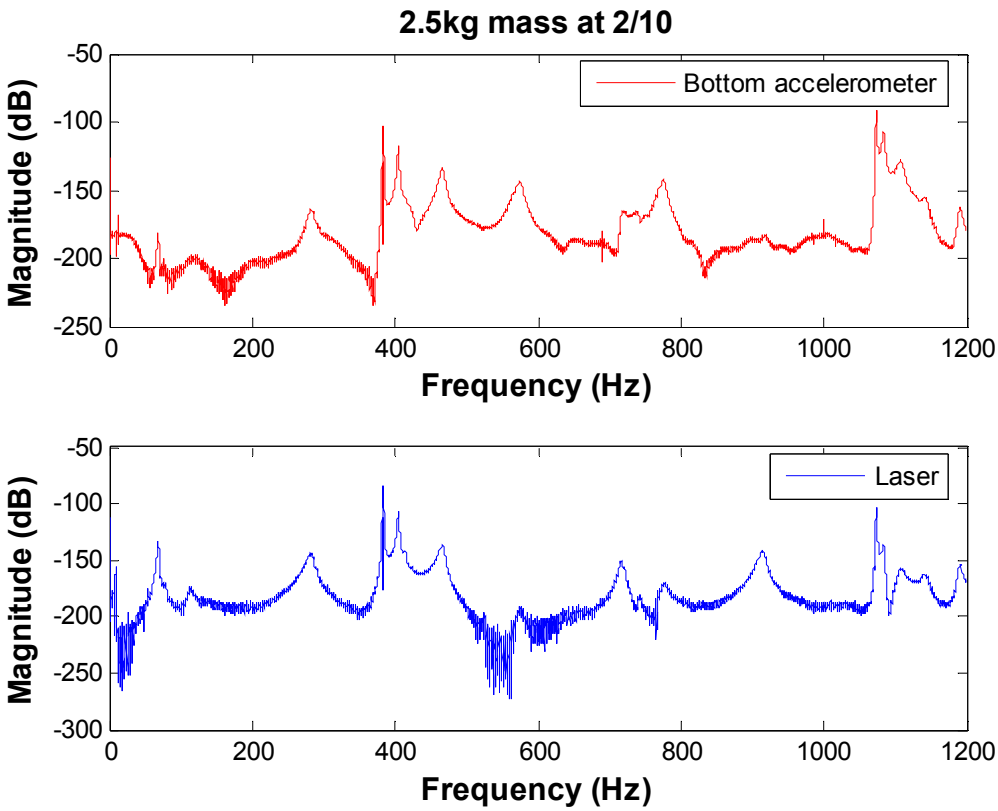

Figure II-25 FRF of 2.5 kg added mass at 2/10 of 1.87 from the bottom point

Table II-25 The resonant frequencies of 2.5kg added mass at 2/10 of 1.87m from the bottom point

Sensor	Resonant frequencies (Hz)						
acc	68.05	119.6	283.1	384	404.9	467	574.9
laser	68.13	114.5	283.2	384	404.9	465.2	572.7
average	68.09	117	283.15	384	404.9	466.1	573.8

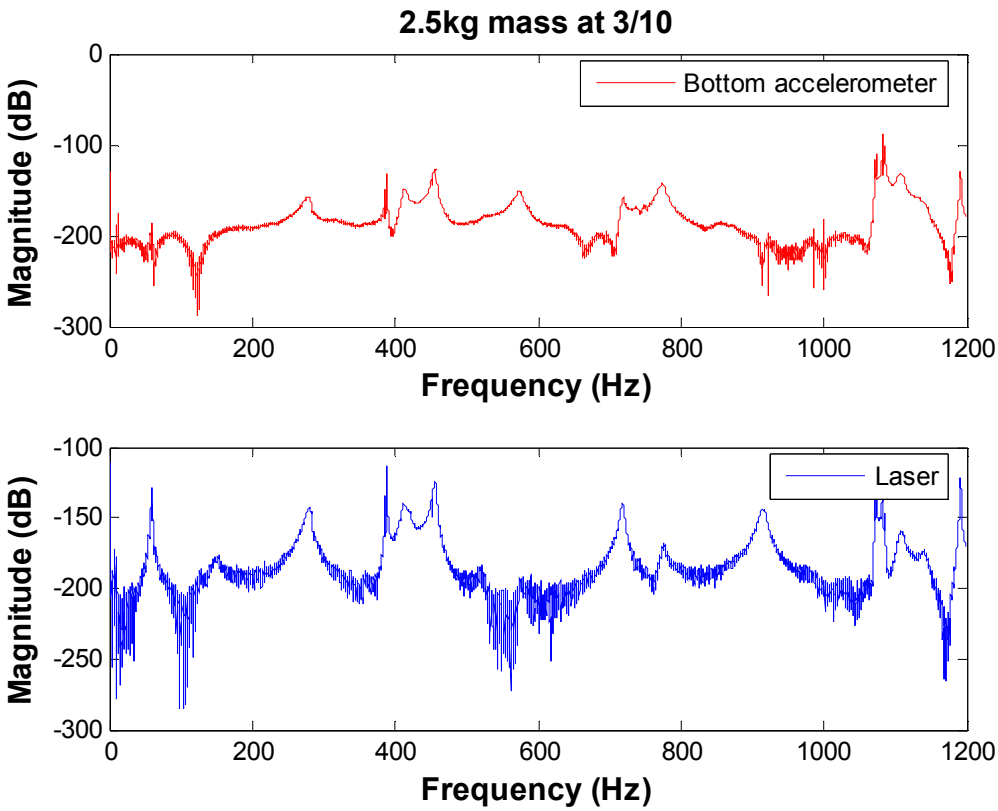

Figure II-26 FRF of 2.5 kg added mass at 3/10 of 1.87 from the bottom point

Table II-26 The resonant frequencies of 2.5kg added mass at31/10 of 1.87m from the bottom point

Sensor	Resonant frequencies (Hz)						
acc	59.43	-	279.1	388.3	412.8	456.2	575.1
laser	59.36	147.5	279.5	388.3	412.6	456.5	575
average	59.395	147.5	279.3	388.3	412.7	456.35	575.05

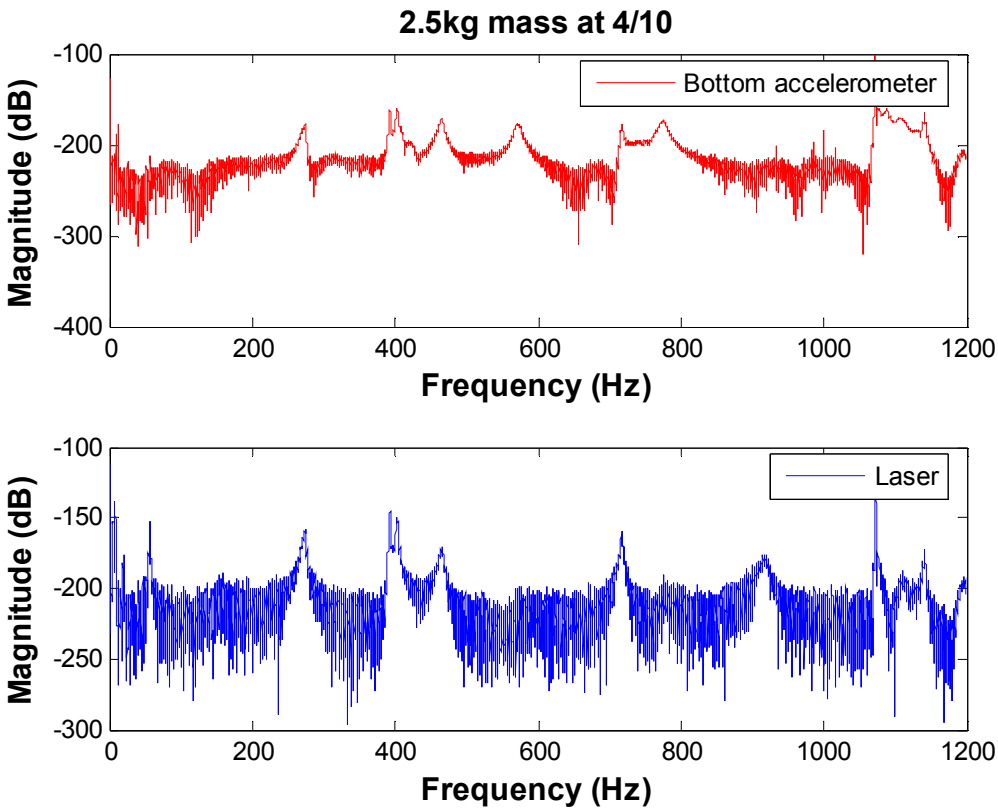

Figure II-27 FRF of 2.5 kg added mass at 4/10 of 1.87 from the bottom point

Table II-27 The resonant frequencies of 2.5kg added mass at 4/10 of 1.87m from the bottom point

Sensor	Resonant frequencies (Hz)					
acc	56.92	274	392.9	403.4	465.1	573
laser	56.84	274.7	392.8	403.1	463.7	573
average	56.88	274.35	392.85	403.25	464.4	573

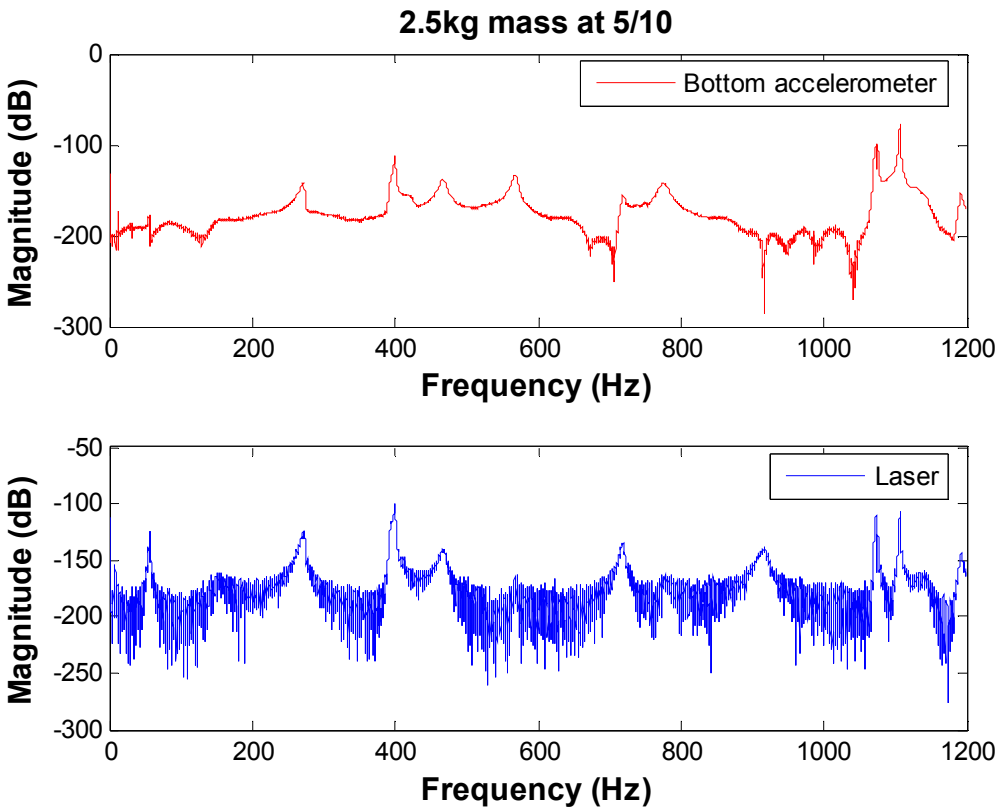

Figure II-28 FRF of 2.5 kg added mass at 5/10 of 1.87 from the bottom point

Table II-28 The resonant frequencies of 2.5kg added mass at 5/10 of 1.87m from the bottom point

Sensor	Resonant frequencies (Hz)						
acc	56.15	-	271.1	399.9	-	467.7	568.4
laser	56.53	160	272.1	399.9	-	467.3	570
average	56.34	160	271.6	399.9	-	467.5	569.2

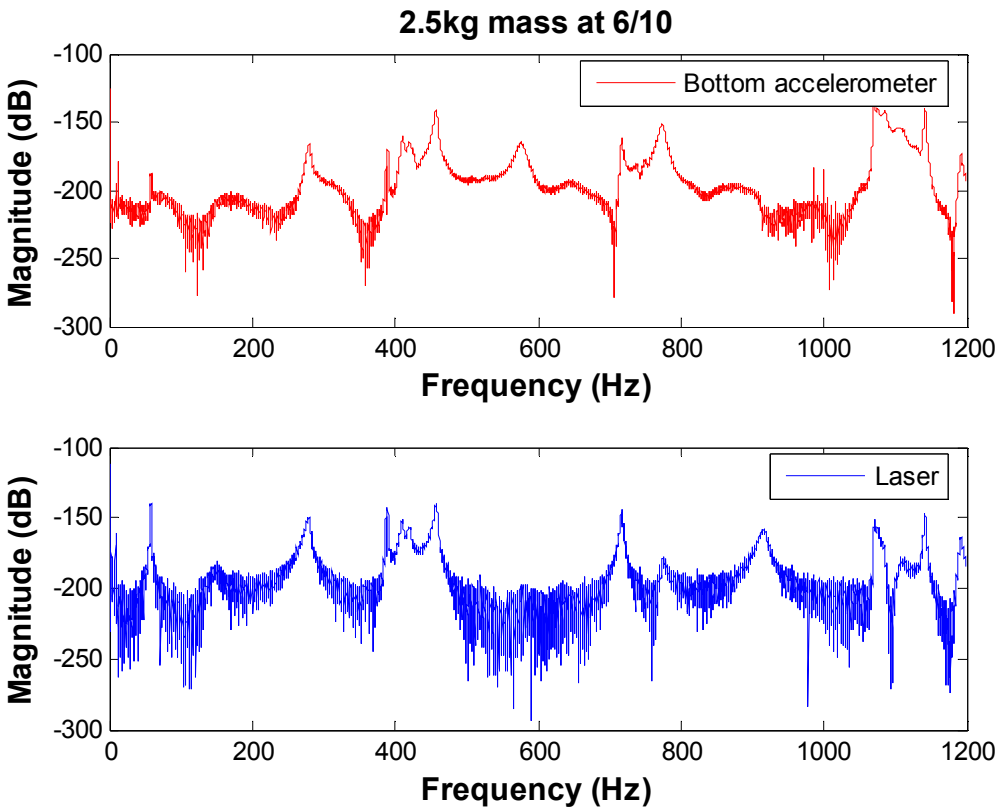

Figure II-29 FRF of 2.5 kg added mass at 6/10 of 1.87 from the bottom point

Table II-29 The resonant frequencies of 2.5kg added mass at 6/10 of 1.87m from the bottom point

Sensor	Resonant frequencies (Hz)							
acc	58.36	-	279.9	389.9	410.5	420	456.8	576.6
laser	57.98	150	279.1	389.9	409.5	419.7	457.5	576
average	58.17	150	279.5	389.9	410	419.85	457.15	576.3

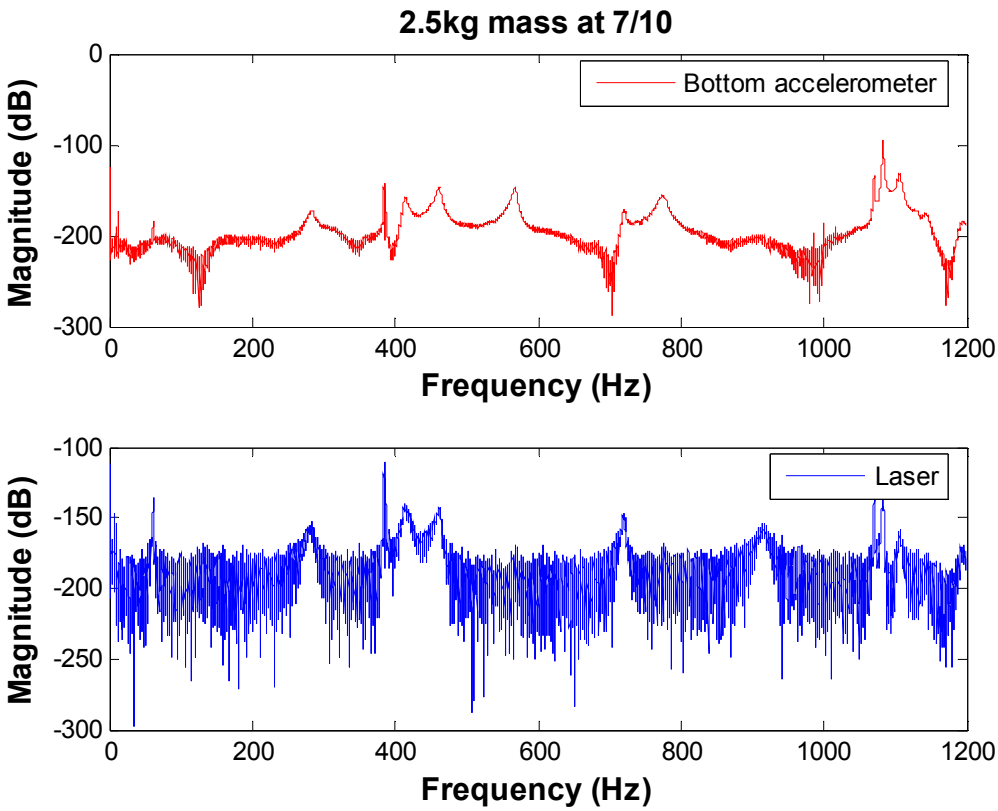

Figure II-30 FRF of 2.5 kg added mass at 7/10 of 1.87 from the bottom point

Table II-30 The resonant frequencies of 2.5kg added mass at 7/10 of 1.87m from the bottom point

Sensor	Resonant frequencies (Hz)					
acc	61.34	283.3	386.4	414.8	462.8	567.8
laser	61.57	283.1	386.4	414.3	461.7	568
average	61.455	283.2	386.4	414.55	462.25	567.9

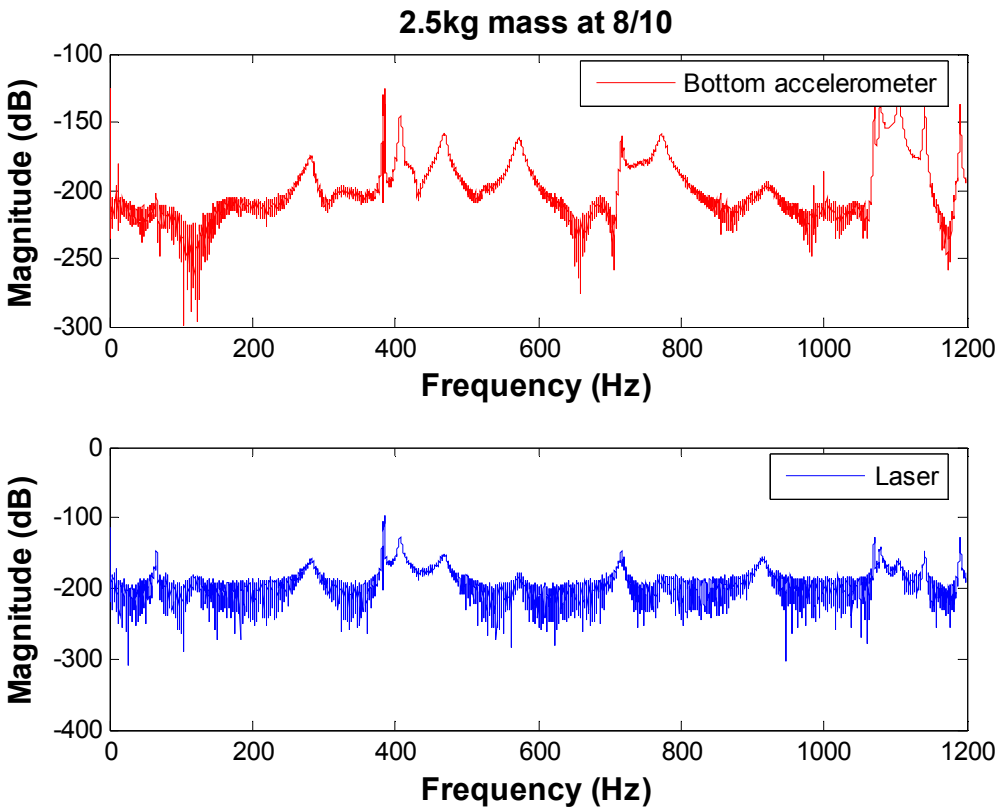

Figure II-31 FRF of 2.5 kg added mass at 8/10 of 1.87 from the bottom point

Table II-31 The resonant frequencies of 2.5kg added mass at 8/10 of 1.87m from the bottom point

Sensor	Resonant frequencies (Hz)					
acc	66.32	282.5	384.5	407.1	468.3	574.6
laser	66.3	283.4	384.5	407	469.1	575
average	66.31	282.95	384.5	407.05	468.7	574.8

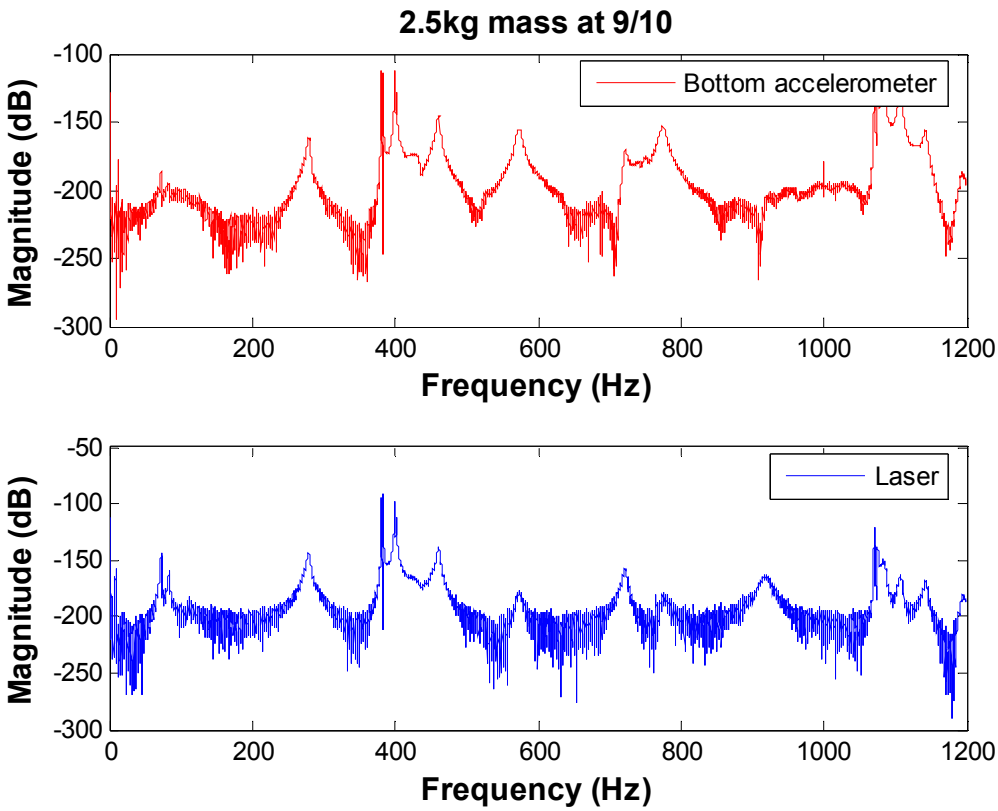

Figure II-32 FRF of 2.5 kg added mass at 9/10 of 1.87 from the bottom point

Table II-32 The resonant frequencies of 2.5kg added mass at 9/10 of 1.87m from the bottom point

Sensor	Resonant frequencies (Hz)						
acc	72.25	83.01	278.9	383.1	397.9	461.4	573.6
laser	72.25	84.06	279.8	383	397.9	461.1	573.3
average	72.25	83.535	279.35	383.05	397.9	461.25	573.45

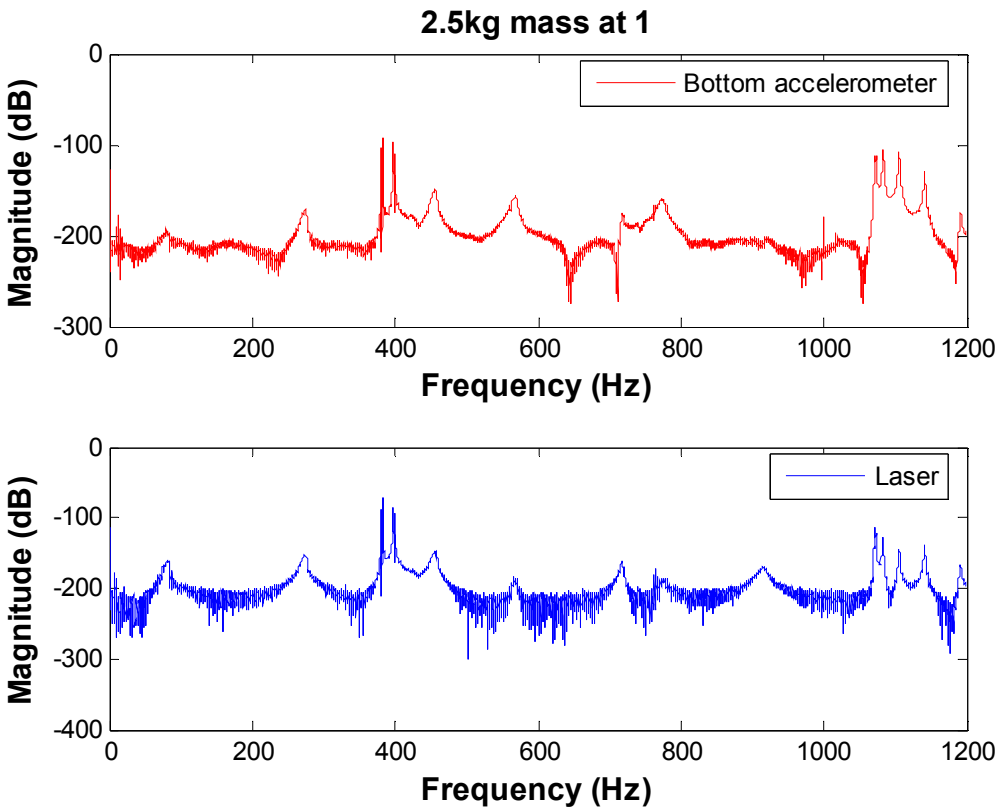

Figure II-33 FRF of 2.5 kg added mass the top point

Table II-33 The resonant frequencies of 2.5kg added mass the top point

Sensor	Resonant frequencies (Hz)					
acc	80.34	274.9	382.5	397.7	455.9	568.1
laser	83.39	274.2	382.5	397.7	456.1	569.2
average	81.865	274.55	382.5	397.7	456	568.65

Appendix III Data of damping ratio of induced flour at bottom support point

Table III-1 79 Hz of natural logarithm slope and damping ratio

Amount of flour (cups)	Slope of the fitting natural logarithm data (79)				79Hz damping ratio
	Acc1	Acc2	Laser	Average	
0	0.70	0.72	0.71	0.71	0.001431
0.1	0.73	0.75	0.80	0.76	0.001532
2	0.70	0.68	0.74	0.71	0.001424
4	0.59	0.64	0.62	0.62	0.001243
6	0.75	0.71	0.68	0.71	0.001438
8	0.80	0.85	0.83	0.83	0.001666

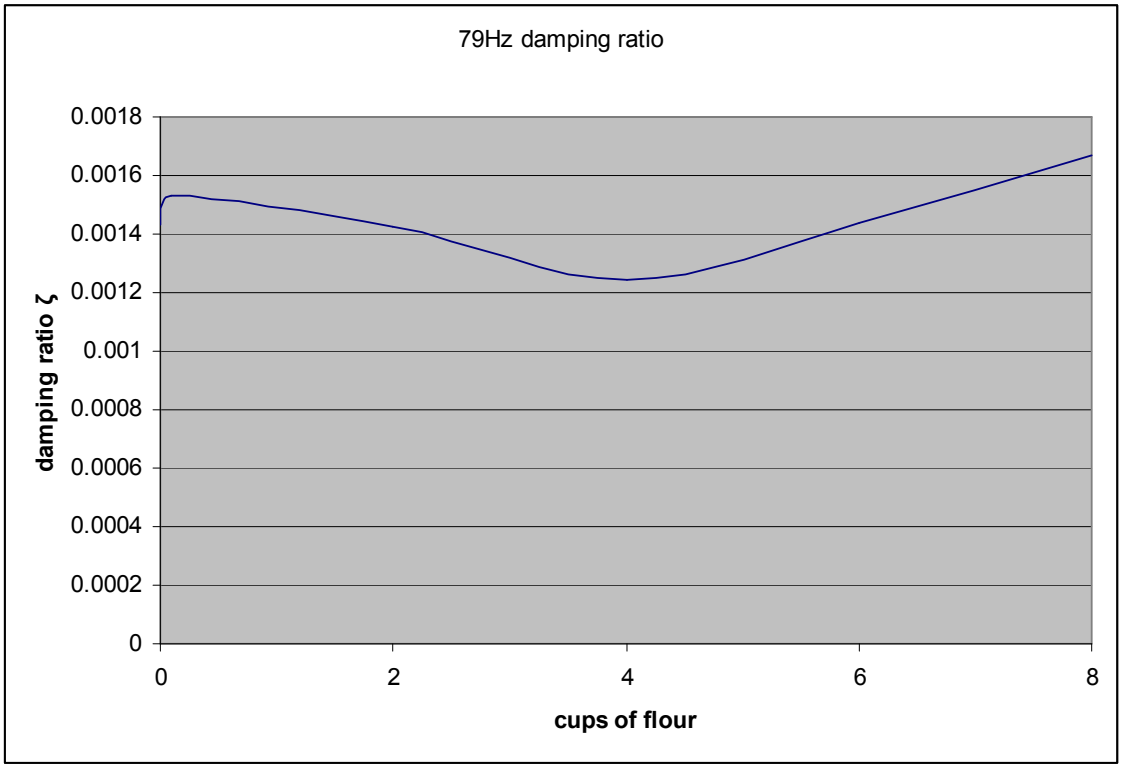

Figure III-1 79 Hz damping ratio with amount of flour

Table III-2 270 Hz of natural logarithm slope and damping ratio

Amount of flour (cups)	Slope of the fitting natural logarithm data(270)				270Hz damping ratio
	Acc1	Acc2	Laser	Average	
0	15.00	16.00	16.00	15.67	0.0092396
0.1	15.00	16.00	14.00	15.00	0.00884643
2	30.00	28.00	32.00	30.00	0.01769285
4	55.00	54.00	52.00	53.67	0.03165055
6	69.00	73.00	71.00	71.00	0.04187308
8	72.00	76.00	72.00	73.33	0.04324919

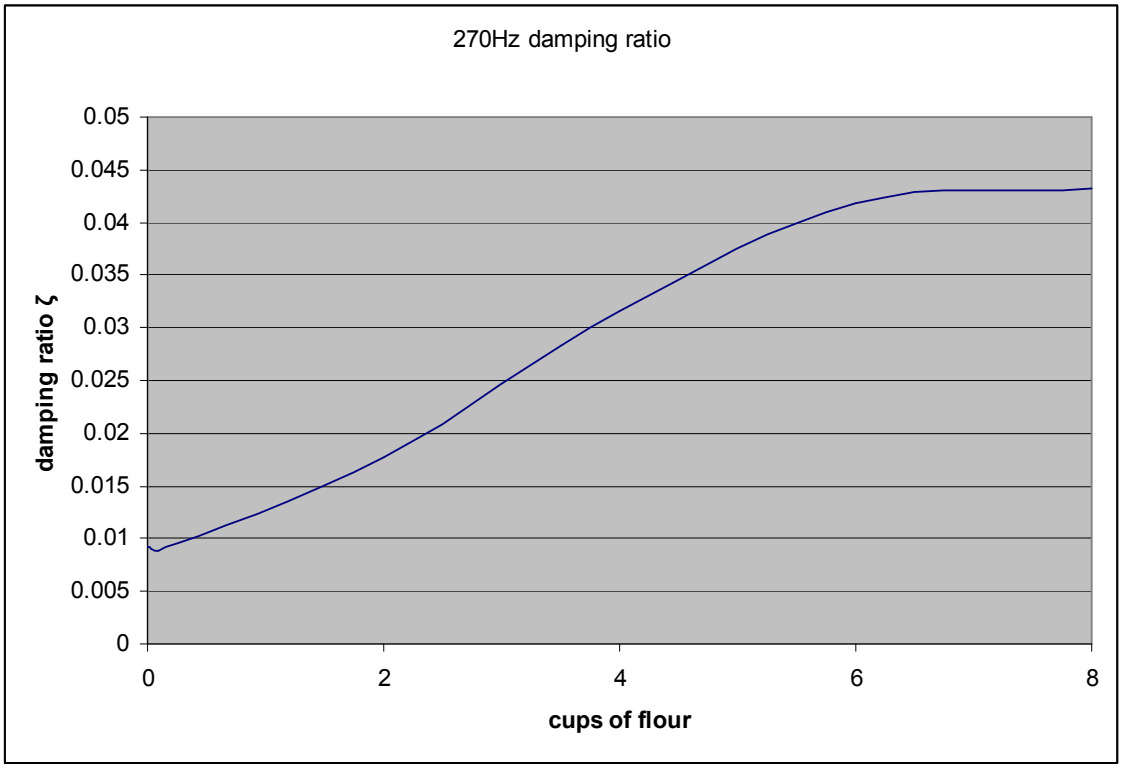

Figure III-2 270 Hz damping ratio with amount of flour

Table III-3 380 Hz of natural logarithm slope and damping ratio

Amount of flour (cups)	Slope of the fitting natural logarithm data(380)				380Hz damping ratio
	Acc1	Acc2	Laser	Average	
0	0.40	0.43	0.40	0.41	0.00017181
0.1	0.60	0.70	0.56	0.62	0.00025981
2	1.90	2.30	2.20	2.13	0.00089395
4	4.30	4.50	4.80	4.53	0.00189965
6	17.00	17.00	17.00	17.00	0.0071237
8	19.00	18.00	18.00	18.33	0.00768242

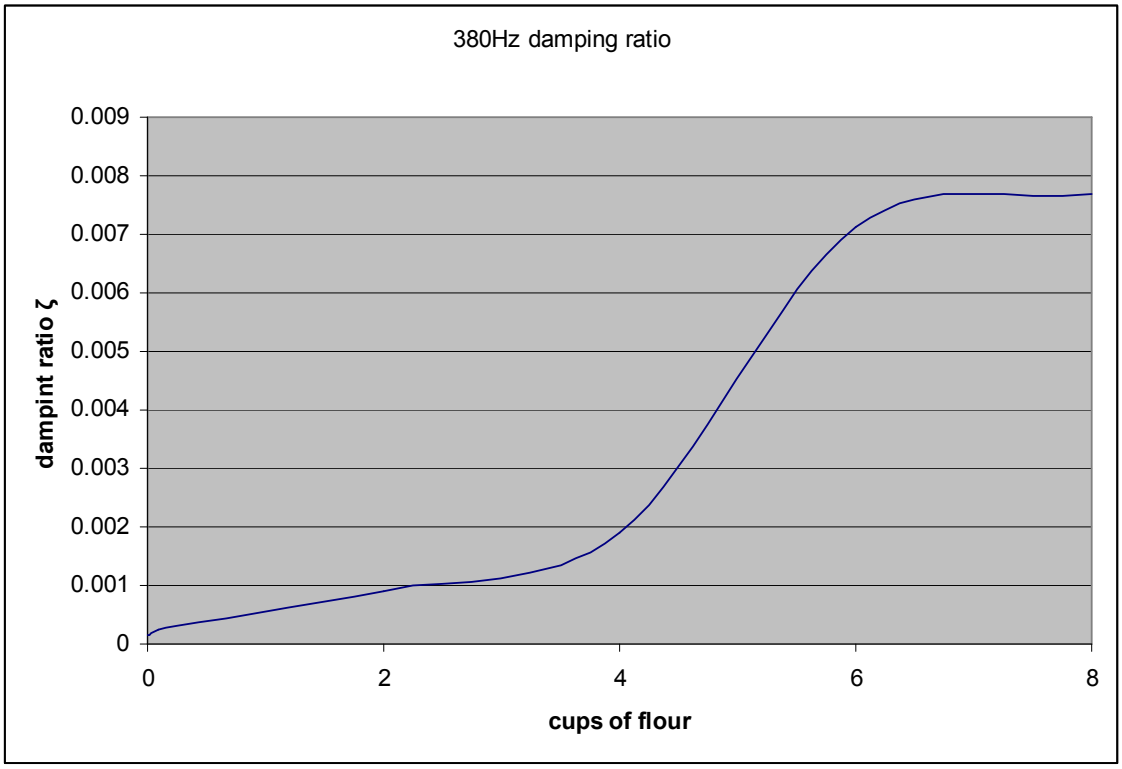

Figure III-3 380 Hz damping ratio with amount of flour

Table III-4 398 Hz of natural logarithm slope and damping ratio

Amount of flour (cups)	Slope of the fitting natural logarithm data(398)				398Hz damping ratio
	Acc1	Acc2	Laser	Average	
0	0.55	0.53	0.55	0.54	0.00021738
0.1	0.60	0.60	0.59	0.60	0.00023872
2	12.00	14.00	11.00	12.33	0.00493444
4	24.00	24.00	23.00	23.67	0.00946879
6	29.00	27.00	26.00	27.33	0.01093578
8	34.00	34.00	36.00	34.67	0.01386977

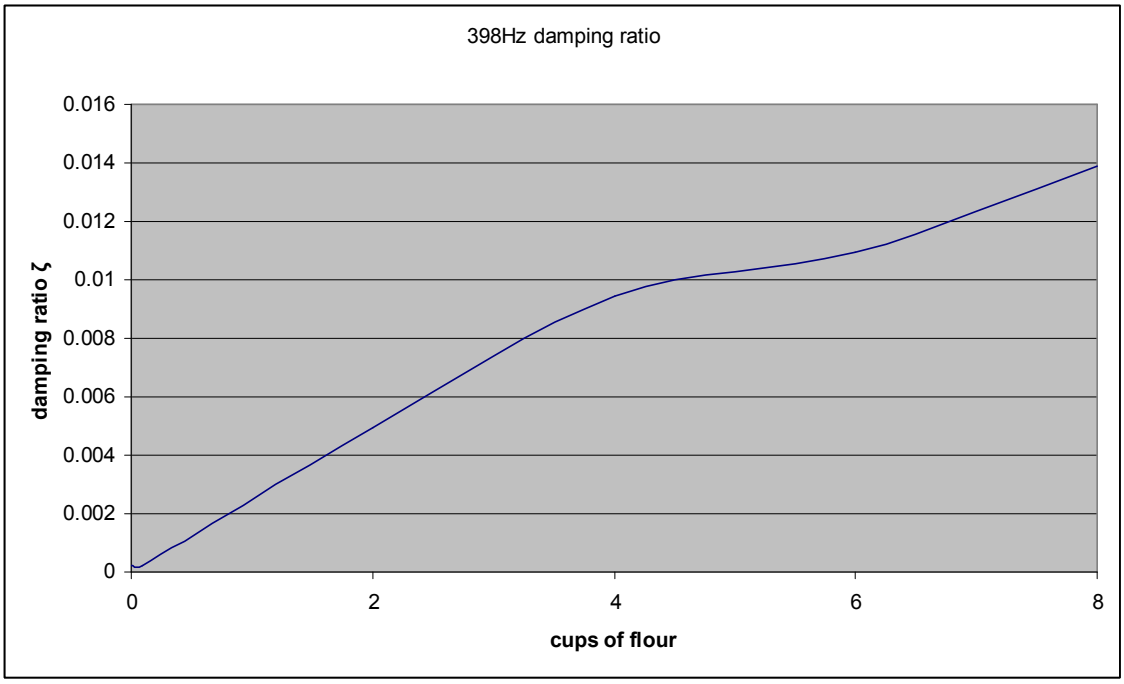

Figure III-4 398 Hz damping ratio with amount of flour

Table III-5 456 Hz of natural logarithm slope and damping ratio

Amount of flour (cups)	Slope of the fitting natural logarithm data(456)				456Hz damping ratio
	Acc1	Acc2	Laser	Average	
0	11.00	9.20	11.00	10.40	0.00363169
0.1	10.00	9.80	9.80	9.87	0.00344545
2	25.00	23.00	24.00	24.00	0.00838082
4	38.00	41.00	39.00	39.33	0.01373524
6	42.00	43.00	45.00	43.33	0.01513204
8	50.00	50.00	52.00	50.67	0.01769285

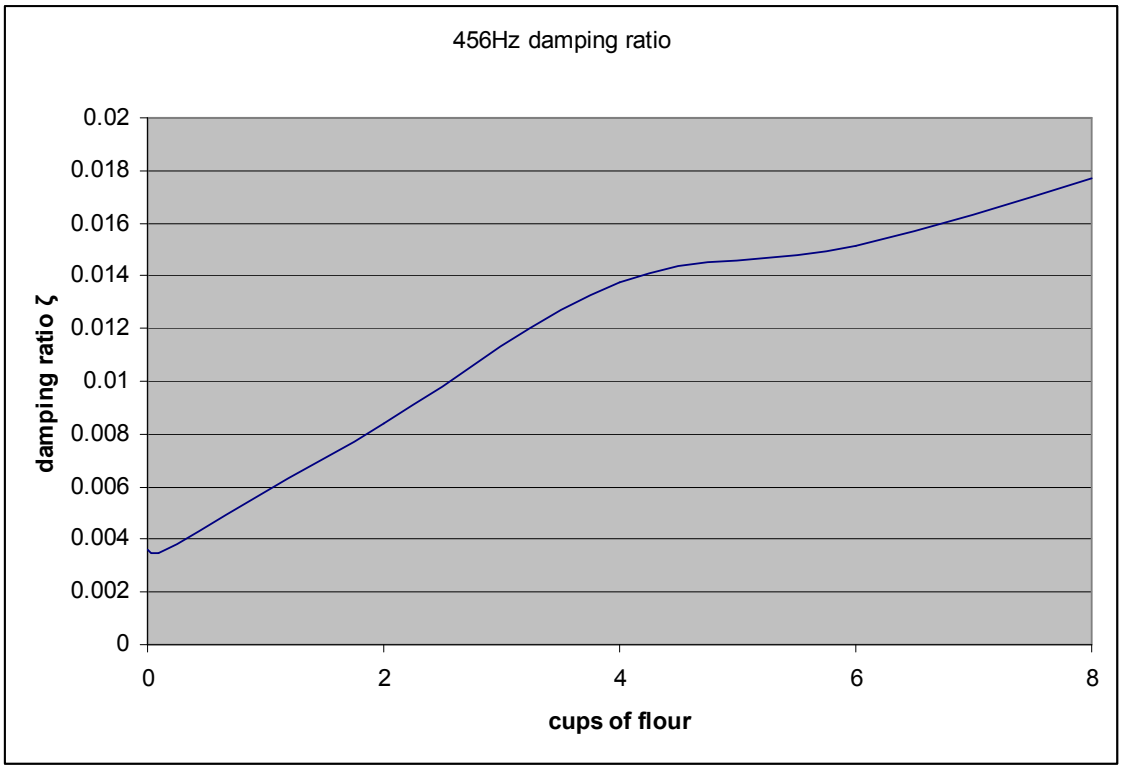

Figure III-5 456 Hz damping ratio with amount of flour

Table III-6 568 Hz of natural logarithm slope and damping ratio

Amount of flour (cups)	Slope of the fitting natural logarithm data(568)				568Hz damping ratio
	Acc1	Acc2	Laser	Average	
0	21.00	20.00	21.00	20.67	0.00579379
0.1	19.00	20.00	18.00	19.00	0.00532655
2	30.00	31.00	27.00	29.33	0.00822344
4	41.00	39.00	40.00	40.00	0.01121378
6	46.00	45.00	45.00	45.33	0.01270895
8	52.00	50.00	53.00	51.67	0.01448447

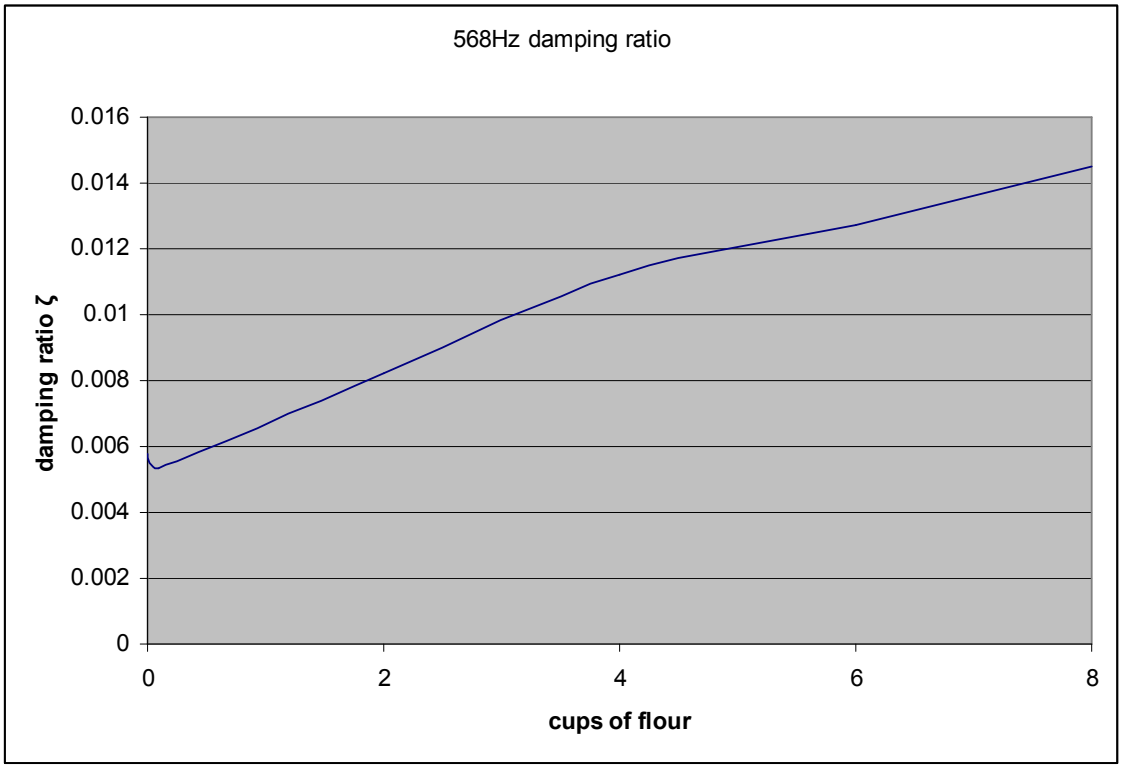

Figure III-6 715 Hz damping ratio with amount of flour

Table III-7 715 Hz of natural logarithm slope and damping ratio

Amount of flour (cups)	Slope of the fitting natural logarithm data(715)				715Hz damping ratio
	Acc1	Acc2	Laser	Average	
0	4.10	3.90	4.00	4.00	0.00089083
0.1	4.10	3.90	4.20	4.07	0.00090568
2	13.00	15.00	12.00	13.33	0.00296943
4	20.00	18.00	18.00	18.67	0.0041572
6	25.00	23.00	24.00	24.00	0.00534497
8	26.00	28.00	26.00	26.67	0.00593886

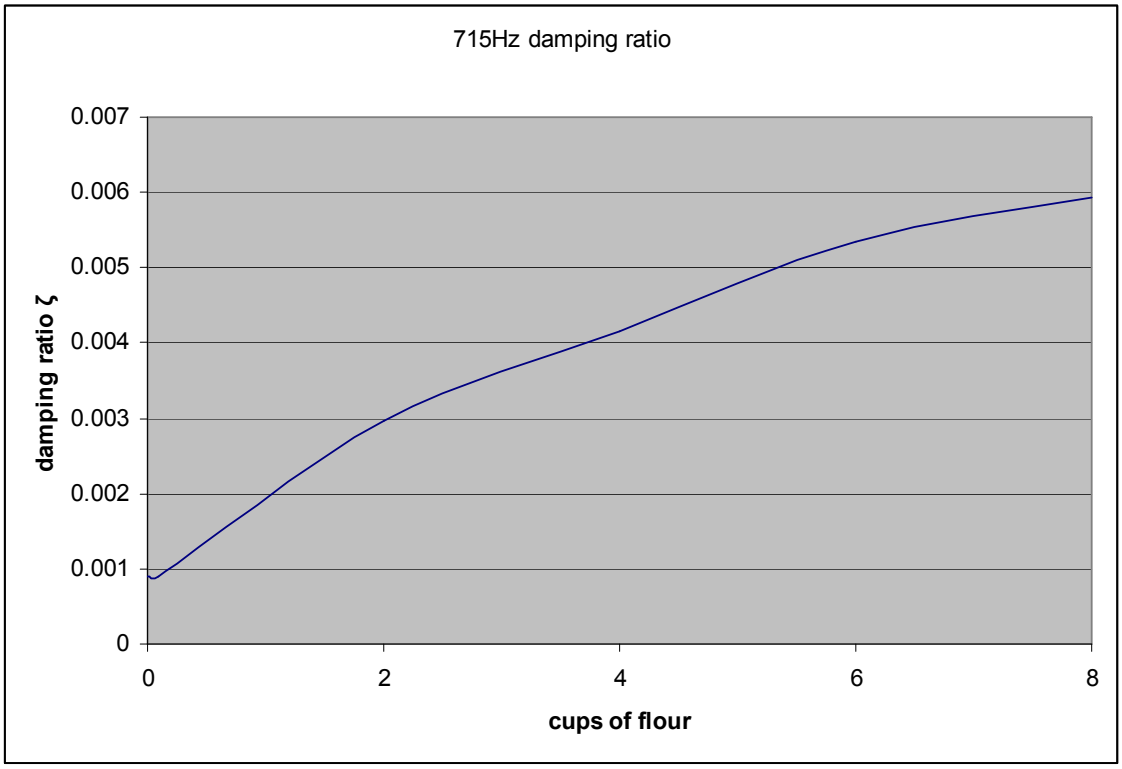

Figure III-7 715 Hz damping ratio with amount of flour

Table III-8 775 Hz of natural logarithm slope and damping ratio

Amount of flour(cups)	Slope of the fitting natural logarithm data(775)				775Hz damping ratio
	Acc1	Acc2	Laser	Average	
0	23.00	25.00	22.00	23.33	0.004794
0.1	25.00	24.00	22.00	23.67	0.00486268
2	26.00	24.00	22.00	24.00	0.00493117
4	27.00	26.00	26.00	26.33	0.00541059
6	30.00	32.00	31.00	31.00	0.00636943
8	40.00	41.00	40.00	40.33	0.0082871

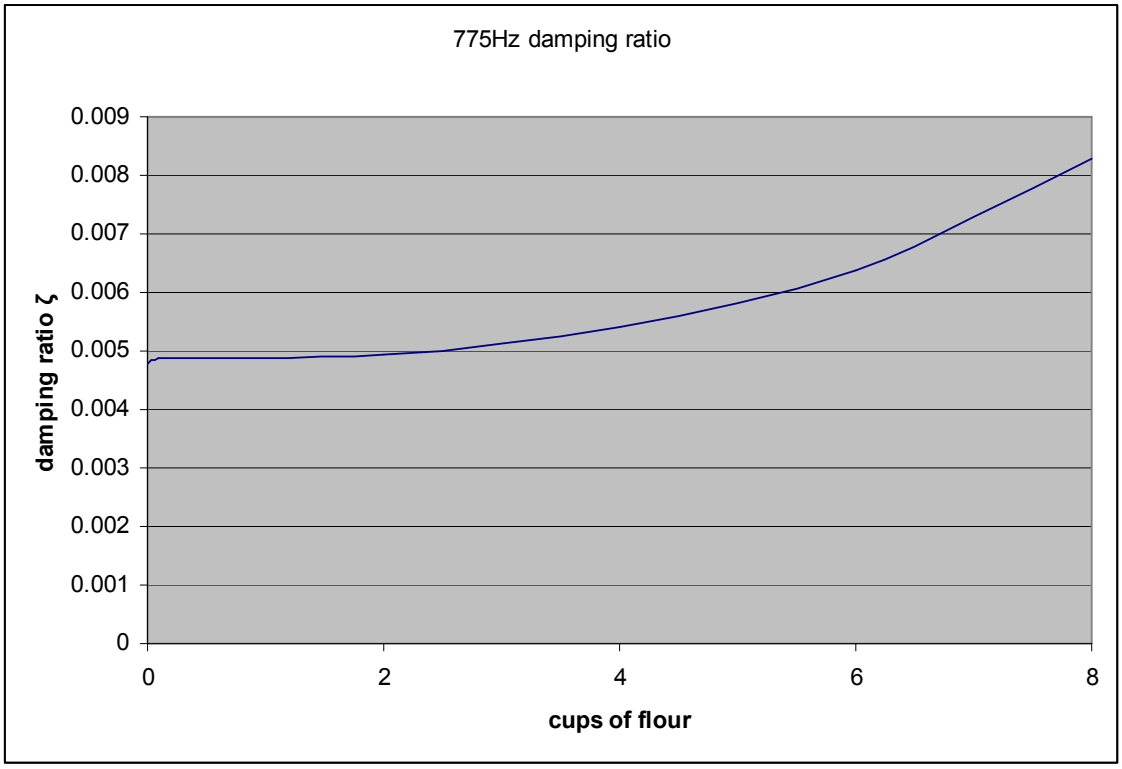

Figure III-8 775 Hz damping ratio with amount of flour

References

1. Masters, K. (1991). Spray drying handbook, Longman Scientific & Technical, Wiley.
2. Prakash, S., Datta, N., Deeth, H. C. (2005). Methods of detecting fouling caused by heating of milk. *Food reviews international Taylor & Francis Inc.* 21, 267-293.
3. Spray drying and spray dryers. Retrieved March 5, 2006, from http://class.fst.ohio-state.edu/Dairy_Tech/14Spraydrying.htm.
4. Othmer, K. (1978). A to alkamolamines. A Wiley Interscience Publication. NY.
5. Heumann, W.L. (1991). Cyclone separators: A family affair. *Chemical Engineering Monographs*. 98, 118-120.
6. Columbus, E.P. (1993). Series cyclone arrangements to reduce gin emissions. *Trans. of ASAE*. 36, 545-550.
7. Chen, X.D., Lake, R., Jebson, S. (1993). Study of milk powder deposition on a large industrial dryer. *Food and Bioproducts Processing: Transactions of the Institution of Chemical Eng.* 71, 180-186.
8. Rennie, P.R., Chen, X. D., Mackereth, A. R. (1998). Adhesion characteristics of whole milk powder to a stainless steel surface. *Powder Technology*. 97, 191-199.
9. Rennie, P.R., Chen, X. D., Hargreaves, C., Mackereth, A. R. (1999). A study of the cohesion of dairy powders. *Journal of Food Engineering*. 39, 277-284.
10. Chong, L.V., Chen, X. D. (1999). A mathematical model of the self-heating of spray-dried food powders containing fat, protein, sugar and moisture. *Chemical Engineering Science*. 54, 4165-4178.
11. Storch, O., Albrecht, J., Hejma, J. (1979). Industrial separators for gas cleaning. *Chemical Engineering Monographs*.
12. Papadakis, E.P. (1999). Ultrasonic instruments & device reference for modern instrumentation, techniques, and technology.
13. Cartz, L. (1995). Nondestructive testing. ASM International.
14. Andersen, M.I. (1997). Ultrasonic instrumentation for on-line monitoring of solid deposition in pipes. *SPE Production Operations Symposium*, 425-431.
15. Gunarathne, G.P.P., Keatch, R. W. (1996). Novel techniques for monitoring and enhancing dissolution of mineral deposits in petroleum pipelines. *Ultrasonics*. 34, 411-419.
16. Gunarathne, G.P.P. (1997). Measurement and monitoring techniques for scale deposits in petroleum pipelines. *IEEE Instrumentation and Measurement Technology Conference Ottawa, Canada*.
17. Withers, P.M. (1994). Ultrasonic sensor for the detection of fouling in UHT processing plants. *Food control*. 5, 67-72.
18. Withers, P.M. (1996). Ultrasonic, acoustic and optical techniques for the non-invasive detection of fouling in food processing equipment. *Trends in Food Science & Technology*. 7, 293-298.
19. Hay, T.R., Rose, J. L. (2003). Fouling detection in the food industry using ultrasonic guided waves. *Food control*. 14, 481-488.
20. Siqueira, M.H.S., Gatts, C. E. N., Da Silva, R. R., Rebello, J. M. A. (2004). The use of ultrasonic guided waves and wavelets analysis in pipe inspection. *Ultrasonics*. 41, 785-797.
21. Lohr, K.R., Rose, J. L. (2003). Ultrasonic guided wave and acoustic impact methods for pipe fouling detection. *Journal of Food Engineering*. 56, 315-324.

22. Moussaoui, M.E., Chati, F., Leon, F., Klauson, A. (2005). Guided wave attenuation due to deposits on the pipe wall. *IEEE Ultrasonics Symposium*, 1007-1010.
23. Cawley, P., Fromme, P., Wilcox, P., Lowe. M. (2004). A Guided wave array for structural health monitoring. *2nd European Workshop on Structural Health Monitoring, Amazeum Conference Centre at Deutsches Museum, Munich, Germany*.
24. Foulkes, M.G., De Clerck, J. P., Singh, R. (2003). Vibration characteristics of cardboard inserts in shells. *SAE International*. 112, 1718-1725
25. Jenkin, P. (2003). On pattern recognition for vibration analysis using Fourier components. School of Engineering. London, Cranfield University. 89.
26. Gelman, L., Petrunin, I., Sanderson, M., Thompson, C. (2003). Vibro-acoustic deposit detection in pipelines. *Insight*. 45, 466-470.
27. Babitsky, V.I., Veprik, A. M. (1993). Damping of beam forced vibration by a moving washer. *Journal of Sound and Vibration*. 166, 77-85.
28. Shahruz, S.M. (1994). Comments on "Damping of beam forced vibration by a moving washer". *Journal of Sound and Vibration*. 178, 141-143.
29. Donskoy, D.M., Sutin, A. M. (1998). Vibro-acoustic modulation nondestructive evaluation technique. *Journal of Intelligent Material Systems and Structures*. 9, 765-771.
30. Clarence, W.S. (2000). Vibration fundamentals and practice. CRC Press LLC.
31. Leissa, A.W. (1993). Vibration of shells. Acoustical Society of America.
32. Yu, Y.Y. (1955). Free vibrations of thin cylindrical shells having finite lengths with freely supported and clamped edges. *Journal of Applied Mechanics* 22, 547–552.
33. B. Schafer, O. (1985). Free vibrations of a gravity-loaded clamped-free beam. *Ingenieur-Archiv*. 55, 66-80.
34. Saito, H., Chonan, S. (1982). Vibrations of vertical rods with an attached mass. *Journal of Sound and Vibration*. 84, 519-527.
35. Mously, M.E. (2003). Fundamental natural frequencies of thin cylindrical shells: a comparative study *Journal of Sound and Vibration*. 264, 1167-1186
36. Wang, C., Lai, J. C. S. (2000). Prediction of natural frequencies of finite length circular cylindrical shells. *Applied Acoustics*. 59, 385-400.
37. Li, B.R., Wang, X .Y. (2005). Study on applicability of modal analysis of thin finite length cylindrical shells using wave propagation approach. *Journal of Zhejiang University Science*. 6A, 1122-1127.
38. Courant, R. (1943). Variational method for the solutions of problems of equilibrium and variations. *Bulletin of the American Mathematical Society*.
39. *ABAQUS/CAE User's Manual*.
40. Seto, W.W. (1964). Schaum's outline of theory and problems of mechanical vibrations. New York, McGraw-Hill.
41. Ozkaya, E., Pakdemirli, M., Oz, H. R. (1997). Non-linear vibrations of a beam-mass system under different boundary conditions. *Journal of Sound and Vibration*. 199, 679-96.
42. De Rosa, M.A., Ascoli, S., Nicastro, S. (1996). Exact dynamic analysis of beam-mass systems. *Journal of Sound and Vibration*. 196, 529-533.
43. Low, K.H. (2003). Natural frequencies of a beam-mass system in transverse vibration: Rayleigh estimation versus eigenanalysis solutions. *International Journal of Mechanical Sciences*. 45, 981-93.
44. Maurizi, M.J., Belles, P. M. (1991). Natural frequencies of the beam-mass system: comparison of the two fundamental theories of beam vibrations. *Journal of Sound and Vibration*. 150, 330-334.

45. Maurizi, M.J., Belles, P. M. (1992). An additional evaluation of free vibrations of beam-mass systems. *Journal of Sound and Vibration*. 154, 182-6.
46. Ozkaya, E., Pakdemirli, M. (1999). Non-linear vibrations of a beam-mass system with both ends clamped. *Journal of Sound and Vibration*. 221, 491-503.
47. Raju, K.K., Venkateswara R. G. (1976). Non-linear vibrations of beams carrying a concentrated mass. *Journal of Sound and Vibration*. 48, 445-449.
48. Yoo, H.H., Seo. S., Huh, K. (2002). The effect of a concentrated mass on the modal characteristics of a rotaing cantilever beam. *Mechanical Engineering Science*. 216, 151-163.
49. McConnell, K.G. (1995). Vibration testing theory and practice. A Wiley-Interscience Publication.
50. Silva, C.W.d. (2000). Vibration fundamentals and practice. CRC Press LLC.
51. Tongue, B.H. (2002). Principles of vibration. New York, Oxford University Press.
52. Doebelin, E.O. (2004). Measurement systems application and design. McGraw-Hill.
53. Frequency response. Retrieved June 10, 2006, from http://zone.ni.com/devzone/cda/tut/p/id/1082.
54. McGillem, C. (1984). Continuous and discrete signal and system analysis. HRW.
55. DAQ 6023E/6024E/6025E User Manual.
56. Lüke, H.D. (1999). The origins of the sampling theorem. *IEEE Communications Magazine*, 106–108.
57. Bracewell, R.N. (1986). The Fourier transform and its applications. McGraw-Hill, Inc., USA.
58. Adhikari, S. (2000). Damping models for structural vibrations. Cambridge University.
59. Lamarque, C.H., Pernot, S., Cuer, A. (2000). Damping identification in multi-degree-of -freedom systems via a wavelet-logarithmic decrement - Part 1 theory. *Sound and Vibration*. 235, 361-374.
60. Hans, S., Ibraim, E., Pernot, S., Boutin, C., Lamarque, C. H. (2000). Damping identification in multi-degree-of-freedom system via a wavelet-logarithmic decrement--part 2: study of a civil engineering building. *Journal of Sound and Vibration*. 235, 375-403.
61. Iglesias, A.M. (2000). Investigating various modal analysis extraction techniques to estimate damping ratio. Mechanical engineering. Virginial Polytechnic Institute and State University. 126.
62. Karjalainen, M., Antsalo, P., Peltonen, T. (2002). Estimation of modal decay parameters from noisy response measurements. *J. Audio Eng. Soc.* 50, 867-878.
63. Collot, G. A new method for loss factor measurements using the Hilbert Transform implementation in a software to automize the 'Oberst' method. *International Modal Anlysis Conference Proceedings*, 389-393.
64. Cabanilla, N., Choudhury, N., Kachner, J., Yu, G. N. Determining the damping factor for the first four frequencies of vibration of a fixed-free beam and locating the nodes of vibration. Retrieved July 15, 2006, from http://www.seas.upenn.edu/courses/belab/LabProjects/2002/be310s02m5.doc.